Using multi-wavelength correlations to understand blazar physics.

Thesis for the Degree of Doctor of Philosophy

Pfesesani Victoria van Zyl

The University of the Witwatersrand,
Wits School of Physics

Academic advisors:
Dr. Andrew Chen[1], Dr. Aletha de Witt[2] & Dr. Roopesh Ojha[3]

May 30, 2023

[1]University of the Witwatersrand (WITS), 1 Jan Smuts Ave, Braamfontein, Johannesburg, 2000
[2]South African Radio Astronomy Observatory (SARAO), Farm 502 JQ, Hartebeesthoek, Broederstroom Road,1740
[3]NASA Goddard Space Flight Center, Greenbelt, MD 20771, USA

Declaration

I declare that this dissertation is my own, unaided work.

It is being submitted for the degree of Doctor of Philosophy at the University of the Witwatersrand, Johannesburg. It has not been submitted before for any degree or examination at any other University. All sources that I have used or quoted have been indicated and acknowledged by means of complete references.

P. V. van Zyl

Signed: Pfesesani Victoria Van Zyl

on this 30th day of May 2023 in Thohoyandou, Limpopo

Acknowledgements

"If I have seen further than others, it is by standing upon the shoulders of giants." - Sir Isaac Newton, 1675

I would like to take this moment to thank God for this journey and for placing the following people in my life who have been instrumental to my success.

I am deeply grateful to my academic supervisor, Dr. Aletha de Witt, for her unwavering encouragement, support, and guidance through the most challenging periods of my life. Her expertise and advice have been invaluable to me, and I will always be grateful for the many years we have worked together.

I also extend my sincere appreciation to my advisors, Dr. Roopesh Ojha and Dr. Andrew Chen, for their guidance and expertise in the preparation of this thesis. I would like to thank Chris Jacobs for sharing his JPL data and Christopher P. Volk for calibrating the JPL data. I am especially grateful to Dr. Stephan Larsson for generously sharing his correlation code and going above and beyond to help me set up everything on my machine. Roberto Nesci also deserves a special mention for generously sharing his optical data and taking the time to answer my questions and concerns.

I would like to thank Dr. Janeth Veronica Valverde Quispe for her patience, support, and advice with the Fermi analysis. To Dr. Stefanus van den Heever and Dr. Marisa Nikola, thank you for the discussions about the calibration problems and my code. I am also grateful to Heystek Grobler and Roelf Botha for always coming through for me with the IT and server problems and sharing their servers with me. My analysis would not have been possible without their help.

I am grateful to Dr. Tiffany Lewis and Dr. Jabulani Maswanganye for being mentors and listening ears when I needed it. I would also like to extend my thanks to Prof. Nukri for his understanding and patience with me. I would like to also extend a thank you to anyone who I may have missed, I appreciate your help and this work would not have been possible without you.

To my parents, siblings, and in-laws, I am deeply grateful for your unwavering prayers, support, and love. To my children, Liora, Tiahna, and Xavier, thank you for bringing sunshine into my life, especially during stressful times. You are a blessing, and I am so grateful to have you in my life.

I want to express my appreciation to my husband, Eugene, for his constant support, love, and strength.

Finally, I acknowledge the financial support of the South African Radio Astronomy Observatory, without which this work would not have been possible.

Abstract

Blazars are a subclass of Active Galactic Nuclei (AGN) with a jet pointing toward the observer's line of sight. These objects are highly variable, violent emitters of non-thermal radiation from radio to gamma-rays. The Hartebeesthoek Radio Astronomy Observatory (HartRAO) has been monitoring AGNs since the 1970s and has established itself as a key contributor of radio observations in the southern hemisphere, particularly for sources south of 30° that are beyond the reach of most northern telescopes. Currently, the HartRAO 26-m radio telescope monitors over 40 continuum and spectral line sources without a dedicated data reduction and analysis software package. This has resulted in a backlog of unprocessed observations, including critical observations necessary for the observatory's operations. In this work, I present a software solution for the HartRAO data reduction and analysis problem and test it on three blazar sources monitored at HartRAO in a multi-wavelength study. My project is arranged in two parts.

The first part of my project is a scientific investigation into the potential correlated relationships in multi-wavelength light curves of three HartRAO-monitored blazar sources to establish whether multi-resolution data can be used to support the models claiming that the higher energy gamma-ray emission leads the radio. Using the discrete correlation function (DCF), I estimate the correlations and time lags between the radio and gamma-ray wavelengths of my sample and find positive correlations with the gamma-rays leading the radio wavelengths by $\sim$ 100 to 200 days, which supports existing literature on the topic. These time lags represent the delay between the emission of gamma-rays and radio wavelengths and provide insight into the physical processes occurring in the blazar's jet, particularly the processes that lead to the emission of non-thermal radiation, an aspect of AGN studies that is still poorly understood.

The second part of my project focuses on the technical challenges of data reduction and analysis at HartRAO. I describe how data calibration is performed at HartRAO and test and evaluate the calibration processes to ensure the validity of the results. I also develop a software solution for the continuum data reduction and analysis of HartRAO data. The proposed solution includes a data reduction pipeline that utilizes an SQLite database to store the reduced and intermediate data products, as well as a user-friendly graphical user interface (GUI) for easy and quick processing of data. The new software provides the option to perform both batch and single-file processing and provides better performance compared to the old spectroscopy analysis program (LINES), previously used to process continuum data. By providing a software solution for data reduction and analysis, this thesis will enable HartRAO to make use of the critical observations that are currently backlogged and improve the observatory's operations.

Dedication

To my children, Liora, Tiahna and Xavier.

List of Abbreviations

4FGL-DR2	Fourth Fermi-LAT catalog based on the first 10 years of science data
DRAN	drift scan data reduction and analysis software
FERMIPY	open-source python framework that facilitates the analysis of data collected by the Fermi Large Area Telescope (Fermi-LAT)
FORTRAN	formula translation/translator program language
LINES	spectroscopy analysis program
PYTHON	Interpreted high-level general-purpose programming language.
4FGL	Fourth Fermi-LAT catalog based on the first 8 years of science data
ACD	Anticoincidence Detector
AGILE	Astro-rivelatore Gamma a Immagini LEggero
AGN	Active Galactic Nuclei
ATCA	Australian Telescope Compact Array
BLL	BL Lacertae or BL Lac, type of blazar
BLR	Broad Line Region
BSU	active galaxy of uncertain type
BVID	Bordeaux VLBI Image Database
CAL	Calorimeter
CLI	command-line interface
CMB	cosmic microwave background
DAQ	Data acquisition system
DCF	discrete correlation function
DEC	declination
DSN	Deep Space Network

DSS	Deep Space Station
EGRET	Energetic Gamma-Ray Experiment Telescope
EM	electromagnetic
ESRF	European Synchrotron Radiation Facility
EVN	European VLBI Network
FERMI-GBM	Fermi Gamma-ray Burst Monitor
FERMI-GST	Fermi Gamma-ray Space Telescope
Fermi-LAT	Fermi Large Area Telescope
FITS	Flexible Image Transport System
FNBW	first null beam width
FoV	Field-of-view
FSRQ	Flat Spectrum Radio Quasar
FST	FERMI SCIENCE TOOLS
GBM	Gamma Ray Burst monitor
GeV	giga electron-volt
GHz	Giga-hertz
GRB	Gamma Ray Burst
GSFC	Goddard Space Flight Center
GUI	graphical user interface
Hart26m	Hartebeesthoek Radio Astronomy Observatory (HartRAO) 26-m radio telescope
HartRAO	Hartebeesthoek Radio Astronomy Observatory
HDU	header data unit
HE	high energy
HPBW	half power beam width
HPN	half power north
HPS	half power south
Hz	hertz
IC	inverse Compton
ICRF	International Celestial Reference Frame
IRF	Instrument Response Function
ISM	interstellar matter
IVS	International VLBI Service for Geodesy and Astrometry

JPL	Jet Propulsion Laboratory
LAT	Large Area Telescope
LCP	left circular polarization
mas	milliarcsecond
MeV	mega electron-volt
MHz	mega hertz
MJD	modified julian date
MW	Milky Way
MWL	multi-wavelength
NASA	National Aeronautics and Space science Administration
NLR	Narrow Line Region
ON	on source scan
PSF	point spread function
PSS	point source sensitivity
QSO	Quasi-stellar object
RA	right ascension
RCP	right circular polarization
REM	Rapid Eye Mount
RF	Radio Frequency
RFI	radio frequency interference
rms	root mean square
RoI	Region of Interest
ROSS	Rapid Eye Mount (REM) Optical Slitless Spectrograph
SAA	South Atlantic Anomaly
SED	spectral energy distribution
SMBH	supermassive black hole
SNR	signal-to-noise ratio
SSC	synchrotron self-Compton
TeV	tera electron-volt
TKR	Tracker/Converter
TS	Test statistic
UDCF	Unbinned cross-correlation function

VLBA	Very Long Baseline Array
VLBI	Very Long Baseline Interferometry
ZDCF	Z-Transformed Cross-Correlation function

Contents

List of Figures

List of Tables

1 Active galactic nuclei

Active Galactic Nuclei (AGN) is the term used to describe some of the most powerful and consistent sources of radiation in the Universe. These sources are extragalactic objects that show astrophysical phenomena across varied scales throughout the entire electromagnetic (EM) spectrum, from radio wavelengths to gamma-rays. This observed variability is believed to come from the presence of a highly magnetized jet believed to emanate from a compact nucleus at the center of the galaxy. The nucleus can at times outshine the entire galaxy by a factor of a thousand, making these sources appear as extremely luminous point sources in the sky much like the stars we observe in our own galaxy the Milky Way (MW), only much further away. In this chapter, I provide an overview of the discovery of AGN in §1.1. I then follow up with a review of the physical properties of AGN focusing on properties most prominent in blazar sources which are the subject of this work in §1.2. I then discuss the energy distribution of blazar sources in §1.3 followed by an overview on source variability in §1.4. Lastly, §1.5 gives an overview of this thesis. This introductory chapter including various definitions and most of the illustrative calculations are based on the text books of Longair (2011), Beckmann and Shrader (2012), Carroll and Ostlie (2017), and Ghisellini (2013).

1.1 Brief introduction to AGN discovery.

AGN are luminous astronomical objects that have been frequently misidentified as stars due to their condensed structure, which renders them as point sources when observed from substantial distances. The first indication of their existence was discovered in the early 1900s by Curtis (1918), who observed an optical jet

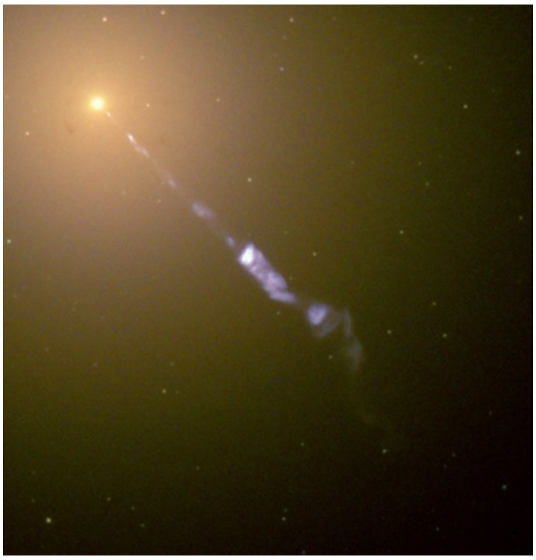

Figure 1.1: Hubble Space Telescope (HST) image of M 87, showing a bright unresolved nucleus and a narrow jet pointed away from the observer. *Credit: NASA and the Hubble Heritage Team (STScI/AURA)*

emitting from the galaxy M 87 [1] while studying images of nearby nebulae[2]. Curtis described M 87 as *"Exceedingly bright; the sharp nucleus shows well in* 5^{m} *exposure. The brighter central portion is about 0′.5 in diameter, and the total diameter about 2'; nearly round. No spiral structure is discernable. A curious straight ray lies in a gap in the nebulosity in p.a.* 20°*, apparently connected with the nucleus by a thin line of matter. The ray is brightest at its inner end, which is 11" from the nucleus."*, as seen in Figure 1.1.

Although not known at the time, Curtis had come across what would later become formally identified as a powerful source of broadband non-thermal high energy (HE) activity. Clues into the nature of these peculiar objects would remain a mystery until the discovery of extraterrestrial radio emission (Jansky, 1933; Reber, 1944), which marked the birth of radio astronomy and opened a new window to the Universe.

Seyfert (1943) conducted the first systematic study of the optical spectra of a sample of spiral galaxies and found that they had very bright central regions. He also observed strong broad emission lines (first noted by Fath, 1909; Slipher, 1917) in the nuclei of

[1] M 87 is one of 103 Nebulae and star clusters cataloged by Messier (1781).
[2] Giant clouds of gas and dust in space.

some of these galaxies with speeds[1] $\sim 10^3$ km s^{-1}. These galaxies were later named Seyfert galaxies in honor of Seyfert's pioneering work in this field.

After the technological advancements in radio brought about by World War II, particularly the application of interferometry techniques to radio observations (Michelson, 1920; Ryle, 1952), astronomers began to uncover features that gradually revealed the characteristics of galactic nuclei. The discovery of more radio sources, referred to as "radio stars", led to the development of the first complete catalogs of radio sources such as the Third Cambridge catalog (3C, Edge et al., 1959; Bennett, 1962a; Bennett, 1962b) of the northern hemisphere sources ($\delta^2 > -5°$) at 158 and 178 mega hertz (MHz), and the Parkes catalog (PKS, Ekers, 1969) of southern hemisphere sources ($\delta < +20°$).

Radio sources were known to be bright, discrete, and compact objects (Ryle and Smith, 1948). Their positions could be accurately identified (Smith, 1951; Hazard, Mackey, and Shimmins, 1963) and compared with those of their optical counterparts (Baade and Minkowski, 1954) if an optical counterpart had been identified in earlier studies. For example, the source, 3C 273 was found to be postionally consistent with an optical point source with a spectrum that presented strange spectral lines that did not match any known elements. It was Schmidt (1963) who later interpreted the lines as redshifted Balmer lines with a redshift (z) of 0.158. The discovery intrigued astronomers because the high redshift; at the time, implied that the source was extragalactic and had a high intrinsic luminosity $\sim 10^{46}$ erg s^{-1}. Following further discoveries of similar sources, these objects were later classified as Quasi-stellar objects (QSOs) or quasars.

As research on AGN continued to advance, different types of AGN were identified based on variations in orientation, features such as emission lines, and jet presence. One type of AGN that is particularly relevant to this thesis is the blazar. Blazars are a sub-type of quasar that come in two flavours; Flat Spectrum Radio Quasar (FSRQ) and BL Lacertae or BL Lac, type of blazar (BLL) (Pauliny-Toth et al., 1978). They are highly compact, variable sources that display variable behaviour across the

[1] Some galaxies like NGC 1068 showed speeds of 3600 km s^{-1} while NGC 4151 had speeds of 7500 km s^{-1}. Galaxies with the NGC naming convention are from the New General Catalog of nearby nebulae published by Dreyer, 1888.

[2] δ = declination

EM spectrum. Blazars are the most powerful type of AGN and emit most of their radiation through a highly magnetized jet that is aimed towards the observer.

In the following section, I will provide an overview of the commonly accepted physical explanations for the different observed AGN types, with a focus on blazars. For a more in-depth understanding of AGN, I refer the reader to the recent review by Padovani (2017).

1.2 Anatomy of AGN

AGN are a class of extremely luminous ($L_{bol} \sim 10^{43\text{–}48}$ erg s^{-1}) objects powered by an actively accreting supermassive black hole (SMBH) ($M_{SMBH} \sim 10^{6\text{–}10}$ $M_{\odot}$; where $M_{\odot}$[1] is the solar mass) lying at the center of a galaxy. These objects emit enormous amounts of radiation across the entire EM spectrum, from radio to gamma rays. They are also believed to consist of several key components, including a central black hole, an accretion disk that generates ultra violet (UV) emission, a dusty torus that produces infrared (IR) radiation, and a Broad Line Region (BLR) and Narrow Line Region (NLR) responsible for producing broad and narrow emission lines respectively.

AGN can be classified into different types based on the dominance and brightness of one or more of these components, as well as the viewing angle. The unification model suggests that all AGN are essentially identical objects, only differing in the amount of material the emission must traverse before reaching the observer. For instance, in the case of blazars, the observer is viewing the source head-on down the jet, leading to less absorption of the emitted radiation by surrounding interstellar matter (ISM). In contrast, Seyfert galaxies exhibit a significant reduction in the amount of observable radiation due to absorption and scattering effects from a dusty torus. AGN can also be classified based on the ratio of the strength of their radio emission to optical emission. The ratio seperates AGN into two main categories (i) radio quiet and (ii) radio loud (Kellermann et al., 1989). If the 5-GHz radio flux of the AGN source is more than 10 times the optical (B-band) flux ($F_5/F_B > 10$) at 6.8×10^{14}Hz (Urry

[1] $M_{\odot} = 1.989 \times 10^{30}$ kg

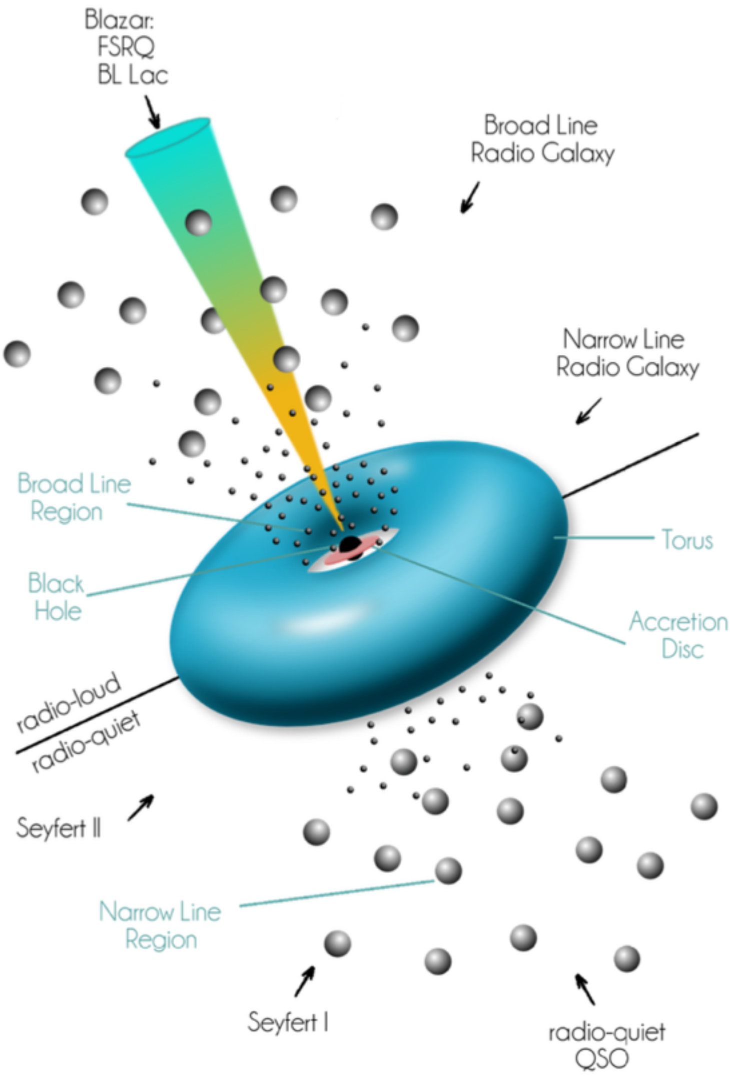

Figure 1.2: AGN unification model showing the radio-loud (top) and the radio-quiet (bottom) paradigm. All AGN are believed to host the same basic building blocks, a SMBH at the center, a dusty torus and an accretion disk around the SMBH. *Credit: adapted from Beckmann and Shrader (2012)*

and Padovani, 1995), then the AGN is classified as a radio loud source ("jetted" AGN), otherwise as a radio quiet source ("non-jetted" AGN)[1]. Figure 1.2 shows a schematic of the AGN model based on this classification scheme.

1.2.1 Non-jetted AGN

Radio quiet AGN account for the vast majority of observed AGN, with approximately 90% of these objects classified as such, primarily found in spiral galaxies (see Figure 1.3). Unlike their radio loud counterparts, these AGN do not exhibit significant jet emission, and are further divided into two main types: Seyfert 1 and Seyfert 2 galaxies, based on the visibility of both broad and narrow emission lines in Seyfert 1 galaxies, and the presence of only narrow emission lines in Seyfert 2 galaxies. Emission lines in AGN are produced by clouds of high-velocity gas surrounding the nuclei, specifically the NLR and the BLR, with typical Doppler shifts[2] of between 10^2 $\mathrm{kms^{-1}}$ and 10^3 $\mathrm{kms^{-1}}$ for particles in the NLR and BLR, respectively. The BLR, located in close proximity to the SMBH, is thought to be the primary source of HE production in AGN. Understanding the fundamental physics of radio quiet AGN is essential for gaining insight into the role that SMBHs play in shaping the galaxies in which they reside. The Seyfert classification system provides a useful framework for observing and analyzing the diverse range of AGN, and has led to many important discoveries about the structure and behavior of these fascinating objects.

1.2.2 Jetted AGN

Despite being the most luminous sources in the Universe, radio loud sources make up only about 10% of the total AGN content. These sources, known as Quasi-stellar object (QSO)s, are particularly bright and commonly observed at high redshifts primarily in elliptical galaxies (Schmidt, 1963, $z \sim 2$ - 6). Quasars are the most powerful type of AGN due to the presence of their highly relativistic jets. Based on the strength of their jet emissions, radio loud sources are divided into two types: Radio

[1] Applying the terms jetted and non-jetted to describe AGN were first suggested by Padovani, 2017.

[2] Doppler effect $\Delta\lambda/\lambda = \nu/c$ where $\nu << c$

galaxies and Blazars (Blazing Quasi-stellar objects). Radio galaxies have weaker jet emissions and their radio power is mainly concentrated in the Very Long Baseline Interferometry (VLBI) radio core (Fanaroff and Riley type I, FR I) and radio lobes (Fanaroff and Riley type II, FR II). Radio lobes are diffuse radio emissions that extend on either side of the AGN's polar axis. The FR I and FR II morphologies are further classified based on the presence or absence of broad emission lines, as shown in Figure 1.2. Blazars, on the other hand, have the strongest jet presence and are categorized into two main groups: BLL and FSRQ. This dissertation focuses on blazars and provides a comprehensive discussion of these sources in the following section.

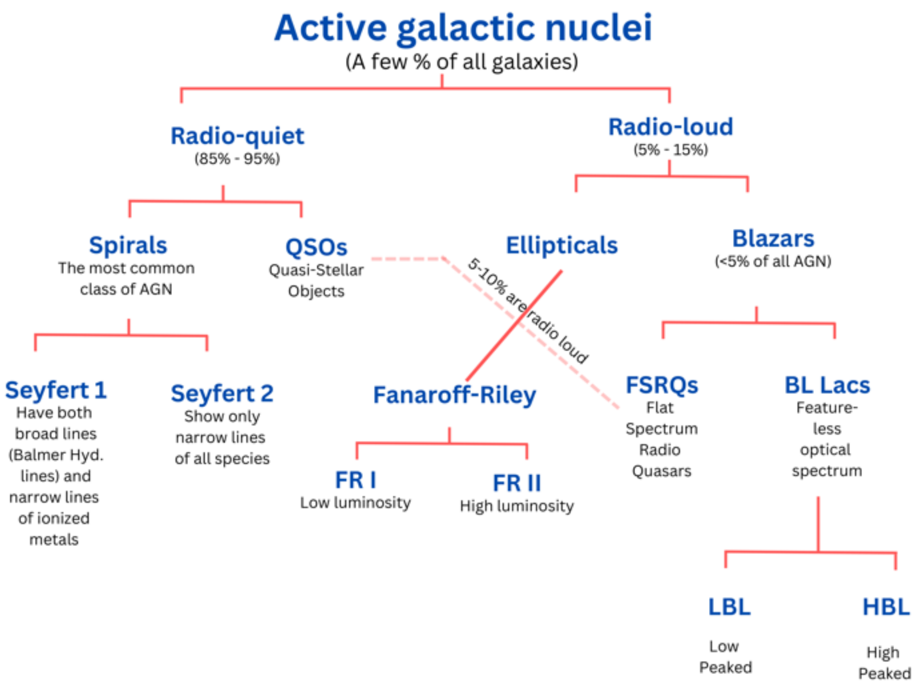

Figure 1.3: AGN classification diagram. *Credit: Adapted from D. Horan.*

1.2.3 An overview of blazar sources

In contrast to normal galaxies where the luminosity is contributed by the light produced by individual stars, AGN generate their luminosity through energetic phenomena in their nuclei. This emission is non-thermal in nature, produced by particle interactions that result in the acceleration of relativistic particles. This emission surpasses the luminosity emitted by the embedded stars and is brightest at the highest and lowest frequencies, appearing as a broadband continuum with a luminosity that is over a thousand times greater than a normal galaxy, originating from a region no larger than our solar system. Such a high level of energy generation cannot be explained by the thermonuclear processes of stars, but requires a more efficient mechanism. Currently, the most widely accepted explanation for AGN emission is matter accretion (§1.3.2.1) onto a SMBH.

While all AGN are fascinating, blazars are particularly intriguing due to their extreme properties. These highly variable objects emit non-thermal radiation from a bright nucleus at their center and are known to display rapid fluctuations in intensity within extremely short timescales, sometimes as short as a few minutes (DuPuy et al., 1969). The high degree of variability exhibited by blazars makes them captivating targets for scientific investigation, as scientists strive to unravel the mechanisms that drive their activity. As mentioned previously in §1.2.2, blazars come in two main flavors, BLL objects, also called Highly Polarized Quasars (HPQ), and FSRQs, also known as Optically Violent Variables (OVV)s. BLL objects are defined by their minimal or absent optical emission lines, which are typically overwhelmed by continuum emission. Furthermore, these objects are divided into four types of AGN based on the peak frequency of the synchrotron emission: Radio-selected BL Lac (RBL), X-ray selected BL Lac (XBL), Low-frequency peaked BL Lac (LBL) or red blazars, and High-frequency peaked BL Lac (HBL) or blue blazars (Padovani and Urry, 2001). In contrast, FSRQs are characterized by stronger line emission and high luminosity. Despite both BLLs and FSRQs being classified as blazars, these objects generally exhibit the following distinctive features. First, a substantial portion of their energy is radiated above 100 mega electron-volt (MeV). Second, they exhibit multi-wavelength variability and a flaring behavior. Finally, they have rapidly variable polarized optical and radio counterparts, with fluctuations occurring over timescales ranging from minutes to months.

1.3 Distribution of energy in AGN

1.3.1 Multi-wavelength emission

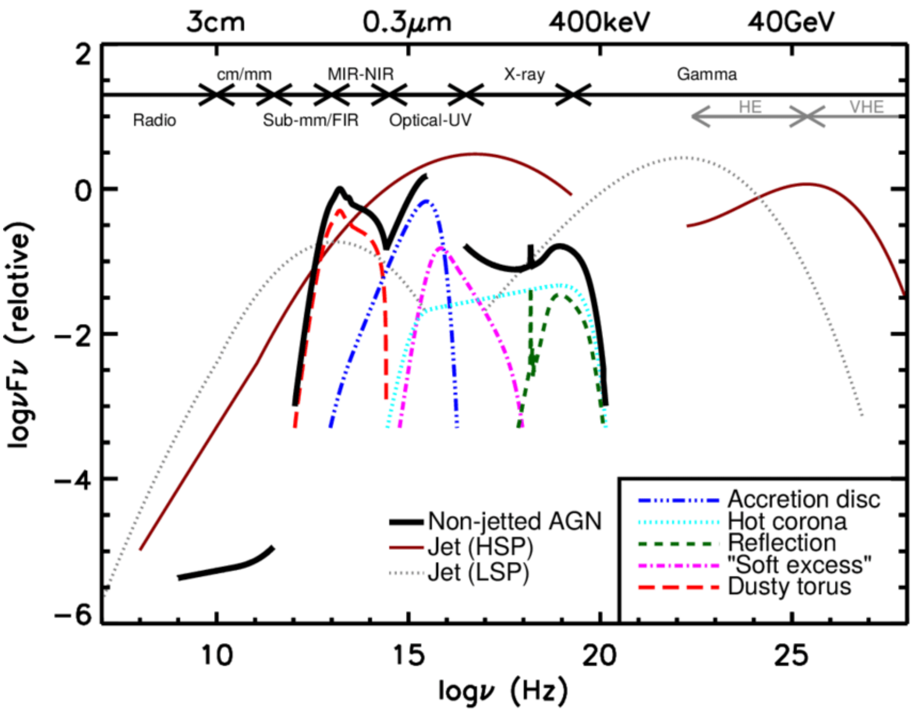

Figure 1.4: The blazar emission spectrum from a power-law distribution of electrons. *Credit: Padovani et al., 2017*

The emission from blazars is unique and can be characterized as a broad-band spectral energy distribution with a double-peaked shape, as shown in Figure 1.4. The first peak, which spans from radio to UV/X-rays, is associated with synchrotron electrons in the AGN's jet component. The location of this peak varies depending on the type of blazar, with RBLs and LBLs having their peak in the IR to optical range and HBLs and XBLs in the UV to X-ray range. Synchrotron radiation is responsible for the high polarization and rapid variability of blazars, which is caused by the relativistic motion of the electron particles. The second peak at giga electron-volt (GeV) and sometimes tera electron-volt (TeV) energies is due to inverse Compton (IC) scattering, which is thought to be produced by the same electron population responsible for synchrotron radiation. This process, known as synchrotron self-Compton (SSC), is still a topic of debate and is one of the essential scientific questions that need to be answered concerning AGN emission zones, particle content, and acceleration, as well as cooling near a black hole.

1.3.2 AGN energy sources

1.3.2.1 Accretion of Matter onto a black hole

Our understanding of AGN sources is primarily based on the radiation they emit, which arises from a diverse range of processes occurring in different regions of the AGN. AGN are thought to derive most of their energy from a highly magnetized central luminous core ($L_{AGN} \sim 10^{42} - 10^{48}$ erg sec^{-1}), which releases energy over a small region of a few parsecs (Fabian, 1999), occasionally surpassing the luminosity of the entire host galaxy. In order to sustain this massive energy release for extended periods of time, the SMBH at the center of the AGN must accrete surrounding ISM, gas, and dust particles at a high accretion rate

$$\dot{M} = \frac{L_{AGN}}{\eta c^2} \sim 1 - 2 \ M_{\odot} \ yr^{-1} \tag{1.1}$$

where η = the energy conversion efficiency and c = speed of light. Accretion of matter onto a black hole is an efficient mechanism for converting gravitational energy into electromagnetic radiation (Blandford, 2002), and it is one of the main sources of power for AGN.

As the ISM falls toward the SMBH, it contributes mass and angular momentum to the system. This incoming material forms an accretion disk around the black hole, as angular momentum must be conserved. Some of the material in the accretion disk is converted into radiated energy and accelerated/ejected as one or more narrow outflows of highly magnetized plasma along the accretion disk's rotation axis, forming a jet-like structure (see Figure 1.2). Matter accretion in AGN sources can generate energy that is two or more orders of magnitude brighter than what is observed from non-active galaxies, over timescales of a few hours or less. On these timescales, the inferred emission region's size, r, cannot be larger than

$$r \lesssim c\triangle t \tag{1.2}$$

where c is the speed of light and $\triangle t$ is the variability timescale. The energy generated by the accretion process in AGN is limited by the Eddington luminosity (L_{edd}), which is the maximum luminosity at which an object can continue to accrete matter at a steady rate (Equation . 1.1). The Eddington luminosity is given by the equation

$$L_{AGN} < L_{edd} = \frac{4\pi G m_p c}{\sigma_T} M \simeq 1.3 \times 10^{38} \mathrm{erg\,s^{-1}} \frac{M}{M_\odot} \tag{1.3}$$

For efficient accretion to continue, the gravitational forces (f_g) must always be greater than the radiated pressure (f_{rad}) (i.e., $f_g > f_{rad}$), as determined by the mass M of the source, the mass m_p of the protons and the Thompson cross section σ_T. However, there are instances where the radiative forces become greater than the gravitational forces ($f_g > f_{rad}$) causing the source luminosity to exceed the Eddington luminosity for short periods of time. When this occurs it is referred to as "flaring" or an outburst.

1.3.2.2 Relativistic jet emission

Blazars exhibit an extraordinary phenomenon where an excessive amount of energy is ejected out of the galaxy along the poles of the rotation axis, towards the observer's line of sight, in the form of one or two highly collimated polarized jets (Blandford and Konigl, 1979; Tammi and Oksman, 2013). These jets are believed to be the main sources of highly energetic and variable emission observed throughout the EM spectrum. The energy released in blazars can vary on short timescales, from hours to days (Marscher and Jorstad, 2010; Gupta et al., 2012), as well as on longer timescales of months to years (Hovatta et al., 2008; Nieppola et al., 2009; Pushkarev, Kovalev, and Lister, 2010). Relativistic jets in blazars are believed to form at a distance between roughly 10 and 10^3 Schwarzschild radii from the SMBH (Böttcher, Harris, and Krawczynski, 2012), making them remarkable structures to study. However, understanding the physics behind jet formation remains a complex and active area of research in blazar astronomy, particularly in determining the exact particle content of the jet structures, among other factors.

The magneto-hydrodynamics (MHD) acceleration model (Lovelace, 1976; Blandford and Znajek, 1977) is widely used to provide a fundamental analysis of jet physics. Particle acceleration of relativistically moving particles is believed to be the most probable mechanism for jet creation based on current understanding. Once created, the jets require a significant injection of energy to sustain the bulk acceleration of the particles. The excess energy can be extracted from the rotating accretion disk (Blandford and Payne, 1982; Meier and Koide, 2000) or possibly from a spinning black hole (Blandford and Znajek, 1977) and directed into the jet. The plasma flow of high-energy particles that makes up the jet propagates along well-defined paths of highly magnetic collimated streams, which flow along the rotation axis and are twisted along the jet direction by the ergosphere of the rotating black hole, forming helical field lines. Figure 1.5 presents an artist's impression of a quasar's jet structure.

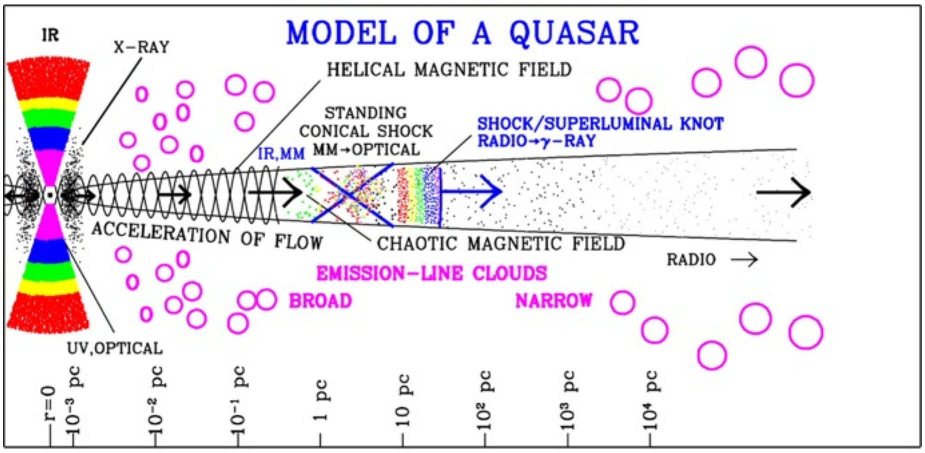

Figure 1.5: Propagation of shocks in the collimated jet stream of a quasar: a schematic diagram showing the distance from the black hole in parsecs. The figure illustrates the expected location of initial flaring during a flaring event, with the first flare occurring closer to the end of the collimation zone region and the second flare within the millimeter-wave core. *Image credit: Boston university blazar group web notes.* [1]

When particles are accelerated perpendicular to magnetic field lines at relativistic speeds, they emit synchrotron radiation as explained in §1.3.3. However, at low frequencies, the emitted radiation appears optically thick due to highly variable

[1]https://www.bu.edu/blazars/Images/quasaremiscol5.jpg

magnetic fields at the base of the jet causing turbulence in the plasma. This results in electrons becoming opaque to their own synchrotron radiation, a process known as synchrotron self-absorption. As particles travel further downstream along the jet, the magnetic field strength decreases as it converts to kinetic energy. As a result, the jet becomes optically thin to radio emission, which is observed as a standing shock or radio core (as shown in Figure 1.5).

The process of shock formation and propagation in radio jets is a complex phenomenon that is not fully understood. However, current research suggests that shocks are likely created when there is a significant disruption in the steady flow of the jet (Marscher, 1990). These disruptions typically occur at points where there are steep pressure gradients, which cause disturbances that propagate down the jet at superluminal speeds. As particles move through the jet and encounter the shock front, they undergo a process of energy gain known as fermi acceleration (Fermi, 1954). This process continues until the energy gained is sufficient for the particles to be accelerated across the shock front, which causes the shock to expand adiabatically (Laan, 1966; Kellermann and Pauliny-Toth, 1968) as it moves down the jet. These shocks are responsible for the variable behavior observed in the emission from radio jet sources, as they produce instabilities in the flow and particle acceleration. It is worth noting that the motion of particles in the jet is highly relativistic, with their bulk motion expressed in terms of the bulk Lorentz factor Γ given as

$$\Gamma \equiv \frac{1}{\sqrt{1-\beta_{\Gamma}^{2}}} \tag{1.4}$$

where $\beta_\Gamma = \nu_j/c$ is the jet plasma velocity and ν_j is the jet bulk velocity.

The study of AGNs, such as blazars, has revealed that the plasma jets emitted by these sources can attain velocities close to the speed of light, resulting in a bulk Lorentz factor Γ of $\sim$10 to 30. In some cases, plasma jets pointing towards the observer may appear to have velocities greater than the speed of light ($\nu_{\mathrm{apparent}} > c$), leading to what is known as superluminal motion. This apparent superluminal motion is a result of the relativistic Doppler boosting effect, which causes an increase in the apparent velocity of the plasma jet. The magnitude of this effect is determined by the Doppler factor δ, which is a crucial parameter in the study of relativistic jets and is given by the equation

$$\delta = \frac{1}{\Gamma(1-\beta_\Gamma \cos\vartheta)} \tag{1.5}$$

which depends on the angle, ϑ, between the jet direction and the observer's line of sight. This factor is boosted along the direction of relativistic motion by a factor of approximately 2Γ, causing the light to be strongly beamed into a cone of opening angle $\vartheta = 1/\Gamma$, typically less than 20°. Precession of jets has been observed in some cases (Smith, 2012), causing variations in observed flux density. This has led to suggestions of possible binary SMBH systems that could produce periodicity in observed light curves (Rieger, 2005).

1.3.3 Radio emission processes

1.3.3.1 Synchrotron emission

The radio emission from AGN jets is produced by synchrotron radiation, which is a non-thermal process involving the acceleration of relativistic electrons in the presence of a magnetic field (B). The emitted radiation has a characteristic frequency, ν_c, which is determined by the energy of the electron ($E = \gamma m_e c^2$) and the strength of the magnetic field. The peak frequency of the emission, ν_{peak}, is typically around $0.29\nu_c$ with

$$\nu_c = \frac{3\gamma^2 eB}{4\pi m_e c} \tag{1.6}$$

$$\gamma = \frac{1}{\sqrt{1-(\nu/c)^2}} \tag{1.7}$$

where e = electron charge, m_e = mass of electron (511 keV/c^2), c = speed of light, and γ = the Lorentz factor

In order for an electron to radiate at a frequency $\nu \sim 10$ GHz in a magnetic field $\sim 10^{-4}$ G, it would need to have a minimum Lorentz factor of about $\sim 10^5$. This indicates that the electrons in AGN jets must be highly relativistic. When an electron is moving at relativistic speeds in a magnetic field, it will generate an average total radiated power, P_{rad}, of

$$P_{rad} = \frac{4}{3}\sigma_T c \beta^2 \gamma^2 U_B \tag{1.8}$$

where σ_T is the Thompson cross-section and $U_B = B^2/8\pi$ is the energy density of the magnetic field, assuming an isotropic distribution of electron velocities (Rybicki and Lightman, 1979). As an electron radiates, it emits energy and consequently cools down over time (as shown in Equation 1.9). This cooling rate provides a means for estimating the electron's lifetime, τ_{rad}, by dividing the total energy by the instantaneous power, as shown in Equation 1.10 .

$$\frac{dE}{dt} = P_{rad} \propto \gamma^2 U_B \tag{1.9}$$

$$\tau_{rad} = \frac{E}{dE/dt} \propto \frac{1}{\gamma^2 U_B} \tag{1.10}$$

At lower frequencies, the synchrotron radiation emitted by electrons that were accelerated some time ago will typically be emitted by electrons that have lifetimes on the order of $\tau_{rad} \sim 10^8$ years. The energy radiated in the frequency range ν to $\nu + d\nu$ for an electron distribution with energies between E and E + dE, and an electron number density, $N(E) = KE^{-p}$, can often be described in terms of a power-law relationship of the form

$$F_\nu \propto \nu^{-\alpha} \tag{1.11}$$

where F_ν is the flux density of the source, and α is the radio spectral index of the synchrotron emission spectrum. The radio spectral index is related to the particle distribution index p which is the slope of the log-log representation of N(E) through the equation

$$\alpha = \frac{(p-1)}{2} \tag{1.12}$$

The emitted radiation from electrons spiraling around a magnetic field covers a wide range of frequencies, with the energy spectrum following a power-law distribution that peaks at the critical frequency (Equation . 1.6) of the emitting electron. By adding up the contributions of all electrons, a characteristic spectrum is obtained which shows a steady decline in flux density with increasing frequency and is also described by Equation 1.11. Figure 1.6 shows this spectrum, which represents the synchrotron emission over a broad range of frequencies with ν_{max} (turnover frequency) being the frequency at which the flux density reaches a maximum. At frequencies lower than ν_{max} ($\nu << \nu_{max}$), the source becomes optically thick to synchrotron radiation, resulting in a characteristic spectrum described by $F_\nu \propto \nu^{5/2}$, typical of self-absorbed ($\tau \sim 1$) opaque synchrotron sources. Conversely, at frequencies higher than ν_{max} ($\nu >> \nu_{max}$), the source becomes optically thin to synchrotron radiation with a characteristic spectrum described by $F_\nu \propto \nu^{-(p-1)/2}$.

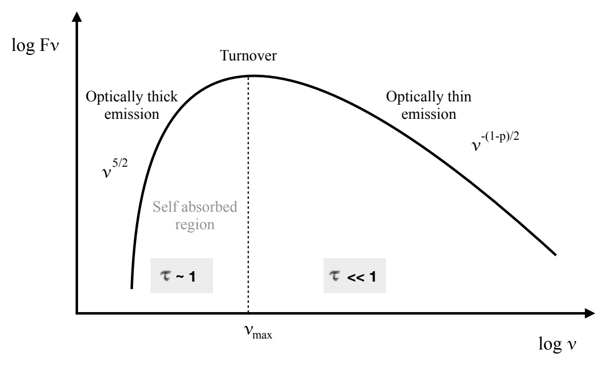

Figure 1.6: Synchrotron emission spectrum from a power-law distribution of electrons showing the characteristic power-law decline in flux density with increasing frequency. *Image credit: Adapted from Rybicki and Lightman, 1979.*

1.3.4 Gamma-ray emission processes

Gamma-ray emission is characterized by short wavelengths and high frequencies, typically falling between 10^{16}Hz $< \nu <$ 10^{26}Hz with energies that surpass the MeV range. For such energy levels to be generated, the emission must come from a region within 1 pc of the source core in the BLR, near the jet base. However, the exact location where gamma-rays are formed within this region and the particle content responsible for the observed emission remains a topic of intense debate. Currently, two models have been put forth to explain the origin of the high-energy component of blazar jets: the leptonic and hadronic models. These models propose different particle contents and emission methods.

1.3.4.1 Leptonic model

The Leptonic model assumes that the main particles responsible for gamma-ray emission are leptons, specifically electrons and positrons. According to this model, gamma-ray emission occurs when these electrons interact with low-energy radio photons, causing the photons to gain energy and transform into higher-energy gamma-ray photons. This process, known as IC scattering, results in the electron losing energy while transferring it to the radio photon. The boosted photon energy can be up to a factor of $\sim \gamma^2$ times the original energy, where γ is the electron's Lorentz factor and $m_e c^2$ is its rest mass energy. There are two forms of IC scattering, depending on the origin of the seed photons that are scattered. When the seed photons are from the same population of relativistic electrons that produce synchrotron emission within the jet, it is called SSC Marscher and Gear, 1985. On the other hand, if the seed photons originate from an external source, such as the BLR (Sikora, Begelman, and Rees, 1994), accretion disk (Dermer and Schlickeiser, 1993), or cosmic rays, it is referred to as external Compton (EC). In this study, we will focus solely on SSC which involves radio synchrotron emission forming a crucial part of the thesis. The total power emitted by relativistically boosted photons in an isotropic distribution of electrons due to IC scattering takes the form

$$P_{IC} = \frac{4}{3}\sigma_T c\beta^2\gamma^2 U_{ph} \tag{1.13}$$

where U_{ph} is the radiation energy density of the photons before scattering. IC losses have the same energy dependence as the synchrotron losses, except for the energy density being attributed to the photons instead of the magnetic field (Equation 1.8). The equations (Equation 1.8 and Equation 1.13) describe the interaction of an electron with an EM field. Downstream of the jet, electrons accelerated across a shock front lose energy, making it difficult to produce synchrotron radiation at higher frequencies because they cannot radiate much above the critical frequency (Equation 1.6). The lifetimes of IC electrons are $\sim 10^4$yrs. To sustain these electrons, a continuous injection of relativistic particles would need to occur throughout the jet continuously, not just at the base where the radio emission is believed to be generated. The ratio of the IC to synchrotron losses,

$$\eta = \frac{P_{IC}}{P_{rad}} = \frac{U_{ph}}{U_B} \tag{1.14}$$

is a significant result. Electrons in a region that has both photon and magnetic energy will emit both synchrotron and IC radiation. However, there are limitations to this result. If the photon energy density becomes larger than the magnetic energy density, an IC catastrophe will occur (Kellermann and Pauliny-Toth, 1969). This results in high-energy electrons losing more energy more quickly because more energy is needed to scatter the X-rays to gamma-rays. Like synchrotron emission, if the particle energy spectrum is a power-law, the radiation spectrum is also a power-law. The radiation produced by IC scattering has a power-law spectrum.

The leptonic model has been widely accepted as a model that can accurately model the spectral energy distribution (SED)s of most blazar classes. For magnetic fields of ~ 1 G, radiative cooling times are ~ 1 d and $\lesssim 1$ hr in optical and x-rays, respectively, compatible with observed intraday variability. However, the leptonic model is not the only one suggested for describing high-energy emission regions (Dermer and Lott, 2012; Ojha, 2012; Böttcher et al., 2013)

1.3.4.2 Hadronic model

The hadronic model offers an alternative explanation for the high-energy emission in blazars. The model suggests that the dominant particles are relativistic protons, with the high energy emission explained through the creation of gamma-rays from secondary particle interactions. The assumption is that although synchrotron emission still dominates the low frequency regime, the high energy emission is a product of the relativistically accelerated protons. Because of the mass of the proton (m_p = 1836 m_e) a lot more energy is required to accelerate the protons. Accelerated protons produce neutral and charged pions that decay into electrons and positrons, which then ultimately produce the radiated gamma-ray photons and neutrinos. To produce γ-rays with energies (E > 100 MeV) scattering of photons from the following processes, π^0 decay ("π^0 cascade"), electrons from $\pi^{\pm} \rightarrow \mu^{\pm} \rightarrow e^{\pm}$ decay ("$\pi^{\pm}$ cascade"), p-synchrotron photons ("p-synchrotron cascade"), and μ-, π- and K-synchrotron photons ("$\mu^{\pm}$-synchrotron cascade") can produce the required protons needed for relativistic proton acceleration (for a full breakdown of the hadronic processes please refer to Boettcher, 2010; Böttcher et al., 2013).

The Hadronic model however has not been as widely accepted due to its large energy dependencies. In some extreme cases when the SEDs of blazars cannot be explained using the leptonic model, the Hadronic model generally works well as shown by Böttcher, Reimer, and Marscher, 2009. For further details on hadronic processes the reader is referred to, e.g. Böttcher et al. (2013) and Cerruti (2020).

1.4 Variability and multi-wavelength studies

The field of study concerning the origin of emission mechanisms in blazars remains unresolved, despite the effectiveness of current emission models in describing the behavior of blazar emission (Costamante, 2012; Xue et al., 2019). Ongoing research is being conducted on the radio jets in blazar sources, as they are believed to hold crucial information about high energy phenomena. The variability in the emission of these sources is thought to be caused by the shocks experienced by the relativistically moving particles in the parsec-scale structures. Additionally, a correlation between radio and gamma-ray emission has been observed in these sources (Kovalev et al., 2009; Max-Moerbeck et al., 2014; Appl and Camenzind, 1988). On very small scales, such as those observed through techniques such as VLBI or milliarcsecond (mas) scales (Figure 1.7a), the frequency-dependent core shift can be measured. This shift in the radio core position, which is more pronounced at lower frequencies, is attributed to the SSC (Figure 1.7b, Sokolovsky et al., 2011). The core shift also provides information about the time delay between light curves at independent frequencies.

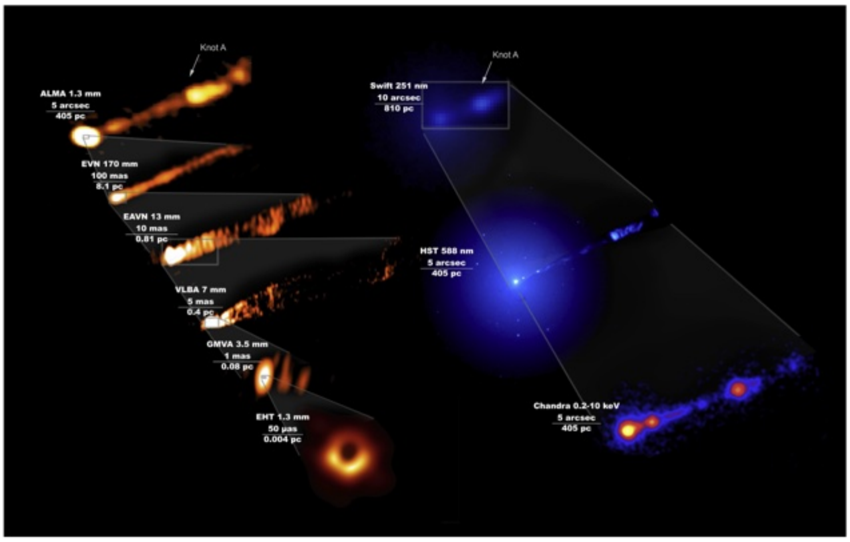

(a) Multi-resolution images of the galaxy M87. The image shows the different parts of the galaxy that are observed at different scales or resolutions. *Image credit: The EHT MWL Science Working Group et al., 2021*

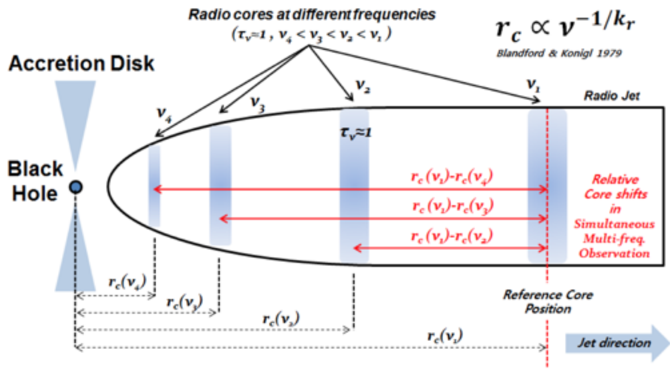

(b) Schematic impression of the radio VLBI cores at various frequencies from lowest (ν_1) to highest (ν_4). *Image credit: JUNG et al., 2015.*

Figure 1.7: Figure(a) shows multi-resolution VLBI images of the galaxy M 87. The images show the jet structure on mas scales, and (b) illustrates the radio VLBI core at different frequencies.

Assuming that the particle content of the jet is purely made up of electrons, the Shock-in-jet or internal shocks model, developed by Marscher and Gear, 1985, is employed in attempts to explain the jet features. While there are other more complex models, such as those involving magnetic reconnections (Giannios, 2013), shock/jet recollimation (Cohen et al., 2014; Perucho, 2013), and binary SMBH (Rieger, 2005), the Shock-in-jet model is widely used. During flaring events, the physical conditions in the jet undergo significant changes. These changes result in the formation of shocks within the expanding jet, which in turn accelerate the electrons to higher energies, producing optically thin radio synchrotron and gamma-ray emission. The variations in flux density observed during the ejection of a new jet component can be attributed to some particles gaining more energy while others lose energy. In certain cases, multiple flaring events can be observed. These flares are believed to be caused by inhomogeneities in the jet region or a shock resulting from a previous, slowly propagating flare. The shocks produced in blazar jets give rise to emission spread across the EM spectrum. This is why it is important that these sources are observed at multiple wavelengths to study the variability and possible connections between different frequencies. Blazar light curves can also tell us about the creation and evolution of synchrotron emission.

The year 2008 provided a breakthrough in probing these objects with the launch of the Fermi Gamma-ray Space Telescope (FERMI-GST)[1]. Its mission was to detect and image gamma-rays from a low Earth orbit. Commissioned for detecting gamma-rays with energies between 20 MeV and 1 TeV, this meant that galaxies could now be probed through the most violent of events occurring very close to the black hole, providing a gateway to studying the inner workings of these sources. Given the nature of these structures, it is very difficult to draw conclusions about their behavior by using only single-frequency observations. Thus, a multi-wavelength analysis is required to establish the true nature, location, and effect of the emitted radiation. Furthermore, having an adequate dataset, e.g. from monitoring observations, becomes increasingly important in order for scientists to draw conclusions on the true source activity, especially for flaring blazar sources whose flux can vary within minutes or days. Constant and consistent monitoring ensures we get epochs for both the long-term and fast-varying activity.

[1] http://www-glast.stanford.edu/

1.5 Research plan

Long-term multi-wavelength (MWL) monitoring of blazar sources may hold the key to getting a comprehensive physical understanding of AGN. AGN are high-luminosity galaxies with a compact core believed to host a SMBH. A blazar is a type of AGN that displays highly variable non-thermal emission generated by a relativistic jet aligned to our line of sight (Rees, 1978). These objects have been observed to vary over a range of timeframes throughout the EM spectrum, from within a few months, to days and in some rare but extreme cases shown to vary within minutes (Liodakis et al., 2018; Agarwal et al., 2019; Meyer, Scargle, and Blandford, 2019). Studying the variable nature of these sources is critical for understanding high energy activity. These studies inform our understanding of the particle content as well as the acceleration mechanisms inherent in these systems, thus allowing us to place constraints on the size and location of the emitting region. However, if any meaningful information is to be extracted from blazar observations, the observations must be carried out simultaneously or quasi-simultaneously to get adequate source coverage. This is especially important during epochs of interest, for example, during a flaring event where the source fluxes can vary over very short timeframes providing valuable insights into the acceleration processes. This can be challenging for various reasons, one being the ability of different observatories to collaborate on MWL projects, especially in the southern hemisphere where southern sources are currently underexploited due to the relatively small number of astronomical sites on that side of the equator compared to the northern hemisphere.

In this work, I present a multi-wavelength study of a set of three Hartebeesthoek Radio Astronomy Observatory (HartRAO) monitored blazar sources. Two of the blazars I present are gamma-ray emitting sources, but the fourth is not, even though it is found to be highly compact on mas scales. The study aims to use a set of long-term, MWL, multi-resolution monitoring observations to study and characterize the source activity of my sample sources by investigating the possible cross-correlated relationships between the light-curves. I present this work in two parts.

The first part, *Multi-wavelength study of HartRAO monitored blazar sources* is an astronomy science project aimed at understanding the long-term behavior of the selected sample of blazar sources monitored at HartRAO. This work presents a detailed study of the relationship between the blazar radio and gamma-ray wavelengths. The results presented here are aimed at furthering our understanding of blazar emission processes during flaring events and also add new sets of previously unpublished radio flux density lightcurves from the HartRAO 26-m radio telescope (Hart26m). IIn Chapter 2 I detail the main characteristics of the instruments used to make the observations for all the data used in the study. Chapter 3 discusses the data analysis processes for the instuments mentioned in chapter 2. Chapter 4 lists the results, which are then concluded on in Chapter 5.

The second part, *HartRAO 26-m calibration and development of new software pipeline* provides the technical overview of the project. This part of the project is solely based on the HartRAO 26-m radio telescope (Hart26m) data processing. HartRAO has been in operation for over 30 years, and yet it does not have its own standard, fully automated in-house data processing software. In this work, I provide a detailed study into the calibration and data reduction processes carried out at HartRAO to develop an understanding of how radio calibration is done. I also use my new skills to develop a fully automated data reduction and analysis software program designed to run daily data reduction of regularly monitored calibrator sources. The software has also been adapted to cater to processing and analyzing target sources as well. In Chapter 6, the calibration process and issues with calibration of HartRAO sources are discussed. In Chapter 7 I describe and discuss the new software I developed, tested, and used to calibrate and process HartRAO data. Finally, in Chapter 8 I summarize on what the new software means for HartRAO and the future of data reduction and calibration of HartRAO monitored sources.

Part I

Multi-wavelength study of HartRAO monitored blazar sources

2 The detectors

Multi-epoch and multi-wavelength observations of extragalactic sources offer critical observational evidence and support to ideas and theories developed to improve our understanding of HE astrophysics. However, observations on their own are not useful unless a thorough understanding of the instruments used to detect them has been established. This project looks at three specific energy ranges within the electromagnetic spectrum: the radio, optical, and gamma-ray, each requiring its own specialized detectors.

The Hart26m and the Fermi Large Area Telescope (Fermi-LAT) were used as the main instruments for data collection, while the Rapid Eye Mount (REM) as well as other various VLBI networks supplemented the data set with archival data. In this chapter, I discuss the primary operational and technical properties of these telescopes. Since the Hart26m and the Fermi-LAT are the main instruments used in this study, a significant portion of this chapter is dedicated to their discussion.

2.1 HartRAO 26-m Radio Telescope

All continuum radio observations were carried out using the Hart26m. This section highlights the properties of the Hart26m that are relevant to the observing techniques used in this study.

2.1.1 Brief history of HartRAO

In 1958, the National Aeronautics and Space science Administration (NASA) [1] developed a deep space communications and navigation network, called the Deep Space Network (DSN)[2], in support of its interplanetary spacecraft missions. The DSN at the time consisted of an array of three 26-m radio telescopes called the Deep Space Station (DSS) antennas. These DSS sites consisted of DSS 11[3] at Goldstone, California, United States (built in 1958, retired in 1981 to become a museum exhibit), DSS 41[4] at Island Lagoon, Woomera, Australia (built in 1960, decommissioned and demolished in 1972) and DSS 51[5] at Hartebeesthoek, near Johannesburg, South Africa (built in 1961, decommissioned in 1974, and transformed into a radio astronomy telescope).

The 26-m antenna at the DSS 51 site in South Africa originally had a primary aluminum surface that operated at around 960 MHz ($\sim$30 cm). The station supported missions that provided the first close-up images of the planet Mars (Mariner IV Mission, 1965), explored and mapped the lunar surface (e.g. Ranger VII, 1964 and Surveyor VII, 1968), measured solar winds and flares (Pioneer VIII, 1967), landed men on the moon (Apollo 15 moon landing, 1971), and numerous other noteworthy missions listed on the HartRAO DSS 51 missions page[6]. Figure 2.1a shows the 26-m antenna at the official opening of DSS 51 in 1961. An image of the plaque presented to the DSS 51 site after the Ranger VII lunar imaging mission is shown in Figure 2.1b.

After spending over a decade tracking spacecraft for NASA, in 1974 the 26-m telescope at DSS 51 site was decommissioned and the site was handed over to the Council for Scientific and Industrial Research (CSIR) to become a radio astronomy facility due to rising political conflicts. In 1988, the site started operating as a national facility, called HartRAO, under the Foundation for Research and Development (FRD) which was restructured as the National Research Foundation (NRF) in 1999. The observatory has since become a part of the South African Radio Astronomy Observatory (SARAO),

[1] https://www.nasa.gov
[2] https://www.nasa.gov/directorates/heo/scan/services/networks/deep_space_network/about
[3] https://www.gdscc.nasa.gov/index.php/history/
[4] https://www.nasa.gov/directorates/heo/scan/services/networks/DSN50Gallery-13.html
[5] http://www.hartrao.ac.za/other/dss51/dss51.html
[6] http://www.hartrao.ac.za/other/dss51/missions.html

(a) The official opening of the DSS 51 site in 1961. **(b)** Ranger VII lunar mission plaque.

Figure 2.1: The figures shows historical photos from DSS 51. Figure (a) shows the 26 m antenna at the official opening ceremony of DSS 51 in 1961, and (b) the plaque commemorating one of the many highly successful lunar exploration missions involving DSS 51, the Ranger VII mission.

a facility of the NRF responsible for managing radio astronomy research facilities in South Africa, and now operates as SARAO.

The original idea to develop DSS 51 into a radio astronomy observatory started even before 1974 and the task was handed to the then NASA engineer George Nicolson. Nicolson developed a noise-adding, gain-stabilized radiometer for continuum observations which he also used to map the Milky Way. As part of the agreement NASA had with the CSIR, Nicolson ran radio astronomy experiments during non-operational periods when the antenna wasn't tracking spacecraft (Gaylard and Nicolson, 2007; Nicolson, 1965; Nicolson, 1966). In his bid to grow and develop new research areas, instruments, and observing techniques, many young graduates from local Universities (Rhodes and the University of the Witwatersrand) were recruited by Nicolson to participate in astronomy projects using the 26-m telescope. Among them was Peter Mountford and Justin Jonas who developed the HP1000 mini-computer-based control system which operated the telescope in the 1970s, and Michael Gaylard who developed the spectroscopy observing program and the spectroscopy analysis program called spectroscopy analysis program (LINES), in the 1980s. The LINES software package has been the main data processing software at HartRAO for over 30 years and has become obsolete for the kind of research projects being run in the current day. The case for its replacement is thoroughly discussed in Chapter 7.

Since the conversion of DSS 51 into a radio astronomy observatory, the Hart26m has contributed significantly to the field of radio astronomy. This is thanks to the upgrade of the 250 mesh panels that made up Hart26m's primary surface[1]. Replacing the mesh panels with solid aluminum panels increased the sensitivity of the telescope from a 2.5 mm rms surface accuracy to a 0.5 mm surface accuracy, pushing the antenna upper-frequency limit from 15 GHz to 22 GHz. Contributions from Hart26m include but are not limited to the detection of the discovery of periodic variability in methanol maser transitions associated with high-mass star formation regions (Goedhart, Gaylard, and Walt, 2003) the detection of the Vela Pulsar glitches (Buchner and Flanagan, 2008), the discovery of a triple SMBH system (Deane et al., 2014), and the location of the origin of the neutrino HESE-35[2] (Nemenashi, Gaylard, and Ojha, 2013; Kadler et al., 2016).

Throughout its 61 years of existence, the Hart26m has only had one major operational failure. On the 3rd of October 2008, the South end of the main polar shaft bearing failed, causing the telescope to be immediately decommissioned for at least two years while it underwent repairs[3]. Since then, the telescope has returned to full working condition and has had no major incidents to date. Due to its unique location in the Southern hemisphere, the Hart26m is also an important element in many VLBI networks for both astronomy and geodesy applications (e.g. Witt et al., 2013 and Mayer et al., 2014). For example, the Hart26m played a crucial role in the realization of the third and most recent International Celestial Reference Frame (ICRF) (Charlot et al., 2020). HartRAO is a multifaceted research unit, operating a host of different instruments for radio astronomy and space geodesy. It is also home to the HartRAO 15-m telescoped, originally called the eXperimental Development Model (XDM)[4] telescope, the prototype of the MeerKAT[5] telescope which is the precursor to the square kilometer array (SKA)[6]. The reader is referred to the HartRAO website for a full list of the HartRAO instruments[7].

[1]The panels were upgraded from the previous mesh panels used by the DSN between 1998 and 2003. See, http://www.hartrao.ac.za/news/030910surface/index.html

[2]The single-dish HartRAO radio data used in this study were collected and processed by the author. See, https://www.dst.gov.za/index.php/media-room/opinion-pieces/1762-hartrao-helps-to-find-big-birds-nest

[3]http://www.hartrao.ac.za/news/100906_26m_repair/index.html

[4]The XDM is equipped with a concentric feed 2.3/8.4-GHz cryogenic receiver used primarily for geodetic VLBI operations.

[5]A 64-element array made up of 13.5-m antennas. https://www.sarao.ac.za/science/meerkat/

[6]https://southafrica.skatelescope.org/welcome/

[7]http://www.hartrao.ac.za/summary/sumeng.html

2.1.2 The detector

All of the single-dish radio observations discussed in this work were made using the Hart26m. The Hart26m is a parabolic, equatorially-mounted telescope nestled in a valley in the Magaliesberg hills (27.685° East, 25.887° South), about 50 km north-west of Johannesburg. The optics of the telescope follow a Cassegrain design, with a 26-m solid aluminum primary reflector of 250 individually adjustable panels and a 3-m diameter hyperbolic secondary reflector. The telescope has a focal ratio f/D of 0.424, and a surface accuracy of 0.5-mm rms. During observations, the telescope steers an approximately two hundred-ton steel structure across the Southern skies, tracking and monitoring radio sources at a slew rate of 0.5° per second in each axis. For single-dish observing the telescope operates under direct computer control by the Linux-based New Control Computer System (NCCS), which is maintained by the European Synchrotron Radiation Facility (ESRF). Figure 2.2 shows an image of the Hart26m with the HartRAO 15-m telescope in the background. The image also shows a magnified insert of the 26-m primary reflector, secondary reflector (hereafter, sub-reflector), the L-band 18 cm (1.7 GHz) receiver, and the feed housing which contains all the other receivers.

2.1.3 Observing limits and operating modes

The Hart26m is used for astronomical, astrometric, and geodetic observations and operates in both single-dish and VLBI modes. It is limited by an absolute declination of 45° north of the equator. The observing limits of the telescope are imposed by a complex function that is constrained by the telescope's mechanical limits in the north and south, and the local topography surrounding the Hart26m in the north-east and south-west. Figure 2.3a shows the elevation limits that restrict the observing capabilities of the Hart26m.

For single-dish flux measurements of unresolved continuum sources, the Hart26m primarily observes in drift-scan mode, in which the telescope is parked a little west of the object of interest and the signal is sampled as Earth rotation moves it through the telescope beam. (Briggs et al., 1997). This technique has many benefits, the most important being that the telescope is passive, i.e. it is not required to track

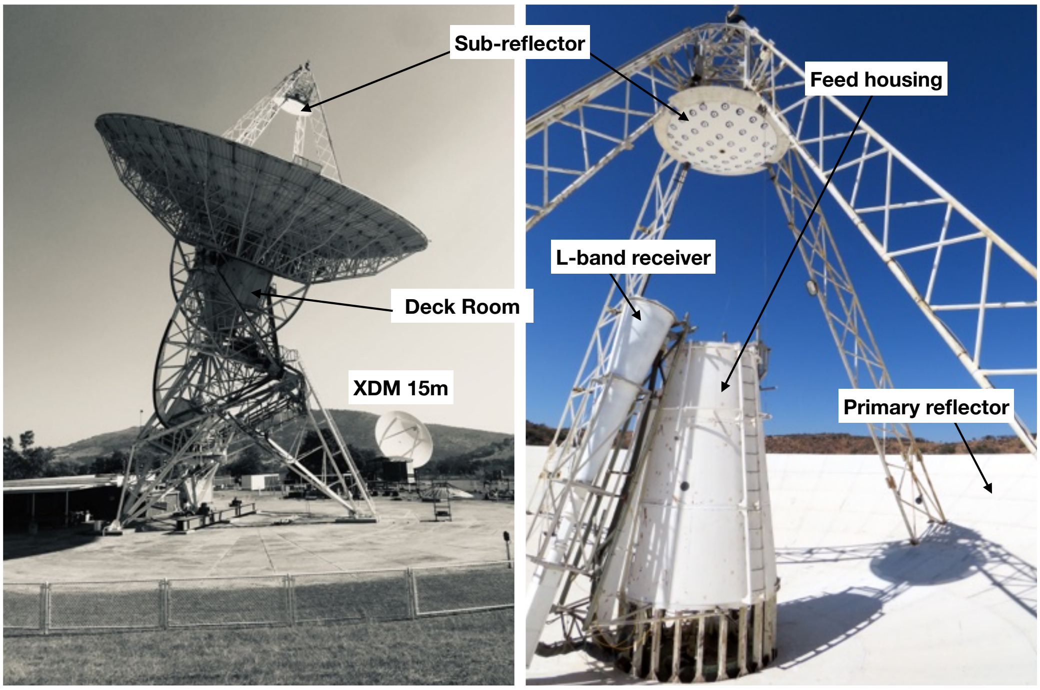

Figure 2.2: Images of the Hart26m and 15-m antenna on the left. (*Image credit: Author*). On the right, an insert of the Hart26m primary reflector, sub-reflector, feed housing, and L-band receiver is shown. The L-band receiver, due to its larger size, is not located inside the feed housing but next to it. (*Image credit: Dr. Aletha de Witt.*)

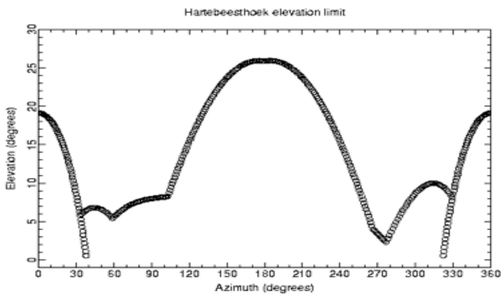

(a) The Hart26m's elevation limit as a function of azimuth.

(b) A partial view of the HartRAO terrain surrounding the Hart26m.

Figure 2.3: Elevation limitations at HartRAO. (Image credit: HartRAO)

the source across the sky, which may require additional calibration steps to account for errors caused by the movement of the antenna structure. However, this mode of observation can become problematic when observing sources in the far south. The length of the drift scan depends on the declination of the source (1/cos(declination)), and a source at a declination of 60° south will, for example, take twice as long to observe than a source at 0° declination. For sources in the far south, where the scan length becomes much longer than the atmospheric coherence time, it is better to make use of driven scans of user-defined length, where the signal is sampled as the telescope beam is driven across the source.

2.1.4 The receiver system

Two main types of receivers are used at HartRAO, namely the total power (Appendix 1.1) and Dicke-switched (Appendix 1.2) receivers. The feed housing shown in Figure 2.2 houses six of the seven microwave receivers used by the Hart26m. The seven receivers operate at the standard frequencies of 1.7 GHz (18 cm), 2.3 GHz (13 cm), 4.8 GHz (6 cm), 6.7 GHz (4.5 cm), 8.4 GHz (3.5 cm), 12.2 GHz (2.5 cm), and 22 GHz (1.3 cm). A list of the receivers and frequency bands used in this study are given in Table 2.1[1].

Band	λ range (cm)	ν range (Giga-hertz (GHz))	ν used
S	7.5 - 15	2 - 4	2.3 GHz
C	3.75 - 7.5	4 - 8	4.8 GHz
X	2.5 - 3.75	8 - 12	8.4 GHz
Ku	1.67 - 2.5	12 - 18	12.2 GHz
K	1.11 - 1.67	18 - 26.5	22 GHz

Table 2.1: Table of frequency bands used in radio observations of this study. Band is the code used to describe the specified frequency. λ is the corresponding wavelength in centimeters. ν is the corresponding frequency in GHz and ν used is the applied frequency used in the actual observations discussed.

All receivers, except for the 12.2-GHz receiver are cooled to cryogenic temperatures, which greatly reduces thermal noise contributions from the receiver elements, improving signal detection. The 2.3, 12.2, and 22-GHz receivers operate in total power mode. The 4.8 and 8.4-GHz receivers each have two feeds aligned in an East-West configuration, to permit Dicke-switched radiometry. During observations, radio signals may be

[1] A full list of the Hart26m receivers can be found at http://www.hartrao.ac.za/hh26m_factsfile.html

filtered through 4, 8, 16, or 32-MHz bandwidth filters that help exclude interference from external signals at the observing frequencies. Table 1 gives a detailed list of the basic specifications of all HartRAO receivers currently in operation.

2.1.4.1 The receiver signal chain

This section describes the Hart26m signal chain, i.e. how the observed signal moves through the receiver system. Figure 2.4 shows a schematic diagram of the Hart26m receiver system signal chain. All of the Hart26m receivers are dual-polarization, and the observed signal is split into constituent left circular polarization (LCP) and right circular polarization (RCP) states. In general, total power and dicke switched receiver systems have the same layout, with the exception that switches are added to the dicke system. The following discussion will only highlight the total power receiver for one polarization; LCP. The RCP polarized signal follows the same path.

During an observing session, the radio waves from the astronomical object being observed are reflected from the primary antenna surface towards the secondary surface (the sub-reflector), from where it is focused onto the receivers located in the feed housing at the focal point of the antenna. When the signal reaches a receiver, a polarization splitter located at the base of each feed horn splits the signal into its constituent EM polarization states (LCP and RCP) and feeds each polarization to its separate receiver chain[1]. Next, a high-stability noise diode (ND) injects a known noise signal which is added to the respective incoming signal using a directional coupler. Because astronomical radio signals are very faint and noise-like, and by nature much weaker than the noise (10^{-26} W m^{-2} Hz^{-1}) generated by the components that detect them, they need to be amplified to get them to a detectable level. The Cryogenically cooled low noise amplifier (LNA)s are used to reduce the thermal noise contribution from the amplifier itself and maximize the sensitivity. Signal losses in the passive components (e.g. signal attenuation during transmission through the coaxial cables) are then minimized by downconverting the previously amplified Radio Frequency (RF) signal to lower frequencies. The RF signal is fed to a mixer which multiplies the RF signals with a locally generated signal from a local oscillator (LO).

[1]This process, however, does not apply to the 12.2 GHz receiver, which has a quarter-wave plate polarization converter in front of the feed and dual linear polarization outputs.

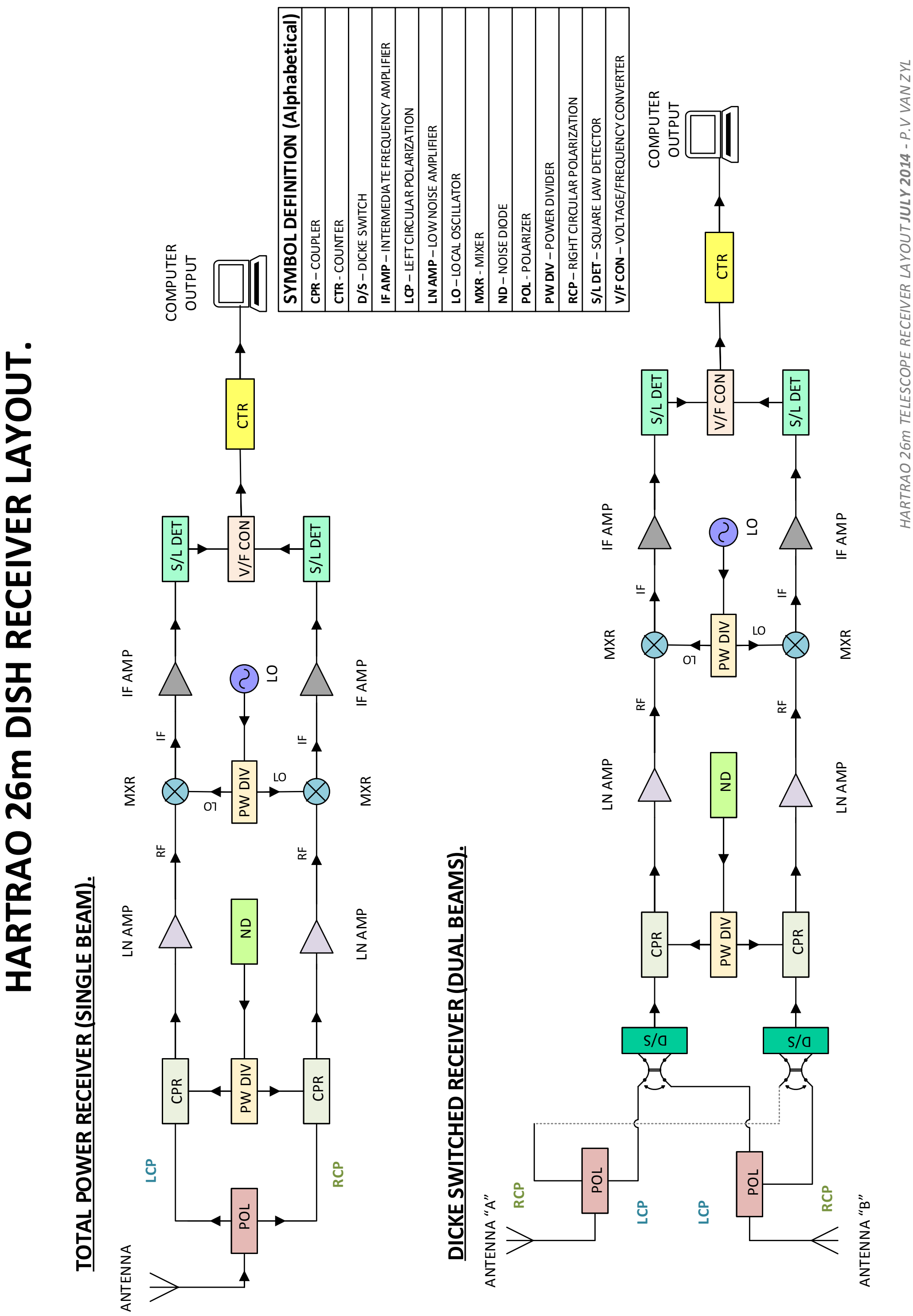

Figure 2.4: The figure is a representation of the layout of the HartRAO 26m radio telescope receiver signal chain.

The output signal that is used is the difference frequency component (RF - LO) of the product, called the Intermediate Frequency (IF). The resulting IF signal is amplified and converted into an output direct current (DC) voltage proportional to the input power using a Square-Law detector. The signal is converted into square waves (the amplitude remains constant but the frequency is proportional to the DC voltage output) by a voltage to voltage to frequency converter. These oscillations are then measured with a counter such that the count rates in units of hertz (Hz) are proportional to the original IF signal power. Results are then recorded into Flexible Image Transport System (FITS) files using the convention of universal time, target name, and observer name to identify the FITS files and saved to the HartRAO server. At this stage, the data is ready for display and further processing as discussed in Chapter 7).

2.1.5 Signal detection

Initially discovered by Karl Jansky, radio astronomical signals are naturally occurring EM waves from space. The radio regime of the EM spectrum spans over 5 decades between about 10 MHz (30 m) to 1.5 THz (0.2 mm) (see Figure 2.5).

Radio emission from astronomical thermal emitters, i.e. objects such as the planets that produce radio emission only due to black body radiation, to non-thermal radiators e.g. blazar jets, penetrates the Earth's atmosphere and reaches ground-based radio telescopes like the Hart26m. However, certain windows in the radio spectrum place constraints on Earth-based observations due to atmospheric emission/absorption and in some cases refraction of the incoming radio signal. At 22 GHz frequencies for example, radio observations suffer from atmospheric absorption by vibrating water molecules and at lower frequencies, the ionosphere reflects radio waves below 10 MHz (Meeks, 1976). The radio emission that does however make it past the atmospheric barriers gets collected by the telescope detectors on the ground.

The fundamental function of a parabolic radio telescope is to collect and focus the incoming radio emission to a single focal point where the radio waves can be measured (see Figure 2.6).

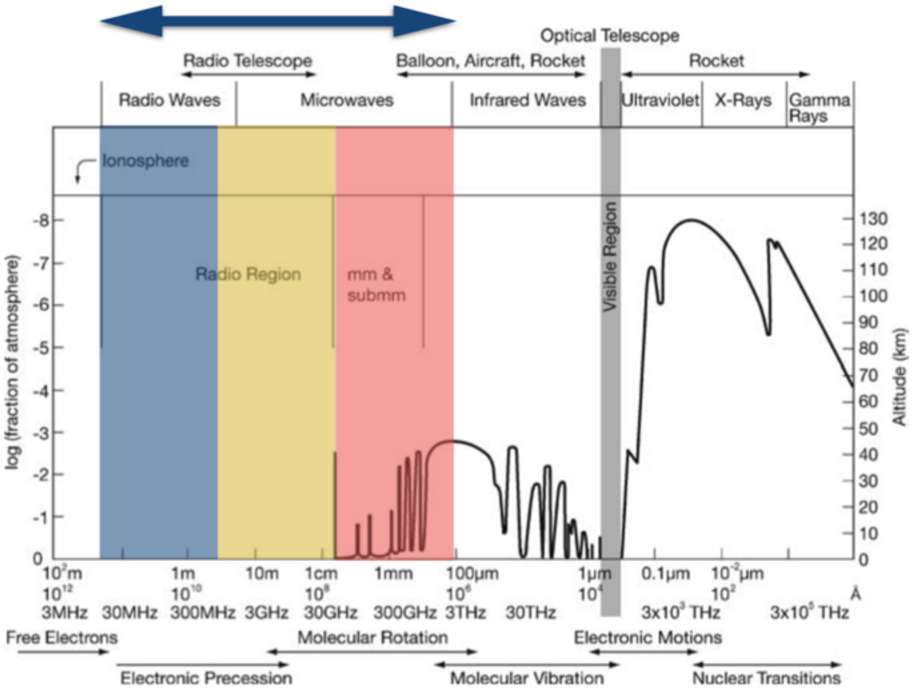

Figure 2.5: The electromagnetic transmission of photons within the Earth's atmosphere. Image credit: Adapted from Wilson, Rohlfs, and Hüttemeister (2013)

The response of a radio telescope to the incoming radiation is described as the antenna beam pattern (see Figure 2.6b). The antenna beam pattern (a dimensionless quantity) is simply a measure of the power, $\mathrm{P}(\vartheta, \varphi)$, received by the antenna as a function of direction (ϑ,φ) normalized so that $\mathrm{P_n}(0,0)=1$ over a source whose extent is much smaller than the beam size, i.e. a point source. If the power received is subtended over a solid angle of 4π, then the antenna beam pattern is better approximated by the integral

$$\Omega_\mathrm{A} = \iint_{4\pi} \mathrm{P_n}(\vartheta, \varphi)\mathrm{d}\Omega \qquad [\mathrm{sr}] \tag{2.1}$$

where Ω_A is the beam solid angle or angular area measured in units of steradians (sr). Another important quantity provided by the antenna beam pattern is called the resolution or half power beam width (HPBW), the angular separation between the two points on either side of the antenna beam pattern where the power received

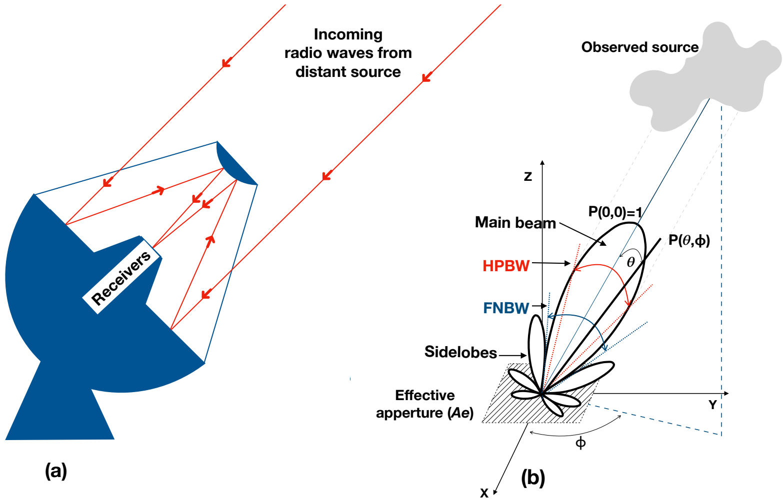

Figure 2.6: The image (a) shows the signal path traveled by radio waves from the target object to the telescope receivers, (b) shows the antenna beam pattern as a function of polar coordinates ϑ and φ.

from a point source is half its peak value and is defined as:

$$\vartheta_{\mathrm{HPBW}} \propto \frac{\lambda}{\mathrm{D}} \qquad [\text{radians}] \tag{2.2}$$

where λ is the wavelength of observation and D is the diameter of the primary reflector of the telescope[1]. To increase the resolution, one can either observe at higher radio frequencies or increase the physical size of the telescope dish. However, even the largest radio telescopes used at their highest frequencies have a resolution that is about 10 times poorer than that of ground-based optical telescopes. Also, in practice, there are cost and constructional limitations[2] on the size that a single-dish telescope can reach, the physical size of the radio antenna can not be increased indefinitely. Radio interferometry (Thompson, 1999; Thompson, Moran, and Swenson, 2017), a technique that synthesizes a very large radio telescope by combining the signals from two or more smaller telescopes separated by anything from a few meters to

[1] For a large and fully steerable single-dish antennas, e.g. a 100m telescope at 3.5 cm, the highest achievable resolution is ∼1 arcminute.

[2] The largest fully steerable dish to date has a 100-m diameter e.g. Effelsberg radio telescope in Germany (https://www.mpifr- bonn.mpg.de/en/effelsberg). Dishes larger than this limit cannot be physically supported by mechanical structures and are thus built into naturally occurring depressions in the Earth e.g. the 500-m FAST radio telescope in China (https://fast.bao.ac.cn)

thousands of kilometers solves the problem of the resolution limit which plagues large single-dish antennas[1]. A telescope pointing at a region of the sky can measure the brightness of the emitting source, which for a black body radiator can be expressed by Planck's law in which the brightness and hence the power measured by a radio telescope is uniquely related to the physical temperature of the emitting source, for a given wavelength. For a blackbody radiator, the spectral brightness B_ν is defined as:

$$B_\nu = \frac{2h\nu^2}{c^2}\frac{1}{e^{h\nu/k_B T} - 1} \qquad [\mathrm{W\,m^{-2}\,Hz^{-1}\,sr^{-1}}], \tag{2.3}$$

where T = brightness temperature [K],
$h = 6.63\times10^{-34}$ [J s] is Planck's constant,
ν = frequency [Hz],
$c = 3\times10^8$ [m s^{-1}] is the speed of light in free space and
$k_B = 1.38\times10^{-23}$ [J K^{-1}] is Boltzmann constant.

For low frequencies, i.e. the radio part of the EM spectrum, the dimensionless quantity $h\nu/K_B T \ll 1$, and Equation 2.3 can be expressed by the Rayleigh-Jeans law[2] which reduces to:

$$B_\nu = \frac{2k_B T\nu^2}{c^2} \qquad [\mathrm{W\,m^{-2}\,Hz^{-1}\,sr^{-1}}], \tag{2.4}$$

As mentioned previously, telescopes respond to the incoming radiation as a function of direction in the sky given by the antenna beam pattern . If the position in the sky of an observed object subtends a solid angle (Ω_s) much smaller than the antenna beam size (i.e. observing a point-like or unresolved source), the total received radiation measured, also known as the spectral flux density (S_ν), is just the product of the spectral brightness with the solid angle:

[1]The distance between any two telescopes is called a baseline (B) and can span as wide as the diameter of Earth to provide mas resolution when Equation 2.2 is represented as $\vartheta_{HPBW} \propto \frac{\lambda}{B}$.

[2]For example a source radiating at 1 GHz, gives $h\nu/K_B T$=0.048 [K].

$$S_\nu = \frac{2k_B T \nu^2}{c^2}\Omega_s \qquad [\mathrm{W\,m^{-2}\,Hz^{-1}}], \tag{2.5}$$

For a point source, the observed flux density (S_o) is essentially the brightness of the source $S_o = B_\nu$. For extended sources, however, Equation 2.5 can be expressed as the integral of the temperature distribution over the observed object

$$S = \frac{2k_B \nu^2}{c^2} \iint\limits_{\text{source}} T(\vartheta, \varphi) d\Omega \tag{2.6}$$

The Rayleigh-Jean law, Equation 2.4, is one of the most important relations in radio astronomy, in which the brightness (B) and hence the power (P) measured by a radio telescope is proportional to the temperature (T) of the emitting source (Karttunen et al., 2016; Wilson, Rohlfs, and Hüttemeister, 2013). Nyquist (1928) was the first to discover this relationship when he found that the power P_N of a band-limited signal in a circuit is proportional to the temperature of that circuit

$$P_N = k_B T_A \quad [\mathrm{W\,Hz^{-1}}] \tag{2.7}$$

where T_A [K] = the resistor temperature or equivalent antenna temperature[1] (Campbell, 2002; Meeks, 1976; Baars, 2007). If we consider a radio telescope as an electrical circuit; i.e. a device that converts EM waves into a current, and a radio source as an equivalent resistive load connected to the telescope via EM waves, we can equate the power emitted by the source to the power received by the radio telescope, i.e. we can think of the signal in terms of the noise generated by a resistor. Consequently, the total power received by a radio telescope P_{tot} can also be considered as the product of the observed flux density (S_o) with the effective collecting area (A_e) of the telescope:

[1] It is important to note that T_A is not a physical temperature but is the temperature a resistor would have if it were to generate an equivalent power per unit bandwidth from the voltage measured by an antenna.

$$P_{tot} = A_e S_o \qquad [\mathrm{W\,Hz^{-1}}] \tag{2.8}$$

Equating the power from the antenna (Equation 2.7) and the source (Equation 2.8) gives:

$$k_B T_A = A_e S_o \tag{2.9}$$

where,

$$S_o = \frac{k_B T_A}{A_e} \qquad [\mathrm{Jy}] \tag{2.10}$$

It is important to note that to get the total flux density, the sum of the flux density measured in each polarization (LCP and RCP) is required. Furthermore, to obtain the true flux density we also need to introduce a source size correction factor K_s and set $S_o = S$. From equation 2.10, the true flux density (S) is then defined as:

$$S_{LCP} = \frac{2k_B T_{LCP} K_s}{A_e} \quad [\mathrm{Jy}], \quad \text{and} \quad S_{RCP} = \frac{2k_B T_{RCP} K_s}{A_e} \quad [\mathrm{Jy}] \tag{2.11}$$

per polarization where T_{LCP} and T_{RCP} are the antenna temperature in LCP and RCP respectively. Radio signals from celestial sources are very weak, thus we measure them in units of Jansky [Jy], where 1 Jy = 10^{-26} W m^{-2} Hz^{-1}. §3.1 describes how the single-dish radio data are calibrated, reduced, and analyzed.

2.2 Fermi Gamma-ray Space Telescope

For the past 30 years, our view of the HE gamma-ray sky has been shaped by the work carried out mainly by the following space-based detectors, Energetic Gamma-Ray Experiment Telescope (EGRET)[1] (Hartman et al., 1992), Astro-rivelatore Gamma a Immagini LEggero (AGILE)[2] (Tavani et al., 2009) and more recently the

[1] https://heasarc.gsfc.nasa.gov/docs/cgro/egret/
[2] http://agile.rm.iasf.cnr.it/

Fermi Gamma-ray Space Telescope (FERMI-GST)[1] (Atwood et al., 2009). Table 2.2 highlights some of the significant improvements from the development of the detectors over the years. The FERMI-GST is a powerful space observatory that opens a wide window on the high energy Universe. Launched on June 11th, 2008 aboard a Delta II 7920-H rocket at Cape Canaveral, it is currently the most sensitive HE space-based telescope, $\sim$30 times more sensitive than EGRET. The purpose of launching the Fermi mission was to improve our current understanding of the Universe by observing its most extreme environments e.g. AGN, supernova remnants, and pulsars. Studying these systems allows us to gain an understanding of the underlying physics behind the mechanisms that fuel these systems.

To study these mechanisms using the FERMI-GST requires the use of its two onboard instruments. The first instrument, the Gamma Ray Burst monitor (GBM) (Meegan et al., 2009) monitors transient events in the 8 keV to 30 MeV range. Gamma Ray Burst (GRB)s are bursts of energy that can outshine entire galaxies over very short periods of time. The second, the Large Area Telescope (Fermi-LAT, hereafter LAT)[2] (Atwood et al., 2009) maps the HE gamma-ray events in the 20 MeV to $>$ 300 GeV range. This is the principal observing instrument on the FERMI-GST and also the instrument responsible for the data presented in this work.

In 2018 the Fermi collaboration celebrated a notable milestone of a decade of highly successful operations with the FERMI-GST (Ajello et al., 2021)[3]. The celebrations showcased some of the mission's greatest discoveries, including the discovery of the large Fermi bubble structures (Crocker and Aharonian, 2011) as well as a possible multi-messenger event coincident with the GRB 150914 (Connaughton et al., 2018). The telescope continues to operate at full capacity, making new discoveries and pushing the boundaries of what is currently possible with current gamma-ray detectors. In the following sections, I highlight the LAT instrument and its data analysis techniques.

[1]https://fermi.gsfc.nasa.gov/science/overview.html

[2]https://fermi.gsfc.nasa.gov/science/instruments/lat.html

[3]Originally only planned to only operate over a 5-year period, the highly successful operation of the telescope led to a further 5-year extension. The telescope is currently in its 14th year of operation at the time of writing this thesis.

Table 2.2: Table of improvements of space-based telescopes.

Instrument	EGRET	AGILE	FERMI-GST
Launch	1991	2007	2008
Operational	until 2000	yes	yes
Energy range	20 MeV to 30 GeV	30 MeV to 50 GeV	20 MeV to >1 TeV
Tracker	spark chamber	silicon strips	silicon strips
Calorimeter	NaI (TI)	CsI (TI)	CsI (TI)
Effective area	1500 cm^2 @ 500 MeV	700 cm^2 @ 1 GeV	10^4 cm^2 @ 10 GeV
Field-of-view (FoV)	0.5 sr.	2 sr.	2.4 sr.
Angular resolution	5.8° @ 100 MeV	0.6° @ 1 GeV	0.15° @ 10 GeV 4° @ 100 MeV
Localization	5' to 10'	3'	0.4'
Dead time	< 0.1 ms	< 100 µs	< 100 µs

Highlights of some of the significant improvements in gamma-ray observations brought on by the development of the EGRET, AGILE and FERMI-GST (Thompson, 2015; Tavani et al., 2009; Atwood et al., 2009)

2.2.1 The Large Area Telescope

In order to observe HE photons (E > 100 MeV), a detector needs to move beyond Earth's atmosphere; Earth's atmosphere is opaque to gamma-ray photons. HE photons can not be focused as is normally the case with traditional ground-based telescopes. At these energies, photons can only be detected through particle ($e^{\pm}$) pair-production processes. The LAT (Figure 2.7) is a pair-conversion telescope that has been monitoring the HE sky for over 14 years. It observes the HE skies in one of two modes, survey, or pointing. The former, which is the standard data-taking mode of operations is used to monitor daily gamma-ray activity. The latter, however, is used when the need arises, e.g. for Target of Opportunity (ToO) events. The telescope has been in full operating mode over this period collecting data continuously with the exception of the South Atlantic Anomaly (SAA)[1] passages, or when performing technical operations e.g. calibration and major software upgrades. At an altitude of 565 km, the LAT with its large FoV (2.4sr) is able to observe 20% of the sky at any given instant. Within 3 hours, the telescope completes a scan of the entire sky at a 50° rocking angle[2] on the north and south of zenith in alternating orbits.

[1] An area where orbiting satellites are subject to an increased flux of charged particles.
[2] This angle was originally 35° at launch, it has since increased to 50° (Ajello et al., 2021)

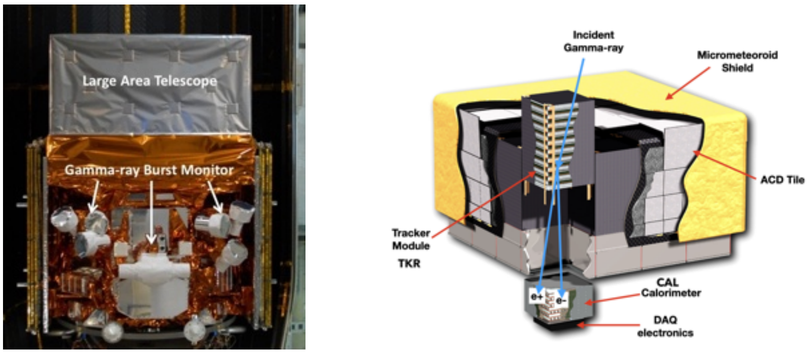

Figure 2.7: ***Left:*** Image of the FERMI-GST[1]. ***Right:*** Artist rendition of the sub-systems that make up the LAT; the ACD, TKR, and CAL covered by a Micrometeoroid shield. *Credit: adapted from Atwood et al., 2009.*

Table 2.4: Overview of LAT instrument parameters and performance.

Parameter	Value or Range
Energy range	∼20 MeV to above 1 TeV
Energy resolution (1σ)	
100 MeV to 1 GeV	9% to 15%
1 to 10 GeV	8% to 9%
10 to 300 GeV	8.5% to 18%
> 10 GeV	≤ 6%
Single photon angular resolution, on-axis, 68% space angle containment radius ($\vartheta_{68\%}$:)	
> 10 GeV	< 0.15°
1 GeV	< 0.6°
100 MeV	< 3.5°
on-axis, 95% containment radius	$< 3 \times \vartheta_{68\%}$
off-axis, 95% containment radius at 55°	< 1.7 × on-axis value
FoV	2.4 sr
Event readout time	26.5 μs per event
Timing accuracy	< 10 μs
Background rejection (after analysis)	< 10% for E = 100 MeV to 300 GeV
Point source location determination[a]	< 0.5'
Point source sensitivity (> 100 MeV)[b]	$< 3\text{x}10^{-9}$ ph $\text{cm}^{-2}\text{s}^{-1}$, 5σ after 1 year

Note.- Table adapted from (Atwood et al., 2009). [a] For a steady source after a one-year all-sky survey, assuming a high-latitude diffuse flux of 1.5×10^{-5} cm^{-2} s^{-1} sr^{-1} (>100 MeV) and a photon spectral index of -2.1, with no spectral cutoff. [b] High latitude source of 10^{-7} cm^{-2} s^{-1} flux at >100 MeV with a photon spectral index of -2.0 above a flat background and assuming no spectral cutoff at high energy; 1σ radius; one-year all-sky survey.

[1] https://fermi.gsfc.nasa.gov/science/eteu/about/

2.2.2 Large Area Telescope signal chain

A photon incident on the LAT is detected, measured, and recorded through the systematic collaboration of the LATs three main instruments, Tracker/Converter (TKR), Calorimeter (CAL), and the segmented Anticoincidence Detector (ACD) (see Figure 2.7). The TKR converts and tracks HE photons as they move through the detector. The CAL measures and images the energy deposition, and the ACD rejects cosmic ray backgrounds. Once the onboard analysis is completed, the data are downlinked for further processing and promptly released to the public. These systems are briefly discussed in the sections that follow.

2.2.2.1 The Tracker/Converter

The TKR (Figure 2.8) consists of an array of 16 identical tracker modules made of Silicon Strip Detectors (SSD) and interleaved tungsten foils arranged in a 4×4 grid. These planes convert high energy photons to electron-positron ($e^{\pm}$) pairs. Within each module is 18 layers of paired $x - y$ tracker planes, tracking the trajectory of the secondary pairs. These planes are divided into two regions, FRONT and BACK. The initial 12 planes (FRONT) are "thin" layers of 3% radiation length tungsten (high Z) designed to minimize the effects of multiple scattering of the converted particles, which results in a better determination of the incident particle direction. The following 4 planes (BACK) are "thick" layers of 18% radiation length tungsten to optimize the effective area of the LAT at high-energies, which results in a large photon conversion probability. The remaining two planes have no conversion layers. An incoming gamma-ray ray produces an electron and a positron ($e^{\pm}$) by pair production on impact with the tungsten foil. The resulting pair then ionizes the silicon atoms on their trajectory through the detector and the silicon strip detectors track the pair as they propagate through the instrument.

2.2.2.2 The Calorimeter

When the ($e^{\pm}$) pair reaches the CAL (Figure 2.9) located at the bottom of the LAT, the calorimeter makes accurate measurements of the energy from the pairs produced

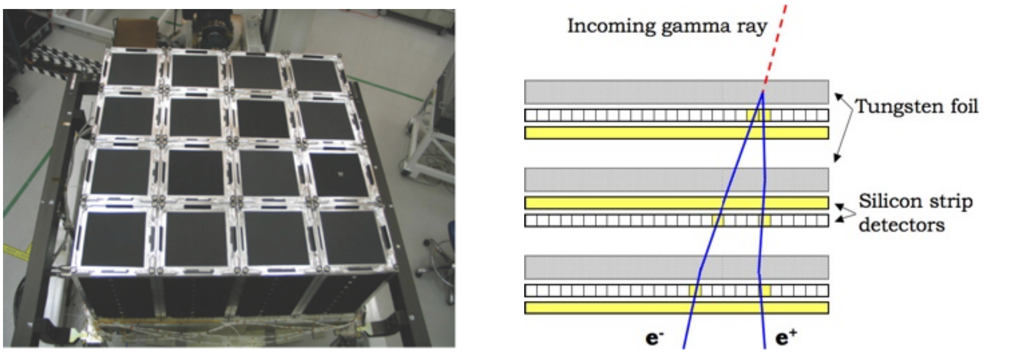

Figure 2.8: ***Left:*** The completed tracker module showing its 16 tracking towers, *Credit: Atwood et al., 2009*. ***Right:*** Highlight the different elements a gamma-ray photon would encounter along its trajectory upon entry into the LAT. The detectors that measure the signal along the path are highlighted in yellow. *Credit: Elizabeth Hays*

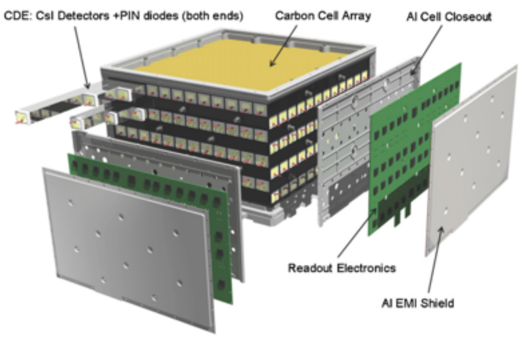

Figure 2.9: LAT calorimeter module. *Credit: Atwood et al. (2009)*

or creates an image of the shower development which can be used to distinguish between different types of background. The CAL consists of 96 CsI (TI) scintillation crystals arranged in 8 layers of 12 crystals each. Each end of a crystal is equipped with two photodiodes that provide the readout of the scintillation signals in the CAL. With a total depth of 8.6 radiation lengths (increasing to 10.1 radiation lengths if we consider the depth of the whole LAT) at normal incidence, the CAL is able to have exceptional energy resolution at high energies, and a significant background rejection of cosmic rays.

2.2.2.3 The Anticoincidence Detector

The ACD consists of 89 plastic scintillator tiles. Apart from providing a protective covering for the TKR array, a programmable trigger, and the Data acquisition system (DAQ), the main purpose of the ACD is to suppress or reject charged particles i.e. cosmic rays so they are not mistakenly classified as gamma-ray photons. Cosmic rays are the most dominant charged particle in space, and outnumber gamma-ray photons by a factor of $\sim10^5$. This makes them the largest contributor of background noise for gamma-ray observations. Pair conversion telescopes like the LAT suffer from the bombardment of these particles and thus require a highly efficient mechanism to and handle these kinds of events. The ACD can detect and reject these events at an impressive rate of more than 99,97%. Sometimes cosmic rays that are mistakenly identified as gamma-ray photons can be vetoed and proceed to create particle showers similar to those generated from gamma-ray photons that can travel back up past the ACD and generate signals that can potentially be identified as valid gamma-ray photons. To overcome this problem, the ACD is segmented, which enables it to suppress this effect so that only the events that trigger an ACD tile upon entry or are on the trajectory of the incoming particle are vetoed. Segmenting the ACD significantly improved the sensitivity of the LAT to higher energy photons, a feature that EGRET lacked, causing reduced efficiency of the instrument at energies >10 GeV (Atwood et al., 2009).

2.2.2.4 The Data acquisition system

Data registered as valid photon events are collected and analyzed by the DAQ. The DAQ also performs command, control, and instrument monitoring; housekeeping, and power switching. The analysis performed by the DAQ is the initial data reduction process that occurs onboard the telescope. Onboard processing serves to filter and reduce the data to a size suitable for the telemetry bandwidth. The LAT can detect ~10000 events/s. These are reduced to ~400 events/s where ~2-5 events/s are the actual photon events[1]. The processed data are then recorded and transferred together with housekeeping information to the ground Missions Operation Center

[1] https://fermi.gsfc.nasa.gov/ssc/data/analysis/documentation/Cicerone/Cicerone_Introduction/LAT_overview.html

(MOC). At ground level, the data are evaluated, cleaned, and transferred to the relevant instrument science operation center. At the LAT center, the photon events are reconstructed (§2.2.3), and the resulting data is released to the public. This data can be accessed via the LAT data server[1] for further targeted analysis.

2.2.3 Event filters and classifications

To understand how the LAT data are analyzed, an understanding of how observations are treated is required. Prior to any analysis being done, each event observed by the LAT is filtered and classified according to its probability of being a photon and the quality of its reconstruction. The classification algorithms event classes. There are currently four basic event classes that describe the LAT events. Each event class follows a nested hierarchy, where the events containing the most background contamination and least photon probability nest other event classes in order of decreasing background contamination and increasing photon probability i.e. narrower point spread function (PSF). The classes are listed as TRANSIENT, SOURCE, CLEAN and ULTRACLEAN. The classes provide high-level event descriptions to maximize the photon count of the sources under investigation. TRANSIENT event class has the most background contamination, making it ideal for very high short timescale events e.g. GRBs. SOURCE pointlike and extended sources observed on medium to long time scales e.g. AGN. CLEAN & ULTRACLEAN are the strictest classes ideal for analysis in large regions that are more sensitive to spectral features caused by instrumental backgrounds. Each event class can also be further subdivided into three distinct divisions. The events can be described according to the photon conversion locations[2] (FRONT/BACK) (§2.2.2.1), the point spread function (PSF) quality, and the quality of the energy reconstruction. Properties for the second and third are both ranged between 0(low) to 3(high). Depending on the science, a variety of cuts can be performed on the data for this work the conservative SOURCE event classification was used.

[1] https://fermi.gsfc.nasa.gov/cgi-bin/ssc/LAT/LATDataQuery.cgi

[2] The conversion location is also known as the event type (evtype) in the LAT analysis software.

2.2.4 Instrument response functions

Each event triggers a response from the LAT. The response gives a measure of the performance of the detector depending on the instrument design, event reconstruction algorithms, and the background and event quality selections (§2.2.3). Thus each event class has its own Instrument Response Function (IRF). Instrument Response Function (IRF)s provide a translation between the true flux of gamma-rays on the sky and the measured distribution of energy and direction in the LAT parameterized representations of the performance of the instrument as a function of gamma-ray energy and its arrival direction in the LAT coordinate system, which is factored into three important parts:

- The effective area, A_{eff} $(E,\hat{v},t)$, which depicts the detection probability of a given event with energy E and direction $\hat{v}$ for the event class s. Figure 2.10a.
- The energy dispersion, $D(E';E,\hat{v},t)$, the probability to reconstruct the energy E' of an event with energy $(E,\hat{v})$ for the event class s. Figure 2.10c.
- The PSF, $P(\hat{v}';E,\hat{v},t)$, the probability to reconstruct the incident direction $\hat{v}'$ for an event with energy $(E,\hat{v})$ for the event class s. Figure 2.10b.

This response of the LAT can thus be expressed as:

$$R(E', \hat{v}'; E, \hat{v}, t) = A_{eff}(E, \hat{v}, t)D(E'; E, \hat{v}, t)P(\hat{v}'; E, \hat{v}, t) \tag{2.12}$$

Anytime the IRFs are significantly improved, the new version is called a pass. There have been several upgrades since the launch of the FERMI-GST, and the most recent one is called Pass 8 (P8) (Atwood et al., 2013). This work utilizes P8R3 which considers the in-flight performance of the instrument, something that was not applied to earlier versions which led to significant improvements in the rejection of background events.

The new P8 version shows a significant improvement in the PSF from the FRONT

[1] https://www.slac.stanford.edu/exp/glast/groups/canda/lat_Performance.htm

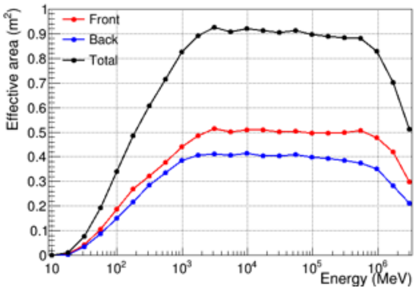

(a) On axis effective area

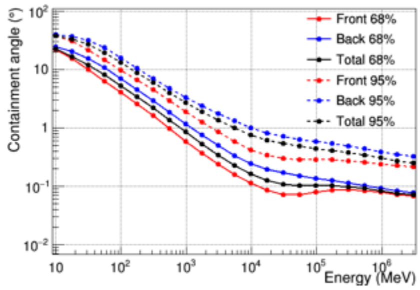

(b) Weighted PSF at normal incidence

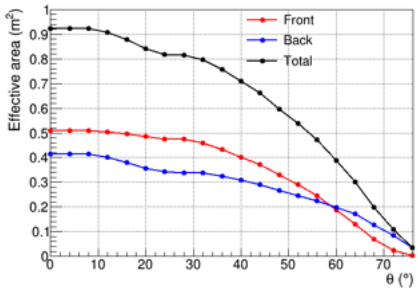

(c) Effective area at 10 GeV, averaged over φ

Figure 2.10: ***a:*** the IRF of the P8R3_SOURCE_V3 depicting the performance of the effective area as a function of photon energy. ***b:*** the IRF of the P8R3_SOURCE_V3 depicting the performance of the PSF. ***c:*** the IRF of the P8R3_SOURCE_V3 depicting the performance of the effective area as a function of incidence angle (φ). *Credit: Ajello et al., 2021*[1]

compared to the BACK (∼ a factor of 2) for high energy photons (Figure 2.10b). Higher energy photons are less impacted by scattering than their lower energy counterparts during particle reconstruction. This translates to a larger collection area (Figure 2.10a) and improved detection (Figure 2.10c) for high energy photons. Lower energy photons however suffer when reconstructing the photon direction, due to the energy dispersion being worse at lower energies because a higher fraction of the energy is lost before the pair reaches the calorimeter, and is therefore harder to measure. §3.2.1 describes how the LAT data is analysed.

2.3 Supplementary observations

To support the findings from the primary detectors, additional data from other detectors were gathered from archives and included in the study. The data from the following observatories or catalogs was already calibrated and received in that form from their respective institutions.

2.3.1 Optical data

The REM[1] (Zerbi et al., 2003) provided observations of the target sources at optical wavelengths. The REM, is a fully robotized fast slewing 60-cm telescope located on the European Southern Observatory (ESO) site La Silla, in Chile (29° 15'S, 70° 44'W). The telescope was primarily designed to provide prompt follow-up observations of GRB afterglow events observed by high energy detectors such as the Fermi Gamma-ray Burst Monitor (FERMI-GBM) and the Neil Gehrels Swift Observatory's X-Ray telescope (Swift-XRT, Burrows et al., 2005). I obtained arsecond resolution J, H, and K archival data for one of my target sources from data taken by its REM Optical Slitless Spectrograph (ROSS) instrument. All of the optical lightcurves used in this study were processed by R. Nesci from the Italian National Institute for Space Astrophysics and Planetology (INAF)/Institute for Astrophysics (IAPS) in Rome. Typical exposure times were approximately 150s for each band per object and each band observed consecutively from J to K.

2.3.2 Radio interferometric data

When two or more telescopes are connected to each other, they function as a giant radio telescope whose diameter is the size of the distance between them called a baseline (B). By replacing the value of D in Equation 2.2 with B, we get the Equation

[1] http://www.rem.inaf.it

$$\vartheta_{\mathrm{HPBW}} \propto \frac{\lambda}{\mathrm{B}} \tag{2.13}$$

where B can span over a few kilometers (kms) to thousands of kms. For example, the longest baseline achievable on Earth is limited to the diameter of the Earth $\geq$ 12000 km or 8000 miles. When observations are carried out with telescopes that are connected to each other through cables, the setup is called an interferometer. If the telescopes are not connected to each other, the setup is referred to as a VLBI. Interferometers provide arcminute to arcsecond resolution, while VLBI allows us to get finer angular resolution reaching sub-mas levels (Petretti, Fish, and Akiyama, 2021). The VLBI technique is used for astronomy (to produce high-resolution maps of radio sources and measure proper motion and parallax)(Readhead and Wilkinson, 1978) absolute astrometry (to get very accurate angular positions of radio sources, in particular, quasars) (Petrov and Taylor, 2011) and space geodesy (to use observations of quasars to get very accurate positions of the telescopes on Earth) (Schuh and Behrend, 2012).

Supplementary data obtained from various radio interferometers were used in this study. I obtained the source flux densities from the Bordeaux VLBI Image Database (BVID), the International VLBI Service for Geodesy and Astrometry (IVS), NASA, Jet Propulsion Laboratory (JPL), the Australian Telescope Compact Array (ATCA), Goddard Space Flight Center (GSFC) and Astrogeo. The supplemented data consisted of pre-calibrated correlated fluxes in arcminute to mas resolution fluxes in S/C/X and Ka-band.

2.3.2.1 Australian Telescope Compact Array

ATCA[1] is a connected element array, the first millimiter interferometer to be built in the Southern Hemisphere, consisting of six 22-m antennas spread over 6km's. It can observe in 15 different baselines[2] using a 3-km railway track aligned in an east-west direction. Its full range of possible baselines covers distances from a minimum of 30-m to a maximum of 6-km. The array operates in the millimeter and centimeter

[1] https://www.narrabri.atnf.csiro.au/observing/users_guide/html/chunked/ch01s02.html#table_sensitivity
[2] An array of n telescopes has n(n-1)/2 baselines.

wavebands centered around 20-, 13-, 6-, 3-, 1.2-, 0.7- and 0.3-cm, and post 2003 observes at 12- and 3mm as well (Minier, 2004). For this study, I obtained arcminute resolution archival data from the ATCA calibrator database[1] for all my target sources at S/X-band.

2.3.2.2 Jet Propulsion Laboratory

The DSN is a network of three sites[2], each consisting of a large 70-m antenna and several smaller 34-m antennas[3] that provide space navigation support for NASA's interplanetary space missions. The network is operated by the JPL[4], a research and development facility run by the California Institute of Technology (Caltech)[5]. For this study I obtained DSN quasar flux measurements for three of my sources in X/Ka bands, from observations run by Christopher Jacobs and calibrated by Christopher P. Volk. DSN fluxes are emperical, because the DSN doesn't image the sources, they obtain the flux from converting the signal-to-noise ratio (SNR) from their observations.

2.3.2.3 International VLBI Service for Geodesy and Astrometry

The International VLBI Service for Geodesy and Astrometry (IVS) (Nothnagel et al., 2017) is an international partnership of organizations that conduct or support VLBI activities. The IVS collaborates closely with the International Earth Rotation and Reference Systems Service (IERS), which is responsible for maintaining the international reference frames for celestial and terrestrial positions. The ICRF is a realization of the International Celestial Reference System (ICRS) and comprises a catalog of precise equatorial coordinates of extragalactic radio sources observed through VLBI. Similar to the JPL, IVS also estimates flux measurements from the

[1]https://www.narrabri.atnf.csiro.au/calibrators/

[2]The sites located near Goldstone (California), Madrid (Spain), and Canberra (Australia), are at exactly at 120° latitude separations from each other to ensure there is constant communication with orbiting spacecraft and at least one ground-based station as the Earth rotates.

[3]DSN 810-005 details the differences between the antennas of the DSN. Details at https://deepspace.jpl.nasa.gov/dsndocs/810-005/

[4]https://www.jpl.nasa.gov

[5]https://www.caltech.edu

SNR obtained during observations. The sked[1] flux catalogue is currently used for SNR-based scheduling of all IVS geodetic and astrometric sessions. For this study, I obtained S/X band pre-calibrated flux measurements.

2.3.2.4 Goddard Space Flight Center

The GSFC[2], located in Greenbelt, Maryland, is a NASA space research institution that has been at the forefront of space exploration since its establishment in May 1959 as NASA's first space flight center. The data obtained from GSFC is collected from astrometric and geodetic observations similar to the IVS. I obtained pre-calibrated flux measurements from the S/X band. observations.

2.3.2.5 Astrogeo

Astrogeo[3] uses data from the Radio Fundamental Catalog (RFC) to provide VLBI correlated fluxes and images for 21872[4] compact radio sources with mas resolution (B $\sim$1000-8000 km). Astogeo uses data from the Long Baseline Array (LBA), Very Long Baseline Array (VLBA), European VLBI Network (EVN), and Korean and VLBI Exploration for Astrometry VLBI Networks (KVN) at S/C/X/U/K/Ka/Q/W-bands. For this study I obtained pre-calibrated VLBI flux denisities in S/X-band.

2.3.2.6 Bordeaux VLBI Image Database

The Laboratoire d'Astrophysique de Bordeaux (LAB)[5] is an imaging and analysis center for the IVS[6]. LAB conducts astrometric and astrophysical observations to provide VLBI fluxes and images through the BVID[7] using data obtained from

[1] https://github.com/nvi-inc/sked_catalogs
[2] https://www.nasa.gov/centers/goddard/about/index.html
[3] http://astrogeo.org/rfc/
[4] This is the current number of sources at the writing of this thesis.
[5] https://astrophy.u-bordeaux.fr/?page_id=682&lang=en
[6] https://ivscc.gsfc.nasa.gov
[7] http://bvid.astrophy.u-bordeaux.fr/.

Research & Development (RD) or Research & Development with the VLBA (RDV) VLBI sessions. The VLBI sessions are carried out by the three major VLBI networks, the IVS, the EVN, and the VLBA. Observations are done at dual-frequency pairs of S/X and X/Ka bands. At the time of writing this work, the BVID had imaged 1514 sources generating 7862 VLBI maps. For this study I obtained pre-calibrated S/X band fluxes from the BVID for one of my sources.

The data collected from the supplementary detectors discussed here are discussed in Chapter 4.

3 Multi-wavelength observations and data analysis

To build the best dataset for MWL studies, data from several facilities that cover the same period as the Fermi-LAT observations (2008-2018) were gathered. Apart from the Hart26m observations (S/C/X/Ku, and K-band), this MWL study comprised of Fermi-LAT (100 MeV - 500 GeV), REM (J,H, and K - mag), JPL (X/Ka-band fluxes), GSFC (S/X-band fluxes), Astrogeo (S/X-band fluxes and images), BVID (S/X-band fluxes and images), IVS (S/X-band fluxes), and ATCA (S and X-band correlated fluxes) data.

This study examines the long-term behavior of three southern hemisphere blazars regularly monitored by both the Hart26m and the Fermi-LAT. A list of the target sources can be found in Table 3.1. Figure 3.1 shows the source distribution in the sky. Three of the sources in the sample have previously shown variability in gamma-rays, while the third source is peculiar in that it shows no gamma-ray emission despite being highly compact on mas scales. The study was conducted over a decade between 04/08/2008 (MJD 54682) and 05/08/2008 (MJD 58335). Ideally, all observations were to be taken simultaneously with Fermi-LAT observations, but this was not always possible as some sources at radio and other wavelengths were only monitored after a flaring incident was reported by the Fermi-LAT team.

3.1 HartRAO single-dish data

The following sections describe how the radio single-dish data was calibrated, reduced, and analyzed. The drift scan data reduction and analysis software (DRAN) was used to

Table 3.1: List of target objects observed in the study.

Catalog name	4FGL name[a]	RA(J2000)	DEC(J2000)	Class[b]	Redshift
PKS 0454-810	4FGL J0449.6-81000	72.5226	-81.0172	FSRQ	0.444
PKS 0903-57	4FGL J0904.9-5734	136.2215	-57.5849	BSU	0.695
PKS 1424-418	4FGL J1427.9-4206	216.9866	-42.106	BLL	1.522

[a] Target source name as listed in the Fourth Fermi-LAT catalog based on the first 10 years of science data (4FGL-DR2).
[b] Blazar class or type, Flat Spectrum Radio Quasar (FSRQ); BL Lacertae or BL Lac, type of blazar (BLL); active galaxy of uncertain type (BSU)

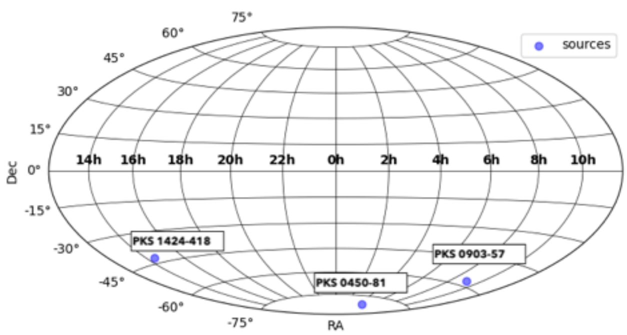

Figure 3.1: Image of source distribution in the sky.

analyze single-dish data obtained from the Hart26m as discussed in Section 7.3.1.

3.1.1 Data calibration

Calibrating single-dish radio data involves a series of steps that include converting the incoming radio signal amplitude in units of counts s–1 [Hz], to units of antenna temperature in Kelvin [K]. In the following sections, I discuss the different steps followed when calibrating Hart26m data.

3.1.1.1 Single-dish radio observations

Observing single-dish sources with the Hart26m telescope typically involves using the drift scan method, with the exception of sources such as PKS 0454-810, which are observed using driven scans due to their low elevation, see §2.1.3. All single-dish monitored sources are observed on a daily basis, as long as the telescope is functioning properly, there are no planned VLBI observations, the weather is clear at the HartRAO site (especially for high frequency observations e.g. at 22 GHz), and the source has a good SNR. Drift scans are useful for observing point sources that have an angular diameter much smaller than the antenna beam pattern .

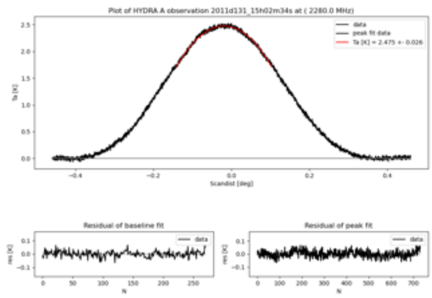

(a) Plot of example single-beam drift-scan (drift scan)

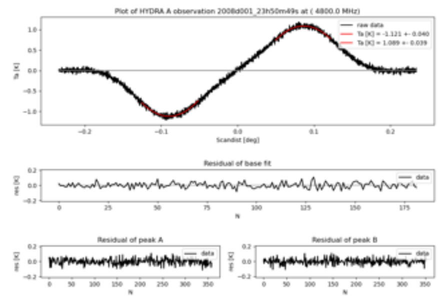

(b) Plot of example dual-beam drift scan

Figure 3.2: Plots showing radiometer output of example drift scans. Figure (a) shows the single beam output. Figure (b) shows the dual beam output.

The radiometer output is the east-west cross-section of the antenna beam pattern, which appears as a Gaussian curve of increasing intensity as the source moves across the beam. Depending on the receiver type, drift scans can produce single or dual beam outputs. Figure 3.2a and 3.2b show typical outputs of the single- and dual-beam drift scans at 2.3- and 4.8-GHz in units of antenna temperature. The dicke switched receivers, see appendix 1.2, used in 4.8-GHz and 8.4-GHz observations contain two separate feed horns placed close to each other, with the "A" horn (multiplied by -1) on the North/South axis, and the "B" horn (multiplied by +1) just west of the "A" horn. The beams are separated by +0.288 decimal degrees at 4.8 GHz and +0.254 decimal degrees at 8.4 GHz. In observations using a dual-beam system, the second feed-horn follows the path of the first feed-horn to produce an output as shown in the figure.

To preserve as much information as possible in weak radio signals, all HartRAO sources were observed in dual polarizations (LCP and RCP) before any further processing could be applied. At frequencies higher than 2.3 GHz, triple drift scan observations were carried out. This method involves observing a source at three different locations: the first scan is made at the nominal declination of the target (referred to as the "on source scan (ON)" position), and then the remaining two points surrounding it, each offset by the half-power beam width in elevation in the north (referred to as "half power north (HPN)") and south (referred to as "half power south (HPS)") of the target, in order to compensate for errors in pointing (see Section 3.1.1.3).

3.1.1.2 Antenna calibration

When a radio telescope observes an astronomical source, it detects not only emissions from the target source, but also contributions from other sources. Although the emission detected is strongest along the bore sight of the antenna beam pattern, contributions from the surrounding environment (e.g. the antenna and the ground) can also be picked up by the sidelobes, as shown in Figure 2.6. These contributions can severely affect the quality of the weak target source signal, which is embedded within the noise. In addition to emission detected in the sidelobes, there are other sources of unwanted radiation that are also detected, such as the cosmic microwave background (CMB) radiation, which is present in all directions. As you approach higher frequencies, such as 22 GHz, the atmosphere also becomes a source of interference (see §6.4) due to the absorption of radio emission by water molecules, hence the need for calibration.

When a radio signal is detected by a telescope, it goes through the receiver signal chain (see §2.1.4.1). As the signal enters the receiver, it is mixed with a known noise signal from a noise diode, which produces an output from the receiver that is the sum of the power received from all sources radiating above absolute zero. It is convenient to describe the noise power in units of temperature as shown in Equation 2.7. The equivalent temperature contribution that is proportional to the total noise power of the output signal is referred to as the system temperature (T_{SYS}). T_{SYS} describes the noise properties of the complete system and can be defined as the sum of the noise temperature of the receiver and any other noise sources (e.g. the atmosphere and the CMB) in the signal path. It can be mathematically represented as:

$$T_{SYS} = T_{SKY} + T_A + T_{ATM} + T_{SPILL} + T_G + T_R \qquad [K] \tag{3.1}$$

where:

- T_{SKY} is the isotropic sky brightness distribution from the CMB (∼2.73 K) including all background radiation from other radio sources and our Galaxy.

- T_A is the antenna temperature, which represents the power received from the astronomical source.

- T_{ATM} is the temperature contribution from the the Earth's atmosphere e.g. water vapour.

- T_{SPILL} is the spill-over arising from radiation picked up beyond the edge of the detector.

- T_G is the tempertaure contribution from the ground.

- T_R is the receiver noise temperature, which represents the noise generated by the elements in the receiver, such as the amplifiers. This type of noise is usually reduced by cooling the receiver to cryogenic temperatures, as mentioned in §2.1.4.

3.1.1.3 Pointing correction

The accuracy with which a radio telescope can observe a target source depends on the telescope's ability to correctly locate the target source. This process is referred to as "telescope pointing." Telescope pointing involves pointing the telescope toward a target source and measuring the antenna temperature at different positions around it. At HartRAO, this is done using triple drift scans, which are described in §3.1.1.1.

Figure 3.3a shows typical outputs of single-beam triple drift scans overlaid on one another.

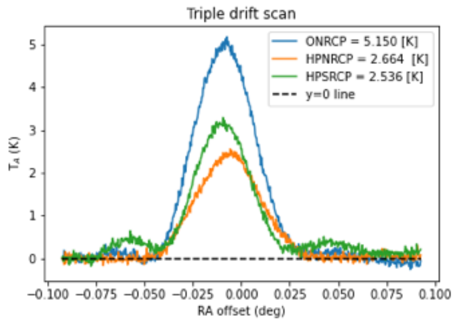

(a) Triple drift scans showing the ON, HPN, and HPS observations overlayed ontop of each other for RCP data.

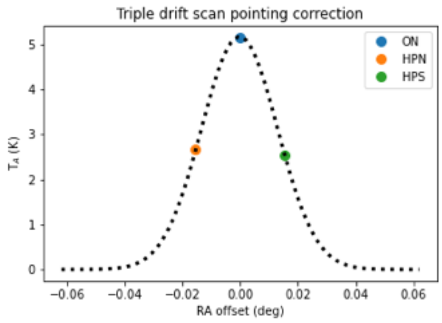

(b) Example of the intensity for the ON, HPN, HPS pointing observations plotted on a bell curve.

Figure 3.3: Example tripple drift scans of Jupiter at 22 GHz.

The drift scans are fitted with a two-dimensional function, typically a parabolic function, and the maximum intensity of the peak fits are measured and used to apply the correction factor required to estimate the true intensity of the source. The pointing correction factor (PC) can then be approximated using different combinations of the ON (T_{ON}), HPN (T_{HPN}), and HPS (T_{HPS}) drift scans, described as:

$$PC = \frac{[\ln(T_{HPS}) - \ln(T_{HPN})]^2}{16\ln(2)} \tag{3.2}$$

for the case where all triple drift scan data is available,

$$PC = \frac{[\ln(T_{HPS}) - \ln(T_{ON}) + \ln(2)]^2}{4\ln(2)} \tag{3.3}$$

This approximation is used when there is no data available from the HPN drift scan.

$$PC = \frac{[\ln(T_{ON}) - \ln(T_{HPN}) - \ln(2)]^2}{4\ln(2)} \tag{3.4}$$

This approximation is used when there is no data available from the HPS drift scan. To obtain the pointing-corrected antenna temperature (T_{CORR}), the correction factor is applied to the measured central drift scan, as shown in the following approximation:

$$T_{CORR} = T_{ON} \times \exp(PC) \tag{3.5}$$

When an observed source does not pass directly through the center of the main beam pattern, it can cause a reduction in the detected radio signal. This is why pointing corrections are important, especially for sources whose beam size is much smaller than the telescope beam width. Telescope pointing can be affected by several factors, including the deformation of the antenna due to gravity, thermal expansion of the antenna, and the offset of the sub-reflector. To minimize these effects, observations are preferably conducted when sources are within 2 hours of zenith. However, this is not always possible as sources are isotropically distributed throughout the sky. These observations would not account for sources at low elevations, especially for sources in the far south where the sky is undersampled compared to the northern hemisphere.

3.1.1.4 Flux density calibration

Telescope sensitivity and the PSS.

The flux density of an astronomical source is intrinsic to the source, and the same flux density should be measured for the same source using any properly calibrated telescope. From Equation 2.10, when observing a radio astronomical source, the measured antenna temperature is proportional to the effective area of the telescope. This relation provides an important calibration factor, k_B/A_e, that converts antenna temperature to flux density for a point source. When Ks = 1, the conversion can be represented as:

$$\frac{k_B}{A_e} = \frac{S_o}{T_A}, \quad [\mathrm{Jy\,K^{-1}}] \tag{3.6}$$

Equation 3.6 is also referred to as the sensitivity of the telescope, called the point source sensitivity (PSS). The PSS indicates the response of a telescope, in terms of the antenna temperature in Kelvins per polarization, obtained per Jansky of source flux density entering the center of the telescope beam. It usually varies with observing frequency. When estimated for each polarization, the PSS can be represented as:

$$\mathrm{PSS_{LCP}} = \frac{\mathrm{S_o}/2}{\mathrm{K_s T_{LCP}}}, \quad [\mathrm{Jy\,K^{-1}\,pol^{-1}}] \quad \text{and} \quad \mathrm{PSS_{RCP}} = \frac{\mathrm{S_o}/2}{\mathrm{K_s T_{RCP}}}, \quad [\mathrm{Jy\,K^{-1}\,pol^{-1}}] \tag{3.7}$$

The factor of half is introduced to indicate that the telescope measures only half the polarization in an EM field. Equation 3.7 provides a measure of how well a telescope can detect a point source of a given flux density, and can be used to compare the sensitivity of different telescopes at different frequencies. For sources that are very small compared to the beam size, $\mathrm{K_s}$=1, the above estimation for the PSS is sufficient. Results of the PSS estimations for the HartRAO calibrators used in this study are given in Chapter 6.

When an observed source is larger than the telescope beam size, such as the Jupiter calibrator, Equation 3.7 no longer holds as extra steps need to be applied to the PSS estimation to correct for the source size. Depending on the observing frequency, other extra corrections may need to be applied as well. The details of how the PSS of Jupiter was estimated are discussed in the second part of this thesis in §6.6.

Calibrator flux estimation.

To measure the sensitivity or PSS of a radio telescope, a source with a known flux density (brightness) is observed. This source is called a calibrator, and it should have stable or slowly-changing flux densities over long periods of time. The flux density of a calibrator monitored by the Hart26m is calculated using the list of absolute radio flux density calibrators provided by Ott et al. (1994). For the calibrator (Hydra A), Ott et al., 1994 represented the flux density model as a polynomial with the log-log form given as:

$$\log(\mathrm{S_{CAL}})[\mathrm{Jy}] = \mathrm{a} + \mathrm{b} * \log\nu[\mathrm{MHz}] + \mathrm{c} * \log^2\nu[\mathrm{MHz}] \tag{3.8}$$

where $\mathrm{S_{CAL}}$ was the calibrator source flux density at a given frequency in MHz, and a = 4.729, b = -1.025, and c = 0.0130 were the coefficients applied for frequencies

1408 MHz < ν < 15000 MHz. The absolute resulting flux densities of Hydra A were then approximated as 27.15 Jy at 2.3 GHz, 13.55 Jy at 4.8 GHz, 8.18 Jy at 8.4 GHz, and 5.71 Jy at 12.2 GHz. All uncertainties in the calibrator PSS are estimated using the propagated error functions described in Bevington and Robinson (2003).

Planets are also used as flux density calibrators, e.g. Jupiter is used at HartRAO to calibrate higher frequency observations at 22 GHz. However, because Jupiter's angular size is much larger than the telescope beam width, its flux can not be estimated using the Ott et al. (1994) estimation. Instead, a series of corrections need to be applied to the data first before the PSS can be estimated. The calibration of Jupiter is discussed in §6.4.

3.1.1.5 Target source flux density estimation

Estimating the flux density of a target source requires the use of the PSS established in Equation 3.7. The PSS is used to obtain a conversion factor from Kelvin to Jansky using the equation;

$$S_{TAR} = PSS_{CAL} \times T_A \quad [Jy] \tag{3.9}$$

where S_{TAR} is the target source flux measured in Jy per polarization, and T_A is the antenna temperature of the target source. To estimate the total flux density of the source for each observation, the average of the flux densities obtained from both polarizations is calculated. The resulting average flux density is then used to study the source activity over time as shown in the radio time-series results in Chapter 4. All uncertainties in the target flux densities are estimated using the propagated error functions described in Bevington and Robinson (2003).

3.1.1.6 Radio frequency interference

All observations prior to processing are required to be clear of radio frequency interference (RFI) interference in order to maximize the chances of estimating the true underlying signal. This can be a challenge, especially in radio observations where the signals are generally very weak, and as such prone to suffer from RFI interference. To minimize this effect, bandwidth filters are applied to the data during observations. At 2.3 GHz a 16MHz filter is passed through the data. At the higher frequencies 4.8 GHz, 8.4 GHz, and 12.2 GHz triple drift scans are carried out one after the other which are later averaged in order to reduce the effect of the noise on the data. Although these methods help, they do not get rid of all RFI. As an added measure, I developed an algorithm to remove the excess RFI that was still getting missed by the bandwidth filters during observations. The algorithm is implemented by the method CLEAN_RFI which is found in the drift scan data reduction and analysis software (DRAN) software package under the FITTING module. Assuming that the signal observed from a the extraterrestrial source is noise-like, we can make assumptions about the distribution of the noise in which the radio signal is embedded. The method CLEAN_RFI takes advantage of the fact that noise is random, hence we can assume that its form follows a gaussian distribution. In the algorithm, it is assumed that all data that is considered as noise will lie close to the central value. Using the root mean squared error (RMSE) equation given as:

$$\mathrm{RMSE} = \frac{1}{\mathrm{N}}\sum_{\mathrm{i}=1}^{\mathrm{N}}(\mathrm{m_i} - \mathrm{o_i})^2 \tag{3.10}$$

where $\mathrm{m_i}$ is a third-degree spline model we fit through the data, and $\mathrm{o_i}$ are the individual measured points of the drift scan, we can establish the sum of the squared errors. The estimated RMSE is then used as a cut-off limit for data that is considered as RFI. The value established to be a good threshold was threshold=3×RMSE. Using an iterative loop, the method calculates the model and RMSE and removes all data points ($\mathrm{o_i}$) that lie above or below the threshold limit. This iteration is evaluated until the value of the cut stops improving or in this case stops decreasing. The data points remaining after the loop is done, are the final data points used for fitting the peak height of the drift scan. The method has been found to work very well, even showing the DRAN software to produce better results than the previous software used to reduce HartRAO data, see Section 7.4.

3.1.2 Data reduction and analysis

The HartRAO data was reduced using the DRAN software package developed specifically for this project that is discussed in Section 7.3. The software was developed to automate the data reduction process, calibrate, and reduce the data using a set of algorithms specifically optimized for drift scan data. In this section, I outline the main data reduction steps which were applied to the data in this work.

3.1.2.1 Data reduction and preparation

The data reduction of all the data in this work was processed following the steps and procedures discussed in detail in §7.3.1.

3.1.2.2 Data analysis

The analysis of HartRAO radio data is dependent on the user and the science case and can be different from source to source. For the data in this study, I analyzed the radio light curves using the DRAN graphical user interface (GUI) discussed in §7.3.3. After the data was prepared using the steps outlined in §7.3.1, the radio flux density of the target source was estimated using the process described in §3.1.1.5. The result of the flux density values together with the errors and other relevant source parameters were then subsequently stored in a database to await further processing.

To process the data, I used the time series and plot-viewer GUIs provided by the DRAN software package. The time series GUI was used to plot the light curve and perform visual inspections and edits to the data e.g. the removal of outliers. While the plot-viewer gui was used to visualize the raw drift-scans. All changes made to the light curve in the software were updated in the database and the final time-series devoid of any obvious outliers was used to estimate the cross-correlations and draw conclusions on the source activity.

3.2 LAT gamma-ray data

Figure 3.4 shows the gamma-ray sky as seen by the LAT averaged over its first 12 years of operation for E > 1 GeV. At the center of the map is bright diffuse emission along the central plane of the MW galaxy most likely powered by energetic accelerated particles. Many of the bright dots above and below the MW plane on the map represent a distant galaxy powered by a SMBH. Along the plane however, many of the bright sources can be attributed to pulsars. The construction of the map relies on event reconstruction software that utilizes energy and incoming trajectory information of detected photons to reconstruct the location of the emitting object.

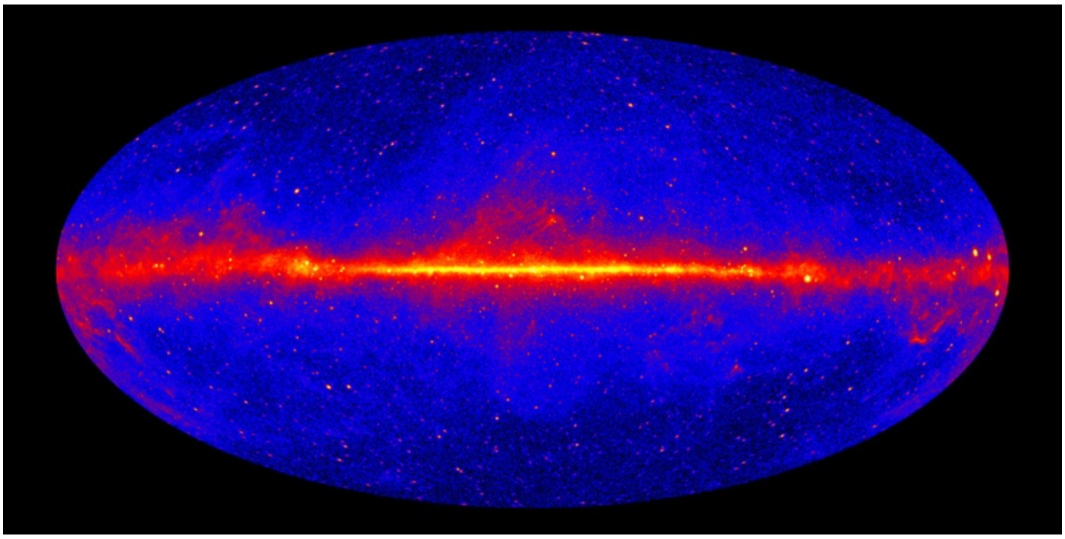

Figure 3.4: Map of the entire sky showing gamma-ray photons as seen by LAT constructed from 12 years of observations. *Credit: NASA/DOE/Fermi-LAT Collaboration*

3.2.1 Large Area Telescope analysis

The standard analysis method used to process LAT data is based on the maximum likelihood (ML) framework. This framework was first applied to photon counting experiments by Cash (1979). Mattox et al. (1996) were the first to apply this method to gamma-ray observations (EGRET data analysis), the success of which subsequently led to an implementation of this framework on LAT data. In this section, I describe the general principles behind the process through which LAT data are analyzed.

3.2.1.1 The Large Area Telecope data analysis model

Given a data set d and a model M(x), the likelihood of the best-fit model is simply given as the probability of obtaining the observed data given an input model i.e. $L(M(x)) = P(d|M(x))$. The idea is to maximize L to get the model parameters that best fit the data. For LAT data, the model provides a description of the distribution of gamma-ray sources on the sky (Figure 3.4), which includes both point sources as well as the diffuse backgrounds. Binning the data in energy and position on the sky means we can express the likelihood function as:

$$L = \prod_{i} \frac{\vartheta_i^{n_i} e^{-\vartheta_i}}{n_i!} \tag{3.11}$$

which gives the probablities over all i energies and positions where n_i are the observed source counts and ϑ_i are the counts predicted by the model. Observed counts in each bin are Poisson distributed. Equation 3.11 describes the binned likelihood analysis. Taking the log of Equation 3.11 simplifies the function to:

$$\log L = \sum_{i} n_i \log \vartheta_i - \sum_{i} \vartheta_i \tag{3.12}$$

If the bin size is allowed to get infenitesimally small i.e. n_i=0 or 1, the likelihood becomes:

$$\log L = \sum_{i} \log \vartheta_i - \vartheta_i \tag{3.13}$$

which gives the definition of the *unbinned likelihood*. The unbinned likelihood method is recommended for point sources, and for short period events where the source count is expected to be small. Counts are evaluated individually and not averaged over a bin, which can become computationally expensive for cases where a large number of counts are involved. However, the binned analysis is preferred for medium to long time bins which greatly reduces computational overheads. This work employs the latter analysis.

To test the significance of a detection at the position estimated by the likelihood function the Test statistic (TS) is estimated in terms of a likelihood ratio. The TS is defined as (Mattox et al., 1996):

$$\mathrm{TS} = -2\log\left(\frac{\mathrm{L}_{\mathrm{max},0}}{\mathrm{L}_{\mathrm{max},1}}\right) \tag{3.14}$$

where $\mathrm{L}_{\mathrm{max},0}$ is the maximum likelihood value excluding the source of interest (null hypothesis), and $\mathrm{L}_{\mathrm{max},1}$ is the maximum likelihood value with the source of interest, provides an estimate of how significantly an image appears over the background emission. For an increasingly large number of counts, asymptotically the TS has the same distribution of the χ^2, and therefore, as a rule of thumb, the square root of the TS is taken as the detection significance for a given source ($\sigma \approx \sqrt{\mathrm{TS}}$).

3.2.1.2 LAT standard point-source data reduction process

The following section explains the steps involved in conducting a binned analysis of the LAT) data using the Fermi Science Tools (FST) and following the recommendations of the Fermi Science Support Center (FSSC). The FST is a set of tools created by the FSSC for analyzing both LAT and GBM data. For more information on different source analysis methods, the reader can refer to the FSSC website[1].

Data processed by the FST can be accessed on the LAT Data ServerData Server[2]. In order to retrieve the data, certain parameters pertaining to the object of study are required, including the source name or coordinates (RA, DEC in degrees), the size of the search radius (typically between 10 and 15 degrees), the observation dates

[1] https://fermi.gsfc.nasa.gov/ssc/data/analysis/scitools/
[2] https://fermi.gsfc.nasa.gov/cgi-bin/ssc/LAT/LATDataQuery.cgi

(TSTART, TEND)[1], and the energy range (EMIN, EMAX in MeV). The query will return a set of raw data files in FITS format, known as event files. There are two types of event files: one containing raw photon data and the other containing spacecraft data, such as information on the telescope's position and orientation during the selected observation period. Both types of event files are necessary for analyzing LAT data.

To prepare the data for analysis, certain standard selection cuts need to be applied to the raw data. The first step in this process, which is done using the GTSELECT tool, involves filtering the event file based on information in the spacecraft file. This filter applies cuts to the center coordinates, Region of Interest (RoI) radius, time, and energy range, as well as the event class and event type (see §2.2.3). In this analysis, the SOURCE class (evclass=128[2]) is used, with an event type of evtype=3, which represents data from both the FRONT and BACK conversion regions. Additionally, a zenith angle cut is applied to avoid contamination from the Earth's limb (usually at $\vartheta < 90°$).

After applying the data cut, another cut is performed on the data using the GTMKTIME tool to select Good Time Intervals (GTI) events. GTI events are events that were obtained when the LAT was in standard data-taking mode. This cut eliminates events from the LAT that were taken while passing through the SAA and ensures that only high-quality data (DATA_QUAL > 0) is used for further analysis.

A binned likelihood analysis organizes all source counts within the RoI into energy and spatial bins. This is done using the GTBIN tool, which creates a 3-dimensional counts cube that includes the source position and energy. In addition to the binned counts, an accurate model that describes the data is also required. The sky model is derived from the LAT source catalog used in the analysis. At the time of this analysis, the latest catalog[3] was the 4FGL-DR2 (Ballet et al., 2020). A user-contributed tool called MAKE4FGLXML.PY is used to create the sky model. This tool creates a list of coordinates and spectral parameters of all objects within the previously specified

[1] The date options vary, between mission elapsed time (MET), modified julian date (MJD) and gregorian dates.

[2] https://fermi.gsfc.nasa.gov/ssc/data/analysis/documentation/Cicerone/Cicerone_Data/LAT_DP.html

[3] The latest catalog at the time of writing this work is the Fourth Fermi-LAT catalog based on the first 12 years of science data (4FGL-DR3) (Abdollahi et al., 2022) which contains 6658 sources in the energy range 50 MeV to 1 TeV.

RoI centered on the target object. The list includes models for isotropic and galactic diffuse emission, as well as the coordinates and spectral information of all sources within an additional 10-degree region. The output of the modeling tool is written to an XML file that includes the coordinates and spectral information for all the sources in the sky model.

After obtaining the sky model and binned photons, further steps need to be taken before conducting the likelihood analysis. To reduce the computational load, it is useful to pre-calculate some processes, such as the livetime and exposure maps. The livetime is the amount of time the LAT observed a particular position in the sky at a specific inclination angle, and the exposure map is an integral of the total response over the entire RoI. The livetime is estimated using the GTLTCUBE tool, which uses data from the spacecraft file and the filtered event file to create a livetime cube, a 3D sky map of position and inclination angle. The exposure map is calculated by using the livetime cube. Pre-computing these processes speeds up the likelihood fitting process, as they do not need to be recalculated every time a fit is performed. Once these quantities have been computed, the maximum likelihood fit can be computed using the GTLIKE tool, which produces the TS and fitted parameter values with statistical errors for all sources (and spectral parameters) in the model that were left free to vary in the fit.

3.2.2 Large Area Telescope data analysis

The analysis of LAT data was carried out using the standard data reduction process outlined in §3.2.1.2. Ten years of LAT Pass 8 data were analyzed using the FERMIPY PYTHON package, which is a wrapper for the FST designed to simplify the analysis of LAT data (Wood et al., 2017). The analysis was conducted using FERMIPY v1.1.6 with the SCIENCETOOLS v2.2.0. For each source, events with energies between 100 MeV and 300 GeV within a 10-degree RoI centered around the 4FGL-DR2 coordinates of the source were extracted. To model the background, the IRF P8R3_SOURCE_V3, along with the latest diffuse models for galactic emission (gll_iem_v07) and isotropic emission (iso_P8R3_SOURCE_V3_v1) were used. These parameters, along with other configuration selections, were input into fermipy to run the analysis.

FERMIPY uses object-oriented programming to create an analysis object, which is used to perform data preparation and response calculations needed for further analysis (such as selecting the data, creating counts and exposure maps, etc.). Once the analysis object was created, the maximum likelihood analysis was run using GTLIKE (§3.2.1.1). The output of GTLIKE must reach convergence and achieve an accuracy or fit quality of 3 for the results to be considered reliable and the likelihood to be accurately maximized. To reach convergence, some model parameters may need to be modified and the likelihood analysis method GTLIKE re-analyzed. The parameters that need to be modified depend on the research goals and vary on a case-by-case basis. For this work, the following guidelines were used to reach convergence:

- Always free the target source and diffuse emission sources.
- Always free sources that lie near the target source (e.g. sources $\leq 1^{\circ}$ away from the target), or highly variable sources to study their effect on the target source.
- Delete or fix sources with a TS$\leq$0, as they do not contribute to the likelihood analysis
- Delete or fix spectral parameters with unrealistic values, or values that differ greatly from catalog values (e.g. spectral index (α) $\geq$5).
- Systematically fix the parameters of weak sources (e.g. the TS) until convergence is reached.

After reaching convergence, further checks were conducted to ensure that the results were reasonable. These checks included visual inspection of the counts and residual maps.

To study the long-term variability of the target objects, standard light curves were computed using bins of equal time frames over the duration of the study period. The size of the data binning depends on the research goals and the significance of the source obtained in the data analysis. I will now proceed to use the results for the source 4FGL J1427.9-4206 (PKS 1424-418) to illustrate the light curve analysis steps. For this specific source, I used 3-day binning widths to create my light curve .

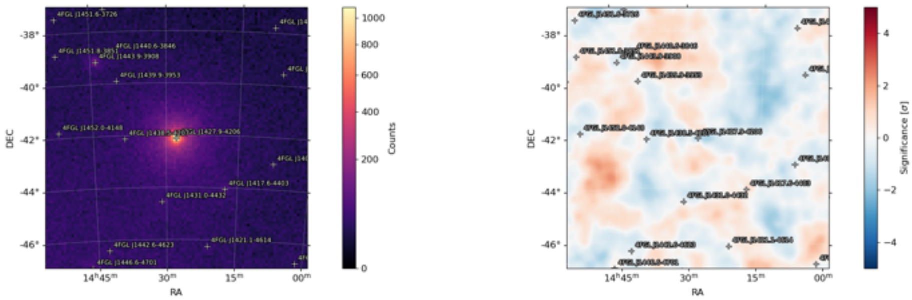

Figure 3.5: Examples of ***Left:*** The counts map, and ***Right:*** Residual map of the blazar 4FGL J1427.9-4206 (PKS 1424-418)

After generating the light curves, I applied several statistical approaches to clean and improve the light curve results. A method to test the goodness of the GTLIKE results is based on the fact that the $\frac{\text{Flux}}{\sigma\text{Flux}}$ ratio should be proportional to the significance ($\sqrt{|\text{TS}|}$) of the source. Through this method, I could determine outliers from the linear dependence of all data points which had TS < 0 and very small uncertainties, see Figure 3.6 top panel. Another sanity check consisted of verifying the good behavior of the distribution of the uncertainties obtained. The bottom left panel of Figure 3.6 shows that the outliers with TS < 0 indicate irregular behavior. These were excluded from the light curve. Further cuts, in addition to those suggested also included looking at the spectral index and beta values of the data and applying cuts based on the catalog values of the source. The approach of analyzing the light curve applied a variation of the methods mentioned here as well as other methods applicable to the data. The final cleaned light curve was then saved and used to estimate the MWL correlations. The results are discussed in Chapter 4.

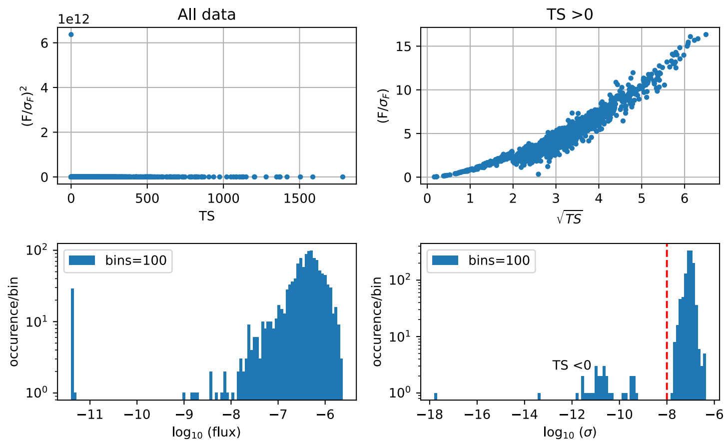

Figure 3.6: Diagnostic plots for Fermi-LAT light curve analysis. **Top:** The proportionality of the ratio $\frac{\text{Flux}}{\sigma\text{Flux}}$ and the significance ($\sqrt{|\text{TS}|}$) of the source is observed for bins with TS > 0, while the bins with TS $\leq$ 0 are outliers. The data were plotted using 100 logarithmically spaced bins. **Bottom:** The outliers are also observed when the distribution of the logarithm of the uncertainties is plotted (right), see the text.

3.3 Multi-wavelength cross-correlation

Blazars are known for their energetic MWL flares from radio wavelengths to high-energy gamma-rays . This behavior makes these sources naturally ideal targets for long-term monitoring observations. The analysis of the correlation between light curves obtained at different wavelengths is crucial to explore the physics of long-term flux variations. The discrete correlation function (DCF) is a widely known method used to study the relationship between two lightcurves (Edelson and Krolik, 1988). In an ideal case, the light curves should be well-sampled and observations should have been done simultaneously. However, as with many cases in astronomical observations, this is rarely the case. Telescope problems, weather conditions, and time-zone constraints can all hinder plans to observe sources simultaneously which directly affects the light curves, creating gaps in the light curve data. The DCF method is a technique that was specifically developed for the estimation of time-lags between unevenly sampled light curves. This method has been used to estimate all the cross-correlation results discussed in this work.

The discrete correlation function

The Unbinned cross-correlation function (UDCF), first introduced by Edelson and Krolik (1988), is a commonly employed technique for analyzing certain characteristics in discrete time series data. The UDCF for two time series, represented as a and b, is defined as:

$$\mathrm{UDCF_{ij}} = \frac{(\mathrm{a_i} - \bar{\mathrm{a}})(\mathrm{b_j} - \bar{\mathrm{b}})}{\sqrt{\sigma_\mathrm{a}\sigma_\mathrm{b}}} \tag{3.15}$$

with $\sigma_\mathrm{a}\sigma_\mathrm{b} = (\sigma_\mathrm{a}^2 - \mathrm{e}_\mathrm{a}^2)(\sigma_\mathrm{b}^2 - \mathrm{e}_\mathrm{b}^2)$ where the values, $(\bar{\mathrm{a}}, \bar{\mathrm{b}})$ are the mean flux values, $(\sigma_\mathrm{a}, \sigma_\mathrm{b})$ are the respective standard deviations. and $(\mathrm{e_a}, \mathrm{e_b})$ denotes the corresponding measurement errors of the respective time series. To estimate the DCF, the correlation coefficients ($\mathrm{UDCF_{ij}}$) are averaged over the pairwise lag $\Delta\mathrm{t_{ij}} = \mathrm{t_j}$ - $\mathrm{t_i}$ within the range τ - $\Delta\tau/2 < \Delta\mathrm{t_{ij}} < \tau + \Delta\tau/2$ where τ is the time-lag and $\Delta\tau$ is the chosen bin width as shown in Equation 3.16

$$\mathrm{DCF}(\tau) = \frac{1}{\mathrm{N}} \sum_{\mathrm{ij}} \mathrm{UDCF_{ij}} \tag{3.16}$$

with N as the number of UDCF entries. Estimations in the errors are expressed in terms of the scatter in the $\mathrm{UDCF_{ij}}$ terms expressed as

$$\sigma_\tau = \frac{1}{\mathrm{N}-1}\left[\sum(\mathrm{UDCF_{ij}} - \mathrm{DCF}(\tau))^2\right]^{1/2} \tag{3.17}$$

The DCF is just one of many other cross-correlation functions available for time-lag estimations. An alternate solution to the DCF estimation can be obtained using the Z-Transformed Cross-Correlation function (ZDCF) (Alexander, 1997). The ZDCF method uses a Fisher's z-transform (Fisher, 1922) to estimate the correlation by binning over equal populations rather than equal bin widths. Given that prelimenary tests using both methods on a sample data set revealed very small differences in the uncertainties of the DCF compared to the ZDCF, this work utilized the DCF to estimate the correlations for the data. To estimate the correlations and time lags, the Data Exploration System (DES)[1] software package developed by Dr. Stefan Larsson of Stockholm University was utilized. DES interactively analyzes and simulates astronomical time-series data. For this work, my interest was in the lag obtained from the correlation and not necessarily the correlation itself. To estimate the time lags in the light curves a simple Gaussian was fitted over the dominant peak of each obtained correlation which was evaluated using different bin widths mainly led by the eye with the aim to find the best peak that exhibited a profile closest to the Gaussian profile with no prior assumptions made on the shape of the data.

[1] https://ttt.astro.su.se/groups/head/SL/des7.html

4 Results

Systematic long-term observations of AGN provide valuable insights into the nature of these highly energetic objects. In this chapter, I give the results from the flaring activity and interband correlations for the sources PKS 1424-418, PKS 0454-810 and PKS 0903-57. In this study, a "flare" is defined as an abrupt increase and decrease in source flux, where the peak flux was at least twice the value of half the average flux. I identified flares and their durations by visually inspecting the light curves, selecting intervals between two successive local minima as the duration of a flare. My analysis included a data sample of 3-day averaged Fermi-LAT gamma-ray light curves, as well as daily light curves from HartRAO, and intermittent light curves from REM, ATCA, BVID, IVS, GSFC and Astrogeo.

4.1 The case of PKS 1424-418

4.1.1 Brief introduction

PKS 1424-418, also referred to as LAT source 4FGL J1427.9-4206, is a high redshift (z = 1.522, White et al., 1988) FSRQ blazar located at RAJ2000 = 14:27:56.3 and DECJ2000 = -42:06:19.4 (Johnston et al., 1995; Healey et al., 2007). This source has been continuously monitored by the Fermi-LAT team since the start of Fermi-LAT operations in 2008 and has flared multiple times throughout the EM spectrum[1] (Longo et al., 2009; Donato, 2010; Szostek, 2011; Ojha and Dutka, 2012; Tavecchio et al., 2013; Nemenashi, Gaylard, and Ojha, 2013; Buson et al., 2014; Ursi et al., 2018) making it a subject of interest for numerous research efforts, due to its broadband variability. In this study, I investigated the 10-year variability of PKS 1424-418 using multi-wavelength observations from my selection of detectors.

The observations covered the period between the start of Fermi-LAT gamma-ray monitoring in 2008 and 2018 and are summarized in Table 4.1 and plotted in Figure 4.1. The primary goal of this study was to investigate the gamma-ray and radio emission and establish if the light curves showed a correlated relationship. MWL observations enable us to study the temporal evolution of sources at different wavelengths and provide snapshots of different activities occurring in these sources at the same time, given that the light curves are simultaneous or quasi-simultaneous with adequate time series data. Using MWL multi-resolution data, I analyzed the light curve data of PKS 1424-418 to gain insight into its flaring behavior. The observations revealed multiple flares and long-term increasing flux baselines in all the light curves over the study period.

[1] PKS 1424-418 is a regularly monitored source by the Fermi-LAT team. The source gamma-ray activity can be followed by visiting the link https://fermi.gsfc.nasa.gov/ssc/data/access/lat/msl_lc/source/PKS_1424-41

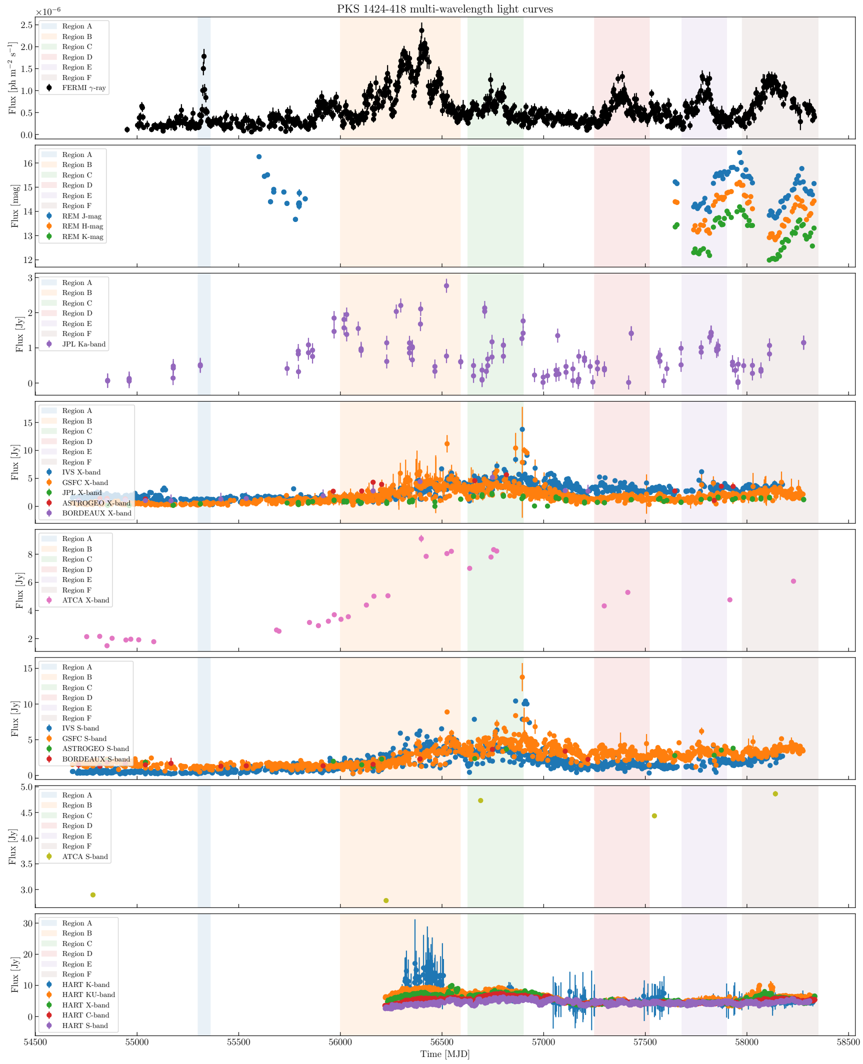

Figure 4.1: The multi-wavelength light curves of PKS 1424-418 are presented in descending order of energy, from top to bottom. The colored highlighted regions indicate periods of Fermi-LAT gamma-ray flaring activity, providing a clear visual representation of the correlation between the different energy bands.

Instrument	Energy band	Period (MJD)	Flux (min)	Flux (max)	Obs[a].
Fermi-LAT	0.1 to 500 GeV	54951 to 58332	5.9 x 10^{-8} [ph cm^{-2} s^{-1}]	2.4 x 10^{-6} [ph cm^{-2} s^{-1}]	902[b]
REM	J mag	55600 to 58330	13.67 [mag]	16.43 [mag]	92
REM	H mag	55600 to 58330	12.83 [mag]	15.20 [mag]	60
REM	K mag	55600 to 58330	11.99 [mag]	14.19 [mag]	58
JPL	Ka band	54855 to 58279	0.01 [Jy]	2.77 [Jy]	124
JPL	X band	54855 to 58279	0.01 [Jy]	2.30 [Jy]	92
IVS	X band	54682 to 58175	0.28 [Jy]	13.77 [Jy]	1018
IVS	S band	54682 to 58175	0.61 [Jy]	31.28 [Jy]	1018
GSFC	X band	54682 to 58276	0.61 [Jy]	33.57 [Jy]	1124
GSFC	S band	54682 to 58276	0.28 [Jy]	13.77 [Jy]	1124
Astrogeo	X band	54817 to 57932	1.07 [Jy]	5.65 [Jy]	14
Astrogeo	S band	54817 to 57932	1.23 [Jy]	3.81 [Jy]	14
BVID	X band	54712 to 57218	0.81 [Jy]	5.19 [Jy]	14
BVID	S band	54712 to 57218	1.29 [Jy]	3.65 [Jy]	14
ATCA	X band	54752 to 58229	1.49 [Jy]	9.11 [Jy]	31
ATCA	S band	54783 to 58140	2.79 [Jy]	4.86 [Jy]	5
Hart26m	K band	56304 to 58327	3.02 [Jy]	17.52 [Jy]	314
Hart26m	Ku band	56221 to 58333	3.15 [Jy]	10.03 [Jy]	1483
Hart26m	X band	56232 to 58334	3.64 [Jy]	9.97 [Jy]	1043
Hart26m	C band	56219 to 58334	3.35 [Jy]	7.46 [Jy]	1115
Hart26m	S band	56220 to 58334	2.48 [Jy]	6.31 [Jy]	830

Table 4.1: Overview of PKS 1424-418 MWL multi-resolution dataset.
Note.- [a] The number of flux points shown in Figure 4.1 for each energy band.
[b] The number of flux points in the 3-day binned light curve.

4.1.1.1 Fermi-LAT gamma-ray light curve

PKS 1424-418 is one of the sources regularly monitored by the Fermi-LAT telescope for flaring activity. For this study, I analyzed Fermi-LAT data collected between August 4th, 2008 (MJD 54682) and August 5th, 2018 (MJD 58335) using the FERMIPY package for data processing and analysis. In this section, I present the results of the LAT analysis described in §3.2.2 for PKS 1424-418. The LAT light curve is shown in Figure 4.2 reveals multiple flaring episodes occurring between 2008 and 2018, which I describe in detail in the following paragraphs.

The source PKS 1424-418 has undergone multiple flaring events since it was first monitored by Fermi-LAT in 2008 (Van Zyl, 2016), and this activity continues to

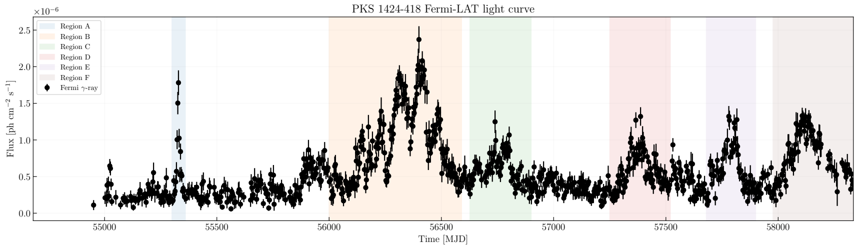

Figure 4.2: Fermi-LAT light curve plot of PKS 1424-418 gamma-ray data with energies above 100 MeV. The plot shows the flaring behavior of the source observed between August 4th, 2008 (MJD 54682) and August 5th, 2018 (MJD 58335), with the data binned using 3-day binning widths. The plot highlights the six different regions (marked as A to F) of significant flaring behavior exhibited by the source during this period.

the present day (Jankowsky and Wagner, 2022). The light curve of PKS 1424-418 reveals at least six distinct regions that indicate flaring outburst events occurring between 2008 and 2018. These regions are labeled A through F in Figure 4.2. Region A represents the source flare that occurred between 2008 and 2011 (Buson et al., 2014), during which I measured a peak flux of 1.78 ± 0.17 x 10^{-6} ph cm^{-2} s^{-1} from my LAT analysis. Region B includes multiple smaller flaring episodes, which I have identified and labeled as B1 through B5 in Table 4.2 and Figure 4.3.

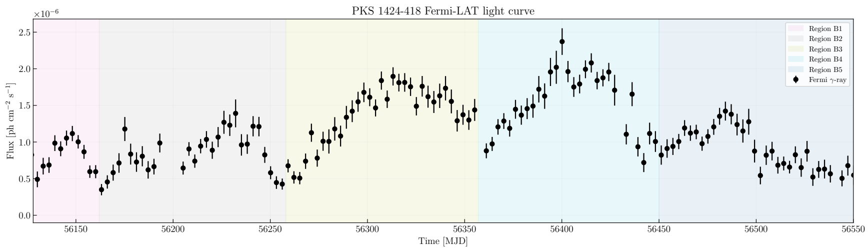

Figure 4.3: Light curve of PKS 1424-418 from Fermi-LAT showing the flaring activity in Region B. This period consists of multiple smaller flaring episodes, identified as B1 to B5

PKS 1424-418 underwent a significant brightening event in 2013, with its flux steadily increasing for a year until it reached its peak value of 2.37 ± 0.18 x 10^{-6} ph cm^{-2} s^{-1} in Region B. This was the longest and most intense outburst ever recorded for the source, and it coincided with the detection of a 2 PeV neutrino from the same location (Kadler et al., 2016). The outburst was also observed in other wavelengths, including X-ray (D'Ammando, 2013), optical (D'Ammando et al., 2013) and radio (Nemenashi, Gaylard, and Ojha, 2013), triggering long-term monitoring of this source at HartRAO (Van Zyl, 2016). Following the outburst, PKS 1424-418 gradually returned to its quiescent stage, with a flux of ~0.2 ± 0.1 x 10^{-6} ph cm^{-2} s^{-1} . However, it subsequently underwent four weaker outbursts, peaking on March 23, 2014 (Region C), December 31, 2015 (Region D), January 27, 2015 (Region E), and December 20, 2017 (Region F), with an average flux of 1.3 ± 0.1 x 10^{-6} ph cm^{-2} s^{-1}. These results are summarized in Table 4.2.

Flare	Start date (MJD)	End date (MJD)	Peak date (MJD)	Peak flux (1 x 10^{-6} ph cm^{-2} s^{-1})	α^a
A	55300	55360	55329	1.78 ± 0.17	1.79 ± 0.08
B1	56128	56162	56148	1.12 ± 0.10	1.95 ± 0.08
B2	56162	56258	56232	1.39 ± 0.19	2.14 ± 0.12
B3	56258	56357	56313	1.90 ± 0.12	2.02 ± 0.06
B4	56357	56450	56400	2.37 ± 0.18	1.97 ± 0.07
B5	56450	56550	56484	1.42 ± 0.13	1.92 ± 0.08
C	56627	56900	56739	1.25 ± 0.15	2.13 ± 0.11
D	57250	57520	57387	1.32 ± 0.13	2.23 ± 0.08
E	57680	57900	57780	1.32 ± 0.14	2.28 ± 0.11
F	57977	58350	58107	1.33 ± 0.11	2.09 ± 0.08

Table 4.2: Locations and peak fluxes of PKS 1424-418 gamma-ray flares.
Note.- [a] The peak spectral index.

The strength of each peak in a flare can exhibit temporal variability, with some peaks rising rapidly over short periods (strong flares), while others rise slowly over longer periods (weak flares). These features can provide insight into the strength of the underlying emission mechanism. Table 4.3 summarizes the rise and fall times of each peak during a flaring episode. Among the six flare regions identified in PKS 1424-418, Region A exhibited the fastest rise time (~19 days), while Region D had the longest rise time (~137 days). Similarly, Region B1 had the shortest fall time (~12 days), while Region F had the longest fall time (~238 days).

Flare region	Rise period	Rise days	Fall period	Fall days
A	55310 - 55329	19	55329 - 55350	21
B1	56128 - 56148	20	56148 - 56160	12
B2	56161 - 56232	71	56232 - 56259	27
B3	56260 - 56313	53	56313 - 56350	37
B4	56360 - 56400	40	56400 - 56443	43
B5	56450 - 56484	34	56484 - 56550	66
C	56627 - 56739	112	56739 - 56900	161
D	57250 - 57387	137	57387 - 57520	133
E	57680 - 57780	100	57780 - 57900	120
F	57977 - 58107	130	58107 - 58345	238

Table 4.3: Rise and fall times of the flaring episodes in PKS 1424-418.

4.1.2 VLBI and radio interferometeric results

To complement the gamma-ray observations, I obtained interferometric data from a variety of different observatories. The ATCA and VLBI measurements give details on the source behavior at high resolution. In Figure 4.4 the ATCA S/X band light curves show a long-term gradual increase in flux that peaks in Region B (for X band) where the gamma-ray flaring is the strongest. We observed the same effect for the JPL ka band shown in Figure 4.5. The IVS and GSFC X and S band data however show peaking in Regions B and C, see Figures 4.6 and 4.7. The Astrogeo, BVID however shows peaking only in Region C in both S and X bands.

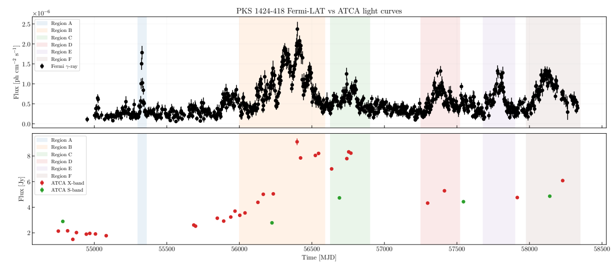

Figure 4.4: PKS 1424-418 ATCA X/S band light curves. **Top:** Fermi-LAT vs **Bottom:** ATCA X/S band light curves.

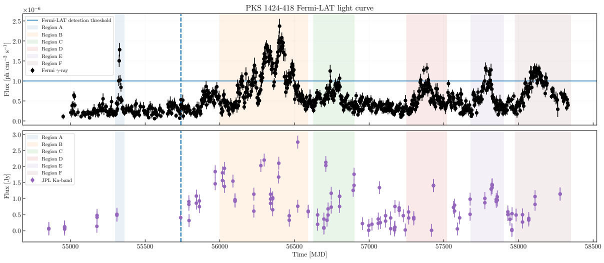

Figure 4.5: PKS 1424-418 JPL Ka band VLBI light curve. **Top:** Fermi-LAT vs **Bottom:** JPL Ka band light curve.

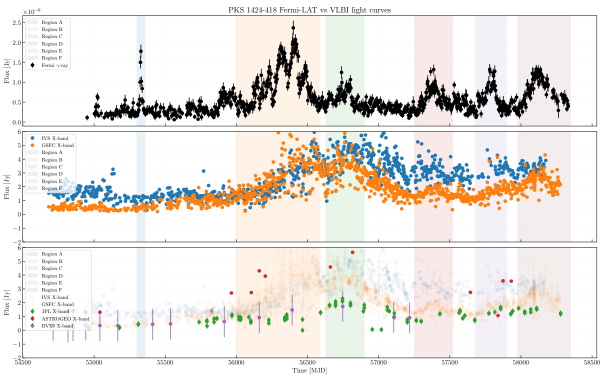

Figure 4.6: PKS 1424-418 VLBI light curves. **Top:** Fermi-LAT vs **Middle and Bottom:** VLBI X band light curves. In the middle and bottom plots, the IVS and GSFC light curveshave been scaled for clarity.

4.1.3 Single dish radio results

Simultaneously, the HartRAO radio light curves also began to show increasing flux trends, with the radio frequencies exhibiting a steep rise in flux almost instantaneously at 2.3 GHz, 4.8 GHz, 8.4 GHz, and 12.2 GHz (see Figure 4.8). In addition to the HartRAO single-dish radio observations showing a sharp increase coincident with the gamma-ray flare periods, the radio data also shows radio flaring episodes. Figure 4.9 displays two broad humps at 4.8 GHz, 8.4 GHz, and 12.2 GHz, with the first one occurring before MJD 56600 (November 4, 2013) and the second between MJD 56600 and MJD 57200 (June 27, 2015). The source enters a period of quiescence between MJD 57200 and MJD 57920 (June 16, 2017), following which it begins flaring again

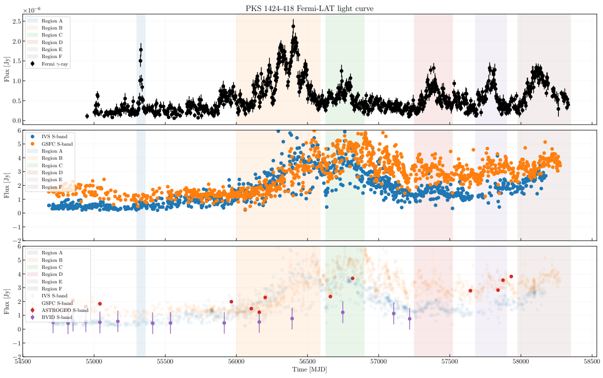

Figure 4.7: PKS 1424-418 VLBI light curves. **Top:** Fermi-LAT vs **Middle and Bottom:** VLBI S band light curves. In the middle and bottom plots, the IVS and GSFC light curveshave been scaled for clarity.

shortly thereafter. These regions are indicated by the black dashed lines. Additionally, three smaller humps or "mini radio flares" are visible in Figure 4.8, centered on MJD 56320 (January 28, 2013), 56550 (September 15, 2013), and 58100 (December 13, 2017), indicated by yellow dashed lines. Although the humps coincide with all the radio light curves on these dates, they appear to a lesser extent on the lower radio frequencies. At 4.8 GHz, the mini flare appears shifted to the right to MJD 57010 (December 19, 2014) (see Figure 4.9). Table 4.4 lists the peak fluxes of the radio data obtained by fitting a second-order polynomial to the highest radio flare region before MJD 58000 (September 4, 2017). The peak brightness of the light curves was chosen in this way because the flare at MJD 58100 is a steep increase that is part of the mini flares I mentioned previously, which may be due to other source activity that may not necessarily be the general trend of the lightcurve. For instance, the blazar may be ejecting some material over and above the brightening of the source, which may require its own different set of analyses. This flare is visible in all HartRAO light curves. With regards to the peak flux, all single-dish radio fluxes appear to peak in Region C. This is excluding the secondary flaring episodes.

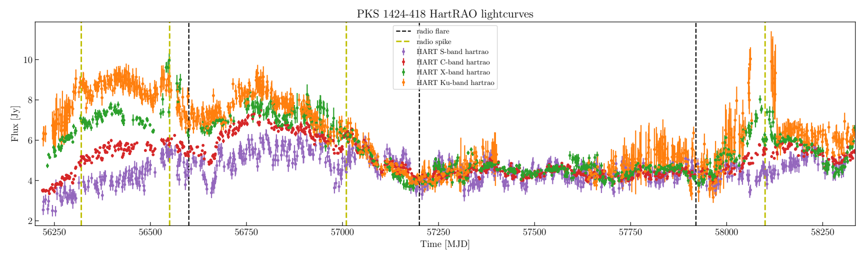

Figure 4.8: Plot of HartRAO light curves showing the different radio flares at 2.3 GHz, 4.8 GHz, 8.4 GHz, and 12.2 GHz overlaid on top of each other. The black dotted lines indicate the end or beginning of a radio flaring period. The yellow dotted lines indicate dates of sudden rises in flux density that do not correspond to the general long-term trend of the data. The 22 GHz light curve has been deliberately left out from the plot for clarity.

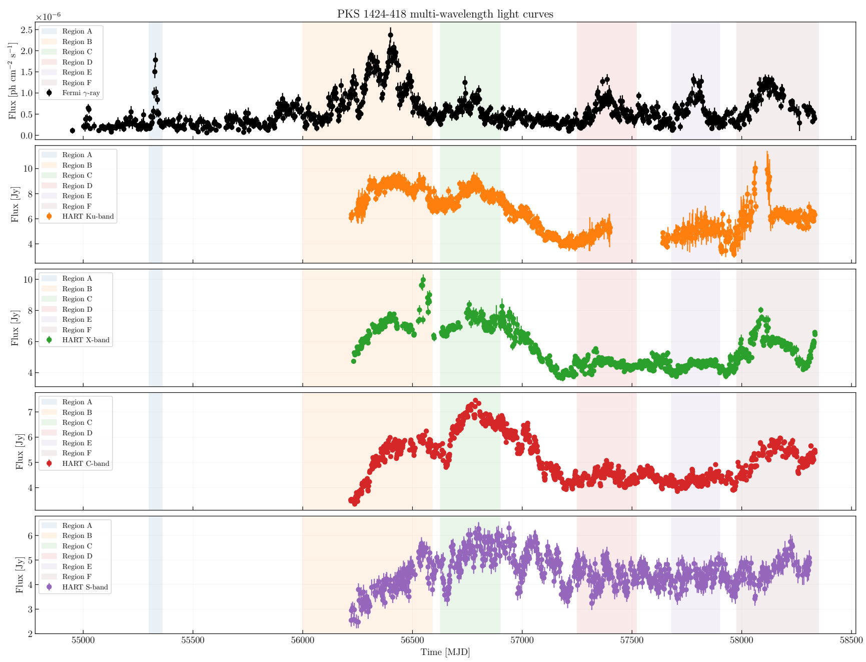

Figure 4.9: Plot of HartRAO light curves showing the different radio flares at 2.3 GHz, 4.8 GHz, 8.4 GHz, 12.2 GHz and 22 GHz. The gaps in the 12.2 GHz light curve are due to the receiver being taken off the antenna.

Table 4.4: Peak fluxes for radio flare regions of PKS 1424-418.

Freq	Peak date (MJD)	Flux min Jy	Flux max Jy	Peak fit flux. Jy	Peak fit err Jy
12.2 GHz	56434	3.15	10.04	8.90	0.42
8.4 GHz	56814	3.64	9.97	7.47	0.39
4.8 GHz	56823	3.35	7.46	6.92	0.28
2.3 GHz	56912	3.23	6.10	5.20	0.53

4.1.4 multi-wavelength Cross-correlations

The main objective of this study was to explore the potential correlation between gamma-ray, optical, and radio emission from PKS 1424-418. To achieve this, I used the DCF technique (described in §4.1.4) to measure the correlation between two light curves. The analysis was performed in two ways. First, I used the complete data sets of each wavelength to estimate the DCF (§4.1.4.1), Table 4.1 summarizes the epochs. Next, I analyzed the DCF for the different flaring regions (A to F, §4.1.4.1), Table 4.2 summarizes the epochs. The aim of the analysis was to identify the time lag between two light curves, which indicates whether a flare observed in one band was followed by a corresponding flare in another. Such interband correlations provide essential insights into the underlying source activity and temporal behavior of blazar sources, helping us better understand these objects.

To determine the DCF peak, I fitted a Gaussian function to the DCF. This allowed me to determine the correlation coefficient at the peak as well as the corresponding time lag (τ) and its uncertainty. Due to the sparcity of the optical data, I was unable to establish strong correlations between the gamma-ray and optical wavelengths, which emphasizes the need for further research in this area and highlights the significance of future observations in the optical wavelength range. The strongest correlations established were found to be between the gamma-ray and radio light curves. Table 4.5 lists the time lags established for the the strong correlations.

The results indicate strong correlations (correlation coefficients ≥ 0.5) between the gamma-ray and radio emissions, with time lags averaging around $\sim$200 days for single-dish radio data. These findings provide important insights into the underlying

Table 4.5: Time lags from the DCF estimations

Light curves	Lag (days)
From entire dataset	
Fermi-LAT (Gamma-ray) vs IVS (X band)	204.33 ± 10.59
Fermi-LAT (Gamma-ray) vs HartRAO (X band)	209.05 ± 14.63
From flaring region B	
Fermi-LAT (Gamma-ray) vs IVS (X band)	197.82 ± 4.99
Fermi-LAT (Gamma-ray) vs IVS (S band)	110.38 ± 5.23
Fermi-LAT (Gamma-ray) vs GSFC (S band)	199.84 ± 5.09
Fermi-LAT (Gamma-ray) vs HartRAO (Ku band)	107.81 ± 6.04
Fermi-LAT (Gamma-ray) vs HartRAO (X band)	203.41 ± 7.18
Fermi-LAT (Gamma-ray) vs HartRAO (C band)	190.92 ± 6.62
From flaring region F	
Fermi-LAT (Gamma-ray) vs HartRAO (Ku band)	-27.07 ± 5.87
Fermi-LAT (Gamma-ray) vs HartRAO (X band)	-21.07 ± 7.98
Fermi-LAT (Gamma-ray) vs HartRAO (C band)	26.89 ± 7.16
Fermi-LAT (Gamma-ray) vs HartRAO (S band)	85.93 ± 5.60

source activity and temporal behavior of PKS 1424-418, suggesting a common origin for gamma-ray and radio emissions that can be used to further examine the exact location of the gamma-ray emission site. From the data it can also be seen that the most of the strong correlations occur during the major outburst (region B) which occurred 2012-2013. Results of the DCF plots are shown below.

4.1.4.1 DCFs from the entire data set

The results from the DCF estimated over the entire length of a dataset are shown below. The DCF analysis revealed some strong correlations between the gamma-ray emission and the interferometric emission from X band ATCA observations (Figure4.10a), as well as single-dish emission from HartRAO (Figure4.10b). Despite efforts to measure correlations between the Fermi-LAT, optical, and the radio VLBI bands, the DCF estimations over the entire term of the study did not reveal any strong correlations at these wavelengths.

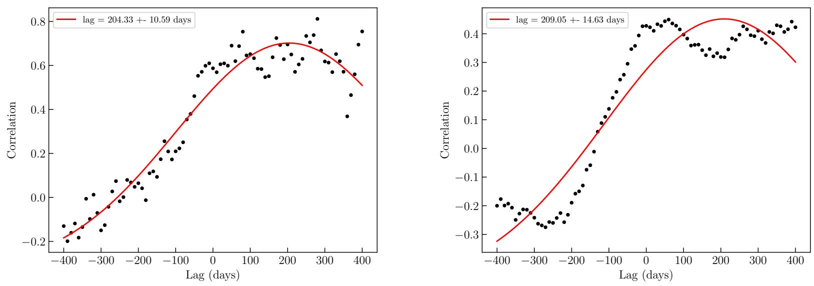

(a) Fermi-LAT vs ATCA X band

(b) Fermi-LAT vs HartRAO X band

Figure 4.10: Results from the DCF analysis over the entire dataset

4.1.4.2 DCFs from the flaring regions

The results from the DCF estimated over the flaring regions are shown below. The DCF revealed strong correlations in events occuring between regions B and F only.

4.1.4.3 Region B flares

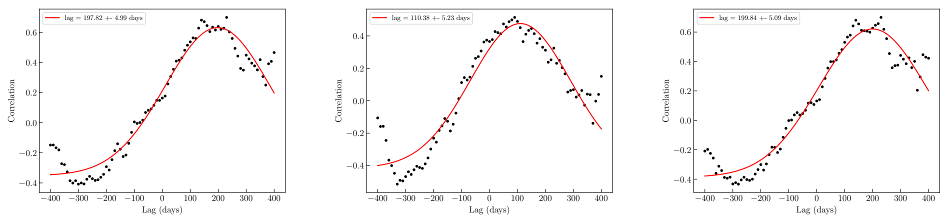

(a) Fermi-LAT vs IVS X band

(b) Fermi-LAT vs IVS S band

(c) Fermi-LAT vs GSFC S band

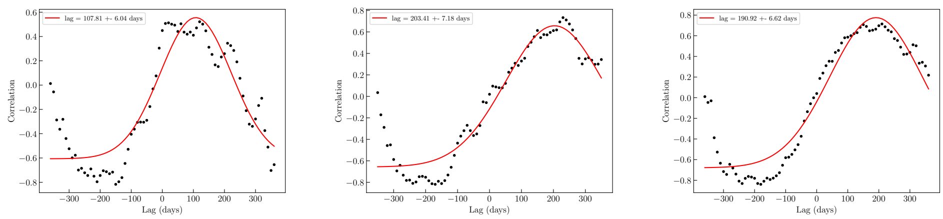

(d) Fermi-LAT vs HartRAO Ku band

(e) Fermi-LAT vs HartRAO X band

(f) Fermi-LAT vs HartRAO C band

Figure 4.11: DCF results from region B flares

4.1.4.4 Region F flares

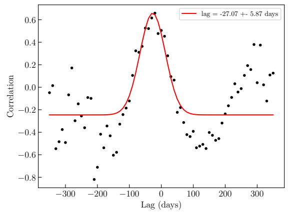

(a) Fermi-LAT vs HartRAO Ku band

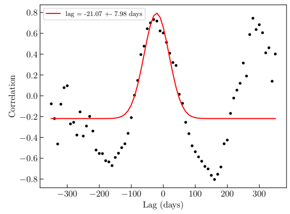

(b) Fermi-LAT vs HartRAO X band

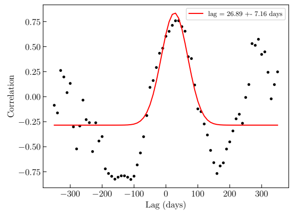

(c) Fermi-LAT vs HartRAO C band

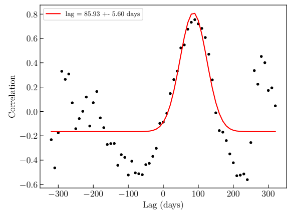

(d) Fermi-LAT vs HartRAO S band

Figure 4.12: DCF results from region F flares

It is important to note that while the structure visible in the DCF plots is indicative of a strong correlation, the Gaussian fit used to determine the correlation coefficients and time lags has its limitations. While the fit provides a reasonable approximation of the peak values, it may not fully capture the complexity of the observed structure. Therefore, further tests are required to establish the significance of the estimated correlations. Evaluating whether the structure visible in the DCF plots is real or not is beyond the scope of this work and will be the subject of future investigation.

4.2 The case of PKS 0450-810

4.2.1 Brief introduction

4FGL J0449.6-81000 (PKS 0454-810) is a highly compact source that recently showed up in the Fermi-LAT 4FGL-DR2 (Ballet et al., 2020) catalog of Fermi-LAT sources. However, the source shows weak gamma-ray emission, as the source flux falls below the Fermi-LAT detection threshold for a source with gamma-ray activity. PKS 0454-810 is a highly compact source on mas scales. Making it an ideal calibrator for VLBI, geodetic and astrometric purposes. It forms part of the ICRF sources and is a defining source for the celestial reference frame (Charlot et al., 2020). PKS 0454-810, also referred to as LAT source 4FGL-J0449.6-8100, with redshift (z = 0.444, White et al., 1988) is an FSRQ blazar located at RAJ2000 = 04:50:05.4 and DECJ2000 = -81:01:02.2 (Johnston et al., 1995; Healey et al., 2007). For celestial reference frame, highly compact radio sources are considered perfect candidates. Since the objects are extragalactic, they are all sufficiently distant, so that parallaxes and proper motions are negligible. There are currently 4536 ICRF sources and only 303 of them are considered defining radio sources i.e. refrence frame sources. PKS 0454-810 is a defining source, highly compact with weak gamma-ray emission.

4.2.2 MWL light curves

The PKS 0454-810 multi-wavelength light curve, presented in Figure 4.13, shows detailed radio emission in single-dish and VLBI frequencies. The light curve indicates although the source is known to be compact on mas scales, it appears to show some small scale variability as shown in the GSFC and HartRAO light curves of Figure 4.13 (Shabala et al., 2017). The data also shows some indication of the single-dish radio data possibly increasing at the end of the study period, but I require more data in order to test if that is indeed the case. Although some small-scale variability is expected, the radio single-dish light curves also show quite a defined trend in the light curves whereas the JPL and ATCA do not. The GSFC data also appears to be showing some defined variable trends after MJD 57000. However, despite all the features we can currently observe, a strong correlation could not be established between the light curves. To properly analyze this source's behavior more data is required. I leave the further analysis of this source to future work.

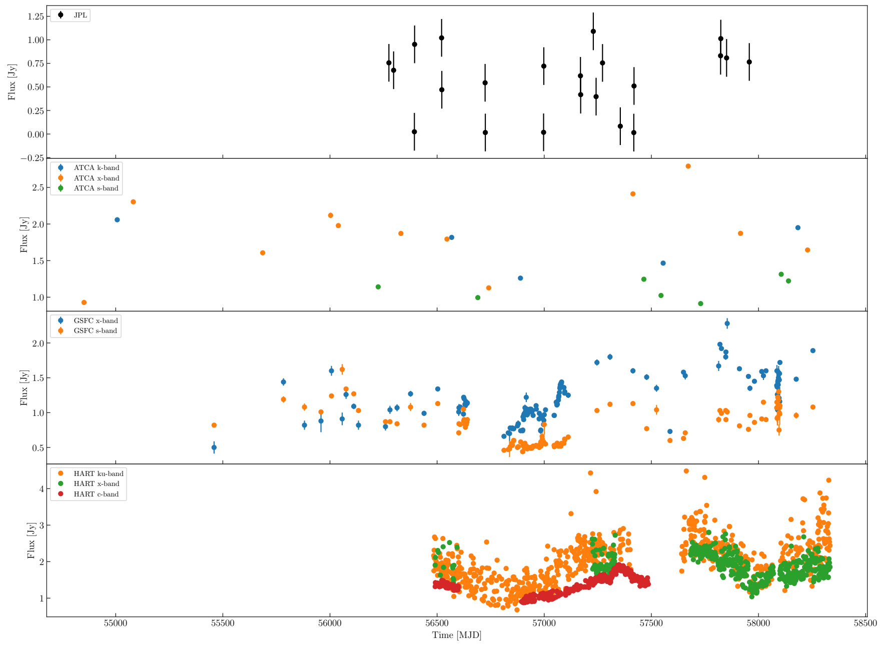

Figure 4.13: The multi-wavelength light curves of PKS 0454-810.

4.3 The case of PKS 0903-57

4.3.1 Brief introduction

I obtained Fermi-LAT, Hart26m, GSFC s/x-band, and ATCA x-band data for this source. The MWL light curve study of 4FGL J0904.9-5734 (PKS 0903-57) also known as 4FGL J0904.9-5734 an active galaxy of uncertain type (BSU) very high energy (VHE; E > 100 GeV) blazar source, is presented. Located at right ascension $(RA)_{J2000}$ = 09:04:53.2 and declination $(DEC)_{J2000}$ = -57:35:05.8 (Charlot et al., 2020), this source has been known as a bright gamma-ray blazar since its debut in the Abdo et al. (LAT 1-year Source Catalog (1FGL), 2010) in 2010, and has a high redshift (z) of 0.6956 (Thompson, Djorgovski, and Carvalho, 1990). The source is also included in Fermi-LATs regularly monitored source list[1], and is also known to emit radiation in TeV energies[2].

4.3.2 Multi-wavelength light curves

During the study, PKS 0903-57 only flared once in gamma-rays in a period of 10 years. Creating the bump shown in Figure 4.14.

As shown in Figure 4.15 the Fermi-LAT light curve (see Figure 4.14) the source appears to have been in quiescence for most of our observing period and has flared only once throughout, reaching a maximum of 2.2e-06 ph cm^{-2} s^{-1}over 130 days, showcasing what appeared as two separate flares Figure 4.16. The radio light curves however appear quite peculiar, showing behavior indicative of flaring, prior to the gamma-ray flare in all frequencies at, 2.3 GHz, 4.8 GHz, 8.4 GHz, and 12.2 GHz. The minimum and maximum flux values are indicated in Table 4.6. Due to the scarcity of gamma-ray flaring events, this source could not be studied any further but, but will however be evaluated in future work as it is a HartRAO continuously monitored source and also indicates a flaring state beginning at the end of this study.

[1]https://fermi.gsfc.nasa.gov/ssc/data/access/lat/msl_lc/
[2]http://tevcat.uchicago.edu/?mode=1&showsrc=339

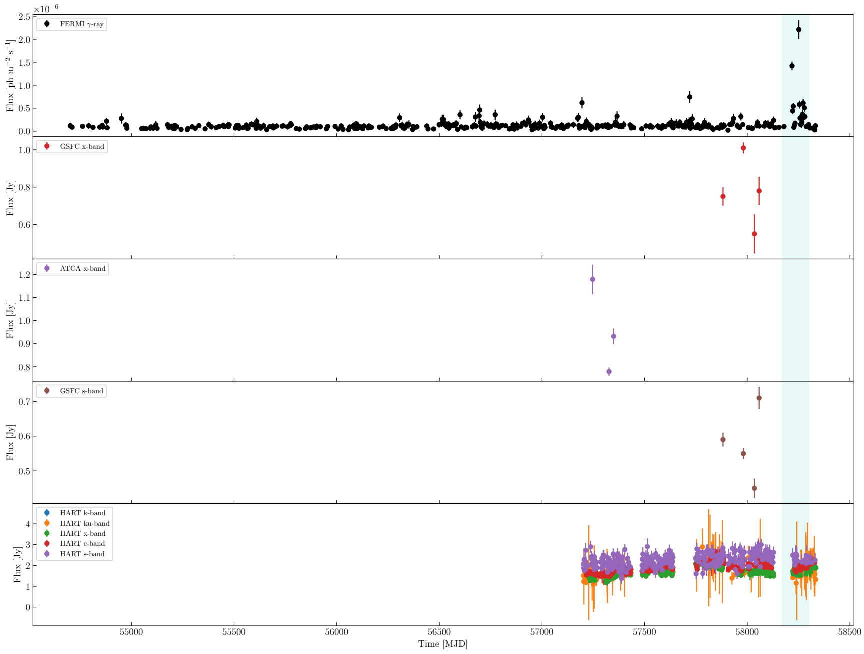

Figure 4.14: MWL light curves of PKS 0903-57 data.

Instrument	Energy band	Period (MJD)	Flux (min)	Flux (max)	Obs
Fermi-LAT	0.1 to 500 GeV	54702 to 58332	2.2e-08 [ph cm^{-2} s^{-1}]	2.2e-06 [ph cm^{-2} s^{-1}]	381
Hart26m	Ku band	57202 to 58333	1.09 [Jy]	2.89 [Jy]	90
Hart26m	X band	57230 to 58334	1.18 [Jy]	2.29 [Jy]	272
Hart26m	C band	57214 to 58329	1.47 [Jy]	2.68 [Jy]	365
Hart26m	S band	57202 to 58333	1.37 [Jy]	3.00 [Jy]	312

Table 4.6: Target source observation information for PKS 0903-57.
Note.- Table of target source observation information. Source is the name of the observed target. Flux is the flux or magnitude limit of the observation. The period is the duration of the observation, and Obs. is the number of observations obtained during this period.

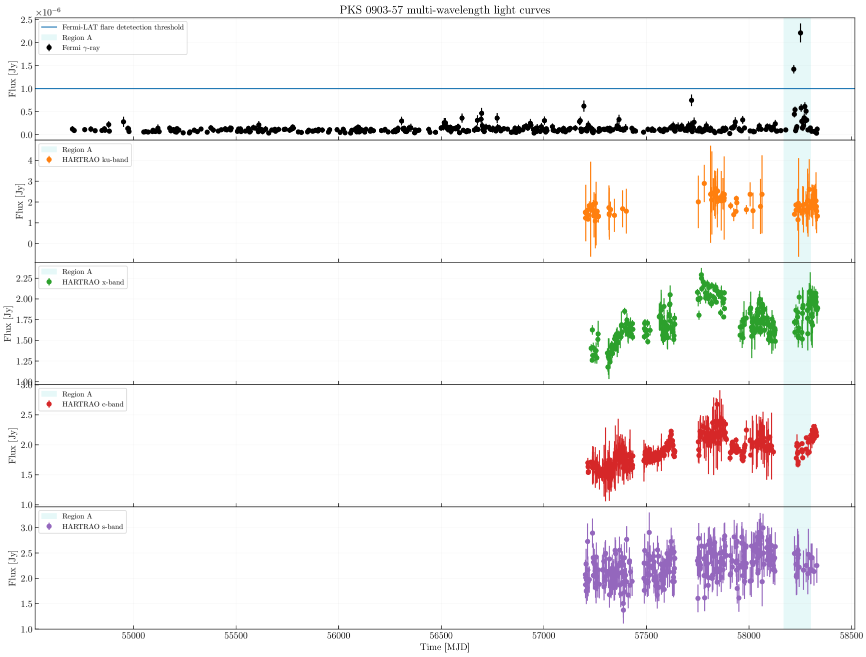

Figure 4.15: MWL light curves of PKS 0903-57 showing only Fermi-LAT and Hart26m data.

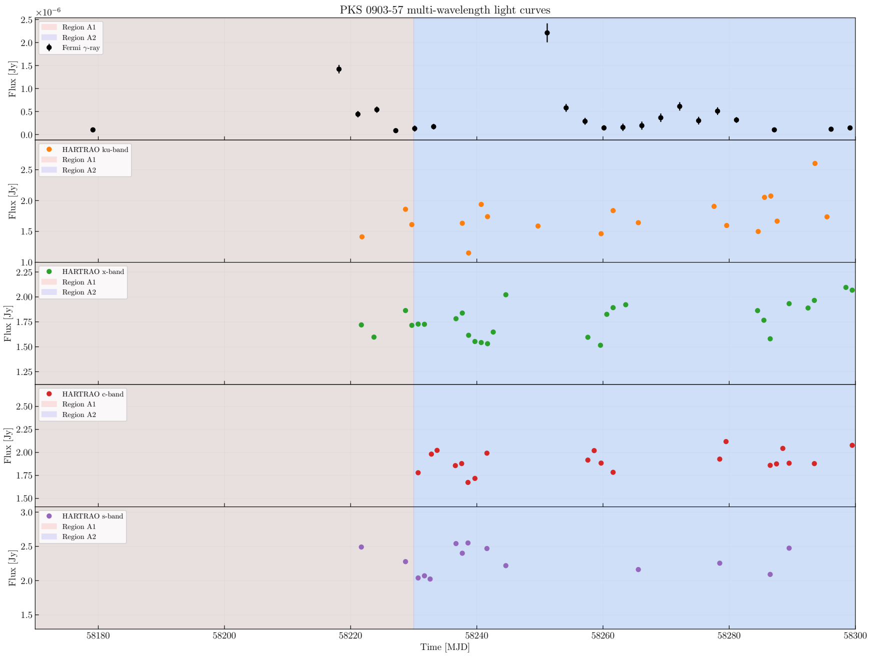

Figure 4.16: MWL light curves of PKS 0903-57 flaring activity region.

5 Discussion and conclusion

The blazar PKS 1424-418 shows flux variability (flares with increasing and decreasing trends) in the gamma-rays, optical, and radio wavelengths. The brightest gamma-ray flare occurred between MJD 56000 and MJD 56500 peaking at a high of 2.3 ± 0.18 ph cm^{-2} s^{-1} . Furthermore, the data shows the VLBI observations from the JPL Ka band and ATCA X band peak fluxes occurring within the same region. In order to determine the location of the gamma-ray emission site in blazars, we investigate the time-domain relationship between their radio and gamma-ray emission. This is because the radio and gamma-ray are thought to be produced by the same particle population (Boula, Petropoulou, and Mastichiadis, 2018). Investigations into the time-domain relationship are done through the use of cross-correlation estimations between the gamma-ray and radio wavelengths. According to theory, higher frequencies have been proven time and again to lead the lower frequencies (Kramarenko et al., 2021).

The aim of this research part of my thesis was to use multi-wavelength, multi-resolution datasets to study blazar sources monitored by HartRAO. I wanted to test whether my new software package provides science-ready data and produces reproduceable results. Using the data processed by the newly developed software for Hart26m data reduction (see Part 2) I studied three blazars by investigating the possible correlated relationships in the MWL light curves of HartRAO-monitored blazar sources. This research was guided by the following questions:

- **Is there a correlation between gamma-rays and radio waves and other wavelengths ?**

  The cross-correlation analysis of the single-dish radio data revealed strong correlations with an average time-lag of approximately 200 days, as shown in

Table 4.5. These results are consistent with previous studies of radio light curves, such as the work by León-Tavares et al. (2011). The observed time-lag is likely indicative of the physical processes occurring in the source, and further investigation is needed to fully understand their underlying mechanisms. It is important to note that the interpretation of the observed time-lag is not always straightforward, as several physical mechanisms can contribute to the observed delays. In this regard, the use of additional techniques such as Monte Carlo simulations can provide more robust results and help us to better understand the correlations between the light curves. Overall, the strong correlations between the single-dish radio data and other wavelengths provide important insights into the temporal behavior and underlying physical processes of the source. Future studies can build upon these results to investigate the nature of the emission and its location within the source, which can shed light on the overall structure and evolution of the object.

- **Can we get correlations in gamma-ray to radio for a multi-wavelength, multi-resolution data sample ?**

  León-Tavares et al. (2011) reported a strong connection between gamma-ray and mm flares using 37 GHz radio data from a 3-year study. Specifically, they found that significant gamma-ray events are often linked to VLBI flaring events that are either ongoing or in the early stages of a flare. Interestingly, the most significant gamma-ray peaks occur at specific phases of mm significant flares. Our results confirm this correlation, as can be seen in Figures 4.1, where a significant flare is observed in the JPL Ka band data around the same time as the start of the most significant gamma-ray flare (Region B) during the observing period (Lähteenmäki and Valtaoja, 2003). This provides further evidence for the close relationship between gamma-ray and mm flares and highlights the importance of continued observations and analysis of these phenomena.

- **Can we learn more from having a dense sample of data points ?**

  The investigation into the sources PKS 0903-57 and PKS 0454-810 had to be halted due to a lack of data. Even though trends were established in the data, the available datasets were not sufficient enough to draw conclusions on the source variability. This is specifically the reason why monitoring data sets is critical to blazar studies in order to see the variability of a source over time e.g. Figure 4.8.

- **Does having a larger data set with more regular observations provide better results with regard to what is happening within these sources?**

  Having more regular observations does provide better results. For PKS 1424-418, VLBI data from IVS and GSFC and JPL were light curves of astrometric, geodetic and space navigation operations. Because there are not T_{sys} measurements at these observations, the flux cannot be properly calibrated, however they can convert SNR to obtain a useable flux value. All these light curves except for the JPL had dense observations showing the same flaring trend as the properly calibrated sources. Combined with the light curves from the single-dish operations, I was able to find both large and small scale variations in the data, which would not have been possible with a small scale data set. Long term well monitored data is critical to our understanding of these objects.

On the optical data

The optical data appear to flare after the gamma-ray flare, but unfortunately, I do not have enough data to conclusively prove or disprove this theory as shown in Figure 4.1. The optical data acquired in the study was sparse, however, I am aware that the Small and Moderate Aperture Research Telescope System (SMARTS[1]) team has historical optical/IR data within the period range where I am lacking data and hope to incorporate that data for my future analyses on this source.

5.1 Future work

My research career has made me fortunate enough to have access to long-term ongoing observations of a variety of sources in multiple scales and frequencies, some of which I have had the ability to monitor since my M.Sc e.g. PKS 1424-418. Looking

[1] http://www.astro.yale.edu/smarts/glast/home.php

into the future, I plan to ensure I use this opportunity to add to blazar science using the following streams:

1. Building long-term monitoring data sets, especially of sources in the south is important in adding to our understanding of blazar sources, and my work has begun the journey with two notable sources PKS 1424-418 and PKS 0903-57 which have more recently been frequently in high energy gamma-ray states. Since the end of my study period, the sources have flared multiple times and HartRAO has exclusive radio data of all these events awaiting processing with my software (see Chapter 7.3.1). Figure 5.1 and 5.2 show the current state of PKS 1424-418 and PKS 0903-57 as seen by the Fermi-LAT telescope, courtesy of the monitored source list website.

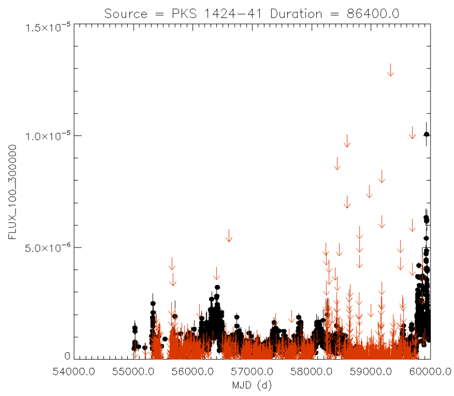

Figure 5.1: Fermi-LAT PKS 1424-418 daily light curve.

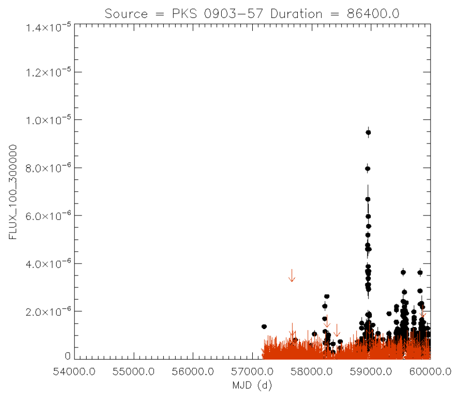

Figure 5.2: Fermi-LAT PKS 0903-57 daily light curve.

As part of my future work I would be processing the data post 2018 with my software and analyzing the flaring activity that has occured since the end of this work.

2. Due to the observatory being part of the global VLBI network, its participation in the monitoring of strong calibrator sources for celestial reference frames provides me with unprecedented access to VLBI fluxes as well as s/x band images of HartRAO monitored sources. I've also been made aware of a recent paper that has been accepted and is in the process of being published called "*The Celestial Reference Frame at K-band: Imaging. I. The First 28 Epochs.* - by de Witt et al." which will provide additional k-band fluxes and imaging.

I would like to look at incorporating using VLBI images to to study the jet emission of my sources by looking at the source structure.

3. In addition, according to Shabala et al. (2017) "*for observed highly variable quasars, the flux density is strongly anti-correlated with structure and position stability*". Meaning that during flaring, matter gets ejected by the jet. In light of this I would like to use the source structure indicators such as the "compactness ratio" and "source structure index" to test if we can see any correlation between source structure (e.g. emerging jets) and the flares we see in the radio. I also want to test is we can predict flaring events by looking at these indicators.

4. I also plan to restart some abandoned monitoring programs. This work was originally intended to follow the MWL journey of 10 HartRAO blazar sources, six had to be removed from the study due to a lack of good observations. Working on improving observing processes will allow us to add more continuum sources to our long-term monitoring program and expand our AGN research. I would like to look into this as part of future work as well.

5. Observing sources in the far south like PKS 0454-810 is challenging. Currently that source is monitored using cross scans. Because the sources are so far south, gravity becomes an added problem as the telescope has to track the source at such low elevations. This causes a considerable amount of scatter in our observations and improving the techniques used to monitor these kind of sources will also be part of my future work.

Part II

HartRAO 26-m calibration and development of new software pipeline

Data calibration is an essential aspect of observatory operations. It is the process of correcting for irregularities or imperfections in the data prior to any data analysis being carried out. Proper calibration ensures that:

1. The data meets global standards

2. There are timeous identification and correction of problems that may impact the system and instrumentation.

3. The integrity and consistency of the results is mantained.

However, to be able to effectively monitor calibration source behavior requires that the observatory have a solid software package in place to process all the data in a timely manner. HartRAO has been operating without a standard data calibration software package for over 30 years. Resulting in a lack of proper monitoring of systematic changes in HartRAO data that have now been identified through this work. This study, which focuses on blazar monitoring of HartRAO sources (see Part I), discovered several issues with the telescope calibration process. I have addressed these issues in this research and in Chapter 6, I discuss the detailed calibration processes used to calibrate Hart26m sources, the challenges faced, and the solutions applied. Additionally, I have developed a software package to regularly monitor all HartRAO calibrators and facilitate data analysis, which is discussed in Chapter 7. Finally, I summarize and conclude on this topic in Chapter 8.

6 Single-dish calibration of Hart26m data

Monitoring radio calibrator sources on a regular basis is essential for radio telescopes to produce accurate and reliable results. These sources, which can differ in size, distance, and location in the sky, need accurate calibration to gain a better understanding of them. Failure to monitor and properly calibrate these sources can negatively impact the research output of the detector and observatory. In this chapter, I will discuss the challenges encountered when calibrating the HartRAO data and present the results of the telescope calibration described in §3.1.1.4.

6.1 Introduction

The ultimate goal of calibration is to generate a scientifically valuable and up-to-date data set that can be used to calibrate sources with unknown fluxes. This can only be achieved by ensuring consistent observations of calibrator sources and applying appropriate calibration techniques to the data. However, calibrating radio sources becomes increasingly challenging as you approach higher frequencies. For instance, at 22 GHz, atmospheric effects caused by water and oxygen molecules can scatter or absorb incoming radio waves (Meeks, 1976), thereby reducing the measured brightness of a source. By regularly monitoring these objects, these effects and other sources of error and distortion can be detected and corrected for (§6.4).

Furthermore, calibrators can also be utilized to identify and diagnose issues with the telescope or its associated equipment. For instance, if the measurements of a calibrator vary from expected values, it may indicate a problem with the telescope's receiver or other components that may need repairs or adjustments. Regularly monitoring calibrators enables us to track both short-term and long-term changes in the properties of the sources, which can provide valuable insights into their underlying physics.

6.2 The calibrator sources

To calibrate the target sources, I employed two of the brightest calibrator sources in the southern hemisphere, Hydra A and Jupiter. Hydra A (also known as 3C218 or PKS 0915-11, Lane et al., 2004; Morganti, Killeen, and Tadhunter, 1993), a powerful FR I radio galaxy is an excellent calibrator for single-dish observations. It is a compact[1], bright, and stable radio source that can be easily detected by the Hart26m. Hydra A was used to calibrate target sources at 2.3 GHz, 4.8 GHz, 8.4 GHz, and 12.2 GHz. For higher frequencies at 22 GHz, I used the planet Jupiter as a calibration (Gibson, Welch, and Pater, 2005; Hafez et al., 2008). Jupiter's radio emission is relatively stable over time, making it a useful calibrator for the long-term monitoring of radio telescopes. Table 6.1 lists the sources and their observed epochs. Calibrator observations were carried out on a daily basis depending on the availability of the telescope and that there were no major repairs that hindered observations.

Table 6.1: Calibrator observation.

Source	Freq	Observing period (Time)	Observing period (MJD)	Obs.
Jupiter	22 GHz	2008-09-15 to 2018-08-05	54724 to 58335	1530
Hydra A	12.2 GHz	2008-09-03 to 2018-08-05	54712 to 58335	2692
Hydra A	8.4 GHz	2008-08-09 to 2018-08-05	54687 to 58335	1787
Hydra A	4.8 GHz	2008-08-11 to 2018-08-05	54689 to 58335	1756
Hydra A	2.3 GHz	2011-05-05[a] to 2018-08-05	55686 to 58335	1629

Note.- Table of calibrator epochs prior to data processing. **Note.**- Source is the name of the observed target. Freq is the observed frequency. Obs is the number of observations over the observing period. [a] - The 2.3 GHz receiver was removed from the antenna for the first three years of monitoring and only returned in 2011.

[1]This holds true for the cm scale single-dish observations. On VLBI scales Hydra A can be resolved showing a large jetted structure.

6.3 Light curve analysis

In this study, PSS light curves for the calibrators were generated for each polarization. The PSS was estimated from drift scan observations of Hydra A by calibrating each drift scan to estimate the antenna temperature from observations (refer to §3.1.1.2 for details on the calibration process). The peak of the drift scan signal was then estimated by fitting a second-degree polynomial to the top 30-50% of the peak. Pointing corrections (described in §3.1.1.3) were applied to all data with frequencies above 2.3 GHz before the PSS was estimated using the equations shown inEquation 3.7. For Jupiter, the PSS was calculated using the equations described in §6.4.3.

After calculating the PSS, the light curves were generated. To clean the data, an iterative RFI removal algorithm was used (refer to §7.3.1 for details on the data cleaning). The algorithm effectively removes the most obvious outliers. However, it does not account for noise and effects that may be inherent in the signal. To minimize these effects in the measurements, the light curves were then averaged using a monthly binning width of 28 days[1]. The resulting light curves are shown in Figures 6.4a, 6.4b, 6.4c, 6.4d,6.4e, 6.4f and 6.3a. These light curves provide insight into the long-term behavior of Hydra A at the respective frequencies. A detailed analysis of each light curve is provided in the §6.6,§6.7.1,§6.7.2,§6.7.3 and §6.7.4.

6.3.1 The HartRAO 26-m radio telescope bearing failure

During the early phase of the study period, the Hart26m telescope experienced a major failure[2] that resulted in its decommissioning for almost two years. Between October 3, 2008 (54742) and July 28, 2010 (55405) the Hart26m halted operations due to a bearing failure of the southern end of the main polar shaft. This period is represented by the orange blocked-out regions in the light curves where no observations were recorded. Because the observations at 2.3 GHz in Figure 6.4a only began in 2011, the bearing failure period is not indicated in the respective plot.

[1] Averaging measurements can help to reduce the effects of variability and provide a more accurate representation of the source's true flux, thus improving the quality of the data.

[2] For further information on the failure and repair operations of the Hart26m, the reader is referred to the HartRAO websites http://www.hartrao.ac.za/hart26m_status/ and http://www.hartrao.ac.za/news/100906_26m_repair/index.html

6.4 Investigating antenna corrections at high frequencies: the case for Jupiter calibrations

The Hart26m telescope uses Jupiter as a radio calibrator at higher frequencies because it is one of the brightest sources in the southern hemisphere. However, using Jupiter as a calibrator can be challenging because it is not a point source and its angular size is larger than the telescope beam i.e. $K_s >> 1$. To correct this, a size correction factor (SCF) must be applied. Additionally, radio waves at higher frequencies can be affected by weather-related effects, particularly attenuation caused by water vapor resonances at 22 GHz. To correct this, an atmospheric correction (ATM_CORR) must be applied.

The upcoming sections will outline the mathematical formulas necessary to implement the corrections and demonstrate the methods used to confirm the accuracy of the correction factors.

6.4.1 Applying a size correction

To determine the size correction, the angular diameter of Jupiter must be obtained for each day of observation. This data can be accessed from the NASA JPL New Horizons website[1]. The size correction factor (SCF) is then calculated using the following equation:

$$\mathrm{SCF} = \frac{\vartheta_{\mathrm{SCF}}^2}{(1 - \mathrm{e}^{(-\vartheta_{\mathrm{SCF}}^2)})} \tag{6.1}$$

where ϑ_{SCF} is the size correction factor in the beam given by:

$$\vartheta_{\mathrm{SCF}} = \frac{\vartheta_{\mathrm{DIAM}}}{2\sqrt{0.935}/(0.6 \times \vartheta_{\mathrm{HPBW}})} \tag{6.2}$$

[1] http://ssd.jpl.nasa.gov/horizons.cgi#top

where $\vartheta_{\mathrm{DIAM}}$ is the planet angular diameter, and $\vartheta_{\mathrm{HPBW}}$ is the HPBW in arcsec.

6.4.2 Applying a weather correction

To implement a weather correction, the properties of the medium through which the radio signal is traveling must be taken into account. The atmospheric correction necessitates knowledge of the optical depth to be applied. The optical depth at 22 GHz is estimated as

$$\tau = 0.0140 + 0.00780 \times \mathrm{PWV} \tag{6.3}$$

from Gaylard and Kolbe (2010) and references therein, where PWV is the precipitable water vapor. PWV can be estimated using measurements of humidity and ambient temperature[1]. The atmospheric correction can thus be estimated as:

$$\mathrm{ATM\_CORR} = \exp\left(\frac{\tau}{\cos(\mathrm{ZA\_RAD})}\right) \tag{6.4}$$

where $\mathrm{ZA\_RAD} = \mathrm{ZA} \times \frac{\pi}{180}$ is the zenith angle in radians and ZA is the zenith angle in degrees,.

6.4.3 The corrected antenna temperature and PSS estimation

After determining the size correction factor (§6.4.1) and atmospheric correction factor (§6.4.2), these can be applied to the data to compute the overall source correction factor. This factor is used to adjust the Point Source Sensitivity (PSS). The source correction factor is calculated using the following equation:

[1] Measurements of weather-related parameters e.g. humidity etc. are collected using, 1) weather sensors in a Stevenson screen located a few meters away from the Hart26m, and 2) a Setra 270 barometer pressure sensor inside the control room of the observatory. Inside the Stevenson screen is a Huato HE400-EX sensor that measures the temperature and relative humidity. The screen also has a mercury thermometer to compare readings. Nickola et al. (2021) gives a recent update on the status of the HartRAO weather measurements.

$$K_s = \exp(PC) \times ATM\_CORR \times SCF \tag{6.5}$$

where PC is the pointing correction factor estimated from the equations discussed in §3.1.1.3.

Equation 3.7 is used to calculate the PSS for Jupiter by substituting Ks with Equation 6.5.

6.4.4 Testing the Jupiter correction factors

The PSS values calculated using the source correction factor in Equation 6.5 were utilized to construct long-term light curves to evaluate the calibration correction factors applied to the data. Figure 6.1 presents the results from the light curve test. Five different tests were conducted on the data to determine the optimal calibration correction factor. Different factors were added and removed to analyze their impact on the data. Ideally, laboratory tests are performed before a receiver is installed on the antenna to compare the lab-measured noise diode values to the instrument specifications. These tests are particularly important when an absolute or true PSS is required. The tests were carried out for the old uncooled HartRAO receiver. The results of these tests revealed that the noise diode values were slightly different, and a scaling factor (SF) was determined and applied to all data taken with that receiver. The new cryogenically cooled HartRAO receiver installed on April 23, 2014 was not tested in the lab, and as a result, no scaling factor was applied to the results from this receiver. To investigate the impact of the noise diode on the PSS, I compared PSS results where the source correction factor was given as:

1. T1: K_s = exp(PC)*ATM_CORR*SCF*SF
   All the correction factors were applied as a correction to all the data.

2. T2: K_s = exp(PC)*SF
   Only the scaling factor was applied as a correction to the data.

3. T3: K_s = exp(PC)*ATM_CORR
   Only the atmospheric correction was applied as a correction to the data.

4. T4: K_s = exp(PC)*SCF
   Only the size correction factor was applied as a correction to the data.

5. T5: K_s = exp(PC)*ATM_CORR*SCF
   All the other correction factors excluding the scaling factor were applied as a correction to all the data.

6. T6: K_s = (exp(PC)*ATM_CORR*SCF*SF) < 2014 < (exp(PC)*ATM_CORR*SCF)
   All the correction factors were applied to data from the uncooled receiver i.e. to date before April 23, 2014, and all corrections excluding the scaling factor were applied as a correction to all the data from the cryogenically cooled receiver i.e. to data after 23, 2014.

Figure 6.1 shows the results from the tests mentioned above.

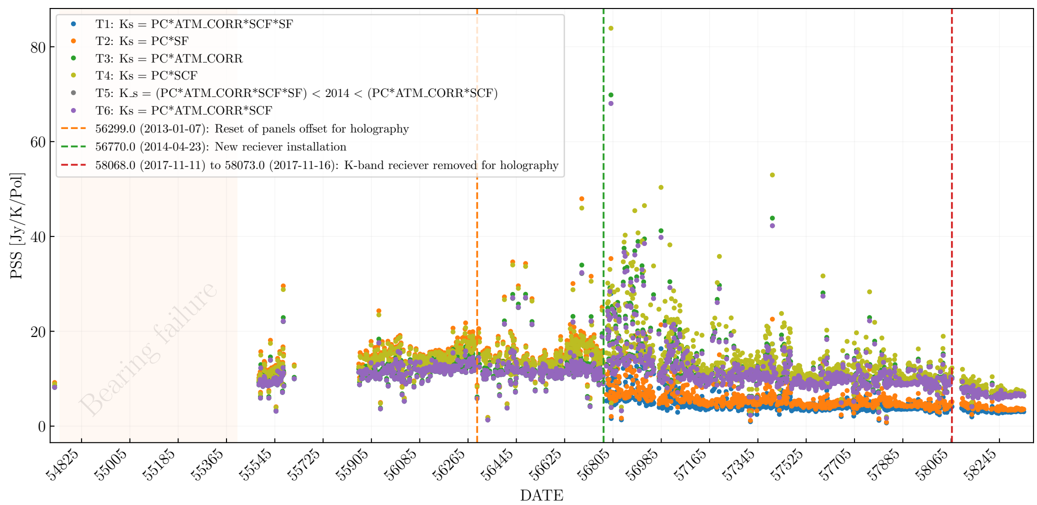

Figure 6.1: Jupiter 22 GHz calibration tests. **Note.-** The data presented here is the raw data from observations. The vertical dotted lines indicate dates where the PSS values were altered due to an event that caused a step change.

From the results, it is clear that applying the scaling factor for the uncooled receiver to data from the cooled receiver made the results worse, as indicated by the T1 and T2 light curves. The scaling factor made the results appear as though the PSS value improved with the installation of the new noise diode, which was not what was expected. This is because the cooled receiver is an independent instrument, and as such, we cannot apply the correction from the old receiver to the new one. The cooled receiver needs to be taken off the antenna and properly tested in the lab to determine if there is a need for a scaling factor that should be applied to the new noise diode and what that scaling factor is specific to that instrument.

Although a scaling factor should probably be applied to data from the cooled receiver, for this work, the scaling factor is not important because it cancels out in the end when applied to the target source. In other words, we are not putting in a correction to get the absolute PSS. Therefore, whether we do not apply the scaling factor at all to the data (T6), or only apply the scaling factor to data from the uncooled receiver and not to data from the cooled receiver (T5), the results appear the same and constant over time. Therefore, it was decided to be best to remove the scaling factor from all estimations of the PSS results used to calibrate the target sources.

6.5 Data calibration - step changes

To ensure that our calibrators are functioning correctly, the PSS values of the calibrators are tracked daily. Since the PSS is expected to remain relatively constant throughout the observing period, and we have a general idea of what these values should be, any changes or deviations in the mean of the PSS may indicate an underlying problem with the calibrator observation or the Hart26m antenna.

From the analysis in §6.4.4, it became apparent that the noise diode plays a crucial role in estimating the PSS. Therefore, when estimating the PSS, we divided the data into blocks or steps of constant noise diode values e.g. Figure 6.3a. Additionally, to account for the impact of weather on data, especially at higher frequencies, the data was further divided into monthly bins of 28 days[1] to produce the final light curves shown in §6.6,§6.7.1,§6.7.2,§6.7.3 and §6.7.4.

Besides the noise diode and weather effects, we also observed changes in the PSS due to telescope and receiver upgrades or tests run on the antenna (e.g. Holography observations, Klein, 2008) which would result in sudden step changes in the PSS

[1] Because of the large datasets, I tested weekly, bi-weekly, and monthly binning and found that the monthly binning provided the best results with the least variations and improved errors.

altering the PSS values. These added effects were also added as extra binning zones or regions in the data. The issues related to the PSS analysis, starting from the highest frequency 22 GHz to the lowest frequency, 2.3 GHz will be discussed in the following sections.

6.6 Jupiter data calibration at 22 GHz

The PSS light curves for Jupiter at 22 GHz are shown in Figure 6.3a. Table 6.3 gives the binned average PSS estimates for the observations in each polarization. Observations at 22 GHz started September 15, 2008 (54724). After shutting down due to the bearing failure, observations resumed on October 24, 2011 (55858). Throughout the observing period, several step changes occurred in the PSS values throughout the observing period. These changes were caused by:

- 56299 - A panel reset on January 7, 2013 for panels that were moved for a holography experiment. Before the beginning of the observations, a group of surface test panels were chosen at random and deliberately moved 3mm and 6mm apart for the calibration of a microwave holography experiment that was conducted by Klein (2008) in 2008.

- 56770 - A new cryogenic receiver installation on April 23, 2014.

- 58098 - A k-band receiver move for a holography experiment on December 11, 2017.

To estimate the target source flux densities, an average PSS was calculated for each region defined by these step changes. The average PSS varied between 6.717 and 11.159 Jy K^{-1} in LCP and 6.158 and 11.249 Jy K^{-1} in RCP with errors between 0.436 and 1.254 Jy K^{-1} in LCP and 0.336 and 1.245 Jy K^{-1} in RCP.

Figure 6.2: Plot of Jupiter PSS over the observing period

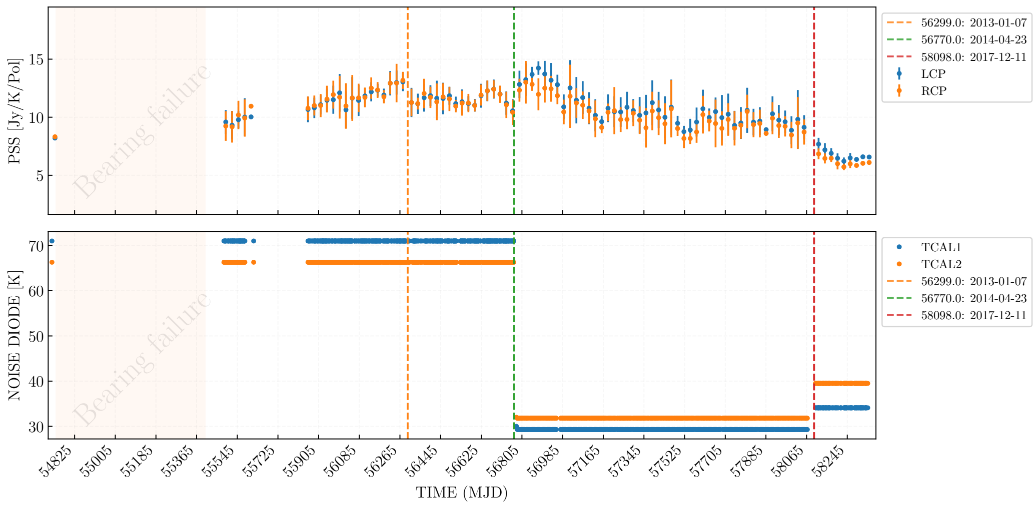

(a) The Jupiter PSS time series (top) with the 22 GHz noise diode (bottom) over the observing period.

Period	Pol	PSS	ΔPSS	min	max
54724 to 56292 (2008-09-15 to 2013-01-06)	LCP	11.159	1.254	8.206	13.047
	RCP	11.249	1.245	8.316	13.177
56293 to 56768 (2013-01-07 to 2014-04-21)	LCP	11.534	0.467	10.551	12.423
	RCP	11.489	0.514	10.422	12.413
56769 to 58068 (2014-04-22 to 2017-11-11)	LCP	10.662	1.388	8.757	14.235
	RCP	10.110	1.249	8.168	13.011
58069 to 58335 (2017-11-12 to 2018-08-05)	LCP	6.717	0.436	6.213	7.680
	RCP	6.158	0.336	5.719	6.844

Table 6.3: Monthly binned PSS at 22 GHz. **Note.-** PERIOD is the time frame of a binned region. POL is the polarization. PSS and ΔPSS are the point source sensitivity and its error respectively. MIN and MAX are the minimum and maximum PSS in a given period or region respectively

6.7 Investigating the PSS estimates for Hydra A

The following sections present the results of the calibration for Hydra A, as illustrated in Figure 6.4. The light curves show the behavior of the PSS during the observing period. The data analysis revealed that, on average, the PSS appeared to be stable, but also varied due to technical issues that arose over time. The most critical instabilities in the light curves, shown by steps in the data, were identified and thoroughly investigated in the following subsections. In addition to plotting the light curves, the plots also indicate the period of bearing failure, marked as orange regions at the beginning of the plots. Periods where the receivers on the Hart26m had to be removed for repairs, appear as gaps in the light curve data as shown inFigures 6.4a, 6.4b, 6.4c and 6.4d.

6.7.1 Hydra A data calibration at 12.2 GHz

The PSS light curves for Hydra A at 12.2 GHz are shown in Figure 6.4b. Table 6.4 gives the binned average PSS estimates for each observation at each polarization. Observations at 12.2 GHz began September 3, 2008 (54712) but were later halted due to the bearing failure, see §6.3.1. After observations resumed on October 24, 2011 (55858) a series of step changes occurred in the PSS throughout the observing period. These changes were caused by:

- 56034 - The replacement of a digital board on the Tilt unit on April 17, 2012.
- 56299 - The offset panel reset for panels that were moved for a holography experiment on January 7, 2013. See §6.6.
- 56763 - The moving of the Ku-band receiver to make room for a new K-band receiver on April 16, 2014.[1].
- 57958 - A complete focus failure, which caused a gradual decrease in PSS up until July 24, 2017, after which sensitivity improved when the focus was disabled.
- 58004 - The refitting of the focus readout unit on September 8, 2017.

To estimate the target source flux densities, an average PSS was calculated for each region defined by these step changes. The average PSS overall varied between 6.413

[1]The old uncooled receiver was being replaced with a new cryogenically cooled receiver

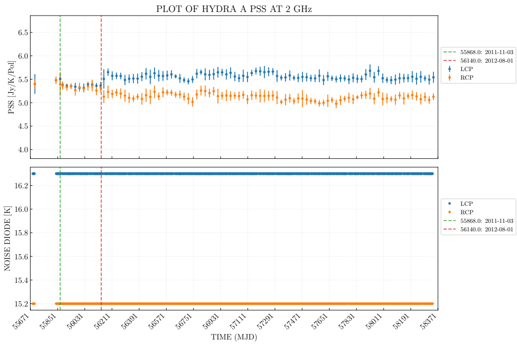

(a) Hydra A PSS at 2.3 GHz.

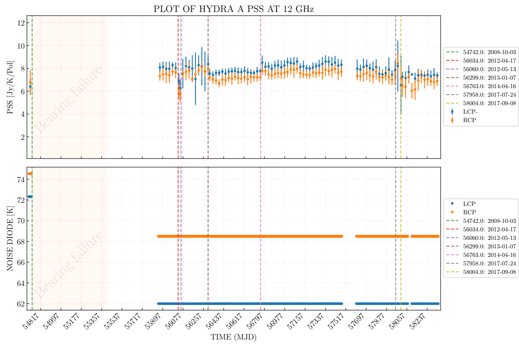

(b) Hydra A PSS at 12.2 GHz.

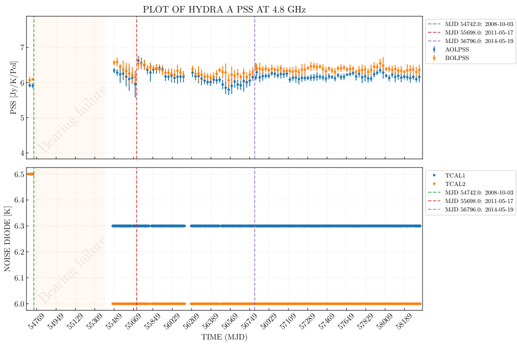

(c) Hydra A LCP PSS at 4.8 GHz.

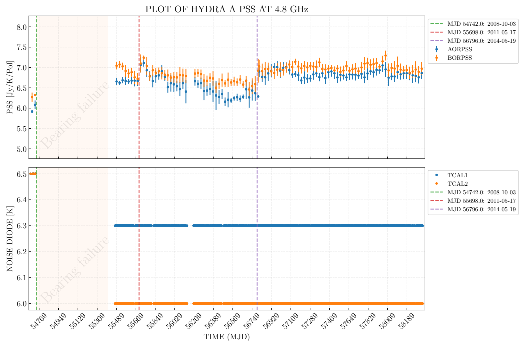

(d) Hydra A RCP PSS at 4.8 GHz.

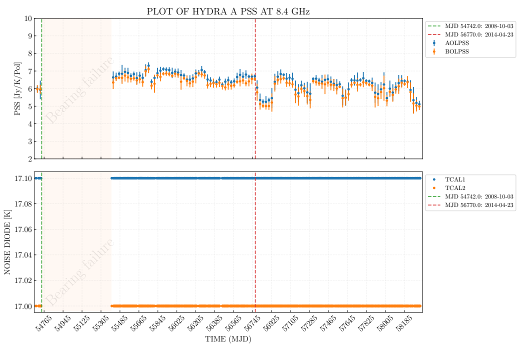

(e) Hydra A LCP PSS at 8.4 GHz.

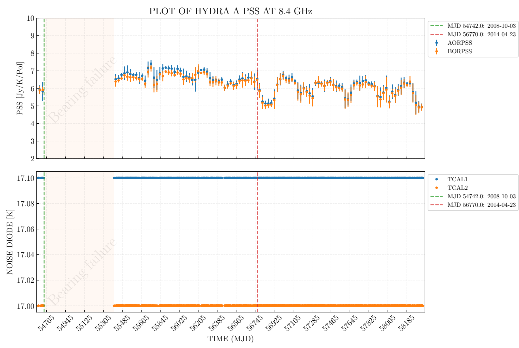

(f) Hydra A RCP PSS at 8.4 GHz.

Figure 6.4: PSS light curves of Hydra A.

and 8.143Jy K^{-1} in LCP and 5.702 and 7.780 Jy K^{-1} in RCP with errors between 0.095 and 0.657 Jy K^{-1} in LCP and 0.138 and 0.108 Jy K^{-1} in RCP.

PERIOD	POL	PSS	ΔPSS	MIN	MAX
54712 to 54736 (2008-09-03 to 2008-09-27)	LCP	6.413	0.657	6.413	6.413
	RCP	6.771	1.108	6.771	6.771
55858 to 56033 (2011-10-24 to 2012-04-16)	LCP	7.902	0.437	6.861	8.285
	RCP	7.317	0.497	6.140	7.726
56037 to 56053 (2012-04-17 to 2012-05-06)	LCP	7.943	0.395	7.087	8.383
	RCP	5.702	0.635	5.702	5.702
56061 to 56298 (2012-05-14 to 2013-01-06)	LCP	6.717	0.436	6.213	7.680
	RCP	7.689	0.294	7.061	8.135
56299 to 56762 (2013-01-07 to 2014-04-15)	LCP	7.658	0.095	7.433	7.784
	RCP	7.104	0.138	6.701	7.265
56764 to 57957 (2014-04-16 to 2017-07-23)	LCP	8.143	0.299	7.444	8.607
	RCP	7.560	0.219	7.022	7.966
57963 to 58000 (2017-07-29 to2017-09-04)	LCP	7.373	0.838	6.535	8.211
	RCP	7.780	0.656	7.125	8.436
58004 to 58335 (2017-09-08 to 2018-08-05)	LCP	7.373	0.146	7.098	7.684
	RCP	6.768	0.390	6.045	7.301

Table 6.4: Monthly binned PSS at 12.2 GHz. **Note.-** PERIOD is the time frame of a binned region. POL is the polarization. PSS and ΔPSS are the point source sensitivity and its error respectively. MIN and MAX are the minimum and maximum PSS in a given period or region respectively.

6.7.2 Hydra A data calibration at 8.4 GHz

Figures Figures 6.4e and 6.4f show the PSS light curves for Hydra A at 8.4 GHz. Table 6.5 presents the average PSS values for each observation and polarization. Observations at 8.4 GHz started on August 9, 2008 (54687) but were also halted due to the bearing failure §6.3.1. When observations resumed on July 30, 2010 (55407), the replacement of the k-band receiver on April 23, 2014 (57135) caused a significant drop in the PSS (± 2 Jy K^{-1}), which continued throughout the rest of the observing period. Due to the systematic variability in the data, it was decided to consider the entire period after the change as one region. To investigate the possibility of the Sun-Hydra A distance probably having an influence on the data at 8 GHz, tests were conducted to determine if the almost periodic variability observed in the data was caused by the changing position of the Sun in relation to Hydra A over time.

However, the results were inconclusive and it could not be determined if this effect was causing the variability in the results. The 8.4 GHz calibration investigation is still an ongoing project and will also be investigated in future work. To estimate the target source flux densities, an average PSS was calculated for each region defined by these step changes. The average PSS overall varied between 5.904 and 6.724 Jy K^{-1} in LCP and 5.881 and 6.692 Jy K^{-1} in RCP with errors between 0.009 and 0.468 Jy K^{-1} in LCP and 0.005 and 0.472 Jy K^{-1} in RCP.

PERIOD	POL	PSS	ΔPSS	MIN	MAX
54687 to 54737 (2008-08-09 to 2008-09-28)	ALCP	5.963	0.037	5.926	6.000
	BLCP	5.965	0.009	5.956	5.975
	ARCP	5.876	0.054	5.823	5.930
	BRCP	5.898	0.005	5.893	5.902
54734 to 56769 (2008-09-29 to 2014-04-22)	ALCP	6.724	0.237	6.230	7.303
	BLCP	6.516	0.245	6.066	7.105
	ARCP	6.692	0.296	6.028	7.403
	BRCP	6.564	0.258	6.035	7.181
56770 to 58335 (2014-04-23 to 2018-08-05)	ALCP	6.096	0.463	5.112	6.829
	BLCP	5.904	0.468	4.984	6.588
	ARCP	5.948	0.466	4.945	6.772
	BRCP	5.881	0.472	4.912	6.713

Table 6.5: Monthly binned PSS at 8.4 GHz. **Note.-** PERIOD is the time frame of a binned region. POL is the polarization. PSS and ΔPSS are the point source sensitivity and its error respectively. MIN and MAX are the minimum and maximum PSS in a given period or region respectively.

6.7.3 Hydra A data calibration at 4.8 GHz

The PSS light curves for Hydra A at 4.8 GHz are shown in Figures 6.4c and 6.4d. Table 6.6 gives the binned average PSS estimates for each observation at each polarization. Observations at 4.8 GHz started on August 11, 2008 (54689 but were shortly thereafter halted due to a bearing failure only to resume over 2 years later on October 19, 2010 (55488). Shortly after the observations were resumed the replacement of an expander disk on May 17, 2011 (55698) caused a step change in the PSS. The PSS was affected again when a cable was removed from the noise diode while troubleshooting issues with the RCP receiver on May 19, 2014 (56796). For each region created by the step changes, an average PSS was estimated and used to calculate the target source flux densities for the sources discussed in Chapter 4. The average PSS overall varied between 5.915 and 6.375 Jy K^{-1} in LCP and 5.999 and 6.992 Jy K^{-1} in RCP with errors between 0.007 and 0.189 Jy K^{-1} in LCP and 0.018 and 0.245 Jy K^{-1} in RCP.

PERIOD	POL	PSS	ΔPSS	MIN	MAX
54689 to 54734 (2008-08-11 to 2008-09-25)	ALCP	5.915	0.007	5.908	5.922
	BLCP	6.078	0.013	6.065	6.092
	ARCP	5.999	0.082	5.917	6.081
	BRCP	6.296	0.025	6.270	6.321
55735 to 55697 (2008-09-26 to 2011-05-16)	ALCP	6.183	0.114	5.953	6.340
	BLCP	6.365	0.148	6.165	6.586
	ARCP	6.663	0.018	6.623	6.686
	BRCP	6.909	0.123	6.719	7.074
55698 to 56794 (2011-05-17 to 2014-05-17)	ALCP	6.155	0.189	5.799	6.626
	BLCP	6.291	0.113	6.065	6.542
	ARCP	6.513	0.245	6.159	7.106
	BRCP	6.761	0.158	6.459	7.241
56795 to 58335 (2014-05-18 to 2018-08-05)	ALCP	6.180	0.057	6.084	6.347
	BLCP	6.375	0.051	6.293	6.547
	ARCP	6.845	0.081	6.681	7.050
	BRCP	6.992	0.080	6.864	7.293

Table 6.6: Monthly binned PSS at 4.8 GHz. **Note.-** PERIOD is the time frame of a binned region. POL is the polarization. PSS and ΔPSS are the point source sensitivity and its error respectively. MIN and MAX are the minimum and maximum PSS in a given period or region respectively.

6.7.4 Hydra A data calibration at 2.3 GHz

The light curve for Hydra A at 2.3 GHz is displayed in Figure 6.4a. The observations and average PSS values for each polarization can be found in Table 6.7. Initially, the 2.3 GHz receiver was out of service for repairs, but upon its reinstallation, a step change in the data occurred due to the installation of a new sub-reflector on November 11, 2011 (55868), as indicated by the green dotted line. This change stabilized the PSS until a crack in the beam was discovered on August 1, 2012 (56140), and temporary chains were added to reduce the load on the box, resulting in another step change in the light curve. To estimate the target source flux densities, an average PSS was calculated for each region defined by these step changes. Overall the average PSS varied between 5.324 and 5.560 Jy K^{-1} in LCP and 5.125 and 5.424 Jy K^{-1} in RCP with errors between 0.025 and 0.057 Jy K^{-1} in LCP, and 0.036 and 0.064 Jy K^{-1} in RCP .

PERIOD	POL	PSS	ΔPSS	MIN	MAX
55686 to 55866 (2011-05-05 to 2011-11-01)	LCP	5.462	0.046	5.399	5.507
	RCP	5.424	0.039	5.394	5.479
55867 to 56138 (2011-11-02 to 2012-07-30)	LCP	5.356	0.025	5.313	5.393
	RCP	5.324	0.036	5.260	5.366
56139 to 58335 (2012-07-31 to 2018-08-05)	LCP	5.560	0.057	5.456	5.681
	RCP	5.125	0.064	4.978	5.259

Table 6.7: Monthly binned PSS at 2.3 GHz. **Note.-** PERIOD is the time frame of a binned region. POL is the polarization. PSS and ΔPSS are the point source sensitivity and its error respectively. MIN and MAX are the minimum and maximum PSS in a given period or region respectively.

7 Software development

Software development forms an integral part of the data reduction and analysis processes in data-driven environments. It is the process of writing computer programs that perform specific tasks in a fraction of the time it would take to complete them manually. When grouped into a software package, these programs can form the backbone of operations performed in astronomical observatories, such as scheduling and running observations, analyzing data, and processing results. Modern software that is regularly maintained and uses a systematic approach to data reduction and analysis provides consistency and can significantly improve the reliability of results. Until recently, the processing of single-dish radio data from the Hart26m (§2.1) relied on a software program developed in 1989 and that was last updated in 2007. The need to replace this legacy software led to the design and implementation of a new and modern software package. This chapter describes the design, functionality, and performance of the new and improved software package developed for single-dish radio astronomical data reduction and analysis at HartRAO.

7.1 History of single-dish data processing at HartRAO

For the past 32 years, the processing of single-dish radio data from Hart26m relied mainly on the spectroscopy analysis program (LINES), a software program developed by Dr. M.J. Gaylard as part of his Ph.D. (Gaylard, 1989). LINES was developed as part of a suite of programs to initiate and carry out single-dish spectral line observations on Hart26m. The core program in LINES, written in FORTRAN77[1] (formula translation/translator program language), consists of various sub-routines, of

[1] https://fortran-lang.org, a scripting language developed by the company International Business Machines corporation (IBM) in the 1950s

which some are imported from external libraries; such as PGPLOT[1] which provides the graphics capability. Initially, LINES existed in a much simpler form on an HP1000 mini-computer that was used for operating Hart26m. LINES was later rewritten for Linux computers and the capability to process drift scan observations of radio continuum sources, including calibrator sources, was added. Before this, the astronomers of the time made use of their own programs and tools (including spreadsheets or modifications of popular astronomical programs) for processing continuum drift scan observations, often with different versions particular to specific sources. This was further complicated by the fact that all observing programs and tools produced their own data formats.

7.2 The need for new software at HartRAO

Until recently, LINES has been the primary tool for processing single-dish data taken with Hart26m. Unfortunately, the software has not been modified nor maintained for many years, with the last formally-recorded software update dating back to 2007. Without sufficient maintenance, the software can become inefficient, difficult to operate, and incompatible with modern systems and applications. On the other hand, supporting and maintaining old systems can be challenging and time-consuming.

Single-dish observations of spectral line and continuum sources at HartRAO are carried out on an almost daily basis using Hart26m. Over time, the large amount of data collected from these observations, the failure to maintain and update the software used for processing, and the absence of any automated or semi-automated pipeline to process the raw data resulted in a data processing backlog, with thousands of observations currently still waiting to be processed. Specialized software to carry out and process observations are one of the most valued resources to address data calibration and processing challenges at any astronomical observatory. Working with old, outdated software only adds further complications to these challenges. Software used for scientific purposes should be sustainable and must be able to replicate and reproduce results to build upon existing research or conduct new research effectively. Failing to do so puts the quality and validity of the research at risk.

[1] https://www.gnu.org/software/gnuastro/manual/html_node/PGPLOT.html

As a means to mitigate these issues, the decision was made to replace the old LINES software at HartRAO, citing the following reasons;

- The LINES program has become difficult to install on modern operating systems.
- The LINES program requires external scripts to allow automation and batch processing.
- The LINES program relies on external scripts to convert the raw data files from FITS to American Standard Code for Information Interchange (ASCII).
- The LINES program relies on external scripts to extract calibration information from the raw data files.
- The LINES program provides the basic data reduction tools but does not provide any additional tools for further data analysis and thus cannot provide the level of reporting required by our changing science needs.
- FORTRAN77 is very old and upgrading the code would require a substantial investment.

Replacing the old LINES software has been on the HartRAO agenda for many years. In 2013, HartRAO M.Sc. student Thorsten Brand developed a C++ based program to calibrate the single-dish continuum drift scan data for calibrator sources observed with Hart26m (Brand, 2013). This work, however, did not make it to an observatory-wide implementation but still served as a motivation towards finding a working solution to ultimately replace LINES. In 2016, significant progress towards realizing a new software program was made when the fundamental astronomy research group at HartRAO began drawing up a project plan for the development of a new software package. The following items were considered as the key goals of this project;

- Develop one centralized software package for students and researchers to reduce, calibrate and analyze all single-dish data (both continuum and spectral line) from Hart26m.

- Develop a program that is easy to install and navigate.
- Develop a program that processes data in single-file and batch mode.
- Develop a program that provides both a command-line and a user-friendly graphical interface with interactive plotting.
- Develop a program that can be fully automated to produce final calibrated data from the raw data files.
- Develop an automated pipeline for the daily processing of single-dish calibration and monitoring observations at HartRAO.

One of the biggest challenges for the single-dish observing programs at HartRAO is the need for timeous processing of the daily calibrator and monitoring observations. Observations of calibrator sources provide us with information on the overall performance of the telescope system and the timeous processing of the calibration observations can help with the early detection of any abnormalities or issues with the telescope system. HartRAO has several single-dish observing programs and sources of interest that are monitored on a daily to weekly basis. The timeous processing of these observations will provide us with current information on the behavior of these sources, which may affect how and how often they should be observed. For example, a source undergoing a sudden flaring event may be monitored more frequently and at multiple frequencies. Being able to process the data promptly will be of enormous benefit to the science community using HartRAO data, significantly improving turnaround times for publications. For these reasons, the need for a new observatory standard software package has become essential to the future of data processing at HartRAO. The work presented here provides a solution to these problems and a fresh start for continued source monitoring at HartRAO.

7.3 The new data processing software

The drift scan data reduction and analysis software (DRAN) is a new software package developed at HartRAO and presented in this work. DRAN provides a new and improved processing platform for continuum drift scan data from single-dish observations using Hart26m. The new software improves the data reduction and analysis process by providing an easy-to-use, user-friendly platform in which data can be processed in both single- and batch-mode. DRAN forms part of a larger software project that will also provide for spectral-line data processing. However, for this work, the focus will only be on that part of the software project that deals with the processing and analysis of the single-dish continuum data (i.e., the DRAN software package).

DRAN was developed in Interpreted high-level general-purpose programming language. (PYTHON) – a fast-growing programming language that has become a favorite in the astronomical community. This is mainly because PYTHON comes with a host of applications, including; web development (e.g., FLASK[1], DJANGO[2]), data manipulation (e.g., PANDAS[3]), machine learning (SCIKIT-LEARN[4]), and artificial intelligence (TENSOR FLOW[5]). In addition, PYTHON is versatile, powerful, platform-independent, and continuously benefits from having a large community of developers actively working on it. Although generally considered slower than formula translation/translator program language (FORTRAN) in terms of computational speed, it has been proven in several applications that the capabilities of PYTHON are just as good, if not better. For example, the open-source python framework that facilitates the analysis of data collected by the Fermi-LAT (FERMIPY) software (§3.2), used to analyze the gamma-ray data collected by Fermi-LAT, is almost entirely written in PYTHON. The following section provides a detailed overview of the DRAN software package and outlines overarching processes that control the data processing procedures.

7.3.1 Software overview and analysis workflow

It was decided to develop DRAN using PYTHON version 3.8, the same version of PYTHON that was installed on the host server at the time, to ensure easy integration with the existing system. The latest release of PYTHON at the time of writing this thesis is version 3.10. There are plans to upgrade DRAN to the latest PYTHON version in the

[1]https://www.fullstackpython.com/flask.html
[2]https://www.djangoproject.com
[3]https://pandas.pydata.org
[4]https://scikit-learn.org/stable/
[5]https://www.tensorflow.org

future. DRAN consists of a set of modules that control the program operation. Because PYTHON has a rich set of predefined libraries, many of the basic operations performed by the DRAN program leverage functionality from existing PYTHON scientific libraries, including NUMPY[1], SCIPY[2], PYFITS[3] (Barrett and Bridgman, 2000), and ASTROPY[4] (Astropy Collaboration et al., 2013) for the mathematical data conversions, as well as MATPLOTLIB[5] and PYQT5[6] for the visualizations and the graphical user interface.

Regarding the overall approach to the program design, the DRAN software package was built using a dual interface interoperability system approach. Dual interoperability occurs when a single program is developed with two user interfaces, the Command Line Interface (hereafter called the command-line interface (CLI)) and the Graphical User Interface (hereafter called the GUI), that use the same resources (e.g. operating on the same underlying code and accessing the same database/s) but behave independently of one another. Creating a program that shares resources between interfaces ensure consistency in results, an uninterrupted workflow, easier management of the system, and faster development of new interoperable features. To control the operations of the internal system, DRAN uses an object-oriented model (OOM) approach. The object-oriented model (OOM) is a model that uses object instances to call methods to execute specific chains of events. Objects are created and destroyed along the different workflow phases and can be used anywhere within the program. However, for this approach to work, the software needs to be seamless in its application and provide a relatively easy flow of processes from one step to the next.

An outline of the workflow of the DRAN software package is shown in Figure 7.1. The workflow diagram illustrates the sequence of tasks that should be executed to process the observed data from the raw data files into the final processed data output. The workflow of the DRAN software package can be grouped into three main phases; data preparation, data processing, and data visualization. Each of the main phases consists of three components; input, operations, and output. The input and output components define the type, format, and location of the input and output data required by and manipulated through the operations components, and subsequently

[1] https://numpy.org
[2] https://scipy.org
[3] https://pyfits.readthedocs.io/en/latest/
[4] https://www.astropy.org
[5] https://matplotlib.org/stable/index.html
[6] https://pypi.org/project/PyQt5/

reads in the desired data for further processing and writes out the processed data in the desired format. The operations components each deploy different methods to extract information and modify or analyze the data during each of the three main phases.

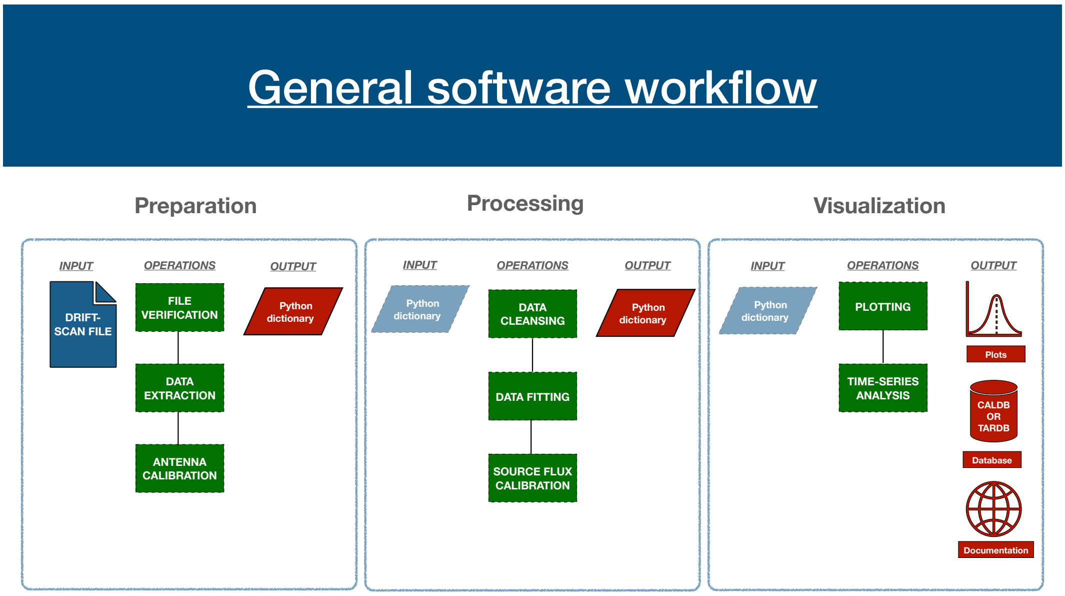

Figure 7.1: General software workflow outlining the preparation, processing, and visualization phases of the DRAN software package. Each phase consists of three steps, data input (shown in blue), data processing (shown in green), and data output (shown in red).

The DRAN program initiation

DRAN uses an object called PROCESSSELECTOR to initiate the program. The PROCESSSELECTOR manages the different interfaces and modes of the program, which the user selects after DRAN is launched and ensures that the correct analysis object is created for each, e.g., executing an automated single- or batch-mode analysis or launching the GUI. In single-mode, only one file is processed. In batch-mode, a group of drift scan files stored in a folder or a directory consisting of multiple folders are automatically processed one after the other. Figure 7.2 shows an example of the output screen that is displayed when the program is initiated. Once the PROCESSSELECTOR is initialized, a typical analysis sequence involves data extraction, data calibration and cleaning, model fitting, plotting, and ultimately writing the results to a database.

Data preparation

```
##################################################################
#                                                                #
#                ######  ######  ###### #    #                   #
#                #     # #    #  #    # # #  #                   #
#                #     # #####   ###### #  # #                   #
#                #     # #    #  #    # #   ##                   #
#                ######  #    #  #    # #    #                   #
#                                                                #
##################################################################

* Disclaimer *: DRAN is a data reduction and analysis software
pipeline developed to systematically reduce and analyze HartRAO's
26m telescope drift scan data. It comes with no guarantees
whatsoever, but the author does attempt to assist those who use it
to get meaningful results.



## SELECT OPTION:
-----------------------------------

 1. Data processing
 2. Data analysis
 3. Launch GUI
 4. Launch CLI
 5. Launch Docs
 0. Exit program

 Please select an option

 Option Selected: █
```

Figure 7.2: Screenshot of the CLI startup screen, showing the primary program interface when running in semi-automated mode. This mode of operation runs both single- and batch-mode operations from predefined routines.

Data preparation is a crucial step in any data processing chain. It is the act of gathering and manipulating raw data into a form that can readily be used for further processing. This step is critical because none of the results obtained after processing can be considered meaningful if the quality of the data and the validity of the data file cannot be verified. In the data preparation phase of the DRAN program, a drift scan file is required as input. This file undergoes a series of checks and calibration steps to prepare the data before the data can be passed on to the processing phase of the program. The operations performed on the data in the preparation phase include file verification, data extraction, and antenna calibration.

A file must comply with three basic criteria to be considered for further processing. First, the file must be a FITS file, and second, the file name must follow the naming convention discussed in §2.1.4.1. Lastly, the file must contain data. Failure during any of the checks to verify the validity of the file will immediately shut down the program, and the user is requested to verify that they are following all noted recommendations listed in the software package README file that is distributed as part of the DRAN software package. If a file passes all of the verification checks, the file is considered ready for further processing, and the next step in the data operations chain is initiated.

Data extraction of drift scan data is managed by an object called the FitsFileReader. The FitsFileReader opens the FITS file and extracts drift scan data using the PYFITS library. The data (see Appendix 1.3), which includes parameters related to the observing conditions (e.g., the observation date, source elevation, system temperature, and weather information), the source properties (e.g., the flux density of a calibrator source), and the recorded data from the observation is extracted and stored in a PYTHON dictionary object. A PYTHON dictionary is an unordered and mutable PYTHON container that facilitates the storage of mappings of unique keys to values. Each observed parameter name is mapped to its historical value from the drift scan file in a PYTHON dictionary. These key-value mappings are updated when the values change or a new key-value pair is created during processing, e.g., during model fitting. After all the processing has been completed, the final version of the PYTHON dictionary is saved and written to a database where the data are stored for further analysis.

The data calibration step requires the actual calculation of the system temperature of the antenna, using the noise diode measurements, and the subsequent conversion of the recorded count-rate measurement of the signal amplitude in units of Hertz (Hz) to an antenna temperature in units of Kelvin (explained in detail in §2.1.5). In addition, data observed using the 22 GHz receiver requires an additional calibration step to correct for attenuation of the signal by the troposphere (explained in detail in §6.4). Data from the receiver noise diode and meteorological data, recorded at the time of the observation, are extracted from the raw data file. All results obtained from the calibration operations are also added to the python dictionary.

Data processing

The data processing stage involves four steps; 1) cleaning the data, 2) model fitting, 3) pointing correction, and 4) peak flux estimation or flux calibration.

- 1) Data cleaning

Data obtained from radio telescopes are often dominated by noise and depending on the frequency of observation can be heavily contaminated by RFI from either local instrumental effects or external sources. For this reason, special care needs to be taken to clean the data of unwanted signals and to minimize losing the underlying signal in the process. The cleaning algorithm used in the DRAN program avoids this by making the following assumptions: 1.) that the recorded drift scan signal of a point source should resemble a section through the telescope's PSF (point spread function or telescope beam pattern), and that the peak in the signal be near the center of the beam pattern (the expected transit position of the source or point of maximum response), and 2.) that the noise should follow a reasonable Gaussian distribution, in which case one would expect the magnitude of the positive extremum of the noise to be similar to the absolute magnitude of the negative extremum of the noise. Any data that does not adhere to these criteria are considered interference and discarded. In DRAN the data is passed through a set of iterative cleaning steps to ensure the best possible results and to remove as much RFI as possible from the data. The method clean_rfi runs the algorithm that cleans the data by removing any RFI.

The data cleaning process consists of the following steps:

- First, a piece-wise, third-degree polynomial (spline) is fitted to the drift scan spectrum; this is done to obtain a model of the shape of the drift scan pattern.

- Next, the spline model obtained above is subtracted from the data, and the rms and residuals are calculated. The rms value is used to define the minimum and maximum limits of allowed values for a particular drift scan spectrum's residuals. Values lying above or below the chosen threshold value of 2.7 times the rms are discarded.

- This process of fitting a spline and evaluating the residuals using the rms is repeated iteratively until all the residuals lie within the set rms limit. This produces a clean drift scan devoid of RFI.

Figure 7.3a shows an example of drift scan data with significant RFI, and Figure 7.3b shows an example of fitting a spline to the data to obtain a model of the drift scan pattern. When the data cleaning process is completed, the result is generally[1] a smooth spectrum, free of any RFI contamination (as shown in Figure 7.3d). Figure 7.3c shows an example of the residuals obtained from subtracting the spline model from the data, demonstrating the effectiveness of the cleaning algorithm.

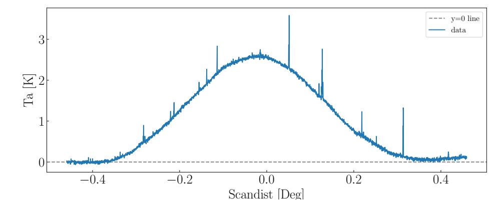

(a) Raw drift scan data

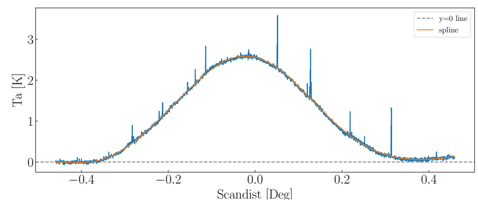

(b) Spline fit to raw data

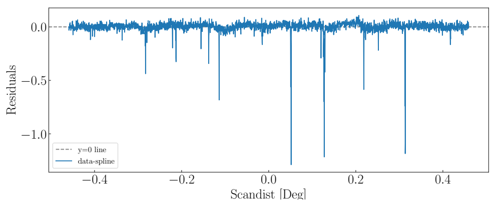

(c) Residual drift scan data

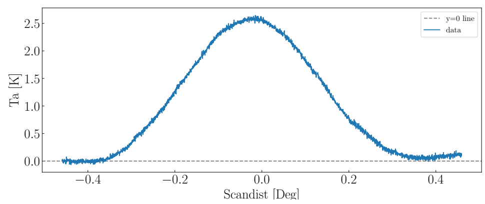

(d) Cleaned drift scan data

Figure 7.3: Plots showing the output from different stages of the fitting process for a representative 2.3 GHz drift scan of the calibrator Hydra A.

- 2) Model fitting

The model fitting process is a two-step process that 1.) fits a first-order polynomial model to the baseline to correct for any telescope drift during observation, and 2.) fits a second-order polynomial to the data to obtain the peak antenna temperature. It is assumed that the drift-scan data will follow the shape of the beam pattern, i.e., there will be at least two local minima on either side of the main beam (more if the scan length is increased to data beyond the first sidelobes).

Correcting the baseline drift

[1] The data cleaning process works best for data with a high SNR, The effectiveness of the method decreases in performance when applied to very weak sources.

The theoretical expected position of the first minima are known a priori and saved under the label first null beam width (FNBW) in the drift scan file (see Appendix 1.3). Using the recorded FNBW positions from the drift scan file generally works well to correct for telescope drift when the data is well behaved and cleaned of any RFI. However, if the data is affected by weather or instrumental errors, or in the case of weak sources, using the recorded FNBW tends to produce inconsistent results. DRAN is equipped with an automated baseline block estimator to mitigate this problem. Instead of using the recorded FNBW positions, the algorithm searches for the local minima on either side of the main beam, using a spline model fit to the cleaned data. The algorithm estimates the location of the first local minima as the point along the spline closest to the central peak, where the beam pattern reaches a value of zero or a value very close to zero[1]. The estimation is made on both sides of the main beam pattern as shown in Figure7.4a. To correct for the drift in the data, however, requires more than just two points, i.e. a set of data points are needed for the model to give a reasonable fit. These points are referred to here as the baseline blocks. Baseline blocks are sections of the data selected within a given range and on either side of the estimated local minima positions. Currently, the width of each baseline block is 2.5% of the total length of the drift scan[2]. If, for example, a drift scan has 2000 data points, each of the baseline blocks will contain 50 data points, 25 on either side of the estimated local minima. An example of the estimated baseline blocks for a drift scan observation is shown in Figure7.4b with the yellow data points being the baseline blocks on either side of the main beam. Using the baseline blocks, a first-degree polynomial is then fitted through the selected segments of data to obtain the final baseline-corrected drift scan spectrum as shown in Figure 7.4d, which is obtained by subtracting a model of the fitted baseline polynomial from the original clean spectrum, as shown in Figure7.4c. The test results from using this model to correct for antenna drift are discussed in §7.4.

follows; for good quality data such as that usually obtained for bright calibrator sources, fitting the top 30

Peak fitting

In this step, the peak height of the baseline-corrected drift scan spectrum (peak

[1] This method is not a perfect estimate, so we need to allow room for error.

[2] Different lengths were tested, and 2.5% achieved the best results that catered for most of the drift scans.

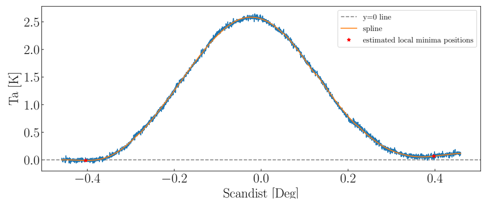

(a) Local minima selection of drift scan.

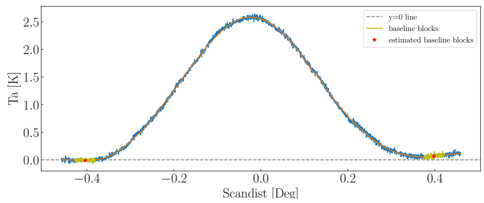

(b) Baseline block selection of drift scan.

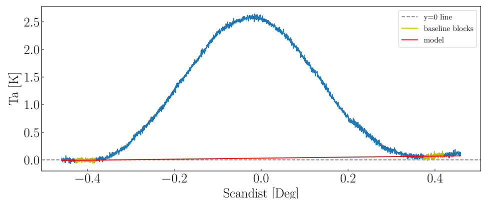

(c) Baseline corrected drift scan.

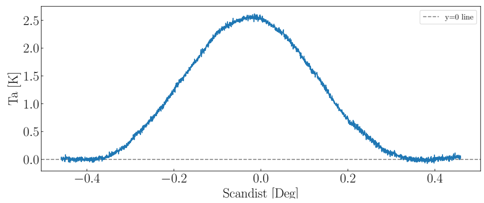

(d) Final fitted drift scan.

Figure 7.4: Plots showing the resulting outputs from different stages of the baseline correction process, for a representative 2.3 GHz drift scan of the calibrator source Hydra A.

antenna temperature) is estimated. The top of the beam pattern closely resembles a parabola and, as such, can be approximated by a second-order polynomial function (as shown in Figure7.5). Depending on the quality of the drift scan data, more or less of the top part of the main beam can be included in the fit to estimate of the peak height. The criteria used to determine how much of the top of the main beam to include in the fit are as follows; because calibrator sources are generally stronger sources with high SNR, the fitting model was applied the top 30% of the main beam as it gives a good approximation of the parabolic shape[1], while for weak sources using the top 50% of the main beam provides a better approximation of the peak height as this data tends to be noisier[2]. These values were obtained using trial-and-error and were tested during the development phase of the DRAN software, and are used as the default values when using DRAN in an automated mode.

- 3) Pointing correction

Observations at frequencies higher than 2.3 GHz require pointing corrections in addition to and before estimating the final antenna temperature. This is because

[1] Fitting fewer points, e.g., using $< 20\%$ of the top part of the main beam forces the parabola to behave more like a first-order polynomial changing the curvature of the main beam pattern.

[2] Fitting fewer points, i.e., using $< 50\%$ of the top part of the main beam for the for fit, generally gives poor results and in most cases, the fit fails completely

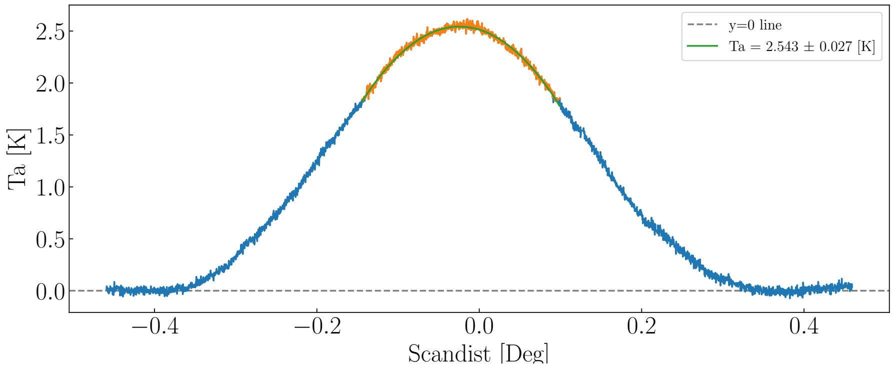

Figure 7.5: Plot showing the resulting output from the peak fitting process for a representative 2.3 GHz drift scan of the calibrator Hydra A. The peak height is estimated using a parabolic function.

the antenna pointing model is not perfectly accurate, i.e. it does not account for all of the factors that may influence the pointing of the antenna such as nonlinear errors. Pointing errors will reduce the antenna gain in the source direction and will contribute to the uncertainty in flux-density measurements of compact sources. Given the fact that the size of the antenna primary beam scales with frequency this means that the effect of pointing errors will get progressively worse at higher frequencies. Hence we need to account for errors in the antenna's pointing during observations (§3.1.1.3). In the case of the drift scan observations, pointing errors will cause the source to not pass directly through the center of the primary beam of the telescope. This will result in the measured amplitude of the signal being lower than the true signal amplitude. Tripple drift scan observations, as described in detail in Section 3.1.1.3, are used to correct for any errors in the antenna pointing. In this method, three drift scans of the source are obtained; one on-source scan, and one scan at the north, and one at the south half power points of the antenna beam. For observations at frequencies higher than 2.3 GHz, the DRAN software, in its automated mode, will automatically process all three drift scans and will calculate and apply any pointing corrections.

- 4) Peak flux estimation or flux calibration

Depending on whether the observed object is a target source or a calibrator source, the final processing step will either be a flux calibration or an estimate of the PSS. If the object is a calibrator source, the PSS will be calculated as described in §6.5. The

PSS, in turn, is then used to calculate the peak flux density of the target source as described in §3.1.1.4. Once all the calculations are done, all the calculated parameters (e.g. the peak fit, peak fit rms, baseline fit coefficients, pressure, humidity, filename) are saved into a database with a unique identifier (some combination of the source name and frequency). If the source is a calibrator, the information extracted is saved in the calibration database (CALDB.db). If the source is a target, its information is saved in the target database (TARDB.db).

Data visualization

The last and final phase of the DRAN program is the visualization phase. The visualization phase handles the visual aspects of the data and the results obtained from the processing phase. This includes making plots of the drift scan during intermediate stages of the processing phase like those shown in Figures 7.3 and 7.4. Plots created during the intermediate stages are saved temporarily in the currentScanPlotsFolder. During model fitting, only the final cleaned plot, corrected for pointing and baseline drift, and in units of antenna temperature is saved permanently to the Plots folder (i.e. , Figure7.5).

In addition, the DRAN program also provides a tool to view and edit the database tables and the recorded results for each source via the SQLITE VIEWER library. A documentation web interface is also provided for easy access to the user manual, recent updates, and any other necessary information a user may require to use the DRAN program.

The steps outlined in the previous paragraphs all run automatically in either single-file or batch mode through the automated version of the CLI or can be manually applied using the manual version of the CLI. The GUI further allows for the interactive setting of specific parameters, such as defining the baseline blocks, and can perform all the steps outlined for the automated analysis but only functions in single-file mode.

The GUI also provides a platform to analyze the time-series data (see §7.3.3). Data analysis can be carried out in various ways depending on the user's research needs. Steps that can be carried out by the DRAN program for a basic analysis include, 1) further refining of the data, 2) estimating basic descriptive statistics, 3) fitting a polynomial through the data and 4) producing plots of the time-series data. Section

3.1.2 describes the exact steps followed in the analysis of the data used in this study.

7.3.2 The command-line interface (CLI).

The CLI is the primary data reduction and processing tool of the DRAN software package. The CLI tool allows the user to interact with the program by typing commands directly into the command line. A user can either run an automated analysis based on the system's predefined settings or run an analysis in manual mode, manually setting the configuration parameters of the fitting routines. This work only focuses on the data processing using the automated fitting routine. A more complete and detailed description of the package and tutorials are available in the web documentation provided with the software package.

Figure 7.2 shows the CLI setup for automated data reduction. The automated mode provides a set of predefined routines that users may select to run through a verified and tested analysis pipeline. A modified version of this automated program component has been used extensively throughout the preparation of this work to test and verify the effectiveness of the DRAN software package against LINES (see §7.4).

In manual mode, the user can set the configuration parameters for fitting, and the drift scan spectrum can be plotted after each calibration step. The data fitting is not interactive (for interactive fitting, the user is referred to the GUI). However, the CLI will run the operations requested by the user in the background and save the resulting plots in the current working directory. All output from fitting (e.g., the peak fit, the rms in the peak fit) and the intermediate steps (e.g., selecting the baseline blocks) is displayed on the CLI screen.

A web-based visualization tool has been built into the CLI to display the software documentation. The web-based documentation provides general information on the DRAN software, tutorials for data processing, and each of the DRAN commands. Figure 7.7 shows a screenshot of the landing page of the web interface for the DRAN documentation. The interface was created using SPHINX[1], a tool developed

[1] https://www.sphinx-doc.org/en/master/

```
###################################################################
#                                                                 #
#                ######  ######  ###### #    #                    #
#                #     # #    #  #    # # #  #                    #
#                #     # #####   ###### #  # #                    #
#                #     # #    #  #    # #   ##                    #
#                ######  #    #  #    # #    #                    #
#                                                                 #
###################################################################

* Disclaimer *: DRAN is a data reduction and analysis software
pipeline developed to systematically reduce and analyze HartRAO's
26m telescope drift scan data. It comes with no guarantees
whatsoever, but the author does attempt to assist those who use it
to get meaningful results.
Command Line Interface initiated.


For help on basic usage of the program type help or help()


DRAN $ No file given, please read in file

DRAN $ read ../data/single_dish/Jupiter_22GHz/2021d100_05h55m28s_Cont_mike_JUPITER.fits

Working on file:
FILENAME : 2021d100_05h55m28s_Cont_mike_JUPITER.fits
HDULENGTH : 7
SOURCEDIR : Jupiter_22GHz
CURDATETIME : 2021-08-18 20:38:57
OBSDATE : 2021-04-10
OBSTIME : 05:55:28
OBJECT : JUPITER
OBJECTTYPE : CAL
CENTFREQ : 22040.0
scans:  ['HPSLCP', 'HPNLCP', 'ONLCP', 'HPSRCP', 'HPNRCP', 'ONRCP']

DRAN $ █
```

Figure 7.6: Screenshot of the CLI startup screen, showing the primary program interface when running in manual-mode.

for creating intelligent and elegant software documentation in a range of output formats. SPHINX was originally developed for PYTHON but has since expanded to other programming languages.

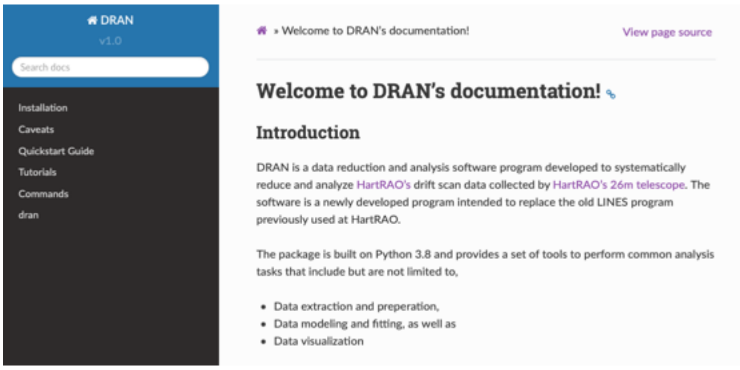

Figure 7.7: HTML interface for the DRAN software package documentation.

7.3.3 The graphical user interface (GUI).

The GUI was built using the PYTHON PYQT5 library. The GUI is just an extension of the CLI package, except for a few routines that had to be written specifically for the GUI. The DRAN GUI can be loaded from the DRAN command-line interface and is a multi-functional tool that provides an easy-to-navigate, interactive space where data can be viewed and modified. The GUI also comes with an additional set of interfaces for data reduction of drift scans, time-series analysis, and plot visualization that can be accessed from the GUI landing page (Figure 7.9). The drift scan data reduction interface is designed as an interactive tool for viewing and editing drift scans. The interface, shown in Figure 7.10, consists of three grids that work together to reduce and analyze drift scan data:

- The info grid - displays the properties (e.g., filename, source name, date of observation, weather information, and information related to the fit procedures and parameters) of the source currently being processed and allows for property modification.

- The display grid - shows previous and upcoming scans to be processed and has navigation buttons to open and view files and save the final processed data and plots.

- The canvas grid - is an interactive plotting window that displays the drift scan data currently being processed. The main window displays the raw or edited drift scan data and any lines that have been fitted to the data, while the bottom panel shows the fit residuals.

The Info grid also has a second tab called the *Fit window* tab shown in Figure 7.11. The Fit window tab contains information about the type of fit (e.g., baseline fitting) and the fit parameters (e.g., the positions of the baseline blocks). The Fit window tab also provides an option to filter or smooth data that suffer from RFI contamination, using Hanning, window, Bartlett, Blackman, or Hamming smoothing. There is also the option to use the spline-fitting technique discussed in §7.3.1.

The GUI time-series interface (Figure 7.12) can be used to view and analyze a

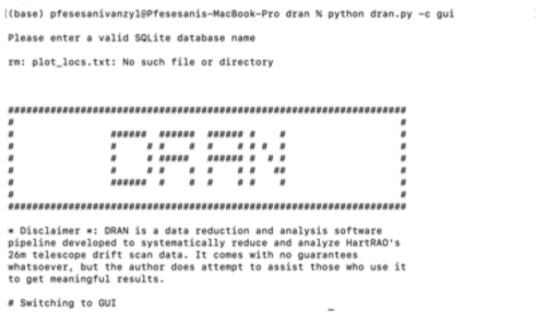

Figure 7.8: DRAN landing page loading the GUI.

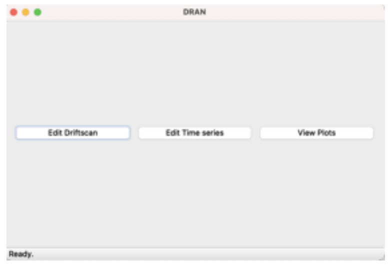

Figure 7.9: GUI landing page.

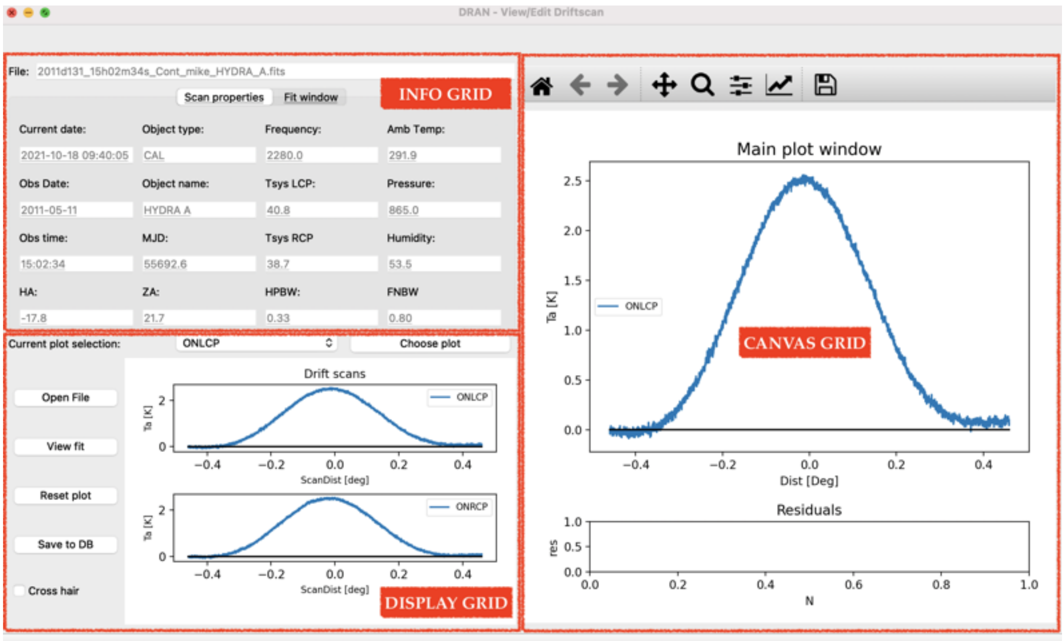

Figure 7.10: A plot of the drift scan data reduction GUI layout. This interface splits into three grids, the info, display, and canvas grids: 1. Basic information on the drift scan and the fitting routines is presented in the info grid. 2. Quick views of other unprocessed drift scans in the file are shown in the display grid. 3. The canvas grid displays the drift scan data on the screen. The canvas grid assists users in interacting with the drift scan directly.

flux-density time-series for sources with multiple observations. The interface reads the database containing the final calibrated data, produces a database with all of the changes applied during the calibration process, and displays a time-series plot of the data, where individual outlier points can be highlighted and removed interactively.

The plot viewer or visualizer interface, shown in Figure 7.13, provides a drop-down

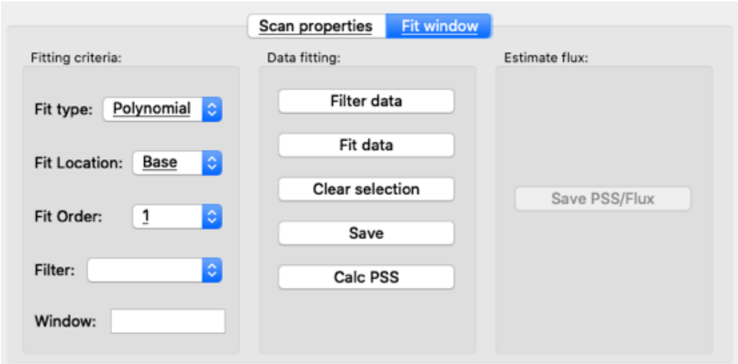

Figure 7.11: A plot of the GUI insert for the Info grid Fit tab. The info grid tab is the primary interface that handles all fitting and smoothing processes for the individual drift scans.

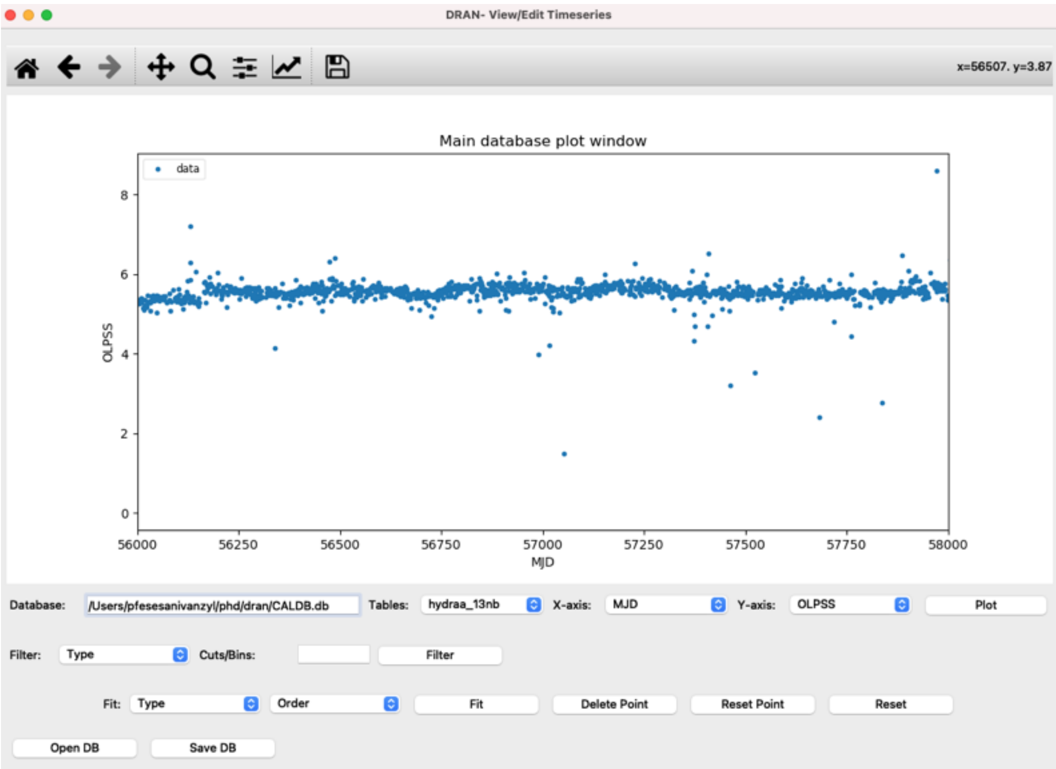

Figure 7.12: A plot of the GUI time-series interface.

list of all the folder names in the DRAN database and displays an HTML page with a thumbnail view of all of the plots in the currently selected folder. Each folder name consists of the source name and the observing frequency. Thus, when a folder is chosen for viewing, the files displayed are of all the plots made for that particular source at that specific frequency arranged in ascending order.

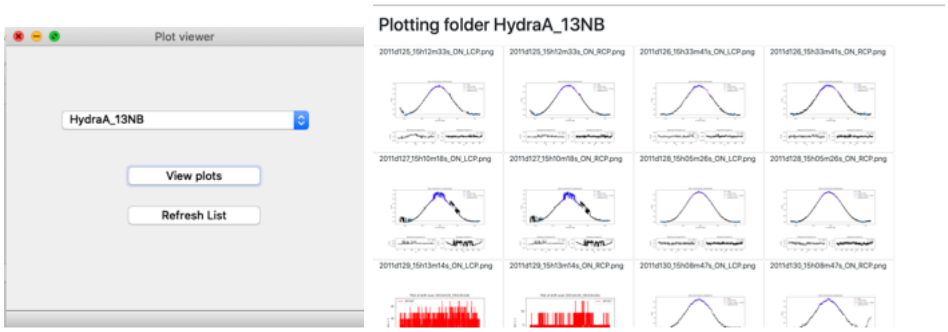

Figure 7.13: Plots of the GUI plot viewer interface. The image on the left shows the actual interface, and the one on the right shows an insert of the results that show up on the web browser for the selected object under investigation.

7.3.4 Summary

In summary, the DRAN software package caters to standard data reduction and analysis of continuum drift scan data taken with HartRAO 26-m radio telescope at 2.3, 4.8, 8.4, 12.2, and 22 GHz. Although the software was primarily designed to process calibrator sources and target sources with adequate SNR for observations with the Hart26m, the software has proven to be flexible enough to provide reasonably good results for weaker radio sources, such as §4.2. The GUI caters to all of the requirements of a simple and easy-to-use drift scan file processor. It gives quick overviews of the whole data set, which is not possible on a CLI. The GUI has also been carefully designed to integrate with the CLI, sharing libraries and allowing direct access to the resources, like the database. All updates performed on the GUI immediately update the drift scan spectrum plot (if the user is re-analyzing a source, otherwise a new plot is created) and the relevant database (e.g., CALDB.db or TARDB.db). Thus, the DRAN program is a truly holistic program bringing together two modes of operation and a variety of use cases to suit every user in processing HartRAO data in the most efficient manner possible.

7.4 Software validation and verification - error analysis

Software verification and validation are critical to any software development life cycle. Verification and validation is the process of ensuring the completeness, accuracy, and quality of the data by making sure the software package meets outlined specifications and fulfills its intended purpose (Wallace and Fujii, 2002). Verification and validation can be achieved by building several checks into a system to test and inspect the operation of the software. For the new DRAN software package, special attention was given to the overall improvement of the software package compared to the old LINES program. In particular, the fitting routines and the implementation of a fully automated processing pipeline.

7.4.1 Data sample selection and considerations.

Twenty-nine drift scan observations (listed in Table 1) of the calibrator source Hydra A were selected, from a random sample of 50 observations taken in 2013 with the Hart26m at 2.3 GHz, to test and verify the new DRAN software package. Observations at 2.3 GHz were selected as they are most affected by RFI and thus provide the means to test the new automated routine for RFI removal that was implemented as part of the DRAN software package. The sample of twenty-nine sources includes both observations that suffer from significant RFI and observations with no RFI. These observations were used to examine the capabilities and performance of DRAN against LINES by investigating the following metrics; the polynomial fit to the spectrum baseline, the rms error of the fit, and the polynomial fit of the main beam to obtain an estimate of the peak height and its uncertainty.

7.4.2 radio frequency interference removal

For the data processing in DRAN, the automated steps for RFI removal, as outlined in §7.3.1 (Data cleaning), were used. The process of RFI removal in LINES, however, is somewhat different. For RFI removal, the LINES program uses a median filter (4253H twice smoother, Velleman and Hoaglin, 1981). This filter applies a combination of running medians and Hanning smoothing for RFI removal and smoothing of the x-values (ordinates). The algorithm calculates the running median of 4, then 2, then 5, and 3 which is then followed by Hanning smoothing.

7.4.3 Polynomial fitting

One of the most important steps that can significantly affect the results of the drift scan processing is the choice of baseline blocks when correcting for drifts in the spectrum baseline. When correcting the baseline of a spectrum, the general aim is to fit the data at locations generally expected to consist of randomized noise. This process, generally, becomes relatively easy when these location choices are made by hand. However, this becomes impractical when faced with thousands of files that require processing. While DRAN was developed with this in mind, the LINES program does not include a built-in feature for automated processing, and the locations of baseline blocks, for example, have to be supplied. In LINES, this can be done either by manually selecting baseline blocks for each observation or by supplying some fixed predefined positions based on the theoretical position of the first null of the FNBW for each receiver/frequency. On the other hand, DRAN provides fully automated processing in which the best locations to fit (for correcting the spectrum baseline to determine the peak height of the main beam) are automatically determined (within reason) to provide the best results.

During the test and verification process, I first compared the results of the fitting routines used in DRAN versus LINES, using the same fit positions in both programs. Secondly, I compared the manual processing results versus the automated pipeline processing in DRAN. The metrics were tested against combinations of data processed by hand, processed by automatically selecting locations to fit, and data with fitting performed at the theoretical locations of the FNBW of the Hart26m telescope beam at 2.3 GHz. The tests were limited to a first-order polynomial fit of the spectrum baseline and a second-order polynomial fit of the top 30-50% of the main beam of the spectrum. (§7.3.1)

7.4.3.1 Data processed by hand

To create a baseline for the comparisons, each observation was manually processed using the LINES program. Fitting the data by hand allowed us to select the positions needed to correct the spectrum baseline and estimate the peak height and its uncertainty. The locations selected as the fit locations for the baseline and peak fitting were then saved and fed to the DRAN software for fitting. Results from this test are listed in tables 3 and 4 for data obtained through manual fitting in the LINES program and tables 1 and 2 for data obtained through automated fitting using the DRAN program.

7.4.3.2 Automatically processed data

These tests aimed to obtain results from automated processing using both LINES and DRAN. However, the automated test took into account two slightly different approaches discussed in the sections that follow.

Theoretical fits

The first approach considered fitting the baseline data at the theoretical locations. This is the location of the FNBW on either side of the main beam. Fitting the theoretical locations can yield great results when working with good data but may provide poor results for low SNR data with high sidelobes, data that suffers from severe weather effects or instrumental errors, and data contaminated with RFI. Results from this test are listed in tables 7 and 8 for data obtained using the LINES program and tables 5 and 6 for data obtained using the DRAN program.

Automated fits

As previously mentioned, DRAN has a unique feature that fits a spline to the data to establish the best-fit positions. These positions are then used as the baseline blocks for the baseline fit and to determine the peak position and amplitude of the main beam, in both DRAN and LINES. In instances where the data suffers from high sidelobes, only those locations where the data is predominately dominated by noise on both sides of the sidelobe are considered for fitting. We found that the method worked relatively well for bright sources and most noisy data with really low SNR. Results from this test are listed in tables 11 and 12 for data obtained using the LINES program and tables 9 and 10 for data obtained using the DRAN program.

7.4.4 Results

Figures 7.14 and 7.15, 7.16, and 7.17 show plots of the rms errors obtained from the baseline and peak fit. The plots on the left show the rms errors for each observation obtained from both LINES and DRAN. The plots on the right-hand side show the difference between the LINES and DRAN rms errors for each observation, where positive values would indicate larger DRAN values, and negative values would indicate larger LINES values.

Errors in the fit

The estimated uncertainties or rms errors from the baseline fits are shown in Figures 7.14 for the LCP data and 7.15 for the RCP data. These plots include the results from the manual selection of the baseline blocks, theoretically determined locations of the baseline blocks, and the automatic selection of baseline blocks in DRAN. Most of the points in the difference plots show a large majority of the deviations in the rms error to be on our below zero. The smallest deviations between DRAN and LINES are seen when the baselines blocks were manually selected, with fewer but much more significant deviations seen for the comparisons where the selection of the baseline blocks was automatically selected in DRAN or based on the theoretical locations of the FNBW. The results indicate that DRAN compares well against LINES, and produces lower error values on average. Even when more significant errors are observed from scans that appear to have some RFI affecting the final result, the DRAN algorithm for outlier detection works better than the LINES version.

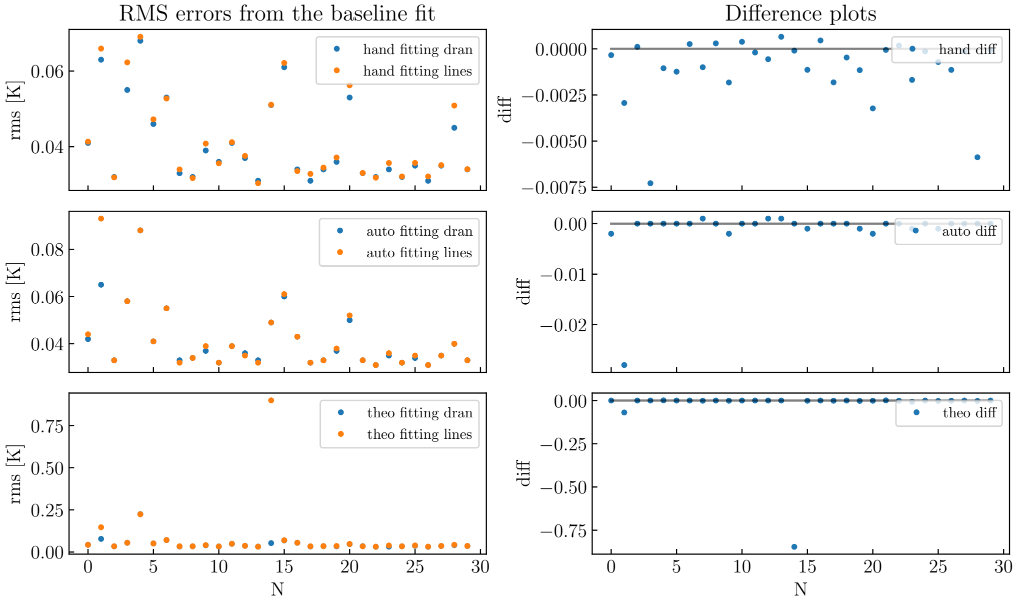

Figure 7.14: Plots of baseline comparison results in LCP

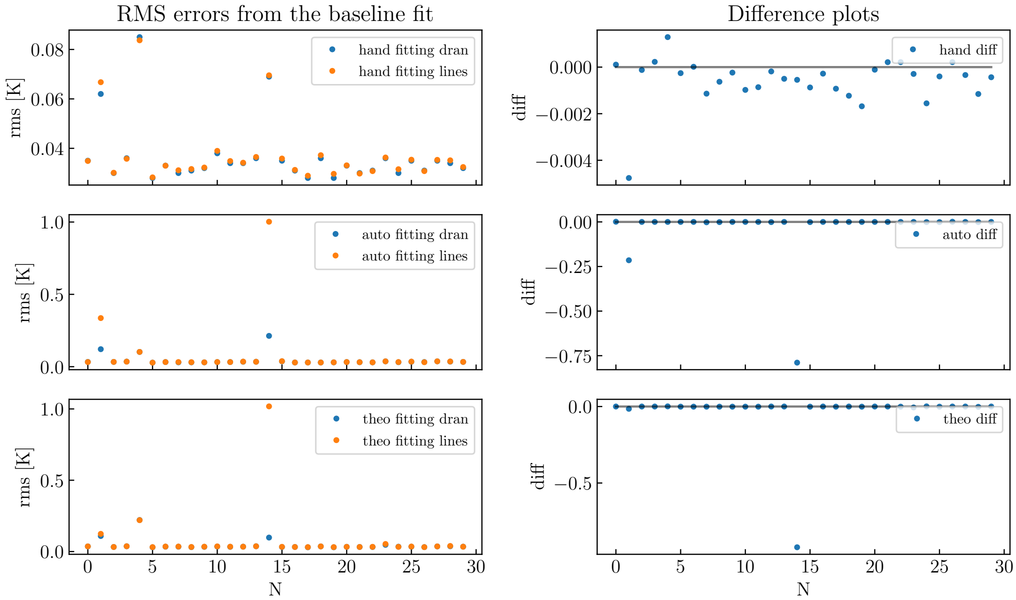

Figure 7.15: Plots of baseline comparison results in RCP

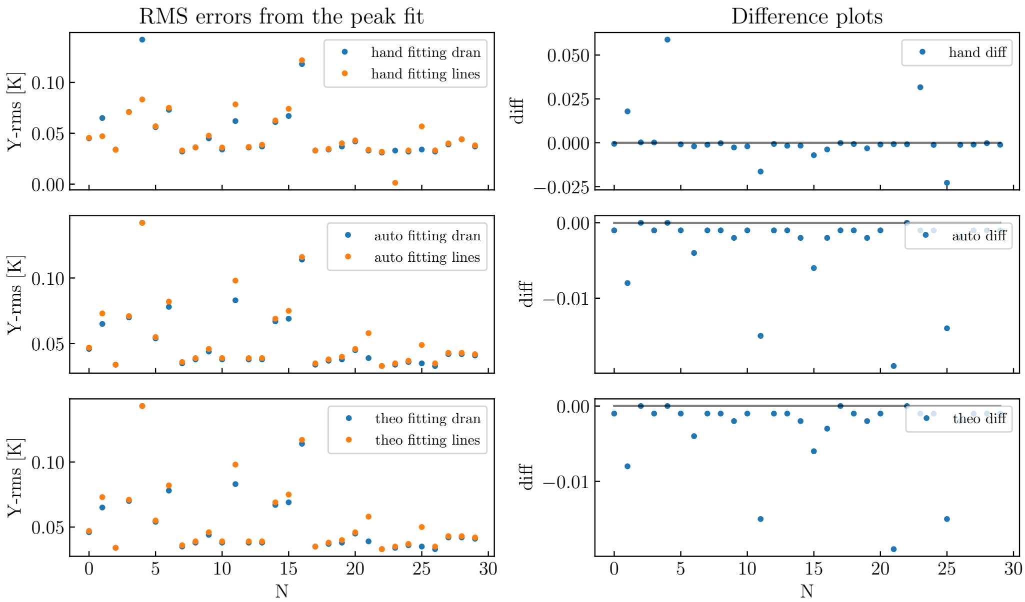

Figure 7.16: Plots of peak rms comparison results in LCP

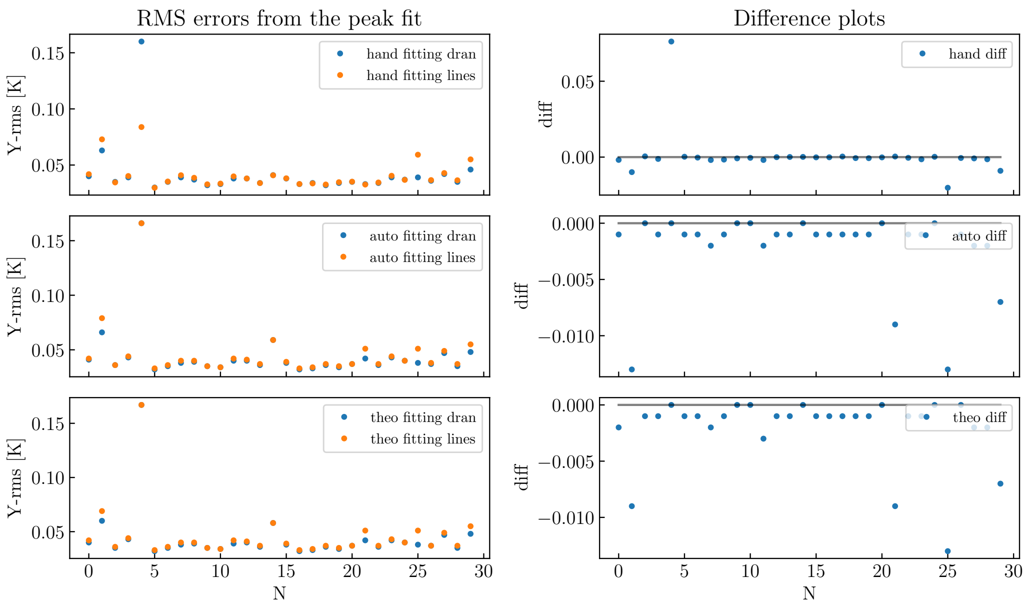

Figure 7.17: Plots of peak rms comparison results in RCP

Similarly, with the plots from the error in the peak fit, the general trend follows that errors from using DRAN are lower than those obtained using LINES (see Figures 7.16 and 7.17).

7.4.4.1 Results analysis

Tables 7.1 and 7.2 provide a breakdown of the basic statistics obtained from the results discussed in the previous sections. The tables list the mean and standard deviation of the rms errors obtained from each comparison for both the LCP and RCP data. From the results, it can be concluded that the DRAN software package does show an improvement over the old LINES program. On average, the rms errors obtained from the DRAN software are lower than those from LINES, mainly attributed to the superior performance of the algorithms used in DRAN for RFI removal.

Table 7.1: Rms errors from the baseline fit. The table shows the descriptive statistics of the results obtained using the different fitting options.

Fitting option	Pol	Mean	Std	Min	Max
Manual - DRAN	LCP	0.041	0.011	0.031	0.068
Manual - LINES	LCP	0.042	0.012	0.030	0.069
Manual - DRAN	RCP	0.037	0.013	0.028	0.085
Manual - LINES	RCP	0.037	0.013	0.028	0.084
Automated - DRAN	LCP	0.041	0.013	0.031	0.088
Automated - LINES	LCP	0.042	0.016	0.031	0.093
Automated - DRAN	RCP	0.043	0.038	0.028	0.213
Automated - LINES	RCP	0.077	0.184	0.028	1.002
Theoretical - DRAN	LCP	0.048	0.036	0.031	0.225
Theoretical - LINES	LCP	0.080	0.160	0.032	0.899
Theoretical - DRAN	RCP	0.045	0.038	0.030	0.221
Theoretical - LINES	RCP	0.077	0.182	0.031	1.018

Fitting options are categorized as follows,
1. Manual - data fitting is done by hand in LINES. The results of the locations used to estimate the the baseline blocks and peak fitting block are recorded and fed to the DRAN program for automatic processing.
2. Automated - data fitting is done by the automated algorithm in the DRAN program. The results of the locations used to estimate the the baseline blocks and peak fitting block are recorded and fed to the LINES program for automatic processing.
3. Theoretical - data fitting is done by the automated algorithm in the DRAN program. The results of the locations used to estimate the the baseline blocks and peak fitting block are recorded and fed to the LINES program for automatic processing.

Table 7.2: Rms errors from the peak fit. The table shows the descriptive statistics of the results obtained using the different fitting options.

Fitting option	Pol	Mean	Std	Min	Max
Manual - DRAN	LCP	0.049	0.026	0.031	0.142
Manual - LINES	LCP	0.048	0.022	0.001	0.122
Manual - DRAN	RCP	0.041	0.023	0.030	0.160
Manual - LINES	RCP	0.041	0.012	0.030	0.084
Automated - DRAN	LCP	0.051	0.026	0.033	0.142
Automated - LINES	LCP	0.054	0.026	0.033	0.142
Automated - DRAN	RCP	0.044	0.024	0.032	0.166
Automated - LINES	RCP	0.046	0.025	0.033	0.166
Theoretical - DRAN	LCP	0.051	0.026	0.033	0.143
Theoretical - LINES	LCP	0.055	0.027	0.033	0.143
Theoretical - DRAN	RCP	0.044	0.024	0.032	0.167
Theoretical - LINES	RCP	0.046	0.024	0.033	0.167

Fitting options are categorized as follows,

1. Manual - data fitting is done by hand in LINES. The results of the locations used to estimate the the baseline blocks and peak fitting block are recorded and fed to the DRAN program for automatic processing.
2. Automated - data fitting is done by the automated algorithm in the DRAN program. The results of the locations used to estimate the the baseline blocks and peak fitting block are recorded and fed to the LINES program for automatic processing.
3. Theoretical - data fitting is done by the automated algorithm in the DRAN program. The results of the locations used to estimate the the baseline blocks and peak fitting block are recorded and fed to the LINES program for automatic processing.

8 Summary and Concluding remarks

This part of the research aimed to study the calibration process for single-dish HartRAO data and improve the data reduction process through the development of a new software package. The main objectives were to test and validate the current calibration steps at HartRAO and to automate the data processing in order to improve the monitoring of calibrator sources and diagnosis of problems with the observations.

Through this project I was able to develop DRAN, a semi/fully-automated program for reducing and analyzing data collected by the Hart26m (§7.3.1). The data processing steps needed to be reproducible, reuseable and accommodate manual data reduction as well. To demonstrate the capabilities of DRAN, I tested DRAN by performing a long-term analysis on four HartRAO blazar sources and compared the results to those from the standard software tool LINES, see section 7.4. I found both analyses to be in good agreement, which is the first step to establish DRAN as a sufficient tool for the reduction and analysis of HartRAO data. Further upgrades to the software are also needed, such as additional fitting algorithms and an online version of the software available.

8.1 Future work

Improvement of calibration processes

With the completion of this work I plan to commense a full data reduction and analysis workflow to process all HartRAO historical data in order to provide PSS estimates for all calibrators monitiored by the Hart26m. The proper calibration of

HartRAO data is of utmost importance and as such the continued work on improving the calibration processes, especially for the 8.4 GHz and 22 GHz data will be a top priority for me.

Software release

I plan to also begin the process of merging the current version of the DRAN program together with the spectral line program from Dr. Stephanus van Den Heever in leu for an immenent release of the HartRAO software package to the public in the near future.

Hart26m incident management

Currently, the incident management for Hart26m is done manually by journaling all incidents in a physical diary located in the control room. During my work with the assistance of Dr. van Den Heever, I had to digitize the diaries containing incidents that occurred within the research period in order to use them in my work. This was a time-consuming task that could have been avoided if we had an incident management software package. Implementing a digital system for incident reporting would: 1) standardize the reporting method by introducing a consistent format for everyone to follow, 2) eliminate issues with legibility caused by different handwriting styles, and 3) make the incidents easily accessible as one does not have to be on-site to view the logbooks. As part of future work, I plan to investigate the possibility of creating a software package specifically for incident management at HartRAO.

Improvement of weather data: Upgrade of weather monitoring systems

To ensure accurate data calibration, it is essential to obtain precise measurements from our instruments. As stated in §6.4.4, weather conditions greatly impact high frequency observations, so it is crucial to properly maintain and update the instruments that measure weather parameters. The weather measurements at HartRAO are currently measured using a Meteorological Monitoring System (MET) that was last updated in 2011 (over 12 years ago). Although we can still calibrate sources with the results from these measurements, a recent study fone by Nickola et al. (2021) showed that some parts of the system are gradually deteriorating and need to get replaced. Marisa Nickola from HartRAO is currently investigating the weather sensors that provide the weather related data used to calibrate HartRAO sources e.g. humidity, pressure and PWV, as well as other important parameters not mentioned in this work. A new MET4 unit has been installed at HartRAO and is undergoing testing and calibration in preperation for it replacing the old MET3 unit that provided the data for PWV used in this study. This project is the work will appear in her forthcoming Ph.D., due later this year. Since the results from the MET unit directly impact the calibration of HartRAO sources, I will be invested in investigating how the new system improves the calibrator PSS measurements.

Bibliography

Abdo, A. A. et al. (June 1, 2010). “FERMI LARGE AREA TELESCOPE FIRST SOURCE CATALOG”. In: *ApJS* 188.2, pp. 405–436. ISSN: 0067-0049, 1538-4365. DOI: 10.1088/0067-0049/188/2/405.

Abdollahi, S. et al. (June 1, 2022). “Incremental Fermi Large Area Telescope Fourth Source Catalog”. In: *The Astrophysical Journal Supplement Series* 260, p. 53. ISSN: 0067-0049. DOI: 10.3847/1538-4365/ac6751.

Agarwal, Aditi et al. (Sept. 21, 2019). “Multiband optical variability of 3C 279 on diverse time-scales”. In: *Monthly Notices of the Royal Astronomical Society* 488.3, pp. 4093–4105. ISSN: 0035-8711, 1365-2966. DOI: 10.1093/mnras/stz1981.

Ajello, M. et al. (Sept. 1, 2021). “Fermi Large Area Telescope Performance after 10 Years of Operation”. In: *The Astrophysical Journal Supplement Series* 256, p. 12. ISSN: 0067-0049. DOI: 10.3847/1538-4365/ac0ceb.

Alexander, T. (1997). “Is AGN Variability Correlated with Other AGN Properties? ZDCF Analysis of Small Samples of Sparse Light Curves”. In: *Astronomical Time Series* 218. Ed. by D. Maoz, A. Sternberg, and M. Leibowitz E., p. 163.

Appl, S. and M. Camenzind (Nov. 1, 1988). “Shock conditions for relativistic MHD jets.” In: *Astronomy and Astrophysics* 206, pp. 258–268. ISSN: 0004-6361.

Astropy Collaboration et al. (Oct. 2013). “Astropy: A community Python package for astronomy”. In: *AAP* 558, A33. DOI: 10.1051/0004-6361/201322068.

Atwood, W. et al. (Mar. 2013). “Pass 8: Toward the Full Realization of the Fermi-LAT Scientific Potential”. In: *arXiv e-prints*, arXiv:1303.3514.

Atwood, W. B. et al. (June 2009). “The Large Area Telescope on the Fermi Gamma-Ray Space Telescope Mission”. In: *ApJ* 697.2, pp. 1071–1102. DOI: 10.1088/0004-637X/697/2/1071.

Baade, W. and R. Minkowski (Jan. 1, 1954). “Identification of the Radio Sources in Cassiopeia, Cygnus A, and Puppis A.” In: *The Astrophysical Journal* 119, p. 206. ISSN: 0004-637X. DOI: 10.1086/145812.

Baars, Jacob W. M. (2007). *The paraboloidal reflector antenna in radio astronomy and communication: theory and practice*. Astrophysics and space science library v. 348. New York: Springer. 113 pp. ISBN: 978-0-387-69734-5.

Ballet, J. et al. (May 1, 2020). *Fermi Large Area Telescope Fourth Source Catalog Data Release 2*.

Barrett, P. E. and W. T. Bridgman (Jan. 2000). "PyFITS. a Python FITS Module". In: *Astronomical Data Analysis Software and Systems IX*. Ed. by Nadine Manset, Christian Veillet, and Dennis Crabtree. Vol. 216. Astronomical Society of the Pacific Conference Series, p. 67.

Beckmann, Volker and Chris R. Shrader (2012). *Active galactic nuclei*. Physics textbook. Weinheim, Germany: Wiley-VCH. 351 pp. ISBN: 978-3-527-41091-0 978-3-527-41078-1.

Bennett, A. S. (Jan. 1, 1962a). "The preparation of the revised 3C catalogue of radio sources". In: *Monthly Notices of the Royal Astronomical Society* 125, p. 75. ISSN: 0035-8711. DOI: `10.1093/mnras/125.1.75`.

– (Jan. 1, 1962b). "The revised 3C catalogue of radio sources." In: *Memoirs of the Royal Astronomical Society* 68, p. 163.

Bevington, Philip R. and D. Keith Robinson (2003). *Data reduction and error analysis for the physical sciences*. 3rd ed. Boston: McGraw-Hill. 320 pp. ISBN: 978-0-07-247227-1.

Blandford R., D. and A. Konigl (1979). "Relativistic jets as compact radio sources". In: *ApJ* 232, pp. 34–48.

Blandford R., D. and G. Payne D. (June 1982). "Hydromagnetic flows from accretion discs and the production of radio jets". In: *MNRAS* 199, pp. 883–903.

Blandford R., D. and L. Znajek R. (1977). "Electromagnetic extraction of energy from Kerr black holes". In: *MNRAS* 179, pp. 433–456.

Blandford, R. D. (2002). "To the Lighthouse". In: *Lighthouses of the Universe: The Most Luminous Celestial Objects and Their Use for Cosmology*. Ed. by M. Gilfanov, R. Sunyeav, and E. Churazov. _eprint: astro-ph/0202265, p. 381. DOI: `10.1007/10856495_59`.

Boettcher, Markus (June 25, 2010). *Models for the Spectral Energy Distributions and Variability of Blazars*.

Boula, Stella S., Maria Petropoulou, and A. Mastichiadis (Dec. 2018). "On the Connection of Radio and gamma-Ray Emission in Blazars". In: *Galaxies*. Vol. 7. DOI: `10.3390/galaxies7010003`.

Brand, T. (Dec. 18, 2013). “A data analysis pipeline for the 26m Hartebeesthoek radio telescope.” MSc Thesis. Germany: Friedrich-Alexander-Universität Erlangen-Nürnberg. 69 pp.

Briggs F., H. et al. (1997). “drifts can surveys in the 21cm Line with the Arecibo and Nancay telescopes”. In: *PASA* 14, p. 37.

Buchner, S. and C. Flanagan (Feb. 27, 2008). “Glitches in the Vela Pulsar”. In: *AIP Conference Proceedings* 983.1, pp. 145–147. ISSN: 0094-243X. DOI: 10.1063/1.2900129.

Burrows, David N. et al. (Oct. 2005). “The Swift X-Ray Telescope”. In: *AJ* 120.3, pp. 165–195. DOI: 10.1007/s11214-005-5097-2.

Buson, S. et al. (Sept. 1, 2014). “Unusual flaring activity in the blazar PKS 1424-418 during 2008-2011”. In: *Astronomy and Astrophysics* 569, A40. ISSN: 0004-6361. DOI: 10.1051/0004-6361/201423367.

Böttcher, M., E. Harris D., and H. Krawczynski (2012). *Relativistic jets from active galactic nuclei*. WILEY-VCH.

Böttcher, M., A. Reimer, and P. Marscher A. (2009). “Implications of the very high energy gamma-ray detection of the quasar 3C279”. In: *ApJ* 703, pp. 1168–1175.

Böttcher, M. et al. (2013). “Leptonic and hadronic modeling of fermi detected blazars”. In: *ApJ* 768, p. 54.

Campbell, Donald B. (Dec. 2002). “Measurement in Radio Astronomy”. In: *Single-Dish Radio Astronomy: Techniques and Applications*. Ed. by Snezana Stanimirovic et al. Vol. 278. Astronomical Society of the Pacific Conference Series, pp. 81–90.

Carroll, Bradley W. and Dale A. Ostlie (Sept. 7, 2017). *An Introduction to Modern Astrophysics:* 2nd ed. Cambridge University Press. ISBN: 978-1-108-42216-1 978-1-108-38098-0.

Cash, W. (Mar. 1, 1979). “Parameter estimation in astronomy through application of the likelihood ratio.” In: *The Astrophysical Journal* 228, pp. 939–947. ISSN: 0004-637X. DOI: 10.1086/156922.

Cerruti, Matteo (Oct. 1, 2020). “Leptonic and Hadronic Radiative Processes in Supermassive-Black-Hole Jets”. In: *Galaxies* 8.4, p. 72. ISSN: 2075-4434. DOI: 10.3390/galaxies8040072.

Charlot, P. et al. (Dec. 2020). “The third realization of the International Celestial Reference Frame by very long baseline interferometry”. In: *A&A* 644, A159. DOI: 10.1051/0004-6361/202038368.

Cohen M., H. et al. (2014). “Studies of the jet in BL Lacertae I. Recollimation shock and moving emission features”. In: *ApJ* 787, p. 151.

Connaughton, V. et al. (Jan. 1, 2018). “On the Interpretation of the Fermi-GBM Transient Observed in Coincidence with LIGO Gravitational-wave Event GW150914”. In: *The Astrophysical Journal* 853, p. L9. ISSN: 0004-637X. DOI: `10.3847/2041-8213/aaa4f2`.

Costamante, L. (2012). “AGNs in the VHE gamma-ray era: a review”. In: *Mem. S. A. It* 83, p. 138.

Crocker, Roland M. and Felix Aharonian (Mar. 1, 2011). “Fermi Bubbles: Giant, Multibillion-Year-Old Reservoirs of Galactic Center Cosmic Rays”. In: *Physical Review Letters* 106, p. 101102. ISSN: 0031-9007. DOI: `10.1103/PhysRevLett.106.101102`.

Curtis H., D. (1918). “Descriptions of 762 nebulae and clusters photographed with the crossley reflector”. In: *Publications of Lick Observatory* 13, pp. 9–42. DOI: `1918PLicO..13....9C`.

D’Ammando, F. (Jan. 9, 2013). “Swift/XRT follow-up of the flaring blazar PKS 1424-41”. In: *ATel* #4717.

D’Ammando, F. et al. (2013). “Detection of a strong optical and gamma-ray flare from blazar PKS 1424-41”. In: *ATel #4714*.

Deane, R. P. et al. (July 3, 2014). “A close-pair binary in a distant triple supermassive black hole system”. In: *Nature* 511.7507, pp. 57–60. ISSN: 0028-0836, 1476-4687. DOI: `10.1038/nature13454`.

Dermer, C. and B. Lott (2012). “On leptonic models for blazars in the Fermi era”. In: *International workshop on beamed and unbeamed gamma-rays from galaxies.* 355. IOP Publishing.

Dermer, C. and R. Schlickeiser (1993). “Model for the high energy emission from blazars”. In: *ApJ* 416, p. 458.

Donato, D. (2010). “\acsfermi detection of a GeV flare from blazar \acspks”. In: *ATel #2583*.

Dreyer, J. L. E. (Jan. 1, 1888). “A New General Catalogue of Nebulæ and Clusters of Stars, being the Catalogue of the late Sir John F. W. Herschel, Bart, revised, corrected, and enlarged”. In: *Memoirs of the Royal Astronomical Society* 49, p. 1.

DuPuy, D. et al. (1969). “Optical observations of BL Lac = VRO 42.22.01”. In: *ApJ* 156, p. L135.

Edelson, R. A. and J. H. Krolik (Oct. 1988). “The discrete correlation function - A new method for analyzing unevenly sampled variability data”. In: *ApJ* 333, p. 646. ISSN: 0004-637X, 1538-4357. DOI: `10.1086/166773`.

Edge, D. O. et al. (Jan. 1, 1959). “A survey of radio sources at a frequency of 159 Mc/s.” In: *Memoirs of the Royal Astronomical Society* 68, pp. 37–60.

Ekers, J. A. (Jan. 1, 1969). “The Parkes catalogue of radio sources, declination zone +20 to -90 .” In: *Australian Journal of Physics Astrophysical Supplement* 7, pp. 3–75.

Fabian A., C. (1999). “Active galactic nuclei”. In: *Proc Natl. Acad. Sci.* USA, pp. 4749–4751.

Fath, Edward Arthur (1909). “The spectra of some spiral nebulae and globular star clusters”. In: *Lick Observatory Bulletins* 5, pp. 71–77. ISSN: 0075-9317. DOI: 10.5479/ADS/bib/1909LicOB.5.71F.

Fermi, E. (1954). “Galactic magnetic fields and the origin of cosmic radiation”. In: *ApJ* 119, p. 1.

Fisher, R. A. (Jan. 1922). “On the mathematical foundations of theoretical statistics”. In: *Phil. Trans. R. Soc. Lond. A* 222.594, pp. 309–368. ISSN: 0264-3952, 2053-9258. DOI: 10.1098/rsta.1922.0009.

Gaylard M., J. and I. Kolbe (2010). “SKA Site comparison of weather parameters from satellite data”. In: 2010 Annual Conference of the SA Institute of Physics Conference. Poster presentation. CSIR Convention Centre.

Gaylard, M. J. (1989). “Radio studies of ionized hydrogen in the southern milky way”. PhD thesis. Rhodes University. 253 pp.

Gaylard, M. J. and G. D. Nicolson (July 2007). “Forty Years of Radio Astronomy at Hartebeesthoek”. In: *African Skies* 11, p. 49.

Ghisellini, Gabriele (2013). *Radiative Processes in High Energy Astrophysics.* Vol. 873. Lecture Notes in Physics. Heidelberg: Springer International Publishing. ISBN: 978-3-319-00611-6 978-3-319-00612-3. DOI: 10.1007/978-3-319-00612-3.

Giannios, D. (2013). “Reconnection-driven plasmoids in blazars: fast flares on slow envelope”. In: *MNRAS* 431, p. 355.

Gibson, James, W. J. Welch, and Imke de Pater (2005). “Accurate jovian radio flux density measurements show ammonia to be subsaturated in the upper troposphere”. In: *Icarus* 173.2, pp. 439–446. ISSN: 0019-1035. DOI: https://doi.org/10.1016/j.icarus.2004.06.020.

Goedhart, S., M. J. Gaylard, and D. J. van der Walt (Mar. 1, 2003). “Periodic flares in the methanol maser source G9.62+0.20E”. In: *MNRAS* 339, pp. L33–L36. ISSN: 0035-8711. DOI: 10.1046/j.1365-8711.2003.06426.x.

Gupta A., C. et al. (2012). “Multiwavelength intraday variability of the BL Lacertae S5 0716+714”. In: *MNRAS* 425, pp. 1357–1370.

Hafez, Yaser A. et al. (Aug. 21, 2008). “Radio source calibration for the Very Small Array and other cosmic microwave background instruments at around 30 GHz”. In: *Monthly Notices of the Royal Astronomical Society* 388.4, pp. 1775–1786. ISSN: 00358711, 13652966. DOI: 10.1111/j.1365-2966.2008.13515.x.

Hartman, R. C. et al. (Feb. 1, 1992). “The EGRET High Energy Gamma Ray Telescope.” In: 3137, pp. 116–125.

Hazard, C., M. B. Mackey, and A. J. Shimmins (Mar. 1, 1963). “Investigation of the Radio Source 3C 273 By The Method of Lunar Occultations”. In: *Nature* 197, pp. 1037–1039. ISSN: 0028-0836. DOI: 10.1038/1971037a0.

Healey, Stephen E. et al. (July 2007). “CRATES: An All-Sky Survey of Flat-Spectrum Radio Sources”. In: *\apjs* 171.1, pp. 61–71. DOI: 10.1086/513742.

Hovatta, T. et al. (2008). “Long-term radio variability of AGN: flare characteristics”. In: *A&A* 485, pp. 51–61.

Jankowsky, F. and J. Wagner S. (July 23, 2022). “Bright optical/GeV-ray flares in Blazars PKS 1424-418 and PKS 1406-076”. In: #15525.

Jansky, Karl G. (Dec. 1, 1933). “Electrical phenomena that apparently are of interstellar origin”. In: *Popular Astronomy* 41, pp. 548–555. ISSN: 0197-7482.

Johnston, K. J. et al. (Aug. 1995). “A Radio Reference Frame”. In: *The Astronomical Journal* 110, p. 880. ISSN: 00046256. DOI: 10.1086/117571.

JUNG, TAEHYUN et al. (Oct. 31, 2015). “MEASURING THE CORE SHIFT EFFECT IN AGN JETS WITH THE EXTENDED KOREAN VLBI NETWORK”. In: *Journal of The Korean Astronomical Society* 48.5, pp. 277–284. DOI: 10.5303/JKAS.2015.48.5.277.

Kadler, M. et al. (Aug. 1, 2016). “Coincidence of a high-fluence blazar outburst with a PeV-energy neutrino event”. In: *Nature Physics* 12.8, pp. 807–814. ISSN: 1745-2481. DOI: 10.1038/nphys3715.

Karttunen, Hannu et al. (2016). *Fundamental astronomy.* 6th edition. New York, NY: Springer Berlin Heidelberg. ISBN: 978-3-662-53044-3.

Kellermann K., I. and I. K. Pauliny-Toth I. (1968). “Variable Radio Sources”. In: *Annual Review of Astronomy and Astrophysics* 6, p. 417. DOI: 10.1146/annurev.aa.06.090168.002221.

Kellermann, K. I. and I. I. K. Pauliny-Toth (Feb. 1, 1969). “The Spectra of Opaque Radio Sources”. In: *The Astrophysical Journal* 155. ADS Bibcode: 1969ApJ...155L..71K, p. L71. ISSN: 0004-637X. DOI: 10.1086/180305.

Kellermann, K. I. et al. (Oct. 1, 1989). "VLA Observations of Objects in the Palomar Bright Quasar Survey". In: *The Astronomical Journal* 98, p. 1195. ISSN: 0004-6256. DOI: 10.1086/115207.

Klein, B. (2008). "Holographic measurement of the 26m HartRAO Telescope". PhD thesis. Johannesburg: University of the Witwatersrand Faculty of Engineering and the Built Environment.

Kovalev Y., Y. et al. (May 2009). "The relation between AGN gamm-ray emission and parsec scale radio jets". In: *ApJ* 696, pp. L17–L21.

Kramarenko, I G et al. (Dec. 21, 2021). "A decade of joint MOJAVE– *Fermi* AGN monitoring: localization of the gamma-ray emission region". In: *Monthly Notices of the Royal Astronomical Society* 510.1, pp. 469–480. ISSN: 0035-8711, 1365-2966. DOI: 10.1093/mnras/stab3358.

Laan, H. van der (Sept. 1966). "A Model for Variable Extragalactic Radio Sources". In: *Nature* 211, pp. 1131–1133. DOI: 10.1038/2111131a0.

Lane, W. M. et al. (Jan. 1, 2004). "Hydra A at Low Radio Frequencies". In: *The Astronomical Journal* 127, pp. 48–52. ISSN: 0004-6256. DOI: 10.1086/379858.

León-Tavares, J. et al. (Aug. 1, 2011). "The connection between gamma-ray emission and millimeter flares in Fermi/LAT blazars". In: *Astronomy and Astrophysics* 532, A146. ISSN: 0004-6361. DOI: 10.1051/0004-6361/201116664.

Liodakis, I. et al. (Nov. 1, 2018). "Multiwavelength cross-correlations and flaring activity in bright blazars". In: *Monthly Notices of the Royal Astronomical Society* 480, pp. 5517–5528. ISSN: 0035-8711. DOI: 10.1093/mnras/sty2264.

Longair, Malcolm S. (Feb. 1, 2011). *High Energy Astrophysics*.

Longo, F. et al. (2009). "Fermi-LAT detection of increasing gamma-ray activity of blazar PKS 1424-418". In: *ATel #2104*.

Lovelace, R. V. E. (Aug. 1976). "Dynamo model of double radio sources". In: *Nature* 262.5570, pp. 649–652. ISSN: 0028-0836, 1476-4687. DOI: 10.1038/262649a0.

Lähteenmäki, A. and E. Valtaoja (June 1, 2003). "Testing of Inverse Compton Models for Active Galactic Nuclei with Gamma-Ray and Radio Observations". In: *The Astrophysical Journal* 590, pp. 95–108. ISSN: 0004-637X. DOI: 10.1086/374883.

Marscher, A. P. and W. K. Gear (Nov. 1985). "Models for high-frequency radio outbursts in extragalactic sources, with application to the early 1983 millimeter-to-infrared flare of 3C 273". In: *APJ* **298**, pp. 114–127. DOI: 10.1086/163592.

Marscher A., P. (1990). "Interpretation of Compact Jet Observations". In: *Parsec-scale radio jets*. Ed. by A. Zensus J. and J. Pearson T., p. 236.

Marscher A., P. and G. Jorstad S. (June 21, 2010). "Rapid variability of gamma-ray emission from sites near the 43 GHz cores of blazar jets". In: *Fermi meets Jansky - AGN at Radio and Gamma-rays*. Ed. by T. Savolianen et al. Bonn, Germany.

Mattox, J. R. et al. (Apr. 1, 1996). "The Likelihood Analysis of EGRET Data". In: *The Astrophysical Journal* 461, p. 396. ISSN: 0004-637X. DOI: 10.1086/177068.

Max-Moerbeck, W. et al. (Nov. 21, 2014). "Time correlation between the radio and gamma-ray activity in blazars and the production site of the gamma-ray emission". In: *Monthly Notices of the Royal Astronomical Society* 445.1, pp. 428–436. ISSN: 0035-8711, 1365-2966. DOI: 10.1093/mnras/stu1749.

Mayer, D. et al. (Sept. 2014). "Importance of the Hartebeesthoek Radio Astronomy Observatory for the VLBI network". In: *Acta Geod Geophys* 49.3, pp. 313–325. ISSN: 2213-5812, 2213-5820. DOI: 10.1007/s40328-014-0063-7.

Meegan, Charles et al. (Sept. 2009). "The Fermi Gamma-ray Burst Monitor". In: *ApJ* 702.1, pp. 791–804. DOI: 10.1088/0004-637X/702/1/791.

Meeks, Marion Littlejohn (1976). *Astrophysics*. Methods of experimental physics 12. New York (N. Y.) London: Academic press. 5–6. ISBN: 978-0-12-475953-4.

Meier D., L. and S. Koide (Apr. 2000). "Magnetohydrodynamic Production Of Highly Relativistic Jets". In: *Astrophysical Phenomena Revealed by Space VLBI*. Ed. by H. Hirabayashi, G. Edwards P., and W. Murphy D., pp. 31–38.

Messier, Charles (Jan. 1, 1781). *Catalogue des Nébuleuses et des Amas d'Étoiles (Catalog of Nebulae and Star Clusters)*, pp. 227–267.

Meyer, Manuel, Jeffrey D. Scargle, and Roger D. Blandford (May 22, 2019). "Characterizing the Gamma-Ray Variability of the Brightest Flat Spectrum Radio Quasars Observed with the *Fermi* LAT". In: *ApJ* 877.1, p. 39. ISSN: 1538-4357. DOI: 10.3847/1538-4357/ab1651.

Michelson, A. A. (June 1, 1920). "On the Application of Interference Methods to Astronomical Measurements". In: *The Astrophysical Journal* 51, p. 257. ISSN: 0004-637X. DOI: 10.1086/142550.

Minier, V. (Sept. 2004). "First Results from the ATCA at Millimetre Wavelengths". In: *Star Formation at High Angular Resolution*. Ed. by Michael G. Burton, Ray Jayawardhana, and Tyler L. Bourke. Vol. 221, p. 275.

Morganti, R., N. E. B. Killeen, and C. N. Tadhunter (Aug. 1, 1993). "The radio structures of southern 2-Jy radio sources." In: *Monthly Notices of the Royal Astronomical Society* 263, pp. 1023–1048. ISSN: 0035-8711. DOI: 10.1093/mnras/263.4.1023.

Nemenashi, P, M. G. Gaylard, and R. Ojha (Feb. 2013). “Sharp increase of radio flux in flaring blazar PKS 1424-41”. In: *ATel* #4819, p. 1.

Nickola, M. et al. (Dec. 1, 2021). “HartRAO weather data”. In: *Proceedings of the 25th European VLBI Group for Geodesy and Astrometry Working Meeting*. 25th European VLBI Group for Geodesy and Astrometry Working Meeting. Gothenburg, Sweden.

Nicolson, G. D. (May 1966). “A Search for Variations in the Flux of the Quasi-stellar Source CTA 102”. In: *Nature* 210.5036, pp. 611–611. ISSN: 0028-0836, 1476-4687. DOI: `10.1038/210611a0`.

– (Aug. 1965). “A Survey of Southern Galactic Radiation at 960 Mc/s”. In: *PASP* 77, p. 260. ISSN: 0004-6280, 1538-3873. DOI: `10.1086/128213`.

Nieppola, E. et al. (2009). “Long-term variability of radio bright BL Lacertae objects”. In: *ApJ* 137, p. 5022.

Nothnagel, A. et al. (July 2017). “International VLBI Service for Geodesy and Astrometry: Delivering high-quality products and embarking on observations of the next generation”. In: *J Geod* 91.7, pp. 711–721. ISSN: 0949-7714, 1432-1394. DOI: `10.1007/s00190-016-0950-5`.

Nyquist, H. (July 1928). “Thermal Agitation of Electric Charge in Conductors”. In: *Phys. Rev.* 32.1, pp. 110–113. DOI: `10.1103/PhysRev.32.110`.

Ojha, R. (2012). “From Radio with Love: an overview of the role of radio observations in understanding high-energy emission from active galaxies”. In: *International Workshop on Beamed and Unbeamed Gamma-Rays from Galaxies*. Vol. 355. J. Phys. Conf. Ser. Muonio Finland.

Ojha, R. and M. Dutka (Oct. 2012). “Increased Gamma-ray Activity from the FSRQ PKS 1424-41”. In: *ATel #4494*.

Ott, M. et al. (Apr. 1994). “An updated list of radio flux density calibrators.” In: *ApJ* 284, pp. 331–339.

Padovani, P. and C. M. Urry (Jan. 2001). “Issues in Blazar Research”. In: *Blazar Demographics and Physics*. Ed. by Paolo Padovani and C. Megan Urry. Vol. 227. Astronomical Society of the Pacific Conference Series. _eprint: astro-ph/0101249, p. 3. DOI: `10.48550/arXiv.astro-ph/0101249`.

Padovani, P. et al. (Aug. 1, 2017). “Active galactic nuclei: what’s in a name?” In: *Astronomy and Astrophysics Review* 25, p. 2. ISSN: 0935-4956. DOI: `10.1007/s00159-017-0102-9`.

Padovani, Paolo (Aug. 1, 2017). “On the two main classes of active galactic nuclei”. In: *Nature Astronomy* 1, p. 0194. ISSN: 2397-3366. DOI: `10.1038/s41550-017-0194`.

Pauliny-Toth, I. I. K. et al. (Nov. 1, 1978). “A deep survey of a region near the North Celestial Pole at a frequency of 4.85 GHz.” In: *Astronomy and Astrophysics Supplement Series* 34, pp. 253–258. ISSN: 0365-0138.

Perucho, M. (Dec. 2013). “Jet dynamics and stability. Recollimation shocks and helical patterns”. In: *European Physical Journal Web of Conferences*. Vol. 61.

Petretti, C., V. Fish, and K. Akiyama (Jan. 2021). “Simulating Observations of M87 with the Event Horizon Telescope and Space VLBI”. In: *American Astronomical Society Meeting Abstracts*. Vol. 53. American Astronomical Society Meeting Abstracts, p. 152.01.

Petrov, L. and G. B. Taylor (Sept. 1, 2011). “PRECISE ABSOLUTE ASTROMETRY FROM THE VLBA IMAGING AND POLARIMETRY SURVEY AT 5 GHz”. In: *The Astronomical Journal* 142.3, p. 89. ISSN: 0004-6256, 1538-3881. DOI: 10.1088/0004-6256/142/3/89.

Pushkarev A., B., Y. Kovalev Y., and L. Lister M. (2010). “Radio/Gamma-ray time delay in the parsec scale cores of active galactic nuclei”. In: *ApJL*, p. L7.

Readhead, A. C. S. and P. N. Wilkinson (July 1, 1978). “The mapping of compact radio sources from VLBI data.” In: *The Astrophysical Journal* 223, pp. 25–36. ISSN: 0004-637X. DOI: 10.1086/156232.

Reber, Grote (Nov. 1944). “Cosmic Static.” In: *ApJ* 100, p. 279. DOI: 10.1086/144668.

Rees, Martin J. (Oct. 1978). “Relativistic jets and beams in radio galaxies”. In: *Nature* 275.5680, pp. 516–517. ISSN: 0028-0836, 1476-4687. DOI: 10.1038/275516a0.

Rieger F., M. (Feb. 2005). “Periodic variability and binary black hole systems in blazars”. In: *High Energy Gamma-Ray Astronomy*. Ed. by A. Aharonian F., J. Völk H., and D. Horns. Vol. 745. American Institute of Physics Conference Series. _eprint: astro-ph/0506720, pp. 487–492.

Rybicki G., B. and P. Lightman A. (1979). *Radiative processes in Astrophysics*. Wiley-VCH.

Ryle, M. (Mar. 1, 1952). “A New Radio Interferometer and Its Application to the Observation of Weak Radio Stars”. In: *Proceedings of the Royal Society of London Series A* 211, pp. 351–375. ISSN: 0080-46301364-5021. DOI: 10.1098/rspa.1952.0047.

Ryle, M. and F. G. Smith (Sept. 1, 1948). “A New Intense Source of Radio-Frequency Radiation in the Constellation of Cassiopeia”. In: *Nature* 162, pp. 462–463. ISSN: 0028-0836. DOI: 10.1038/162462a0.

Schmidt, M. (Mar. 1963). "3C 273 : A Star-Like Object with Large Red-Shift". In: *Nature* 197.4872, pp. 1040–1040. ISSN: 0028-0836, 1476-4687. DOI: 10.1038/1971040a0.

Schuh, H. and D. Behrend (Oct. 2012). "VLBI: A fascinating technique for geodesy and astrometry". In: *Journal of Geodynamics* 61, pp. 68–80. ISSN: 02643707. DOI: 10.1016/j.jog.2012.07.007.

Seyfert, Carl K. (Jan. 1, 1943). "Nuclear Emission in Spiral Nebulae." In: *The Astrophysical Journal* 97, p. 28. ISSN: 0004-637X. DOI: 10.1086/144488.

Shabala, Stanislav S. et al. (2017). "The Effects of Simulated and Observed Quasar Structure on the VLBI Reference Frame". In: *REFAG 2014*. Ed. by Tonie van Dam. Cham: Springer International Publishing, pp. 191–199. ISBN: 978-3-319-45629-4.

Sikora, M., M. C. Begelman, and M. J. Rees (Jan. 1994). "Comptonization of diffuse ambient radiation by a relativistic jet: The source of gamma rays from blazars?" In: *APJ* **421**, pp. 153–162. DOI: 10.1086/173633.

Slipher, V. M. (Jan. 1, 1917). "Nebulae". In: *Proceedings of the American Philosophical Society* 56, pp. 403–409.

Smith M., D. (2012). *Astrophysical Jets and Beams*. Cambridge Astrophysics Series; 49. 71 pp.

Smith, F. G. (Sept. 1951). "An Accurate Determination of the Positions of Four Radio Stars". In: *Nature* 168.4274, pp. 555–555. ISSN: 0028-0836, 1476-4687. DOI: 10.1038/168555a0.

Sokolovsky K., V. et al. (2011). "A VLBA survey of the core shift effect in AGN jets I. Evidence of dominating synchrotron opacity". In: *A&A* 532, A38.

Szostek, A. (2011). "Fermi-LAT detection of a new GeV flare from blazar PKS 1424-41". In: *ATel #3329*.

Tammi, J. and M. Oksman (2013). "Bottom-up modelling of active galactic nuclei: Using radio observations to understand gamma-ray flaring in relativistic jets from supermassive blackholes". In: *XXXII Finnish URSI Convention on Radio Science and SMARAD Seminar 2013*.

Tavani, M. et al. (Aug. 1, 2009). "The AGILE Mission". In: *Astronomy and Astrophysics* 502, pp. 995–1013. ISSN: 0004-6361. DOI: 10.1051/0004-6361/200810527.

Tavecchio, F. et al. (Oct. 11, 2013). "The far emission region of the gamma-ray blazar PKS B1424–418". In: *Monthly Notices of the Royal Astronomical Society: Letters* 435.1, pp. L24–L28. ISSN: 1745-3933, 1745-3925. DOI: 10.1093/mnrasl/slt087.

The EHT MWL Science Working Group et al. (Apr. 2021). "Broadband Multi-wavelength Properties of M87 during the 2017 Event Horizon Telescope Campaign".

In: *The Astrophysical Journal Letters* 911.1. Publisher: The American Astronomical Society, p. L11. DOI: 10.3847/2041-8213/abef71.

Thompson, A. Richard (Jan. 1, 1999). "Fundamentals of Radio Interferometry". In: 180, p. 11.

Thompson, A. Richard, James M. Moran, and George W. Swenson (2017). *Interferometry and Synthesis in Radio Astronomy.* Astronomy and Astrophysics Library. Cham: Springer International Publishing. ISBN: 978-3-319-44429-1 978-3-319-44431-4.

Thompson, D. J., S. Djorgovski, and R. de Carvalho (Nov. 1990). "Spectroscopy of Radio Sources from the Parkes 2700 MHz Survey". In: *PASP* 102, p. 1235. DOI: 10.1086/132758.

Thompson, David J. (2015). "Space detectors for gamma rays (100 MeV–100 GeV): From EGRET to Fermi LAT". In: *Comptes Rendus Physique* 16.6, pp. 600–609. ISSN: 1631-0705. DOI: https://doi.org/10.1016/j.crhy.2015.07.002.

Urry C., M. and P. Padovani (1995). "Unified schemes for radio-loud active galactic nuclei". In: *P.A.S.P* 107, pp. 803–845.

Ursi, A. et al. (Jan. 24, 2018). "AGILE observations of gamma-ray emission from the blazar PKS B1424-418". In: *ATel* #11222, p. 1.

Van Zyl, P.V. (Jan. 4, 2016). "Radio emission from gamma-ray flare sources discovered by Fermi-LAT". PhD thesis. Johannesburg: University of the Witwatersrand.

Velleman, Paul F. and David C. Hoaglin (1981). *Applications, basics, and computing of exploratory data analysis.* Boston, Mass: Duxbury Press. 354 pp. ISBN: 978-0-87150-409-8 978-0-87872-273-0.

Wallace, Dolores R. and Roger U. Fujii (Jan. 15, 2002). "Verification and Validation". In: *Encyclopedia of Software Engineering.* Ed. by John J. Marciniak. Hoboken, NJ, USA: John Wiley & Sons, Inc., sof372. ISBN: 978-0-471-02895-6.

White G., L. et al. (1988). "Redshifts of southern radio sources VII". In: *ApJ* 327, pp. 561–569.

Wilson L., Thomas, Kristen Rohlfs, and Susanne Hüttemeister (2013). *Tools of radio astronomy.* New York: Springer. ISBN: 978-3-642-39949-7.

Witt, A. de et al. (Aug. 2013). "An Overview of Geodetic and Astrometric VLBI at the Hartebeesthoek Radio Astronomy Observatory". In: *21st Meeting of the European VLBI Group for Geodesy and Astronomy*, pp. 45–48.

Wood, M. et al. (Jan. 2017). "Fermipy: An open-source Python package for analysis of Fermi-LAT Data". In: *35th International Cosmic Ray Conference (ICRC2017).* Vol. 301. International Cosmic Ray Conference, p. 824.

Xue, Rui et al. (Nov. 15, 2019). "A Two-zone Model for Blazar Emission: Implications for TXS 0506+056 and the Neutrino Event IceCube-170922A". In: *ApJ* 886.1, p. 23. ISSN: 1538-4357. DOI: 10.3847/1538-4357/ab4b44.

Zerbi, Filippo M. et al. (Mar. 2003). "REM telescope, a robotic facility to monitor the prompt afterglow of Gamma Ray Bursts". In: *Instrument Design and Performance for Optical/Infrared Ground-based Telescopes*. Ed. by Masanori Iye and Alan F. M. Moorwood. Vol. 4841. Society of Photo-Optical Instrumentation Engineers (SPIE) Conference Series, pp. 737–748. DOI: 10.1117/12.459511.

Supplementary radio information.

1 HartRAO receiver types

1.1 Total power receiver

Total power receivers (see Figure 2.4) measure the total, time-averaged power of the input noise from the radio telescope over a well-defined RF. The noise voltage is converted to noise power using a Square-Law detector following the equation

$$\langle \mathrm{P} \rangle = \int_{t-\tau/2}^{t+\tau/2} p_d[t]dt \propto \int_{t-\tau/2}^{t+\tau/2} [v_o(t)]^2 dt \tag{1}$$

where P = power output, τ = time average, $p_d[t]$ = instantaneously measured power by the detector and $v_o[t]$ = amplitude output. Gains in the receiver are assumed to remain constant throughout the observation. However, this can be affected by random fluctuations in ambient temperature or bending RF cables as the telescope moves, ultimately affecting the output power of the system. As a result, this may cause a severe drop in the receiver sensitivity which degrades the data quality of the observation. To combat these gain variations noise diode calibrations are applied before each scan.

1.2 Dicke-switched receivers

The Dicke-switching technique is the technique of rapidly switching between two identical feed horns (A & B) installed next to each other on the telescope (see

Figure 1). When one feed, say feed A, is pointing at a source with an angular size smaller than the beam separation from the two feeds, then another feed, say feed B, will point off-source but measure nearly the same sample of atmosphere in the near field. Because the receiver output is multiplied by +1 when the receiver is connected to A and -1 when it is connected to B, any fluctuations in atmospheric emission and drifts due to changes in receiver gain are canceled out for frequencies below the switching rate. HartRAO 26-m radio telescope switches between the beams at a switching rate of 50 Hz. Atmospheric contributions can severely degrade a source signal which is already a weak radio signal, hence this method is particularly useful for frequencies higher than $\sim$ 5 GHz where atmospheric contributions from water vapor become a problem. The Hart26m has dicke switched receivers for the 4.8 GHz and 8.4 GHz receivers.

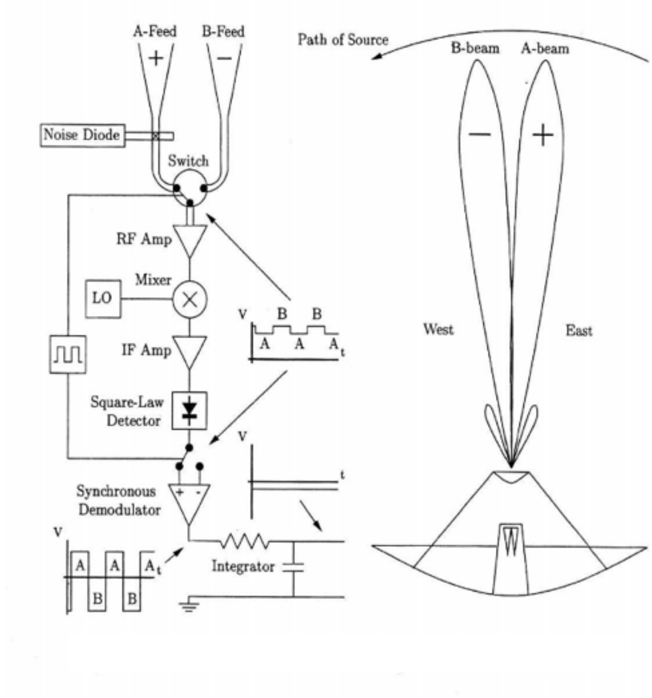

Figure 1: A reprsentation of the Dicke-switched dual-beam receiver system used at HartRAO.

1.3 HartRAO 26-m radio telescope receiver specifications table

Band	13cm	6cm	3.5cm	2.5cm	1.3cm
Feed horns	1 x circular	2 x circular[1]	2 x circular	1 x circular	1 x circular
Polarization	LCP & RCP	LCP & RCP	LCP & RCP	LCP & RCP	LCP & RCP
Amplifier	cryogenic HEMT	cryogenic HEMT	cryogenic HEMT	uncooled PHEMT	cryogenic HEMT
Central frequency (GHz)	2.3	4.8	8.3	12.2	22.04
Lower frequency limit (MHz)	2120	4650	8180	12020	23000
Upper frequency limit (MHz)	2450	5220	8630	12419	22040
Detector bandwidth (MHz)	400	400	400	400	-
Receiver bandwidth (MHz)[2]	160	300	400	400	2000
Beam-width: full width at half max, HPBW (degrees)	0.332	0.160	0.092	0.059	0.033
Beam-width: between first nulls (degrees)	0.80	0.36	0.23	0.16	0.073
Minimum system temperature at Zenith (K)	36	55	50	100[3]	45
Point Source Sensitivity[4] per polarization (Jy/K/Pol)	4.8	6.0	6.1	5.8	10.5[5]

Table 1: The HartRAO 26-m radio telescope receiver specifications[b] for the frequencies expressed in this study. Where *1*: The 6 and 3.5 cm receivers each have two feeds aligned East-West to permit Dicke-switching. *2*: For radiometry, the IF signal can be used unfiltered, or passed through 4, 8, 16, or 32 MHz bandwidth filters to control the bandwidth or exclude RFI signals. Maximum bandwidth is not necessarily usable. At 18cm 16 MHz bandwidth is typically usable, and 32 MHz at 13cm, owing to RFI. The detectors in the radiometers have a 3dB bandwidth of about 450 MHz. The effective response of the receiver-radiometer system at 6 cm is 4840 - 5100 MHz, i.e. 260 MHz bandwidth centered on 4970 MHz. At 3.5 cm the effective radiometry center frequency is 8400 MHz. *3*: Measured at zenith, 2013-03-03, atmospheric Precipitable Water Vapour ~20 mm. *4*: Measured after antenna surface upgrade was completed in 2004. *5*: Cryogenic 22-GHz receiver installed May 2014. Tsys measured at zenith, 2014-05-28, with estimated PWV ~11mm so atmospheric noise contribution about 25K. The receiver moved on axis, but aperture efficiency/point source sensitivity was not yet measured and the value for the uncooled receiver was retained.

[b] http://www.hartrao.ac.za/hh26m_factsfile.html

Comparison tables

The tables below contain the results obtained from fitting the data. A discussion on how they were obtained can be found in §7.4.

Table 1: LCP DRAN manual fitting baseline and peak fitting selections for the software comparison test. Filename is the name of the observing file of the drift scan in the format YYYYdDDD_HHhMMmSSs. Pol is the polarization. Base_locs and Peak_locs are the baseline and peak block locations used to fit the data respectively. M and C are the slope and y-intercept of the baseline fit. Y_max is the maximum of the fit and Rms and Y_rms are the rms of the baseline and peak fit respectively.

Filename	Pol	Base_locs	M	C	Rms	Peak_locs	Y_max	Y_rms
2013d003_23h24m18s	ON_LCP	-0.42, -0.377, 0.403, 0.443	0.051	0.016	0.041	-0.039, 0.087	2.516	0.045
2013d008_00h04m19s	ON_LCP	-0.433, -0.374, 0.383, 0.438	0.067	-0.045	0.032	-0.049, 0.072	2.477	0.034
2013d006_23h03m09s	ON_LCP	-0.414, -0.37, 0.358, 0.384	0.321	0.109	0.063	-0.056, 0.139	2.399	0.065
2013d025_21h46m50s	ON_LCP	-0.429, -0.377, 0.388, 0.45	0.037	0.048	0.055	-0.052, 0.082	2.415	0.071
2013d027_21h35m21s	ON_LCP	-0.343, -0.303, 0.4, 0.418	-0.518	-0.519	0.068	-0.067, 0.131	2.553	0.142
2013d035_21h55m12s	ON_LCP	-0.4, -0.35, 0.373, 0.383	-0.019	0.004	0.046	-0.05, 0.093	2.428	0.056
2013d054_20h03m24s	ON_LCP	-0.44, -0.395, 0.425, 0.458	-0.012	-0.060	0.053	-0.069, 0.098	2.626	0.073
2013d056_20h55m03s	ON_LCP	-0.446, -0.407, 0.396, 0.453	0.035	-0.033	0.033	-0.036, 0.071	2.492	0.032
2013d066_19h25m44s	ON_LCP	-0.44, -0.4, 0.411, 0.447	0.033	-0.066	0.032	-0.038, 0.06	2.515	0.036
2013d069_18h55m23s	ON_LCP	-0.453, -0.386, 0.397, 0.443	0.042	0.022	0.039	-0.043, 0.093	2.470	0.045
2013d082_19h20m32s	ON_LCP	-0.436, -0.361, 0.391, 0.436	-0.090	-0.063	0.036	-0.035, 0.068	2.604	0.034
2013d098_17h10m38s	ON_LCP	-0.428, -0.368, 0.376, 0.428	0.035	0.004	0.041	-0.035, 0.094	2.333	0.062
2013d109_16h17m52s	ON_LCP	-0.421, -0.358, 0.391, 0.447	0.030	0.036	0.037	-0.038, 0.111	2.469	0.036
2013d115_16h05m59s	ON_LCP	-0.431, -0.381, 0.391, 0.442	0.009	-0.022	0.031	-0.042, 0.101	2.461	0.037
2013d116_16h00m04s	ON_LCP	-0.394, -0.35, 0.403, 0.443	0.066	0.063	0.051	-0.028, 0.135	2.494	0.061
2013d121_15h37m53s	ON_LCP	-0.431, -0.376, 0.406, 0.438	0.261	-0.058	0.061	-0.043, 0.108	2.475	0.067
2013d125_15h23m40s	ON_LCP	-0.376, -0.339, 0.405, 0.441	0.320	0.087	0.034	-0.045, 0.115	2.412	0.118
2013d136_14h27m49s	ON_LCP	-0.438, -0.394, 0.396, 0.436	0.028	0.011	0.031	-0.065, 0.052	2.428	0.033
2013d139_14h28m45s	ON_LCP	-0.451, -0.402, 0.387, 0.447	0.047	0.059	0.034	-0.079, 0.041	2.468	0.034
2013d146_13h51m17s	ON_LCP	-0.439, -0.373, 0.351, 0.392	0.023	-0.059	0.036	-0.08, 0.043	2.378	0.037
2013d152_13h35m38s	ON_LCP	-0.453, -0.394, 0.366, 0.409	0.024	0.015	0.053	-0.089, 0.06	2.454	0.042
2013d167_12h43m42s	ON_LCP	-0.422, -0.384, 0.388, 0.422	0.020	-0.025	0.033	-0.082, 0.056	2.441	0.033
2013d179_12h22m45s	ON_LCP	-0.432, -0.383, 0.387, 0.433	-0.054	-0.042	0.032	-0.079, 0.046	2.447	0.031
2013d185_11h36m09s	ON_LCP	-0.423, -0.383, 0.395, 0.442	0.083	-0.003	0.034	-0.113, 0.098	2.561	0.033
2013d186_11h54m18s	ON_LCP	-0.443, -0.399, 0.348, 0.406	0.052	0.021	0.032	-0.087, 0.036	2.421	0.032
2013d197_11h37m58s	ON_LCP	-0.429, -0.37, 0.373, 0.418	-0.021	-0.056	0.035	-0.069, 0.053	2.331	0.034
2013d202_10h09m44s	ON_LCP	-0.432, -0.359, 0.381, 0.428	-0.041	-0.019	0.031	-0.068, 0.049	2.382	0.032
2013d214_09h38m34s	ON_LCP	-0.433, -0.373, 0.361, 0.432	-0.104	-0.009	0.035	-0.075, 0.061	2.427	0.039
2013d217_11h22m10s	ON_LCP	-0.431, -0.389, 0.383, 0.432	0.067	0.031	0.045	-0.078, 0.041	2.423	0.044
2013d229_08h25m47s	ON_LCP	-0.433, -0.399, 0.384, 0.435	0.306	0.101	0.034	-0.063, 0.05	2.421	0.037

Table 2: RCP DRAN manual fitting baseline and peak fitting selections for the software comparison test. Filename is the name of the observing file of the drift scan in the format YYYYdDDD__HHhMMmSSs. Pol is the polarization. Base__locs and Peak__locs are the baseline and peak block locations used to fit the data respectively. M and C are the slope and y-intercept of the baseline fit. Y__max is the maximum of the fit and Rms and Y__rms are the rms of the baseline and peak fit respectively.

Filename	Pol	Base__locs	M	C	Rms	Peak__locs	Y__max	Y__rms
2013d003__23h24m18s	ON__RCP	-0.442, -0.398, 0.4, 0.446	0.177	0.053	0.035	-0.046, 0.091	2.688	0.040
2013d008__00h04m19s	ON__RCP	-0.435, -0.396, 0.387, 0.443	0.090	-0.002	0.030	-0.045, 0.078	2.668	0.035
2013d006__23h03m09s	ON__RCP	-0.444, -0.384, 0.439, 0.458	2.290	1.096	0.062	-0.061, 0.122	2.952	0.063
2013d025__21h46m50s	ON__RCP	-0.429, -0.348, 0.378, 0.451	0.028	0.021	0.036	-0.043, 0.082	2.598	0.039
2013d027__21h35m21s	ON__RCP	-0.346, -0.315, 0.392, 0.431	0.081	-0.292	0.085	-0.075, 0.131	2.917	0.160
2013d035__21h55m12s	ON__RCP	-0.416, -0.361, 0.389, 0.45	0.071	0.011	0.028	-0.03, 0.06	2.653	0.030
2013d054__20h03m24s	ON__RCP	-0.438, -0.395, 0.388, 0.422	0.208	0.031	0.033	-0.06, 0.087	2.637	0.035
2013d056__20h55m03s	ON__RCP	-0.447, -0.406, 0.373, 0.417	0.082	-0.012	0.030	-0.058, 0.089	2.672	0.039
2013d066__19h25m44s	ON__RCP	-0.439, -0.4, 0.392, 0.444	0.107	0.075	0.031	-0.035, 0.084	2.760	0.037
2013d069__18h55m23s	ON__RCP	-0.427, -0.369, 0.412, 0.446	0.034	-0.035	0.032	-0.041, 0.075	2.683	0.032
2013d082__19h20m32s	ON__RCP	-0.432, -0.399, 0.372, 0.441	0.087	-0.028	0.038	-0.045, 0.082	2.649	0.033
2013d098__17h10m38s	ON__RCP	-0.438, -0.383, 0.401, 0.445	0.237	0.087	0.034	-0.042, 0.093	2.662	0.038
2013d109__16h17m52s	ON__RCP	-0.438, -0.37, 0.414, 0.45	0.134	0.061	0.034	-0.031, 0.109	2.646	0.038
2013d115__16h05m59s	ON__RCP	-0.441, -0.388, 0.409, 0.447	0.138	-0.013	0.036	-0.045, 0.089	2.726	0.034
2013d116__16h00m04s	ON__RCP	-0.387, -0.31, 0.403, 0.45	3.449	1.108	0.069	-0.075, 0.113	4.132	0.041
2013d121__15h37m53s	ON__RCP	-0.438, -0.357, 0.406, 0.435	0.058	0.017	0.035	-0.031, 0.086	2.619	0.038
2013d125__15h23m40s	ON__RCP	-0.436, -0.376, 0.395, 0.436	0.206	0.041	0.031	-0.046, 0.078	2.579	0.033
2013d136__14h27m49s	ON__RCP	-0.446, -0.403, 0.399, 0.438	-0.108	-0.052	0.028	-0.078, 0.056	2.951	0.034
2013d139__14h28m45s	ON__RCP	-0.449, -0.402, 0.392, 0.42	-0.017	-0.055	0.036	-0.08, 0.042	2.680	0.032
2013d146__13h51m17s	ON__RCP	-0.443, -0.399, 0.398, 0.442	0.145	-0.012	0.028	-0.073, 0.05	2.596	0.034
2013d152__13h35m38s	ON__RCP	-0.447, -0.389, 0.392, 0.44	0.264	0.062	0.033	-0.08, 0.042	2.630	0.035
2013d167__12h43m42s	ON__RCP	-0.436, -0.396, 0.38, 0.435	0.169	0.037	0.030	-0.068, 0.043	2.661	0.033
2013d179__12h22m45s	ON__RCP	-0.444, -0.385, 0.354, 0.398	0.020	0.038	0.031	-0.078, 0.034	2.598	0.034
2013d185__11h36m09s	ON__RCP	-0.423, -0.381, 0.373, 0.439	-0.144	-0.141	0.036	-0.105, 0.069	2.610	0.039
2013d186__11h54m18s	ON__RCP	-0.429, -0.388, 0.373, 0.42	0.365	0.146	0.030	-0.069, 0.042	2.523	0.037
2013d197__11h37m58s	ON__RCP	-0.435, -0.389, 0.366, 0.414	-0.227	-0.138	0.035	-0.08, 0.047	2.692	0.039
2013d202__10h09m44s	ON__RCP	-0.447, -0.399, 0.387, 0.427	0.158	0.038	0.031	-0.065, 0.031	2.624	0.036
2013d214__09h38m34s	ON__RCP	-0.444, -0.4, 0.383, 0.435	0.132	-0.027	0.035	-0.054, 0.057	2.668	0.042
2013d217__11h22m10s	ON__RCP	-0.455, -0.403, 0.373, 0.413	0.040	-0.008	0.034	-0.091, 0.038	2.637	0.035
2013d229__08h25m47s	ON__RCP	-0.444, -0.395, 0.384, 0.435	0.318	0.102	0.032	-0.084, 0.058	2.673	0.046

Table 3: LCP LINES manual fitting baseline and peak fitting selections for the software comparison test. Filename is the name of the observing file of the drift scan in the format YYYYdDDD_HHhMMmSSs. Pol is the polarization. Base_locs and Peak_locs are the baseline and peak block locations used to fit the data respectively. M and C are the slope and y-intercept of the baseline fit. Y_max is the maximum of the fit and Rms and Y_rms are the rms of the baseline and peak fit respectively.

Filename	Pol	Base_locs	M	C	Rms	Peak_locs	Y_max	Y_rms
2013d003_23h24m18s	ON_LCP	-0.42, -0.377, 0.403, 0.443	0.016	0.051	0.041	-0.039, 0.087	2.516	0.046
2013d008_00h04m19s	ON_LCP	-0.433, -0.374, 0.383, 0.438	-0.045	0.067	0.032	-0.049, 0.072	2.476	0.034
2013d006_23h03m09s	ON_LCP	-0.414, -0.37, 0.358, 0.384	0.111	0.327	0.066	-0.056, 0.139	2.415	0.047
2013d025_21h46m50s	ON_LCP	-0.429, -0.377, 0.388, 0.45	0.029	-0.011	0.062	-0.052, 0.082	2.435	0.071
2013d027_21h35m21s	ON_LCP	-0.343, -0.303, 0.4, 0.418	-0.518	-0.514	0.069	-0.067, 0.131	2.587	0.083
2013d035_21h55m12s	ON_LCP	-0.4, -0.35, 0.373, 0.383	0.005	-0.016	0.047	-0.05, 0.093	2.427	0.057
2013d054_20h03m24s	ON_LCP	-0.44, -0.395, 0.425, 0.458	-0.060	-0.012	0.053	-0.069, 0.098	2.623	0.075
2013d056_20h55m03s	ON_LCP	-0.446, -0.407, 0.396, 0.453	-0.034	0.035	0.034	-0.036, 0.071	2.492	0.033
2013d066_19h25m44s	ON_LCP	-0.44, -0.4, 0.411, 0.447	-0.066	0.032	0.032	-0.038, 0.06	2.515	0.036
2013d069_18h55m23s	ON_LCP	-0.453, -0.386, 0.397, 0.443	0.024	0.042	0.041	-0.043, 0.093	2.468	0.048
2013d082_19h20m32s	ON_LCP	-0.436, -0.361, 0.391, 0.436	-0.064	-0.090	0.036	-0.035, 0.068	2.605	0.036
2013d098_17h10m38s	ON_LCP	-0.428, -0.368, 0.376, 0.428	0.004	0.035	0.041	-0.035, 0.094	2.327	0.078
2013d109_16h17m52s	ON_LCP	-0.421, -0.358, 0.391, 0.447	0.036	0.032	0.038	-0.038, 0.111	2.468	0.037
2013d115_16h05m59s	ON_LCP	-0.431, -0.381, 0.391, 0.442	-0.022	0.010	0.030	-0.042, 0.101	2.461	0.039
2013d116_16h00m04s	ON_LCP	-0.394, -0.35, 0.403, 0.443	0.063	0.066	0.051	-0.028, 0.135	2.494	0.063
2013d121_15h37m53s	ON_LCP	-0.431, -0.376, 0.406, 0.438	-0.059	0.262	0.062	-0.043, 0.108	2.472	0.074
2013d125_15h23m40s	ON_LCP	-0.376, -0.339, 0.405, 0.441	0.086	0.321	0.034	-0.045, 0.115	2.410	0.122
2013d136_14h27m49s	ON_LCP	-0.438, -0.394, 0.396, 0.436	0.010	0.027	0.033	-0.065, 0.052	2.429	0.033
2013d139_14h28m45s	ON_LCP	-0.451, -0.402, 0.387, 0.447	0.059	0.046	0.034	-0.079, 0.041	2.468	0.035
2013d146_13h51m17s	ON_LCP	-0.439, -0.373, 0.351, 0.392	-0.058	0.024	0.037	-0.08, 0.043	2.377	0.040
2013d152_13h35m38s	ON_LCP	-0.453, -0.394, 0.366, 0.409	0.011	0.015	0.056	-0.089, 0.06	2.457	0.043
2013d167_12h43m42s	ON_LCP	-0.422, -0.384, 0.388, 0.422	-0.026	0.021	0.033	-0.082, 0.056	2.441	0.034
2013d179_12h22m45s	ON_LCP	-0.432, -0.383, 0.387, 0.433	-0.042	-0.055	0.032	-0.079, 0.046	2.446	0.032
2013d185_11h36m09s	ON_LCP	-0.424, -0.383, 0.395, 0.442	-0.001	0.080	0.036	-0.113, 0.098	2.560	0.001
2013d186_11h54m18s	ON_LCP	-0.443, -0.399, 0.348, 0.406	0.022	0.051	0.032	-0.087, 0.036	2.419	0.033
2013d197_11h37m58s	ON_LCP	-0.429, -0.37, 0.373, 0.418	-0.057	-0.021	0.036	-0.069, 0.053	2.347	0.057
2013d202_10h09m44s	ON_LCP	-0.432, -0.359, 0.381, 0.428	-0.018	-0.040	0.032	-0.068, 0.049	2.382	0.033
2013d214_09h38m34s	ON_LCP	-0.433, -0.373, 0.361, 0.432	-0.009	-0.104	0.035	-0.075, 0.061	2.427	0.040
2013d217_11h22m10s	ON_LCP	-0.431, -0.389, 0.383, 0.432	0.028	0.071	0.051	-0.078, 0.041	2.426	0.044
2013d229_08h25m47s	ON_LCP	-0.433, -0.399, 0.384, 0.435	0.101	0.306	0.034	-0.063, 0.05	2.420	0.038

Table 4: RCP LINES manual fitting baseline and peak fitting selections for the software comparison test. Filename is the name of the observing file of the drift scan in the format YYYYdDDD_HHhMMmSSs. Pol is the polarization. Base_locs and Peak_locs are the baseline and peak block locations used to fit the data respectively. M and C are the slope and y-intercept of the baseline fit. Y_max is the maximum of the fit and Rms and Y_rms are the rms of the baseline and peak fit respectively.

Filename	Pol	Base_locs	M	C	Rms	Peak_locs	Y_max	Y_rms
2013d003_23h24m18s	ON_RCP	-0.442, -0.398, 0.4, 0.446	0.054	0.178	0.035	-0.046, 0.091	2.688	0.042
2013d008_00h04m19s	ON_RCP	-0.435, -0.396, 0.387, 0.443	-0.003	0.090	0.030	-0.045, 0.078	2.668	0.035
2013d006_23h03m09s	ON_RCP	-0.444, -0.384, 0.439, 0.461	1.102	2.301	0.067	-0.061, 0.122	2.941	0.073
2013d025_21h46m50s	ON_RCP	-0.429, -0.348, 0.378, 0.451	0.021	0.028	0.036	-0.043, 0.082	2.597	0.040
2013d027_21h35m21s	ON_RCP	-0.346, -0.315, 0.392, 0.431	-0.293	0.079	0.084	-0.075, 0.131	2.952	0.084
2013d035_21h55m12s	ON_RCP	-0.416, -0.361, 0.389, 0.45	0.011	0.071	0.028	-0.03, 0.06	2.652	0.030
2013d054_20h03m24s	ON_RCP	-0.438, -0.395, 0.388, 0.422	0.031	0.208	0.033	-0.06, 0.087	2.638	0.035
2013d056_20h55m03s	ON_RCP	-0.447, -0.406, 0.373, 0.417	-0.011	0.082	0.031	-0.058, 0.089	2.672	0.041
2013d066_19h25m44s	ON_RCP	-0.439, -0.4, 0.392, 0.444	0.074	0.109	0.032	-0.035, 0.084	2.759	0.039
2013d069_18h55m23s	ON_RCP	-0.427, -0.369, 0.412, 0.446	-0.035	0.035	0.032	-0.041, 0.075	2.683	0.033
2013d082_19h20m32s	ON_RCP	-0.432, -0.399, 0.372, 0.441	-0.028	0.088	0.039	-0.045, 0.082	2.649	0.033
2013d098_17h10m38s	ON_RCP	-0.438, -0.383, 0.401, 0.445	0.086	0.236	0.035	-0.042, 0.093	2.661	0.040
2013d109_16h17m52s	ON_RCP	-0.438, -0.37, 0.414, 0.45	0.062	0.134	0.034	-0.031, 0.109	2.646	0.038
2013d115_16h05m59s	ON_RCP	-0.441, -0.388, 0.409, 0.447	-0.013	0.138	0.037	-0.045, 0.089	2.726	0.034
2013d116_16h00m04s	ON_RCP	-0.387, -0.31, 0.403, 0.45	1.108	3.447	0.070	-0.075, 0.113	4.132	0.041
2013d121_15h37m53s	ON_RCP	-0.438, -0.357, 0.406, 0.435	0.017	0.057	0.036	-0.031, 0.086	2.637	0.038
2013d125_15h23m40s	ON_RCP	-0.436, -0.376, 0.395, 0.436	0.041	0.206	0.031	-0.046, 0.078	2.579	0.033
2013d136_14h27m49s	ON_RCP	-0.446, -0.403, 0.399, 0.438	-0.052	-0.107	0.029	-0.078, 0.056	2.951	0.034
2013d139_14h28m45s	ON_RCP	-0.449, -0.402, 0.392, 0.42	-0.055	-0.019	0.037	-0.08, 0.042	2.681	0.033
2013d146_13h51m17s	ON_RCP	-0.443, -0.399, 0.398, 0.442	-0.011	0.144	0.030	-0.073, 0.05	2.595	0.035
2013d152_13h35m38s	ON_RCP	-0.447, -0.389, 0.392, 0.44	0.063	0.263	0.033	-0.08, 0.042	2.630	0.035
2013d167_12h43m42s	ON_RCP	-0.436, -0.396, 0.38, 0.435	0.037	0.169	0.030	-0.068, 0.043	2.661	0.033
2013d179_12h22m45s	ON_RCP	-0.444, -0.385, 0.354, 0.398	0.038	0.020	0.031	-0.078, 0.034	2.598	0.034
2013d185_11h36m09s	ON_RCP	-0.423, -0.381, 0.373, 0.439	-0.141	-0.143	0.036	-0.105, 0.069	2.611	0.040
2013d186_11h54m18s	ON_RCP	-0.429, -0.388, 0.373, 0.42	0.146	0.366	0.032	-0.069, 0.042	2.523	0.037
2013d197_11h37m58s	ON_RCP	-0.435, -0.389, 0.366, 0.414	-0.138	-0.225	0.035	-0.08, 0.047	2.703	0.059
2013d202_10h09m44s	ON_RCP	-0.447, -0.399, 0.387, 0.427	0.037	0.157	0.031	-0.065, 0.031	2.624	0.037
2013d214_09h38m34s	ON_RCP	-0.444, -0.4, 0.383, 0.435	-0.027	0.131	0.035	-0.054, 0.057	2.670	0.043
2013d217_11h22m10s	ON_RCP	-0.455, -0.403, 0.373, 0.413	-0.008	0.040	0.035	-0.091, 0.038	2.636	0.036
2013d229_08h25m47s	ON_RCP	-0.444, -0.395, 0.384, 0.435	0.103	0.317	0.032	-0.084, 0.058	2.680	0.055

Table 5: LCP DRAN theoretical fit baseline and peak fitting selections for the software comparison test. Filename is the name of the observing file of the drift scan in the format YYYYdDDD_HHhMMmSSs. Pol is the polarization. Base_locs and Peak_locs are the baseline and peak block locations used to fit the data respectively. M and C are the slope and y-intercept of the baseline fit. Y_max is the maximum of the fit and Rms and Y_rms are the rms of the baseline and peak fit respectively.

Filename	Pol	Base_locs	M	C	Rms	Peak_locs	Y_max	Y_rms
2013d003_23h24m18s	ON_LCP	-0.459, -0.4, 0.4, 0.459	0.039	0.018	0.043	-0.101, 0.139	2.501	0.046
2013d006_23h03m09s	ON_LCP	-0.459, -0.4, 0.4, 0.459	0.357	0.144	0.078	-0.107, 0.145	2.353	0.065
2013d008_00h04m19s	ON_LCP	-0.459, -0.4, 0.4, 0.459	0.044	-0.038	0.034	-0.11, 0.134	2.464	0.034
2013d025_21h46m50s	ON_LCP	-0.459, -0.4, 0.4, 0.459	0.010	0.064	0.055	-0.105, 0.142	2.377	0.070
2013d027_21h35m21s	ON_LCP	-0.459, -0.4, 0.4, 0.459	-0.431	-0.310	0.225	-0.063, 0.128	2.336	0.143
2013d035_21h55m12s	ON_LCP	-0.459, -0.4, 0.4, 0.459	-0.023	0.036	0.051	-0.101, 0.14	2.391	0.054
2013d054_20h03m24s	ON_LCP	-0.459, -0.4, 0.4, 0.459	0.032	-0.038	0.071	-0.105, 0.148	2.612	0.078
2013d056_20h55m03s	ON_LCP	-0.459, -0.4, 0.4, 0.459	0.031	-0.032	0.033	-0.105, 0.141	2.475	0.035
2013d066_19h25m44s	ON_LCP	-0.459, -0.4, 0.4, 0.459	0.027	-0.060	0.034	-0.096, 0.144	2.498	0.038
2013d069_18h55m23s	ON_LCP	-0.459, -0.4, 0.4, 0.459	0.027	0.021	0.040	-0.095, 0.148	2.463	0.044
2013d082_19h20m32s	ON_LCP	-0.459, -0.4, 0.4, 0.459	-0.065	-0.067	0.033	-0.102, 0.138	2.595	0.038
2013d098_17h10m38s	ON_LCP	-0.459, -0.4, 0.4, 0.459	0.053	0.020	0.049	-0.095, 0.13	2.312	0.083
2013d109_16h17m52s	ON_LCP	-0.459, -0.4, 0.4, 0.459	0.015	0.037	0.037	-0.096, 0.153	2.451	0.038
2013d115_16h05m59s	ON_LCP	-0.459, -0.4, 0.4, 0.459	-0.014	-0.018	0.032	-0.093, 0.148	2.445	0.038
2013d116_16h00m04s	ON_LCP	-0.459, -0.4, 0.4, 0.459	0.040	0.074	0.053	-0.088, 0.142	2.465	0.067
2013d121_15h37m53s	ON_LCP	-0.459, -0.4, 0.4, 0.459	0.243	-0.044	0.069	-0.094, 0.152	2.446	0.069
2013d125_15h23m40s	ON_LCP	-0.459, -0.4, 0.4, 0.459	0.221	0.127	0.055	-0.099, 0.156	2.343	0.114
2013d136_14h27m49s	ON_LCP	-0.459, -0.4, 0.4, 0.459	0.015	0.014	0.033	-0.131, 0.111	2.412	0.035
2013d139_14h28m45s	ON_LCP	-0.459, -0.4, 0.4, 0.459	0.049	0.063	0.035	-0.131, 0.114	2.443	0.037
2013d146_13h51m17s	ON_LCP	-0.459, -0.4, 0.4, 0.459	0.067	-0.044	0.034	-0.134, 0.108	2.352	0.038
2013d152_13h35m38s	ON_LCP	-0.459, -0.4, 0.4, 0.459	0.061	0.027	0.047	-0.133, 0.11	2.434	0.045
2013d167_12h43m42s	ON_LCP	-0.459, -0.4, 0.4, 0.459	0.024	-0.012	0.035	-0.14, 0.104	2.411	0.039
2013d179_12h22m45s	ON_LCP	-0.459, -0.4, 0.4, 0.459	-0.055	-0.033	0.031	-0.133, 0.11	2.433	0.033
2013d185_11h36m09s	ON_LCP	-0.459, -0.4, 0.4, 0.459	0.092	-0.009	0.032	-0.136, 0.115	2.564	0.034
2013d186_11h54m18s	ON_LCP	-0.459, -0.4, 0.4, 0.459	0.082	0.039	0.034	-0.14, 0.103	2.386	0.036
2013d197_11h37m58s	ON_LCP	-0.459, -0.4, 0.4, 0.459	-0.003	-0.037	0.037	-0.135, 0.104	2.302	0.035
2013d202_10h09m44s	ON_LCP	-0.459, -0.4, 0.4, 0.459	-0.025	-0.014	0.031	-0.131, 0.111	2.368	0.033
2013d214_09h38m34s	ON_LCP	-0.459, -0.4, 0.4, 0.459	-0.098	-0.003	0.036	-0.13, 0.112	2.399	0.042
2013d217_11h22m10s	ON_LCP	-0.459, -0.4, 0.4, 0.459	0.081	0.044	0.041	-0.143, 0.099	2.399	0.042
2013d229_08h25m47s	ON_LCP	-0.459, -0.4, 0.4, 0.459	0.303	0.109	0.036	-0.131, 0.109	2.403	0.041

Table 6: RCP DRAN theoretical fit baseline and peak fitting selections for the software comparison test. Filename is the name of the observing file of the drift scan in the format YYYYdDDD__HHhMMmSSs. Pol is the polarization. Base__locs and Peak__locs are the baseline and peak block locations used to fit the data respectively. M and C are the slope and y-intercept of the baseline fit. Y__max is the maximum of the fit and Rms and Y__rms are the rms of the baseline and peak fit respectively.

Filename	Pol	Base__locs	M	C	Rms	Peak__locs	Y__max	Y__rms
2013d003__23h24m18s	ON__RCP	-0.459, -0.4, 0.4, 0.459	0.163	0.061	0.036	-0.104, 0.144	2.669	0.040
2013d006__23h03m09s	ON__RCP	-0.459, -0.4, 0.4, 0.458	2.380	1.166	0.109	-0.116, 0.141	2.886	0.060
2013d008__00h04m19s	ON__RCP	-0.459, -0.4, 0.4, 0.459	0.085	0.002	0.032	-0.114, 0.128	2.654	0.035
2013d025__21h46m50s	ON__RCP	-0.459, -0.4, 0.4, 0.459	0.030	0.023	0.037	-0.108, 0.135	2.584	0.043
2013d027__21h35m21s	ON__RCP	-0.459, -0.4, 0.4, 0.459	0.147	-0.124	0.221	-0.087, 0.118	2.766	0.167
2013d035__21h55m12s	ON__RCP	-0.459, -0.4, 0.4, 0.459	0.050	0.025	0.030	-0.109, 0.137	2.627	0.032
2013d054__20h03m24s	ON__RCP	-0.459, -0.4, 0.4, 0.459	0.205	0.041	0.034	-0.105, 0.14	2.620	0.035
2013d056__20h55m03s	ON__RCP	-0.459, -0.4, 0.4, 0.459	0.106	0.001	0.034	-0.105, 0.136	2.659	0.038
2013d066__19h25m44s	ON__RCP	-0.459, -0.4, 0.4, 0.459	0.100	0.077	0.031	-0.1, 0.14	2.737	0.039
2013d069__18h55m23s	ON__RCP	-0.459, -0.4, 0.4, 0.459	0.016	-0.023	0.033	-0.101, 0.144	2.661	0.035
2013d082__19h20m32s	ON__RCP	-0.459, -0.4, 0.4, 0.459	0.097	-0.013	0.035	-0.104, 0.137	2.623	0.034
2013d098__17h10m38s	ON__RCP	-0.459, -0.4, 0.4, 0.459	0.214	0.093	0.033	-0.098, 0.147	2.645	0.039
2013d109__16h17m52s	ON__RCP	-0.459, -0.4, 0.4, 0.459	0.142	0.067	0.034	-0.101, 0.149	2.634	0.040
2013d115__16h05m59s	ON__RCP	-0.459, -0.4, 0.4, 0.459	0.119	-0.006	0.037	-0.097, 0.146	2.716	0.036
2013d116__16h00m04s	ON__RCP	-0.459, -0.4, 0.4, 0.459	3.002	1.294	0.098	-0.153, 0.149	3.923	0.058
2013d121__15h37m53s	ON__RCP	-0.459, -0.4, 0.4, 0.459	0.058	0.023	0.032	-0.097, 0.145	2.598	0.038
2013d125__15h23m40s	ON__RCP	-0.459, -0.4, 0.4, 0.459	0.183	0.050	0.032	-0.1, 0.146	2.565	0.032
2013d136__14h27m49s	ON__RCP	-0.459, -0.4, 0.4, 0.459	-0.101	-0.049	0.030	-0.135, 0.113	2.943	0.033
2013d139__14h28m45s	ON__RCP	-0.459, -0.4, 0.4, 0.459	-0.009	-0.046	0.036	-0.135, 0.109	2.652	0.036
2013d146__13h51m17s	ON__RCP	-0.459, -0.4, 0.4, 0.459	0.147	-0.007	0.030	-0.136, 0.107	2.586	0.034
2013d152__13h35m38s	ON__RCP	-0.459, -0.4, 0.4, 0.459	0.264	0.070	0.033	-0.137, 0.104	2.614	0.037
2013d167__12h43m42s	ON__RCP	-0.459, -0.4, 0.4, 0.459	0.159	0.042	0.032	-0.152, 0.101	2.647	0.042
2013d179__12h22m45s	ON__RCP	-0.459, -0.4, 0.4, 0.459	0.099	0.062	0.032	-0.142, 0.103	2.565	0.036
2013d185__11h36m09s	ON__RCP	-0.459, -0.4, 0.4, 0.459	-0.176	-0.121	0.047	-0.138, 0.105	2.571	0.042
2013d186__11h54m18s	ON__RCP	-0.459, -0.4, 0.4, 0.459	0.359	0.154	0.034	-0.14, 0.101	2.491	0.040
2013d197__11h37m58s	ON__RCP	-0.459, -0.4, 0.4, 0.459	-0.215	-0.132	0.034	-0.14, 0.099	2.682	0.038
2013d202__10h09m44s	ON__RCP	-0.459, -0.4, 0.4, 0.459	0.170	0.042	0.031	-0.139, 0.107	2.610	0.037
2013d214__09h38m34s	ON__RCP	-0.459, -0.4, 0.4, 0.459	0.114	-0.026	0.036	-0.135, 0.108	2.633	0.047
2013d217__11h22m10s	ON__RCP	-0.459, -0.4, 0.4, 0.459	0.071	0.005	0.037	-0.147, 0.093	2.618	0.035
2013d229__08h25m47s	ON__RCP	-0.459, -0.4, 0.4, 0.459	0.296	0.094	0.034	-0.14, 0.109	2.687	0.048

Table 7: LCP LINES theoretical fitting baseline and peak fitting selections for the software comparison test. Filename is the name of the observing file of the drift scan in the format YYYYdDDD_HHhMMmSSs. Pol is the polarization. Base_locs and Peak_locs are the baseline and peak block locations used to fit the data respectively. M and C are the slope and y-intercept of the baseline fit. Y_max is the maximum of the fit and Rms and Y_rms are the rms of the baseline and peak fit respectively.

Filename	Pol	Base_locs	M	C	Rms	Peak_locs	Y_max	Y_rms
2013d003_23h24m18s	ON_LCP	-0.459,-0.400,0.400,0.459	0.018	0.039	0.043	-0.101,0.139	2.501	0.047
2013d006_23h03m09s	ON_LCP	-0.459,-0.400,0.400,0.459	0.177	0.436	0.147	-0.107,0.145	2.322	0.073
2013d008_00h04m19s	ON_LCP	-0.459,-0.400,0.400,0.459	-0.038	0.044	0.034	-0.110,0.134	2.464	0.034
2013d025_21h46m50s	ON_LCP	-0.459,-0.400,0.400,0.459	0.064	0.010	0.055	-0.105,0.142	2.377	0.071
2013d027_21h35m21s	ON_LCP	-0.459,-0.400,0.400,0.459	-0.312	-0.436	0.224	-0.063,0.128	2.338	0.143
2013d035_21h55m12s	ON_LCP	-0.459,-0.400,0.400,0.459	0.036	-0.024	0.051	-0.101,0.140	2.392	0.055
2013d054_20h03m24s	ON_LCP	-0.459,-0.400,0.400,0.459	-0.037	0.034	0.071	-0.105,0.148	2.610	0.082
2013d056_20h55m03s	ON_LCP	-0.459,-0.400,0.400,0.459	-0.033	0.031	0.034	-0.105,0.141	2.475	0.036
2013d066_19h25m44s	ON_LCP	-0.459,-0.400,0.400,0.459	-0.060	0.027	0.034	-0.096,0.144	2.498	0.039
2013d069_18h55m23s	ON_LCP	-0.459,-0.400,0.400,0.459	0.021	0.028	0.041	-0.095,0.148	2.462	0.046
2013d082_19h20m32s	ON_LCP	-0.459,-0.400,0.400,0.459	-0.067	-0.064	0.033	-0.102,0.138	2.595	0.039
2013d098_17h10m38s	ON_LCP	-0.459,-0.400,0.400,0.459	0.021	0.054	0.049	-0.095,0.130	2.307	0.098
2013d109_16h17m52s	ON_LCP	-0.459,-0.400,0.400,0.459	0.037	0.016	0.037	-0.096,0.153	2.451	0.039
2013d115_16h05m59s	ON_LCP	-0.459,-0.400,0.400,0.459	-0.018	-0.014	0.032	-0.093,0.148	2.444	0.039
2013d116_16h00m04s	ON_LCP	-0.459,-0.400,0.400,0.459	0.235	-0.322	0.899	-0.088,0.142	2.314	0.069
2013d121_15h37m53s	ON_LCP	-0.459,-0.400,0.400,0.459	-0.044	0.245	0.070	-0.094,0.152	2.441	0.075
2013d125_15h23m40s	ON_LCP	-0.459,-0.400,0.400,0.459	0.127	0.222	0.055	-0.099,0.156	2.340	0.117
2013d136_14h27m49s	ON_LCP	-0.459,-0.400,0.400,0.459	0.014	0.016	0.034	-0.131,0.111	2.413	0.035
2013d139_14h28m45s	ON_LCP	-0.459,-0.400,0.400,0.459	0.063	0.049	0.035	-0.131,0.114	2.442	0.038
2013d146_13h51m17s	ON_LCP	-0.459,-0.400,0.400,0.459	-0.043	0.067	0.036	-0.134,0.108	2.352	0.040
2013d152_13h35m38s	ON_LCP	-0.459,-0.400,0.400,0.459	0.028	0.059	0.048	-0.133,0.110	2.433	0.046
2013d167_12h43m42s	ON_LCP	-0.459,-0.400,0.400,0.459	-0.012	0.023	0.034	-0.140,0.104	2.413	0.058
2013d179_12h22m45s	ON_LCP	-0.459,-0.400,0.400,0.459	-0.034	-0.056	0.032	-0.133,0.110	2.433	0.033
2013d185_11h36m09s	ON_LCP	-0.459,-0.400,0.400,0.459	-0.009	0.087	0.039	-0.136,0.115	2.563	0.035
2013d186_11h54m18s	ON_LCP	-0.459,-0.400,0.400,0.459	0.039	0.082	0.034	-0.140,0.103	2.386	0.037
2013d197_11h37m58s	ON_LCP	-0.459,-0.400,0.400,0.459	-0.037	-0.004	0.039	-0.135,0.104	2.310	0.050
2013d202_10h09m44s	ON_LCP	-0.459,-0.400,0.400,0.459	-0.014	-0.025	0.032	-0.131,0.111	2.369	0.035
2013d214_09h38m34s	ON_LCP	-0.459,-0.400,0.400,0.459	-0.003	-0.098	0.036	-0.130,0.112	2.399	0.043
2013d217_11h22m10s	ON_LCP	-0.459,-0.400,0.400,0.459	0.044	0.081	0.043	-0.143,0.099	2.399	0.043
2013d229_08h25m47s	ON_LCP	-0.459,-0.400,0.400,0.459	0.109	0.303	0.036	-0.131,0.109	2.402	0.042

Table 8: RCP LINES theoretical fitting baseline and peak fitting selections for the software comparison test. Filename is the name of the observing file of the drift scan in the format YYYYdDDD_HHhMMmSSs. Pol is the polarization. Base_locs and Peak_locs are the baseline and peak block locations used to fit the data respectively. M and C are the slope and y-intercept of the baseline fit. Y_max is the maximum of the fit and Rms and Y_rms are the rms of the baseline and peak fit respectively.

Filename	Pol	Base_locs	M	C	Rms	Peak_locs	Y_max	Y_rms
2013d003_23h24m18s	ON_RCP	-0.459,-0.400,0.400,0.459	0.061	0.163	0.036	-0.104,0.144	2.668	0.042
2013d006_23h03m09s	ON_RCP	-0.459,-0.400,0.400,0.458	1.169	2.387	0.124	-0.116,0.141	2.884	0.069
2013d008_00h04m19s	ON_RCP	-0.459,-0.400,0.400,0.459	0.002	0.085	0.032	-0.114,0.128	2.654	0.036
2013d025_21h46m50s	ON_RCP	-0.459,-0.400,0.400,0.459	0.023	0.029	0.037	-0.108,0.135	2.584	0.044
2013d027_21h35m21s	ON_RCP	-0.459,-0.400,0.400,0.459	-0.126	0.142	0.220	-0.087,0.118	2.768	0.167
2013d035_21h55m12s	ON_RCP	-0.459,-0.400,0.400,0.459	0.026	0.049	0.031	-0.109,0.137	2.627	0.033
2013d054_20h03m24s	ON_RCP	-0.459,-0.400,0.400,0.459	0.041	0.206	0.035	-0.105,0.140	2.620	0.036
2013d056_20h55m03s	ON_RCP	-0.459,-0.400,0.400,0.459	0.001	0.105	0.035	-0.105,0.136	2.659	0.040
2013d066_19h25m44s	ON_RCP	-0.459,-0.400,0.400,0.459	0.077	0.100	0.032	-0.100,0.140	2.736	0.040
2013d069_18h55m23s	ON_RCP	-0.459,-0.400,0.400,0.459	-0.023	0.017	0.034	-0.101,0.144	2.660	0.035
2013d082_19h20m32s	ON_RCP	-0.459,-0.400,0.400,0.459	-0.013	0.098	0.036	-0.104,0.137	2.623	0.034
2013d098_17h10m38s	ON_RCP	-0.459,-0.400,0.400,0.459	0.093	0.214	0.034	-0.098,0.147	2.644	0.042
2013d109_16h17m52s	ON_RCP	-0.459,-0.400,0.400,0.459	0.067	0.142	0.034	-0.101,0.149	2.635	0.041
2013d115_16h05m59s	ON_RCP	-0.459,-0.400,0.400,0.459	-0.006	0.120	0.037	-0.097,0.146	2.716	0.037
2013d116_16h00m04s	ON_RCP	-0.459,-0.400,0.400,0.459	1.468	2.612	1.018	-0.153,0.149	3.749	0.058
2013d121_15h37m53s	ON_RCP	-0.459,-0.400,0.400,0.459	0.023	0.057	0.033	-0.097,0.145	2.597	0.039
2013d125_15h23m40s	ON_RCP	-0.459,-0.400,0.400,0.459	0.050	0.183	0.032	-0.100,0.146	2.565	0.033
2013d136_14h27m49s	ON_RCP	-0.459,-0.400,0.400,0.459	-0.049	-0.101	0.031	-0.135,0.113	2.943	0.034
2013d139_14h28m45s	ON_RCP	-0.459,-0.400,0.400,0.459	-0.046	-0.010	0.036	-0.135,0.109	2.652	0.037
2013d146_13h51m17s	ON_RCP	-0.459,-0.400,0.400,0.459	-0.007	0.146	0.031	-0.136,0.107	2.585	0.035
2013d152_13h35m38s	ON_RCP	-0.459,-0.400,0.400,0.459	0.070	0.264	0.033	-0.137,0.104	2.614	0.037
2013d167_12h43m42s	ON_RCP	-0.459,-0.400,0.400,0.459	0.042	0.159	0.032	-0.152,0.101	2.649	0.051
2013d179_12h22m45s	ON_RCP	-0.459,-0.400,0.400,0.459	0.062	0.098	0.033	-0.142,0.103	2.564	0.037
2013d185_11h36m09s	ON_RCP	-0.459,-0.400,0.400,0.459	-0.119	-0.180	0.053	-0.138,0.105	2.571	0.043
2013d186_11h54m18s	ON_RCP	-0.459,-0.400,0.400,0.459	0.154	0.358	0.033	-0.140,0.101	2.491	0.040
2013d197_11h37m58s	ON_RCP	-0.459,-0.400,0.400,0.459	-0.132	-0.216	0.035	-0.140,0.099	2.688	0.051
2013d202_10h09m44s	ON_RCP	-0.459,-0.400,0.400,0.459	0.042	0.169	0.031	-0.139,0.107	2.610	0.037
2013d214_09h38m34s	ON_RCP	-0.459,-0.400,0.400,0.459	-0.025	0.115	0.036	-0.135,0.108	2.634	0.049
2013d217_11h22m10s	ON_RCP	-0.459,-0.400,0.400,0.459	0.005	0.072	0.039	-0.147,0.093	2.617	0.037
2013d229_08h25m47s	ON_RCP	-0.459,-0.400,0.400,0.459	0.094	0.296	0.034	-0.140,0.109	2.693	0.055

Table 9: LCP DRAN automated fitting baseline and peak fitting selections for the software comparison test. Filename is the name of the observing file of the drift scan in the format YYYYdDDD_HHhMMmSSs. Pol is the polarization. Base_locs and Peak_locs are the baseline and peak block locations used to fit the data respectively. M and C are the slope and y-intercept of the baseline fit. Y_max is the maximum of the fit and Rms and Y_rms are the rms of the baseline and peak fit respectively.

Filename	Pol	Base_locs	M	C	Rms	Peak_locs	Y_max	Y_rms
2013d003_23h24m18s	ON_LCP	-0.393, -0.348, 0.397, 0.443	0.065	0.010	0.042	-0.102, 0.139	2.509	0.046
2013d006_23h03m09s	ON_LCP	-0.411, -0.369, 0.352, 0.397	0.333	0.112	0.065	-0.108, 0.146	2.386	0.065
2013d008_00h04m19s	ON_LCP	-0.411, -0.366, 0.375, 0.42	0.077	-0.047	0.033	-0.11, 0.133	2.472	0.034
2013d025_21h46m50s	ON_LCP	-0.404, -0.359, 0.392, 0.437	0.065	0.041	0.058	-0.106, 0.142	2.399	0.070
2013d027_21h35m21s	ON_LCP	-0.308, -0.263, 0.383, 0.428	-0.581	-0.447	0.088	-0.067, 0.132	2.484	0.142
2013d035_21h55m12s	ON_LCP	-0.42, -0.375, 0.388, 0.433	0.038	0.005	0.041	-0.102, 0.14	2.422	0.054
2013d054_20h03m24s	ON_LCP	-0.45, -0.405, 0.414, 0.459	-0.007	-0.053	0.055	-0.105, 0.148	2.628	0.078
2013d056_20h55m03s	ON_LCP	-0.428, -0.382, 0.414, 0.459	0.040	-0.033	0.033	-0.105, 0.141	2.476	0.035
2013d066_19h25m44s	ON_LCP	-0.388, -0.343, 0.414, 0.459	0.053	-0.077	0.034	-0.097, 0.144	2.514	0.038
2013d069_18h55m23s	ON_LCP	-0.391, -0.346, 0.414, 0.459	0.055	0.006	0.037	-0.096, 0.148	2.478	0.044
2013d082_19h20m32s	ON_LCP	-0.443, -0.397, 0.391, 0.436	-0.070	-0.073	0.032	-0.102, 0.138	2.600	0.038
2013d098_17h10m38s	ON_LCP	-0.428, -0.384, 0.377, 0.421	0.042	0.003	0.039	-0.095, 0.131	2.328	0.083
2013d109_16h17m52s	ON_LCP	-0.391, -0.346, 0.414, 0.459	0.029	0.026	0.036	-0.097, 0.153	2.461	0.038
2013d115_16h05m59s	ON_LCP	-0.382, -0.337, 0.414, 0.459	0.021	-0.034	0.033	-0.093, 0.148	2.460	0.038
2013d116_16h00m04s	ON_LCP	-0.379, -0.334, 0.402, 0.447	0.063	0.064	0.049	-0.089, 0.142	2.475	0.067
2013d121_15h37m53s	ON_LCP	-0.433, -0.387, 0.394, 0.439	0.264	-0.060	0.060	-0.095, 0.152	2.461	0.069
2013d125_15h23m40s	ON_LCP	-0.366, -0.321, 0.346, 0.391	0.157	0.030	0.043	-0.101, 0.159	2.439	0.114
2013d136_14h27m49s	ON_LCP	-0.417, -0.371, 0.414, 0.459	0.028	0.007	0.032	-0.132, 0.111	2.419	0.034
2013d139_14h28m45s	ON_LCP	-0.424, -0.379, 0.374, 0.419	0.057	0.053	0.033	-0.131, 0.114	2.453	0.037
2013d146_13h51m17s	ON_LCP	-0.415, -0.37, 0.343, 0.388	0.032	-0.059	0.037	-0.134, 0.109	2.367	0.038
2013d152_13h35m38s	ON_LCP	-0.454, -0.408, 0.336, 0.382	0.023	0.008	0.050	-0.133, 0.111	2.452	0.045
2013d167_12h43m42s	ON_LCP	-0.435, -0.391, 0.375, 0.419	0.018	-0.030	0.033	-0.141, 0.105	2.428	0.039
2013d179_12h22m45s	ON_LCP	-0.421, -0.376, 0.366, 0.411	-0.063	-0.046	0.031	-0.133, 0.11	2.445	0.033
2013d185_11h36m09s	ON_LCP	-0.423, -0.377, 0.377, 0.422	0.092	0.005	0.035	-0.136, 0.115	2.549	0.034
2013d186_11h54m18s	ON_LCP	-0.438, -0.393, 0.352, 0.397	0.048	0.021	0.032	-0.14, 0.104	2.404	0.036
2013d197_11h37m58s	ON_LCP	-0.411, -0.365, 0.339, 0.384	-0.036	-0.061	0.034	-0.136, 0.105	2.325	0.035
2013d202_10h09m44s	ON_LCP	-0.407, -0.362, 0.361, 0.407	-0.037	-0.018	0.031	-0.131, 0.112	2.371	0.033
2013d214_09h38m34s	ON_LCP	-0.425, -0.38, 0.373, 0.418	-0.099	-0.012	0.035	-0.13, 0.112	2.407	0.042
2013d217_11h22m10s	ON_LCP	-0.446, -0.401, 0.341, 0.386	0.040	0.027	0.040	-0.143, 0.1	2.414	0.042
2013d229_08h25m47s	ON_LCP	-0.416, -0.371, 0.378, 0.423	0.331	0.090	0.033	-0.132, 0.109	2.423	0.041

Table 10: RCP DRAN automated fitting baseline and peak fitting selections for the software comparison test. Filename is the name of the observing file of the drift scan in the format YYYYdDDD_HHhMMmSSs. Pol is the polarization. Base_locs and Peak_locs are the baseline and peak block locations used to fit the data respectively. M and C are the slope and y-intercept of the baseline fit. Y_max is the maximum of the fit and Rms and Y_rms are the rms of the baseline and peak fit respectively.

Filename	Pol	Base_locs	M	C	Rms	Peak_locs	Y_max	Y_rms
2013d003_23h24m18s	ON_RCP	-0.398, -0.352, 0.407, 0.452	0.231	0.030	0.033	-0.106, 0.144	2.698	0.041
2013d006_23h03m09s	ON_RCP	0.447, -0.428, 0.308, 0.372	2.429	1.216	0.121	-0.153, 0.177	2.821	0.066
2013d008_00h04m19s	ON_RCP	-0.417, -0.372, 0.375, 0.42	0.102	-0.009	0.033	-0.115, 0.129	2.665	0.036
2013d025_21h46m50s	ON_RCP	-0.407, -0.362, 0.386, 0.431	0.023	0.022	0.035	-0.108, 0.135	2.585	0.043
2013d027_21h35m21s	ON_RCP	-0.316, -0.271, 0.382, 0.427	-0.058	-0.206	0.102	-0.087, 0.121	2.851	0.166
2013d035_21h55m12s	ON_RCP	-0.408, -0.362, 0.389, 0.434	0.068	0.008	0.028	-0.109, 0.137	2.644	0.032
2013d054_20h03m24s	ON_RCP	-0.433, -0.388, 0.375, 0.42	0.216	0.032	0.032	-0.105, 0.14	2.628	0.035
2013d056_20h55m03s	ON_RCP	-0.398, -0.353, 0.371, 0.416	0.099	-0.018	0.030	-0.105, 0.136	2.677	0.038
2013d066_19h25m44s	ON_RCP	-0.417, -0.371, 0.402, 0.447	0.126	0.069	0.030	-0.1, 0.14	2.744	0.039
2013d069_18h55m23s	ON_RCP	-0.398, -0.353, 0.414, 0.459	0.043	-0.040	0.030	-0.102, 0.144	2.677	0.035
2013d082_19h20m32s	ON_RCP	-0.407, -0.361, 0.36, 0.405	0.082	-0.043	0.032	-0.104, 0.138	2.653	0.034
2013d098_17h10m38s	ON_RCP	-0.396, -0.351, 0.41, 0.455	0.258	0.073	0.032	-0.099, 0.147	2.664	0.040
2013d109_16h17m52s	ON_RCP	-0.399, -0.353, 0.407, 0.452	0.142	0.063	0.034	-0.101, 0.149	2.639	0.040
2013d115_16h05m59s	ON_RCP	-0.422, -0.377, 0.403, 0.448	0.148	-0.017	0.034	-0.098, 0.146	2.725	0.036
2013d116_16h00m04s	ON_RCP	-0.445, -0.397, -0.31, -0.265, 0.414, 0.459	3.207	1.141	0.213	-0.156, 0.151	4.074	0.059
2013d121_15h37m53s	ON_RCP	-0.407, -0.361, 0.395, 0.44	0.059	0.018	0.037	-0.097, 0.145	2.602	0.038
2013d125_15h23m40s	ON_RCP	-0.389, -0.343, 0.386, 0.431	0.225	0.036	0.029	-0.101, 0.146	2.577	0.032
2013d136_14h27m49s	ON_RCP	-0.459, -0.411, 0.398, 0.443	-0.102	-0.052	0.029	-0.135, 0.114	2.946	0.033
2013d139_14h28m45s	ON_RCP	-0.423, -0.377, 0.368, 0.413	0.015	-0.063	0.029	-0.135, 0.109	2.669	0.036
2013d146_13h51m17s	ON_RCP	-0.428, -0.382, 0.364, 0.409	0.141	-0.013	0.030	-0.136, 0.107	2.591	0.034
2013d152_13h35m38s	ON_RCP	-0.438, -0.393, 0.351, 0.396	0.264	0.060	0.032	-0.137, 0.104	2.624	0.037
2013d167_12h43m42s	ON_RCP	-0.442, -0.398, 0.358, 0.402	0.173	0.040	0.031	-0.152, 0.101	2.650	0.042
2013d179_12h22m45s	ON_RCP	-0.459, -0.419, 0.341, 0.386	0.040	0.035	0.030	-0.142, 0.104	2.590	0.036
2013d185_11h36m09s	ON_RCP	-0.423, -0.378, 0.375, 0.42	-0.158	-0.143	0.037	-0.139, 0.106	2.593	0.043
2013d186_11h54m18s	ON_RCP	-0.439, -0.393, 0.37, 0.415	0.366	0.147	0.031	-0.14, 0.101	2.499	0.040
2013d197_11h37m58s	ON_RCP	-0.441, -0.396, 0.355, 0.401	-0.231	-0.144	0.034	-0.14, 0.099	2.692	0.038
2013d202_10h09m44s	ON_RCP	-0.459, -0.416, 0.374, 0.419	0.160	0.036	0.032	-0.14, 0.108	2.615	0.037
2013d214_09h38m34s	ON_RCP	-0.442, -0.396, 0.352, 0.397	0.121	-0.029	0.037	-0.135, 0.108	2.637	0.047
2013d217_11h22m10s	ON_RCP	-0.458, -0.412, 0.359, 0.404	0.032	-0.013	0.035	-0.147, 0.093	2.634	0.035
2013d229_08h25m47s	ON_RCP	-0.442, -0.397, 0.414, 0.459	0.292	0.089	0.033	-0.141, 0.11	2.692	0.048

Table 11: LCP LINES automated fitting baseline and peak fitting selections for the software comparison test. Filename is the name of the observing file of the drift scan in the format YYYYdDDD__HHhMMmSSs. Pol is the polarization. Base_locs and Peak_locs are the baseline and peak block locations used to fit the data respectively. M and C are the slope and y-intercept of the baseline fit. Y_max is the maximum of the fit and Rms and Y_rms are the rms of the baseline and peak fit respectively.

Filename	Pol	Base_locs	M	C	Rms	Peak_locs	Y_max	Y_rms
2013d003_23h24m18s	ON_LCP	-0.393, -0.348, 0.397, 0.443	0.009	0.062	0.044	-0.102, 0.139	2.509	0.047
2013d006_23h03m09s	ON_LCP	-0.411, -0.369, 0.352, 0.397	0.126	0.367	0.093	-0.108, 0.146	2.375	0.073
2013d008_00h04m19s	ON_LCP	-0.411, -0.366, 0.375, 0.420	-0.047	0.076	0.033	-0.110, 0.133	2.472	0.034
2013d025_21h46m50s	ON_LCP	-0.404, -0.359, 0.392, 0.437	0.041	0.064	0.058	-0.106, 0.142	2.399	0.071
2013d027_21h35m21s	ON_LCP	-0.308, -0.263, 0.383, 0.428	-0.447	-0.580	0.088	-0.067, 0.132	2.484	0.142
2013d035_21h55m12s	ON_LCP	-0.420, -0.375, 0.388, 0.433	0.005	0.038	0.041	-0.102, 0.140	2.422	0.055
2013d054_20h03m24s	ON_LCP	-0.450, -0.405, 0.414, 0.459	-0.052	-0.004	0.055	-0.105, 0.148	2.625	0.082
2013d056_20h55m03s	ON_LCP	-0.428, -0.382, 0.414, 0.459	-0.033	0.040	0.032	-0.105, 0.141	2.476	0.036
2013d066_19h25m44s	ON_LCP	-0.388, -0.343, 0.414, 0.459	-0.077	0.054	0.034	-0.097, 0.144	2.514	0.039
2013d069_18h55m23s	ON_LCP	-0.391, -0.346, 0.414, 0.459	0.007	0.056	0.039	-0.096, 0.148	2.476	0.046
2013d082_19h20m32s	ON_LCP	-0.443, -0.397, 0.391, 0.436	-0.073	-0.071	0.032	-0.102, 0.138	2.601	0.039
2013d098_17h10m38s	ON_LCP	-0.428, -0.384, 0.377, 0.421	0.003	0.041	0.039	-0.095, 0.131	2.325	0.098
2013d109_16h17m52s	ON_LCP	-0.391, -0.346, 0.414, 0.459	0.026	0.029	0.035	-0.097, 0.153	2.461	0.039
2013d115_16h05m59s	ON_LCP	-0.382, -0.337, 0.414, 0.459	-0.034	0.022	0.032	-0.093, 0.148	2.460	0.039
2013d116_16h00m04s	ON_LCP	-0.379, -0.334, 0.402, 0.447	0.064	0.063	0.049	-0.089, 0.142	2.474	0.069
2013d121_15h37m53s	ON_LCP	-0.433, -0.387, 0.394, 0.439	-0.060	0.267	0.061	-0.095, 0.152	2.456	0.075
2013d125_15h23m40s	ON_LCP	-0.366, -0.321, 0.346, 0.391	0.031	0.158	0.043	-0.101, 0.159	2.436	0.116
2013d136_14h27m49s	ON_LCP	-0.417, -0.371, 0.414, 0.459	0.007	0.029	0.032	-0.132, 0.111	2.420	0.035
2013d139_14h28m45s	ON_LCP	-0.424, -0.379, 0.374, 0.419	0.054	0.056	0.033	-0.131, 0.114	2.451	0.038
2013d146_13h51m17s	ON_LCP	-0.415, -0.370, 0.343, 0.388	-0.059	0.033	0.038	-0.134, 0.109	2.367	0.040
2013d152_13h35m38s	ON_LCP	-0.454, -0.408, 0.336, 0.382	0.008	0.020	0.052	-0.133, 0.111	2.452	0.046
2013d167_12h43m42s	ON_LCP	-0.435, -0.391, 0.375, 0.419	-0.030	0.018	0.033	-0.141, 0.105	2.430	0.058
2013d179_12h22m45s	ON_LCP	-0.421, -0.376, 0.366, 0.411	-0.046	-0.063	0.031	-0.133, 0.110	2.445	0.033
2013d185_11h36m09s	ON_LCP	-0.423, -0.377, 0.377, 0.422	0.006	0.091	0.036	-0.136, 0.115	2.549	0.035
2013d186_11h54m18s	ON_LCP	-0.438, -0.393, 0.352, 0.397	0.021	0.048	0.032	-0.140, 0.104	2.403	0.037
2013d197_11h37m58s	ON_LCP	-0.411, -0.365, 0.339, 0.384	-0.061	-0.034	0.035	-0.136, 0.105	2.334	0.049
2013d202_10h09m44s	ON_LCP	-0.407, -0.362, 0.361, 0.407	-0.017	-0.036	0.031	-0.131, 0.112	2.371	0.035
2013d214_09h38m34s	ON_LCP	-0.425, -0.380, 0.373, 0.418	-0.012	-0.099	0.035	-0.130, 0.112	2.407	0.043
2013d217_11h22m10s	ON_LCP	-0.446, -0.401, 0.341, 0.386	0.027	0.040	0.040	-0.143, 0.100	2.415	0.043
2013d229_08h25m47s	ON_LCP	-0.416, -0.371, 0.378, 0.423	0.090	0.330	0.033	-0.132, 0.109	2.422	0.042

Table 12: RCP LINES automated fitting baseline and peak fitting selections for the software comparison test. Filename is the name of the observing file of the drift scan in the format YYYYdDDD_HHhMMmSSs. Pol is the polarization. Base_locs and Peak_locs are the baseline and peak block locations used to fit the data respectively. M and C are the slope and y-intercept of the baseline fit. Y_max is the maximum of the fit and Rms and Y_rms are the rms of the baseline and peak fit respectively.

Filename	Pol	Base_locs	M	C	Rms	Peak_locs	Y_max	Y_rms
2013d003_23h24m18s	ON_RCP	-0.398, -0.352, 0.407, 0.452	0.030	0.230	0.032	-0.106, 0.144	2.697	0.042
2013d006_23h03m09s	ON_RCP	0.447, -0.428, 0.308, 0.372	4.915	-7.559	0.336	-0.153, 0.177	-0.259	0.079
2013d008_00h04m19s	ON_RCP	-0.417, -0.372, 0.375, 0.420	-0.009	0.101	0.033	-0.115, 0.129	2.664	0.036
2013d025_21h46m50s	ON_RCP	-0.407, -0.362, 0.386, 0.431	0.022	0.022	0.035	-0.108, 0.135	2.585	0.044
2013d027_21h35m21s	ON_RCP	-0.316, -0.271, 0.382, 0.427	-0.206	-0.059	0.102	-0.087, 0.121	2.851	0.166
2013d035_21h55m12s	ON_RCP	-0.408, -0.362, 0.389, 0.434	0.008	0.068	0.028	-0.109, 0.137	2.644	0.033
2013d054_20h03m24s	ON_RCP	-0.433, -0.388, 0.375, 0.420	0.032	0.216	0.032	-0.105, 0.140	2.629	0.036
2013d056_20h55m03s	ON_RCP	-0.398, -0.353, 0.371, 0.416	-0.018	0.099	0.032	-0.105, 0.136	2.678	0.040
2013d066_19h25m44s	ON_RCP	-0.417, -0.371, 0.402, 0.447	0.070	0.127	0.031	-0.100, 0.140	2.743	0.040
2013d069_18h55m23s	ON_RCP	-0.398, -0.353, 0.414, 0.459	-0.040	0.043	0.030	-0.102, 0.144	2.677	0.035
2013d082_19h20m32s	ON_RCP	-0.407, -0.361, 0.360, 0.405	-0.044	0.081	0.032	-0.104, 0.138	2.654	0.034
2013d098_17h10m38s	ON_RCP	-0.396, -0.351, 0.410, 0.455	0.072	0.257	0.032	-0.099, 0.147	2.663	0.042
2013d109_16h17m52s	ON_RCP	-0.399, -0.353, 0.407, 0.452	0.063	0.143	0.035	-0.101, 0.149	2.639	0.041
2013d115_16h05m59s	ON_RCP	-0.422, -0.377, 0.403, 0.448	-0.017	0.147	0.034	-0.098, 0.146	2.725	0.037
2013d116_16h00m04s	ON_RCP	-0.445, -0.397, -0.310, -0.265, 0.414, 0.459	1.261	2.865	1.002	-0.156, 0.151	3.954	0.059
2013d121_15h37m53s	ON_RCP	-0.407, -0.361, 0.395, 0.440	0.019	0.058	0.038	-0.097, 0.145	2.601	0.039
2013d125_15h23m40s	ON_RCP	-0.389, -0.343, 0.386, 0.431	0.036	0.225	0.029	-0.101, 0.146	2.578	0.033
2013d136_14h27m49s	ON_RCP	-0.459, -0.411, 0.398, 0.443	-0.053	-0.101	0.029	-0.135, 0.114	2.946	0.034
2013d139_14h28m45s	ON_RCP	-0.423, -0.377, 0.368, 0.413	-0.063	0.014	0.029	-0.135, 0.109	2.669	0.037
2013d146_13h51m17s	ON_RCP	-0.428, -0.382, 0.364, 0.409	-0.013	0.140	0.030	-0.136, 0.107	2.591	0.035
2013d152_13h35m38s	ON_RCP	-0.438, -0.393, 0.351, 0.396	0.060	0.264	0.032	-0.137, 0.104	2.625	0.037
2013d167_12h43m42s	ON_RCP	-0.442, -0.398, 0.358, 0.402	0.040	0.173	0.031	-0.152, 0.101	2.652	0.051
2013d179_12h22m45s	ON_RCP	-0.459, -0.419, 0.341, 0.386	0.035	0.041	0.030	-0.142, 0.104	2.590	0.037
2013d185_11h36m09s	ON_RCP	-0.423, -0.378, 0.375, 0.420	-0.143	-0.158	0.037	-0.139, 0.106	2.595	0.044
2013d186_11h54m18s	ON_RCP	-0.439, -0.393, 0.370, 0.415	0.147	0.368	0.032	-0.140, 0.101	2.499	0.040
2013d197_11h37m58s	ON_RCP	-0.441, -0.396, 0.355, 0.401	-0.144	-0.230	0.035	-0.140, 0.099	2.699	0.051
2013d202_10h09m44s	ON_RCP	-0.459, -0.416, 0.374, 0.419	0.036	0.159	0.031	-0.140, 0.108	2.615	0.038
2013d214_09h38m34s	ON_RCP	-0.442, -0.396, 0.352, 0.397	-0.029	0.121	0.037	-0.135, 0.108	2.637	0.049
2013d217_11h22m10s	ON_RCP	-0.458, -0.412, 0.359, 0.404	-0.013	0.032	0.036	-0.147, 0.093	2.634	0.037
2013d229_08h25m47s	ON_RCP	-0.442, -0.397, 0.414, 0.459	0.089	0.293	0.033	-0.141, 0.110	2.698	0.055

FITS file extensions of HartRAO data.

The following images show the basic information recorded on a target object during an observing session at HartRAO. Each image is orderdered by the file extension and will typically show a summary of the header data unit (HDU) for our example source Jupiter. The data supplied is stored in a KEYWORD = VALUE / DESCRIPTION format. Where a description is given, the keyword is self explanatory. However, where a description is not supplied, the reader is referred to the latest FITS standard documentation[1]. At the time of this work, the official reference document that defined the requirements for FITS format data files was Version 4.0 (13 August 2018).

[1] https://fits.gsfc.nasa.gov/fits_standard.html

1 Extension 0

Figure 1: Primary HDU basic setup for data monitored at HartRAO.

```
SIMPLE  =                    T
BITPIX  =                    8
NAXIS   =                    0
EXTEND  =                    T
DATE    = '2012-01-01T17:00:07' / file creation date (YYYY-MM-DDThh:mm:ss UT)
COMMENT information about the object, from scheduler task
OBJECT  = 'JUPITER '           / Name of object
LONGITUD=     28.7726973530753 / Longitude of object
LATITUDE=     10.4785216750824 / Latitude of object
COMMENT information about the scan, from scheduler task
OBSERVER= 'Mike    '           / Principal Investigator
OBSLOCAL= 'mike    '           /  On-site observer
PROJNAME= '22GHz wideband continuum calibration' / Short name for the project
PROPOSAL= '2007.003'           / Observing proposal ID
COMMENT information about the antenna
TELESCOP= 'HartRAO 26m Antenna' / Telescope name
UPGRADE = 'Surface upgrade completed !!' / Antenna surface status
FOCUS   =           4.62890625 / Sub-reflector focus
TILT    =                   0. / Sub-reflector tilt
TAMBIENT=     296.478449737549 / [K] Ambient temperature
PRESSURE=                860.9 / [mbar] Atmospheric pressure
HUMIDITY=     53.4209272460937 / [%] Humidity
WINDSPD =          1.220703125 / [m/s] Wind Speed
SIMULATE=                    0 / Simulation ?
SCANTYPE= 'Drift   '           / Scan type
INSTRUME= 'Total Power'        / Radiometer type
INSTFLAG= 'None    '           / Radiometer flags
STEPSEQ = 'HPNZCAL ZC HPSZ'    / Stepping sequence
SCANDIST=    0.186943666837938 / Scan length (deg)
SCANANGL=                   0. / Scan angle (deg)
SCANTIME=      44.743975097543 / Scan time (s)
STARTX  =                   0. / Start X position (deg)
STARTY  =                   0. / Start Y position (deg)
STOPX   =                   0. / Stop X position (deg)
STOPY   =                   0. / Stop Y position (deg)
SCANS   =                    1 / No of scans per position
SCANDIR = 'Both    '           / Scanning direction
POINTING=                    1 / Pointing corrections applied
```

The figure shows the summary of a typical PRIMARY HDU for the source Jupiter. In the primary header, only general information on the observation is stored. This is basic information about the object under investigation, information on the observer and the scan, as well as information on the telescope and the surroundings conditions.

2 Extension 1

Figure 2: Feed system HDU basic setup for data monitored at HartRAO.

```
XTENSION= 'BINTABLE'           / binary table extension
BITPIX  =                    8 / 8-bit bytes
NAXIS   =                    2 / 2-dimensional binary table
NAXIS1  =                   85 / width of table in bytes
NAXIS2  =                    1 / number of rows in table
PCOUNT  =                    0 / size of special data area
GCOUNT  =                    1 / one data group (required keyword)
TFIELDS =                    6 / number of fields in each row
EXTNAME = '01.3S   '           / name of this binary table extension
FEEDTYPE= 'Circular'           / Feedtype
BMOFFHA =                 0.16 / Beam offset in HA
BMOFFDEC=                   0. / Beam offset in Dec
HPBW    =                0.031 / Half-power beamwidth in degrees
FNBW    =                0.085 / Beamwidth to first nulls in degrees
SNBW    =                0.171 / Beamwidth to second nulls, in degrees
DICHROIC= '(Off)   '           / Dichroic reflector position ON or OFF
PHASECAL= '(Off)   '           / Mark 4 VLBI phase calibration ON or OFF
NOMTSYS =                 250. / [K] Nominal minimum system temperature
TTYPE1  = 'Feedsys '           / label for field
TFORM1  = '25A     '           / format of field
TTYPE2  = 'FeedSys_RF_Hi'      / label for field
TFORM2  = '1D      '           / format of field
TDISP2  = 'D12.5   '
TTYPE3  = 'FeedSys_RF_Lo'      / label for field
TFORM3  = '1D      '           / format of field
TDISP3  = 'D12.5   '
TTYPE4  = 'Mixer   '           / label for field
TFORM4  = '28A     '           / format of field
TTYPE5  = 'Mixer_RF_Lo'        / label for field
TFORM5  = '1D      '           / format of field
TDISP5  = 'D12.5   '
TUNIT5  = 'MHz     '
TTYPE6  = 'Mixer_RF_Hi'        / label for field
TFORM6  = '1D      '           / format of field
TDISP6  = 'D12.5   '
TUNIT6  = 'MHz     '
```

The figure shows the summary of a typical feed system HDU for the source Jupiter. In the feed system header, general information on the feed system is stored. This is basic information about the feed type, as well as the positions in degrees from the center of the scan where the half-power, first- and second-null beam widths are expected to be located for each drift scan. In the data block (i.e. where the TTYPE keyword begins) records of data collected on the feed system are stored.

3 Extension 2

Figure 3: Noise calibration HDU basic setup for data monitored at HartRAO.

```
XTENSION= 'BINTABLE'           / binary table extension
BITPIX  =                    8 / 8-bit bytes
NAXIS   =                    2 / 2-dimensional binary table
NAXIS1  =                  184 / width of table in bytes
NAXIS2  =                  128 / number of rows in table
PCOUNT  =                    0 / size of special data area
GCOUNT  =                    1 / one data group (required keyword)
TFIELDS =                   23 / number of fields in each row
EXTNAME = 'Scan_0_HPNZ_CAL'    / name of this binary table extension
FRONTEND= '01.3S   '           / Frontend ID
CENTFREQ=               22040. / [MHz] Backend centre frequency
BANDWDTH=                 400. / [MHz] Bandwidth of backend
TCAL1   =                 13.6 / [K] Cal noise diode value for channel 1
TCALSIG1=                  3.5 / [K] uncertainty in TCAL1
TCALFRQ1=               23000. / [Hz] Frequency the calibration applies to
TCALDAT1= '20070118'           / Calibration date
TCAL2   =                 11.9 / [K] Cal noise diode value for channel 2
TCALSIG2=                  3.6 / [K] uncertainty in TCAL2
TCALFRQ2=               23000. / [Hz] Frequency the calibration applies to
TCALDAT2= '20070118'           / Calibration date
SCANTYPE= 'Step    '           / Scan type
INSTRUME= 'Total Power'        / Radiometer type
INSTFLAG= 'None    '           / Radiometer flags
STEPSEQ = 'HPNZCAL '           / Stepping sequence
SCANDIST=                   0. / Scan length (deg)
SCANANGL=                   0. / Scan angle (deg)
SCANTIME=                10.24 / Scan time (s)
STARTX  =  -0.0934718334189692 / Start X position (deg)
STARTY  =               0.0155 / Start Y position (deg)
STOPX   =  -0.0934718334189692 / Stop X position (deg)
STOPY   =               0.0155 / Stop Y position (deg)
SCAN    =                    0 / Index no of scan
HZPERK1 =     1923.57791002432 / [Hz/K] Counter calibration
HZKERR1 =    0.526824128739278 / [Hz/K] Counter cal error
HZPERK2 =     2072.65153960745 / [Hz/K] Counter calibration
HZKERR2 =    0.850032283682284 / [Hz/K] Counter cal error
HZZERO1 =     126265.784091414 / [Hz] Counter zero offset
HZZERO2 =     121904.317282469 / [Hz] Counter zero offset
TTYPE1  = 'MJD     '           / label for field
TFORM1  = '1D      '           / format of field
TUNIT1  = 'days    '
TTYPE2  = 'Count1  '           / label for field
TFORM2  = '1D      '           / format of field
TUNIT2  = 'Hz      '
TTYPE3  = 'Count2  '           / label for field
TFORM3  = '1D      '           / format of field
TUNIT3  = 'Hz      '
TTYPE4  = 'Hour_Angle'         / label for field
TFORM4  = '1D      '           / format of field
TUNIT4  = 'deg     '
TTYPE5  = 'Declination'        / label for field
TFORM5  = '1D      '           / format of field
TUNIT5  = 'deg     '
```

The figure shows the summary of a typical noise calibration HDU for the source Jupiter. In the noise calibration header, general information on the noise diode firing is stored. This is basic information about the noise diode values for both left and right polarizations, as well as the bandwidth and conversion factors required to convert source counts into Kelvins. In the data block (i.e. where the TTYPE keyword begins) records of data collected on the drift scan are stored. These include the source counts as well as some other parameters, for example the hour angle and declination of the source during observation. This however is not an exhaustive list of all the data that is recorded. Many of the remaining fields are just position in different fromats and we are mainly interested in the signal 'Count1' and 'Count2, thus they are excluded here due to space restrictions.

4 Extension 4 to 6

Extensions 4 to 6 contain the drift scans themselves starting at the north offset position to the south offset position with the on-target driftscan in the center. Summaries of typical drift scan HDU for the source Jupiter are shown here respectively in the order of observation. In each header, general information on the drift scan is stored. This is basic information about the type of radiometer used in the observation, as well as the scan type and starting and ending positions of each scan respectively. The data blocks have been intentionally left out because they resemble those in the noise diode Figure 3 above.

Figure 4: HPN HDU basic setup for data monitored at HartRAO.

```
XTENSION= 'BINTABLE'           / binary table extension
BITPIX  =                    8 / 8-bit bytes
NAXIS   =                    2 / 2-dimensional binary table
NAXIS1  =                  184 / width of table in bytes
NAXIS2  =                  568 / number of rows in table
PCOUNT  =                    0 / size of special data area
GCOUNT  =                    1 / one data group (required keyword)
TFIELDS =                   23 / number of fields in each row
EXTNAME = 'Scan_1_HPNZ'        / name of this binary table extension
FRONTEND= '01.3S   '           / Frontend ID
CENTFREQ=               22040. / [MHz] Backend centre frequency
BANDWDTH=                 400. / [MHz] Bandwidth of backend
SCANTYPE= 'Drift   '           / Scan type
INSTRUME= 'Total Power'        / Radiometer type
INSTFLAG= 'None    '           / Radiometer flags
STEPSEQ = 'HPNZ    '           / Stepping sequence
SCANDIST=    0.186943666837938 / Scan length (deg)
SCANANGL=                   0. / Scan angle (deg)
SCANTIME=                45.44 / Scan time (s)
STARTX  =  -0.0934718334189692 / Start X position (deg)
STARTY  =               0.0155 / Start Y position (deg)
STOPX   =   0.0934718334189692 / Stop X position (deg)
STOPY   =               0.0155 / Stop Y position (deg)
SCAN    =                    1 / Index no of scan
HZZERO1 =     126265.784091414 / [Hz] Counter zero offset
HZZERO2 =     121904.317282469 / [Hz] Counter zero offset
```

The figure shows the summary of a typical HPN HDU for the source Jupiter.

Figure 5: ON HDU basic setup for data monitored at HartRAO.

```
XTENSION= 'BINTABLE'           / binary table extension
BITPIX  =                    8 / 8-bit bytes
NAXIS   =                    2 / 2-dimensional binary table
NAXIS1  =                  184 / width of table in bytes
NAXIS2  =                  568 / number of rows in table
PCOUNT  =                    0 / size of special data area
GCOUNT  =                    1 / one data group (required keyword)
TFIELDS =                   23 / number of fields in each row
EXTNAME = 'Scan_2_ZC'          / name of this binary table extension
FRONTEND= '01.3S   '           / Frontend ID
CENTFREQ=               22040. / [MHz] Backend centre frequency
BANDWDTH=                 400. / [MHz] Bandwidth of backend
SCANTYPE= 'Drift   '           / Scan type
INSTRUME= 'Total Power'        / Radiometer type
INSTFLAG= 'None    '           / Radiometer flags
STEPSEQ = 'ZC      '           / Stepping sequence
SCANDIST=    0.186943666837938 / Scan length (deg)
SCANANGL=                   0. / Scan angle (deg)
SCANTIME=                45.44 / Scan time (s)
STARTX  =  -0.0934718334189692 / Start X position (deg)
STARTY  =                   0. / Start Y position (deg)
STOPX   =   0.0934718334189692 / Stop X position (deg)
STOPY   =                   0. / Stop Y position (deg)
SCAN    =                    1 / Index no of scan
HZZERO1 =     126265.784091414 / [Hz] Counter zero offset
HZZERO2 =     121904.317282469 / [Hz] Counter zero offset
```

The figure shows the summary of a typical ON HDU for the source Jupiter.

Figure 6: HPS HDU basic setup for data monitored at HartRAO.

```
XTENSION= 'BINTABLE'           / binary table extension
BITPIX  =                    8 / 8-bit bytes
NAXIS   =                    2 / 2-dimensional binary table
NAXIS1  =                  184 / width of table in bytes
NAXIS2  =                  568 / number of rows in table
PCOUNT  =                    0 / size of special data area
GCOUNT  =                    1 / one data group (required keyword)
TFIELDS =                   23 / number of fields in each row
EXTNAME = 'Scan_3_HPSZ'        / name of this binary table extension
FRONTEND= '01.3S   '           / Frontend ID
CENTFREQ=               22040. / [MHz] Backend centre frequency
BANDWDTH=                 400. / [MHz] Bandwidth of backend
SCANTYPE= 'Drift   '           / Scan type
INSTRUME= 'Total Power'        / Radiometer type
INSTFLAG= 'None    '           / Radiometer flags
STEPSEQ = 'HPSZ    '           / Stepping sequence
SCANDIST=    0.186943666837938 / Scan length (deg)
SCANANGL=                   0. / Scan angle (deg)
SCANTIME=                45.44 / Scan time (s)
STARTX  =  -0.0934718334189692 / Start X position (deg)
STARTY  =              -0.0155 / Start Y position (deg)
STOPX   =   0.0934718334189692 / Stop X position (deg)
STOPY   =              -0.0155 / Stop Y position (deg)
SCAN    =                    1 / Index no of scan
HZZERO1 =     126265.784091414 / [Hz] Counter zero offset
HZZERO2 =     121904.317282469 / [Hz] Counter zero offset
```

The figure shows the summary of a typical HPS HDU for the source Jupiter.

5 Extension 7

Figure 7: Basic setup of a Chart HDU for data monitored at HartRAO.

```
XTENSION= 'BINTABLE'           / binary table extension
BITPIX  =                    8 / 8-bit bytes
NAXIS   =                    2 / 2-dimensional binary table
NAXIS1  =                   24 / width of table in bytes
NAXIS2  =                 3300 / number of rows in table
PCOUNT  =                    0 / size of special data area
GCOUNT  =                    1 / one data group (required keyword)
TFIELDS =                    3 / number of fields in each row
EXTNAME = 'Chart   '           / name of this binary table extension
FRONTEND= '01.3S   '           / Frontend ID
CENTFREQ=               22040. / [MHz] Backend centre frequency
BANDWDTH=                 400. / [MHz] Bandwidth of backend
TCAL1   =                  71. / [K] Cal noise diode value for channel 1
TCALSIG1=                  3.6 / [K] uncertainty in TCAL1
TCALFRQ1=               23000. / [Hz] Frequency the calibration applies to
TCALDAT1= '20070118'           / Calibration date
TCAL2   =                 66.3 / [K] Cal noise diode value for channel 2
TCALSIG2=                  3.2 / [K] uncertainty in TCAL2
TCALFRQ2=               23000. / [Hz] Frequency the calibration applies to
TCALDAT2= '20070118'           / Calibration date
INSTRUME= 'Total Power'        / Radiometer type
HZPERK1 =     2855.69657811234 / [Hz/K] Counter calibration
HZKERR1 =     6.72019730710538 / [Hz/K] Counter cal error
HZPERK2 =     2912.10593946239 / [Hz/K] Counter calibration
HZKERR2 =     5.76556064265191 / [Hz/K] Counter cal error
TSYS1   =     259.704516186508 / [K] System temperature
TSYSERR1=    0.616453838890109 / [K] System temp error
TSYS2   =     256.154850413438 / [K] System temperature
TSYSERR2=    0.513070180850764 / [K] System temp error
HZZERO1 =     126265.784091414 / [Hz] Counter zero offset
HZZERO2 =     121904.317282469 / [Hz] Counter zero offset
TTYPE1  = 'MJD     '           / label for field
TFORM1  = '1D      '           / format of field
TUNIT1  = 'days    '
TTYPE2  = 'Count1  '           / label for field
TFORM2  = '1D      '           / format of field
TUNIT2  = 'Hz      '
TTYPE3  = 'Count2  '           / label for field
TFORM3  = '1D      '           / format of field
TUNIT3  = 'Hz      '
```

The figure presented provides a summary of a typical HDU for the astronomical object Jupiter. Within the header, important general information related to the system temperature is stored, along with other crucial housekeeping parameters.